Theoretical Studies of Compressed Xenon Oxides, Tin Selenide Thermoelectrics, and Defects in Graphene

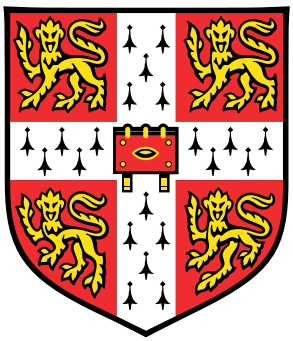

Nicholas Gower Worth

Department of Physics

University of Cambridge

This dissertation is submitted for the degree of

Doctor of Philosophy

King's College

February 2018

I dedicate this thesis to my parents and to my sister Ellie, who have always loved and supported me.

Preface

This dissertation is my own work and includes nothing which is the outcome of work done in collaboration except as declared in the Preface and specified in the text.

The following sections of this dissertation contain work that has been published, or is to be published in the future:

Chapter 4: A. Dewaele, N. Worth, C. J. Pickard, R. J. Needs, S. Pascarelli, O. Mathon, M. Mezouar and T. Irifine, Synthesis and stability of xenon oxides Xe_2O_5 and Xe_3O_2 under pressure. *Nature Chemistry* **8**, 784–790 (2016).

Chapter 5: N. Worth and R. J. Needs, Vibrational and electronic properties of SnSe from first principles. *In preparation.*

It is not substantially the same as any that I have submitted, or, is being concurrently submitted for a degree or diploma or other qualification at the University of Cambridge or any other University or similar institution except as declared in the Preface and specified in the text. I further state that no substantial part of my dissertation has already been submitted, or, is being concurrently submitted for any such degree, diploma or other qualification at the University of Cambridge or any other University or similar institution except as declared in the Preface and specified in the text.

This dissertation contains fewer than 60,000 words including abstract, tables, footnotes and appendices.

Nicholas Gower Worth
February 2018

Acknowledgements

First and foremost, I would like to thank my supervisor, Richard Needs, for his guidance and advice over the years of my PhD, without which this thesis would not have been possible. Many thanks too must go all those people that I have collaborated with in the course of my research, and in particular to Agnès Dewaele, for the great deal of work she carried out in carrying out the experimental aspects of the study into xenon oxides and getting the results published, and to Chris Pickard, for his efforts and advice in that research project.

My time spend carrying out my research in the Theory of Condensed Matter group has been greatly enhanced by those around me. In particular, my office mates Tomeu Monserrat, Jonathan Lloyd-Williams and Joseph Prentice, with whom I have spent many hours in conversation – sometimes even about physics. Their company and advice has enlivened my time in TCM. I greatly appreciate too the advice I have had from, and fun I have had with, Gareth Griffiths, Matt Lyle, Pascal Bugnion, Rob Baldock, Gareth Conduit, John Biggins, Rob Bell, Emma Towlson and James Mayoh. Michael Rutter, TCM's invaluable – and overworked – computer officer has taught me a great deal about computing, academia, and trade unionism, and his conversation, advice and support is very much appreciated.

The work of this thesis has relied on computers well beyond those of the TCM group, and I would like to express my appreciation for the teams running Cambridge's Darwin cluster and the ARCHER machine in Edinburgh. The cost of the time on these computers, and support for PhD, was paid for by the UK Engineering and Physical Sciences Research Council (EPSRC), to which I am extremely grateful. I would like to acknowledge Krishna Kumar for both creating and providing useful support for the LaTeX template used in this thesis.

My time in Cambridge has been made by a great many good friends; too many to mention all of them. Particularly, I would like to thank Katie Reinhart, James Taylor, Charlotte Houldcroft and Scott McKechnie, with whom I have enjoyed many lunches, dinners and films. Many thanks to Scott and James too for proof-reading parts of this thesis. I would also like to express my appreciation to Max Hewkin-Smith,

Andrew Munro (master of the cryptic crossword), Toby Häusermann, Ben Ravenhill, Alison Greggor, Jess Corsi, Jake Howe, Am Chanthong, Krishna Kumar, Wis Wang-Koh, Adam Reid, Anne Musset, Alex Ridge, Luke Edelman, Nicole Grunstra, Anna Bachmann, Katie Fitzpatrick, Mark Schiebler, Renate Fellinger, John Fahy, Stephanie Azzarello, Rowan McAllister, Daniel Unruh, Sarah Williams, Maddie Geddes-Barton and Jack Blaiklock for their friendship; they have made Cambridge, and King's College in particular, such a wonderful place to be in. My friends from secondary school and from my undergraduate days in Oxford have given me so much fun and friendship over the years, for which I am very thankful; without them, I probably wouldn't have been able to carry out this PhD. I thank in particular Carl Hewson, who is very much missed.

I have the privilege of a wonderful extended family, and I would like to pay tribute to my grandparents, uncles, aunts and cousins, who have given me much fun, and love, over these years. Finally, my parents, Erica and Stephen, and my sister Ellie, have provided me with enormous love and support throughout my life, without which this thesis could not have been written. To them I am profoundly thankful.

Abstract

Enormous advances in computing power in recent decades have made it possible to perform accurate numerical simulations of a wide range of systems in condensed matter physics. At the forefront of this progress has been density functional theory (DFT), a very popular approach to tackling the complexity of quantum-mechanical systems that very often strikes a good balance between accuracy and tractability in light of the finite computational resources available to researchers.

This thesis describes work utilising DFT methods to tackle two distinct problems. Firstly, the theoretical prediction of stable and metastable periodic structures under specified conditions using the *ab initio* random structure searching (AIRSS) method, which involves a large scale exploration of the Born-Oppenheimer energy surface, and secondly the use of a vibrational self-consistent field (VSCF) approach to investigate the effects of nuclear motion and anharmonicity in crystal systems, which involves a local exploration of the Born-Oppenheimer energy surface.

The AIRSS crystal structure prediction method is here applied to a study of defect structures in graphene. It is also applied to a study of the xenon-oxygen binary system under a range of geological pressures (83–200 GPa). Novel xenon oxide structures are predicted and characterised theoretically. This work was carried out in collaboration with an experimental study of the system at the lower end of the pressure range.

The VSCF approach to investigating anharmonicity is here applied to the study of tin selenide (SnSe), a material that has recently been shown to demonstrate considerable promise as a thermoelectric material. In this thesis, the effects of the anharmonic nuclear motion on the vibrational and electronic properties of SnSe are investigated quantitatively.

Table of Contents

List of Figures

List of Tables

Nomenclature

Quantum Mechanics and Density Functional Theory

a, b, c, α, β, γ	Lattice parameters
V_{cell}	Unit cell volume
$\vec{L}$	General lattice vector
$\widetilde{a}, \widetilde{b}, \widetilde{c}$	Reciprocal lattice vectors
$\vec{G}$	General reciprocal lattice vector
$\vec{k}$	BZ wavevector
k_F	Fermi wavevector
$\hat{H}_{total}$	Total many-body Hamiltonian
$\hat{H}_{el}$	Electronic Hamiltonian
$\hat{H}_{KS}$	Kohn-Sham Hamiltonian
$\hat{H}_{nucl}$	Nuclear vibrational Hamiltonian
$\hat{T}_e$	Electronic kinetic energy operator
$\hat{T}_N$	Nuclear kinetic energy operator
$\hat{V}_{int}$	Electron-electron Coulomb energy operator
$\hat{V}_{ext}$	Electron-nucleus Coulomb energy operator
$\hat{V}_{KS}$	Kohn-Sham potential
E_{HK}	Hohenberg-Kohn energy functional
$\hat{T}_s$	Independent-particle electronic kinetic energy functional
F_{HK}	Hohenberg-Kohn universal functional
ϵ_{xc}^{hom}	Exchange-correlation energy density of HEG
Ψ	Total electronic wavefunction
Φ	Total vibrational wavefunction
$\phi_i(\vec{\mathrm{x}})$	Hartree-Fock spin-orbital
ψ_i	Single-particle wavefunction
ϵ_i	Single-particle Kohn-Sham eigenvalue
φ_n	Vibrational single-mode wavefunction
E_{xc}	Exchange-correlation energy functional

$n(\vec{r})$	Electron density function
$n_0(\vec{r})$	Ground-state electron density function
E_0	Ground-state energy
E_H	Hartree energy
E_{N-N}	Nucleus-nucleus Coulomb energy
E_{DFT-D}	DFT energy with *SEDC*
E_{cut}	Cut-off energy
μ	Chemical potential
$\hat{O}$	Operator of observable O

Structure Searching

G	Gibbs free energy
H	Enthalpy
N	Number of atoms
P	Pressure
T	Absolute temperature

Acronyms / Abbreviations

AIRSS	*Ab initio* random structure searching
BO	Born-Oppenheimer
BTE	Boltzmann transport equation
BZ	1^{st} Brillouin zone
DAC	Diamond anvil cell
DFT	Density functional theory
DoS	Density of states
eDoS	Density of electronic states
EoS	Equation of state
FFT	Fast Fourier transform
GGA	Generalised gradient approximation
HA	Harmonic approximation
HEG	Homogeneous electron gas
HF	Hartree-Fock
HO	Harmonic oscillator
LDA	Local density approximation
NDSC	Non-diagonal supercell
PAA	Principle axis approximation
PDoS	Partial density of states

PES	Potential energy surface
PXRD	Powder X-ray diffraction
SEDC	Semi-empirical dispersion correction
TEG	Thermoelectric generator
TER	Thermoelectric refrigerator
vdW	van der Waals
VSCF	Vibrational self-consistent field
XAS	X-ray absorption spectroscopy
xc	Exchange-correlation

Chapter 1

Thesis Outline

Predicting and understanding the behaviour of matter in the solid phase is one of the foremost challenges occupying modern physics. This behaviour is enormously dependent on the atomic arrangement within the material. Though crystal structure – where atoms 'sit' in periodic solids – can often be determined experimentally, this can sometimes be challenging or impossible. In such circumstances, theoretical approaches can be highly effective. Chapters 3 and 4 of this thesis describe the application of one such approach to *crystal structure prediction*. Of course, in reality, atoms do not 'sit' in one place, but are in motion. The effects of the quantum and thermal motion of atomic nuclei can be of vital importance to understanding the behaviour of materials. Nuclear motion is commonly treated using the *harmonic approximation*, but in some materials this approximation is simply not accurate enough. Chapter 5 of this thesis describes the application of the *vibrational self-consistent field* (VSCF) approach to dealing with anharmonicity in crystals. Advances in these fields have been made possible by the development of computational approximations to quantum mechanics – the set of physical laws that determines behaviour at an atomic level – coupled with the exponential growth in computing power available to scientists.

This thesis is laid out as follows. In Chapter 2, the theoretical background to the work in this thesis is laid out, beginning with crystal structure. Next, starting from quantum mechanics, density functional theory (DFT) is introduced, including details of its practical implementation within the computational code CASTEP. Having introduced the basic theory, we move on to the application of DFT to real systems, covering the basics of stable crystal structure, and then moving on to theoretical approaches to predicting crystal structure, principally the *ab initio* random structure searching (AIRSS) method. The problem of nuclear vibration is then introduced. Two

approaches to solving this problem are laid out: the harmonic approximation, and the VSCF method.

Chapter 3 reports the results of a project in which AIRSS was used to search for a variety of metastable defects in graphene monolayers.

Chapter 4 reports the results of research conducted in collaboration with experimentalists to predict, identify and characterise stable structures in the xenon-oxygen binary system at high pressures approaching 1 Mbar. Higher-pressure phases are also predicted. These xenon oxides are all characterised using density functional theory, and conclusions drawn about the stability of xenon oxides under geological pressures.

In Chapter 5, the results of a theoretical study of tin selenide (SnSe) are reported. Thermal expansion, and the effects of thermal motion on the vibrational and electronic properties of SnSe are studied using an accurate DFT mapping of the Born-Oppenheimer energy surface together with the VSCF method.

Finally, the work in this thesis is summarised and avenues for future investigation are discussed.

Chapter 2

Theoretical Overview

This chapter lays out the theoretical framework for the work of this thesis, beginning with important concepts in crystal systems. Density functional theory is then introduced, starting from many-body quantum mechanics. Next, crystal structure prediction is introduced, with one particular method – *ab initio* random structure searching – outlined. Finally, the problem of vibrations in solids is outlined, with two approaches to solving the problem – the harmonic approximation and the vibrational self-consistent field approach – laid out.

2.1 Crystal Systems

The work in this thesis concerns the properties of crystalline systems. Crystals are solid materials in which the position of the atoms conforms to a regular, repeating pattern throughout the material. Crystals exist widely in nature, and understanding their properties is of considerable interest. The calculation of crystal properties from first principles requires knowledge of the atomic arrangement in the crystal. The description of this atomic arrangement is called *crystal structure*.

The basic unit used to describe the atomic structure of a crystal is the *unit cell*. This is a theoretical construction that describes the entire crystal system through translation operations in three dimensions. The set of translation operations used to described the crystal is usually considered to be infinite, so that the crystal spans all of space. Of course, this is not true; however crystals will generally contain an extremely large number of unit cells. For example, a one-carat diamond contains $\sim 10^{21}$ conventional unit cells. The bulk of a real crystal is sufficiently far from the edge of the crystal that it behaves in almost exactly the same way as the hypothetical infinite crystal.

The unit cell can be described by six parameters that define the cell itself: three lengths, denoted a, b and c, and three angles, denoted α, β and γ. These six parameters define a parallelepiped box that constitutes the translational repeating unit. There are infinitely many choices that can be made in defining the unit cell of a crystal structure, but conventional choices favour small cells in which the symmetries of the crystal structure are manifest. An example of a generic empty unit cell is depicted in Fig. 2.1.

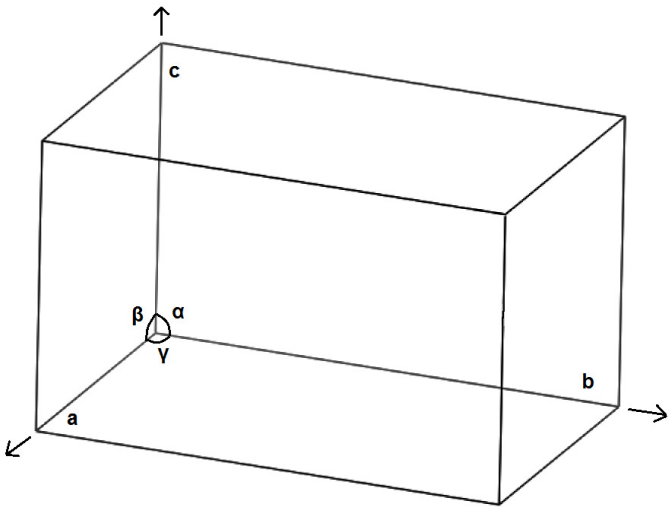

Fig. 2.1 A generic unit cell. The lattice parameters are the lengths of the sides, a, b and c, and the angles between them, α, β and γ.

The atoms that make up the crystal can be fully described within the unit cell, with the full crystal formed by a periodic repetition of the atoms in the unit cell. The atomic positions are thus subject to periodic boundary conditions. In many crystals, the atoms are found at points of symmetry. The generic unit cell has $3(N+1)$ degrees of freedom, where N is the number of atoms contained within the unit cell. This consists of 3 spatial degrees of freedom within the unit cell for each atom, plus 6 degrees of freedom in the unit cell parameters. The translational symmetry of the unit cell that all crystal systems possess removes 3 degrees of freedom.

2.2 Many-Body Quantum Mechanics

Interactions on an atomic scale are described by quantum mechanics. The starting point is the non-relativistic many-body Hamiltonian $\hat{H}_{total}$ – the operator correspond-

ing to the total energy of the atomic system – which is considered to consist of N_e electrons and N_N nuclei. In the absence of an external magnetic field, only the kinetic and electrostatic potential (Coulomb) energies are considered. The Hamiltonian is therefore [1]:

$$\begin{aligned}\hat{H}_{total} = &\sum_i -\frac{\hbar^2}{2m_e}\nabla_i^2 \;+\; \sum_I -\frac{\hbar^2}{2m_I}\nabla_I^2 \;+\; \frac{1}{2}\sum_{i\neq j}\frac{e^2}{4\pi\epsilon_0|\vec{r}_i-\vec{r}_j|} \\ &+\; \sum_{i,I} -\frac{Z_I e^2}{4\pi\epsilon_0|\vec{r}_i-\vec{R}_I|} \;+\; \frac{1}{2}\sum_{I\neq J}\frac{Z_I Z_J e^2}{4\pi\epsilon_0|\vec{R}_I-\vec{R}_J|}.\end{aligned} \tag{2.1}$$

m and Z denote masses and atomic numbers, respectively; $\vec{r}$ and $\vec{R}$ denote the position coordinates for electrons and nuclei, respectively. The first two terms correspond respectively to the kinetic energies of the electrons and of the nuclei. The last three terms correspond to electrostatic potential energies, firstly between pairs of electrons, then between the electrons and the nuclei and finally between pairs of nuclei. The factor of a half in the electron-electron and nucleus-nucleus Coulomb terms is to prevent double-counting. Nuclei are represented by uppercase letters and electrons by lowercase letters.

For the sake of simplicity, we change now to Hartree atomic units ($|e| = m_e = \hbar = 4\pi\epsilon_0 = 1$), which will be used throughout the rest of this thesis. We may now express the Hamiltonian as

$$\hat{H}_{total} = \hat{T}_e + \hat{T}_N + \hat{V}_{int} + \hat{V}_{ext} + \hat{V}_{N-N}, \tag{2.2}$$

in which we have defined

$$\hat{T}_e = -\frac{1}{2}\sum_i \nabla_i^2, \tag{2.3}$$

$$\hat{T}_N = -\frac{1}{2}\sum_I \frac{1}{m_I}\nabla_I^2, \tag{2.4}$$

$$\hat{V}_{int} = \frac{1}{2}\sum_{i\neq j}\frac{1}{|\vec{r}_i-\vec{r}_j|}, \tag{2.5}$$

$$\hat{V}_{ext} = -\sum_i V(r_i) = \sum_i\sum_I \frac{Z_I}{|\vec{r}_i-\vec{R}_I|}, \tag{2.6}$$

and

$$\hat{V}_{N-N} = \frac{1}{2} \sum_{I \neq J} \frac{Z_I \, Z_J}{|\vec{R}_I - \vec{R}_J|}. \tag{2.7}$$

$\hat{T}_e$ and $\hat{T}_N$ are the electron and nuclei kinetic energy operators, respectively, $\hat{V}_{int}$ is the "internal" electrostatic potential energy between the electrons, $\hat{V}_{ext}$ is the "external" electrostatic potential energy of the electrons due to the external potential generated by the nuclei, and $\hat{V}_{N-N}$ is the Coulomb interaction energy between the nuclei. This Hamiltonian is simple enough to write down, but solving it for all the particles found in a crystal system is impossible to do in an exact, analytical way. However, as we shall now see, it is possible to solve it approximately.

2.2.1 The Born-Oppenheimer Approximation

To begin with, the *Born-Oppenheimer (BO) approximation* [2] is applied. The BO approximation assumes that the motions of the electrons and of the nuclei in a quantum system are separable, so that the wavefunction of the system, Ψ_{total}, can be expressed as the product of an electronic wavefunction, ψ, and a nuclear wavefunction, φ. ψ is a function of the collective electronic position vector $\vec{r} = (\vec{r}_1, \ldots, \vec{r}_{N_e})$ and the collective nuclear position vector $\vec{R} = \left(\vec{R}_1, \ldots, \vec{R}_{N_N}\right)$; the latter enters into the problem as a parameter in the electronic part of the Hamiltonian, $\hat{H}_{el}$. φ is a function of the collective nuclear coordinates $\vec{R}$ and time t only.

Let us first define the electronic Hamiltonian $\hat{H}_{el}$ as

$$\hat{H}_{el} = \hat{T}_e + \hat{V}_{int} + \hat{V}_{ext}, \tag{2.8}$$

so that

$$\hat{H}_{total} = \hat{H}_{el} + \hat{T}_N + \hat{V}_{N-N}. \tag{2.9}$$

The BO approximation starts with a trial solution in which the total wavefunction is represented by products of nuclear wavefunctions φ_n and electronic wavefunctions ψ_n [3]:

$$\Psi_{total}(\vec{r}, \vec{R}, t) = \sum_n \varphi_n(\vec{R}, t) \, \psi_n(\vec{r}, \vec{R}). \tag{2.10}$$

The electronic wavefunctions $\psi_n(\vec{r},\vec{R})$ are those that solve the electronic Hamiltonian defined in equation (2.9):

$$\hat{H}_{el}\,\psi_n(\vec{r},\vec{R}) = E_n^{el}(\vec{R})\,\psi_n(\vec{r},\vec{R}). \tag{2.11}$$

Substituting the trial solution (2.10) into the time-dependent Schrödinger equation with the Hamiltonian of equation (2.9), and selecting out a single nuclear wavefunction φ_m by multiplying from the left with $\langle\psi_m(\vec{r},\vec{R})|$, we obtain

$$\begin{aligned}
&\left[i\frac{\partial}{\partial t} + \frac{1}{2}\sum_I \frac{1}{m_I}\nabla_I^2 - \hat{V}_{N-N} - E_m^{el}(\vec{R})\right]\varphi_m(\vec{R},t) = \\
&-\frac{1}{2}\sum_n\sum_I \frac{1}{m_I}\left\langle\psi_m\middle|\nabla_I^2\middle|\psi_n\right\rangle\varphi_n(\vec{R},t) \\
&-\sum_n\sum_I \frac{1}{m_I}\vec{\nabla}_I\varphi_n(\vec{R},t)\cdot\left\langle\psi_m\middle|\vec{\nabla}_I\middle|\psi_n\right\rangle,
\end{aligned} \tag{2.12}$$

in which we have made use of the relation

$$\nabla_I^2\,\varphi_n\psi_n = \psi_n\nabla_I^2\varphi_n + 2\,\vec{\nabla}_I\varphi_n\cdot\vec{\nabla}_I\psi_n + \varphi_n\nabla_I^2\,\psi_n. \tag{2.13}$$

Neglecting the first term on the right hand side of equation (2.13) constitutes the *adiabatic approximation*, which assumes that the evolution of the nuclear wavefunctions $\{\varphi_n\}$ occurs sufficiently slowly to prevent mixing of electronic states $\{\psi_n\}$. The electrons instantaneously follow the motion of the nuclei; a system in a given electronic stationary state – for example, the ground state – will remain in that stationary state as the nuclear wavefunctions evolve (although the state itself will change). The full BO approximation additionally neglects the second term on the right hand side, thereby allowing the total wavefunction to be represented by a single term of equation (2.10):

$$\Psi_{total}(\vec{r},\vec{R},t) = \varphi(\vec{R},t)\,\psi(\vec{r},\vec{R}). \tag{2.14}$$

The validity of the BO approximation rests on the much greater mass of the nuclei compared to the electrons, leading to electronic relaxation occurring on a much shorter timescale than the motion of nuclei. For the purpose of calculating *electronic structure* – the electronic part of the total wavefunction, $\psi(\vec{r},\vec{R})$ – the semi-classical approach is taken, with the nuclei considered to be point particles in a fixed configuration. As such, the nucleus-nucleus Coulomb term is a constant contribution towards the energy of the system, and the electron-nucleus interaction term can be thought of as an interaction

between the electrons and a fixed external potential generated by all of the stationary nuclei. Thus for the electronic problem we can drop the nuclear kinetic energy term and consider the Hamiltonian $\hat{H}$ to be:

$$\hat{H} = \hat{T}_e + \hat{V}_{int} + \hat{V}_{ext} + E_{N-N}, \tag{2.15}$$

where

$$E_{N-N} = \frac{1}{2} \sum_{I \neq J} \frac{Z_I Z_J}{|\vec{R}_I - \vec{R}_J|}. \tag{2.16}$$

We note here that the kinetic and internal electrostatic potential energy terms, because they involve only the electrons, take the same form for all systems of electrons, depending only on N_e. The only non-constant term that is affected by the position of the nuclei is the external potential energy term, as it is the nuclei that are generating the external potential felt by the electrons.

Consideration of the nuclear wavefunction yields the nuclear eigenvalue equation:

$$\hat{H}_{nucl} \varphi_m(\vec{R}, t) = E_m \, \varphi_m(\vec{R}, t), \tag{2.17}$$

where

$$\hat{H}_{nucl} = \sum_I -\frac{1}{2m_I} \nabla^2 + \epsilon_m(\vec{R}), \tag{2.18}$$

$$\epsilon_m(\vec{R}) = E_m^{el}(\vec{R}) + E_{N-N}(\vec{R}) \tag{2.19}$$

Approaches to solving equation (2.17) are presented later in this chapter. For now, we shall only consider the solution of the electronic problem of equation (2.11).

2.2.2 The Electronic Problem

To find the energy eigenvalues and eigenfunctions of the Hamiltonian $\hat{H} = \hat{H}_{el} + E_{N-N}$, and so be able to calculate properties of the system, we must solve the time-independent Schrödinger equation:

$$\hat{H} \Psi(\vec{r}) = E \Psi(\vec{r}) \tag{2.20}$$

The ground state is represented by the solution to equation (2.20) with the lowest value of E. As we are dealing with a system of indistinguishable fermions, the overall wavefunction of the system must be antisymmetric under particle exchange.

The wavefunction contains all information about the state of the system, so that from it we are able to calculate all of the properties of the system. For an observable $\mathcal{O}$, whose operator is denoted by $\hat{\mathcal{O}}$, the expectation value of the operator is given by:

$$\langle \hat{\mathcal{O}} \rangle = \frac{\langle \Psi | \hat{\mathcal{O}} | \Psi \rangle}{\langle \Psi | \Psi \rangle}. \tag{2.21}$$

We consider first the total energy of the system:

$$E = \langle \hat{H} \rangle = \langle \hat{T}_e \rangle + \langle \hat{V}_{int} \rangle + \langle \hat{V}_{ext} \rangle + E_{N-N}. \tag{2.22}$$

We can rewrite the expectation value for $\hat{V}_{ext}$ as an explicit integral over the electron density, $n(\vec{r})$:

$$\hat{V}_{ext} = \int d^3\vec{r} \;\; V_{ext}(\vec{r}) \; n(\vec{r}), \tag{2.23}$$

where the electron density is the expectation value of the density operator:

$$\begin{aligned} n(\vec{r}) = \frac{\langle \Psi | \hat{n}(\vec{r}) | \Psi \rangle}{\langle \Psi | \Psi \rangle} &= \frac{\int d^3\vec{r}_1 ... d^3\vec{r}_N \sum_{i=1}^{N} \delta(\vec{r} - \vec{r}_i) \; |\Psi(\vec{r}_1, ..., \vec{r}_N)|^2}{\int d^3\vec{r}_1 ... d^3\vec{r}_N \; |\Psi(\vec{r}_1, ..., \vec{r}_N)|^2} \\ &= N \frac{\int d^3\vec{r}_2 ... d^3\vec{r}_N \; |\Psi(\vec{r}, \vec{r}_2, ..., \vec{r}_N)|^2}{\int d^3\vec{r}_1 ... d^3\vec{r}_N \; |\Psi(\vec{r}_1, ..., \vec{r}_N)|^2}. \end{aligned} \tag{2.24}$$

Putting this together, we obtain as an expression for the energy of the system:

$$E = \langle \hat{T}_e \rangle + \langle \hat{V}_{int} \rangle + \int d^3\vec{r} \;\; V_{ext}(\vec{r}) \; n(\vec{r}) \;\; + \;\; E_{N-N}. \tag{2.25}$$

Finally, when actually attempting to evaluate the energy terms in a system subject to periodic boundary conditions, Coulomb interaction terms should be arranged into neutral groups to avoid energies diverging. This means that we need to rearrange equation (2.25) to evaluate terms in which the charges involved sum to zero. To do this, we introduce the Hartree term, E_H:

$$E_H = \frac{1}{2} \int d^3\vec{r} d^3\vec{r}' \frac{n(\vec{r}) n(\vec{r}')}{|\vec{r} - \vec{r}'|}. \tag{2.26}$$

This is the energy of a classical continuous charge distribution with a charge density $n(\vec{r})$. By defining a classical Coulomb energy:

$$E_{CC} = E_H + \int d^3\vec{r}\, V_{ext}(\vec{r})\; n(\vec{r}) \;+\; E_{N-N}, \tag{2.27}$$

we can rearrange equation (2.25) to obtain:

$$E = \langle \hat{T}_e \rangle + (\langle \hat{V}_{int} \rangle - E_H) + E_{CC}. \tag{2.28}$$

The first term represents the kinetic energy of the electrons, the third term the Coulomb energy of a continuous classical charge distribution with the same density as the electrons in the space around the nuclei, and the second term represents the energy difference between this picture and the true picture, in which there are discrete electrons with interactions and correlations. The second two terms, which relate to Coulomb energies, are both neutral - the second term has two sub-terms concerning electron-electron interactions that cancel, while the third term has sub-terms relating to equal amount of positive and negative charge. The Coulomb terms are usually evaluated using Ewald summation, which splits the summation two parts: a short-range term evaluated in real space, and a long-range term evaluated in reciprocal space; both terms are rapidly convergent [1, 4].

Equation (2.28) is impossible to evaluate exactly for more than one electron. As the electrons interact, the number of states required to describe the wavefunction grows exponentially with system size. For many-electron crystal systems, equation (2.28) is far beyond our capabilities to solve even numerically, without making some further approximations. There are various approximate methods available. One popular class of methods, encompassing *Hartree-Fock* and *post-Hartree-Fock* theories, will be outlined first, followed by *density functional theory*, which is the primary methodology used for the work of this thesis.

2.2.3 Hartree-Fock Theory and Beyond

Hartree-Fock is a *trial wavefunction*-type method based upon the *ansatz* of using a Slater determinant of single-particle spin-orbitals $\phi_i(\vec{\mathrm{x}}_j) = \psi_i^{\sigma}(\vec{r}_j)\alpha_i(\sigma_j)$ to represent the total wavefunction [1]:

$$\Psi(\vec{\mathrm{x}}_1, \vec{\mathrm{x}}_2, \ldots, \vec{\mathrm{x}}_N) \;=\; \frac{1}{\sqrt{N!}} \begin{vmatrix} \phi_1(\vec{\mathrm{x}}_1) & \phi_2(\vec{\mathrm{x}}_1) & \cdots & \phi_N(\vec{\mathrm{x}}_1) \\ \phi_1(\vec{\mathrm{x}}_2) & \phi_2(\vec{\mathrm{x}}_2) & \cdots & \phi_N(\vec{\mathrm{x}}_2) \\ \vdots & \vdots & \ddots & \vdots \\ \phi_1(\vec{\mathrm{x}}_N) & \phi_2(\vec{\mathrm{x}}_N) & \cdots & \phi_N(\vec{\mathrm{x}}_N) \end{vmatrix}. \tag{2.29}$$

The nature of the determinant ensures that the wavefunction is antisymmetric under exchange, as is required for indistinguishable fermions, so that exchange symmetry is built into the approach. Each term in the Slater determinant is the product of independent-particle wavefunctions, so the electrostatic energy, including exchange effects, is treated in a mean-field approach. The effects of correlation are not considered. The total electronic energy in Hartree-Fock is

$$\begin{aligned} E_{el}^{HF} = \left\langle \Psi \middle| \hat{H} \middle| \Psi \right\rangle = & \sum_i \left\langle \phi_i \middle| -\frac{1}{2}\nabla^2 + V_{ext}(\vec{r}) \middle| \phi_i \right\rangle + \frac{1}{2}\sum_{i,j} \left\langle \phi_i\phi_j \middle| \frac{1}{|\vec{r}-\vec{r}\,'|} \middle| \phi_i\phi_j \right\rangle \\ & -\frac{1}{2}\sum_{i,j} \left\langle \phi_i\phi_j \middle| \frac{1}{|\vec{r}-\vec{r}\,'|} \middle| \phi_j\phi_i \right\rangle, \end{aligned} \tag{2.30}$$

where $V_{ext}(\vec{r})$ is the external potential felt by the electrons due to the nuclei. For the sake of simplicity, let us consider the case of orthonormal spin-orbitals and a spin-independent Hamiltonian. Equation (2.30) then evaluates to

$$\begin{aligned}\left\langle \Psi \middle| \hat{H} \middle| \Psi \right\rangle = & \underbrace{\frac{1}{2}\sum_{i,\sigma}\int d\vec{r}\,\psi_i^{\sigma *}(\vec{r})\left[-\frac{1}{2}\nabla^2 + V_{ext}(\vec{r})\right]\psi_i^{\sigma}(\vec{r})}_{\text{Single-particle energy}} \\ & + \underbrace{\sum_{i<j}\int d\vec{r}d\vec{r}'\,\psi_i^{\sigma_i *}(\vec{r})\psi_j^{\sigma_j *}(\vec{r}')\frac{1}{|\vec{r}-\vec{r}'|}\psi_i^{\sigma_i}(\vec{r})\psi_j^{\sigma_j}(\vec{r}')}_{\text{Direct interaction},J} \\ & - \underbrace{\frac{1}{2}\sum_{i<j}\delta_{\sigma_i\sigma_j}\int d\vec{r}d\vec{r}'\,\psi_i^{\sigma *}(\vec{r})\psi_j^{\sigma *}(\vec{r}')\frac{1}{|\vec{r}-\vec{r}'|}\psi_j^{\sigma}(\vec{r})\psi_i^{\sigma}(\vec{r}')}_{\text{Exchange interaction},K}.\end{aligned} \tag{2.31}$$

The first term is the single-particle term, containing each electron's kinetic energy and Coulomb energy due to interaction with the nuclei. The second term, the *direct* term, denoted J, is the standard Coulomb energy for non-interacting particles. The final term, the *exchange* term, denoted K, is the correction to the Coulomb energy due to exchange effects, which are introduced through the Slater determinant formulation. The antisymmetry of the wavefunction means that the electronic wavefunction must tend to zero as $\vec{r}_i \to \vec{r}_j$, having the effect of reducing the probability of two electrons being close together. As two electrons being close together yields a large Coulomb energy, this exchange effect therefore acts to reduce the total energy of the system.

The Hartree-Fock ground state is found by minimising the system energy using the variational method applied to the individual particle spin-orbitals, which are subject to the mean field potential of the other spin-orbitals. The minimisation proceeds iteratively until the final field from the energy-minimised spin-orbitals is self-consistent with the field the spin-orbitals were minimised in. For this reason Hartree-Fock is known as a *self-consistent field* method. This procedure utilises the fact that the expectation value of the Hamiltonian with respect to a general wavefunction Ψ has the ground state energy as a lower bound (see Appendix A for a proof):

$$E_0 \leqslant \left\langle \Psi \middle| \hat{H} \middle| \Psi \right\rangle. \tag{2.32}$$

The spin-orbitals can be expressed in a computationally convenient basis set, such as Slater-type orbitals [5], or Gaussian-type orbitals [6].

Post-Hartree-Fock methods such as Møller-Plesset perturbation theory, coupled cluster and configuration interaction attempt to build upon Hartree-Fock methods to

include electron correlation effects [3]. This generally improves accuracy, at a cost of greater computational expense. The Hartree-Fock method scales with system size N as $\mathcal{O}(N^4)$, with post-Hartree-Fock methods scaling as $\mathcal{O}(N^5)$ or higher.

Hartree-Fock and post-Hartree-Fock methods are widely used in computational chemistry, but they are less widely used for periodic crystal systems. For these systems, the more commonly-used choice is *density functional theory (DFT)*.

2.3 Density Functional Theory

2.3.1 The Hohenberg-Kohn Theorems

At the heart of density functional theory are the two Hohenberg-Kohn theorems, introduced by Hohenberg and Kohn in 1964 [7], which were extremely important in the development of density functional theory. The theorems tell us that instead of dealing with trial wavefunctions in $3N$ electron position coordinates, it is possible to do exact calculations using only the total electron ground state density, which is a function of three spatial coordinates only, and that a functional of this ground state density exists that determines the total energy of the system. However, the theorems do not establish the form of this functional; as such, they provide no insight into how to actually find the ground state density or how to extract properties from it.

The first of the two theorems states that the ground state electron density, n_0, is sufficient to construct the external potential V_{ext} that the electrons feel, up to a constant energy term. Therefore if two external potentials result in the same ground state electron density, then the two potentials can differ by at most a constant. This theorem can be proven by contradiction. Suppose we have two external potentials, V_{ext} and V'_{ext}, which we take to differ by more than a constant, that both lead to the same ground state electron density $n_0(\vec{r})$. These two external potentials can be used to define corresponding Hamiltonians, $\hat{H}$ and $\hat{H}'$, which have ground state wavefunctions Ψ and Ψ' and corresponding ground state energies E_0 and E'_0. We assume in this proof that the ground states are non-degenerate, but the proof can be extended to other cases [8].

These ground state wavefunctions cannot be eigenstates of the other Hamiltonian: if we had $\hat{H}\left|\Psi'\right\rangle = E\left|\Psi'\right\rangle$ then we would obtain:

$$(\hat{H} - \hat{H}')\left|\Psi'\right\rangle = (\hat{V}_{ext} - \hat{V}'_{ext})\left|\Psi'\right\rangle = (E - E'_0)\left|\Psi'\right\rangle, \tag{2.33}$$

which would require that $\hat{V}_{ext}$ and $\hat{V}'_{ext}$ differ by only a constant, which is contrary to our original definition of the potentials.

As Ψ' therefore cannot be the ground state of $\hat{H}$, we can use the variational method (2.32) to conclude that

$$E_0 = \langle\Psi|\hat{H}|\Psi\rangle < \langle\Psi'|\hat{H}|\Psi'\rangle\,. \tag{2.34}$$

We can re-arrange the rightmost term in (2.34) as follows:

$$\begin{aligned}\langle\Psi'|\hat{H}|\Psi'\rangle &= \langle\Psi'|\hat{H}'|\Psi'\rangle + \langle\Psi'|(\hat{H}-\hat{H}')|\Psi'\rangle \\ &= E'_0 + \int d^3\vec{r}\ (V_{ext} - V'_{ext})\, n_0(\vec{r}),\end{aligned} \tag{2.35}$$

to obtain

$$E_0 < E'_0 + \int d^3\vec{r}\ (V_{ext} - V'_{ext})\, n_0(\vec{r}). \tag{2.36}$$

However, this procedure can be repeated for E'_0, from which we find:

$$E'_0 < E_0 + \int d^3\vec{r}\ (V'_{ext} - V_{ext})\, n_0(\vec{r}). \tag{2.37}$$

Summation of (2.36) and (2.37) yields $E_0 + E'_0 < E_0 + E'_0$, a contradictory result that proves that V_{ext} and V'_{ext} cannot differ by more than a constant if they are to produce the same ground state density $n_0(\vec{r})$.

The implications of this first theorem are profound. Since the ground state electron density is sufficient to fix V_{ext} up to a constant energy shift, if we know n_0 then the Hamiltonian is fully specified. If we know the Hamiltonian then we can in principle solve it to obtain the wavefunctions for all the states of the system, and from the wavefunctions we can determine any properties of the system that we are interested in. We can therefore express any property of the system as a functional of the ground state electron density. However, while the first Hohenberg-Kohn theorem tells us that this is possible *in principle*, it does not directly lead to solutions for physical problems in practice.

The second Hohenberg-Kohn theorem states that for any V_{ext} it is possible to create a functional for the energy of the system, $E[n(\vec{r})]$, which takes as its input the electron density function. Minimising this functional will give the ground state energy and the density function that minimises $E[n(\vec{r})]$ is the ground state density, $n_0(\vec{r})$. Thus we can obtain the ground state density – from which all properties of the system can

in principle be determined – by knowing the form of the energy functional. Mermin extended this theorem to excited electron states corresponding to finite-temperature thermal equilibrium [9].

The second Hohenberg-Kohn theorem is derived from the first. Let us consider only "V-representable" densities $n(\vec{r})$, which are those densities that are the ground state density of some external potential V_{ext}. As each of these densities corresponds to a particular Hamiltonian (up to a constant energy shift) – from which in turn the wavefunction and so all of the properties of the system can be deduced – all of the properties of the system can be expressed as a functional of the density:

$$\begin{aligned} E_{HK}[n] &= T[n] + E_{int}[n] + \int d^3\vec{r}\, V_{ext}(\vec{r})n(\vec{r}) + E_{N-N} \\ &= F_{HK}[n] + \int d^3\vec{r}\, V_{ext}(\vec{r})n(\vec{r}) + E_{N-N}. \end{aligned} \tag{2.38}$$

The Hohenberg-Kohn functional $F_{HK}[n]$, made up of the electrons' kinetic energy and internal electrostatic potential energy terms, is a *universal functional*, in that it is the same for all electron systems, and does not depend on the external potential.

Let us now consider a system with external potential V_{ext}, which gives rise to a Hamiltonian $\hat{H}$, a ground state wavefunction Ψ_0 and a non-degenerate ground state density $n_0(\vec{r})$. Then the ground state energy, which is the expectation value of the Hamiltonian $\hat{H}$ in the ground state Ψ_0, is also given by the Hohenberg-Kohn functional with the ground state density:

$$E_0 = E_{HK}[n_0] = \langle \Psi_0 | \hat{H} | \Psi_0 \rangle . \tag{2.39}$$

If we now consider a wavefunction, Ψ', leading to a different density, $n'(\vec{r})$, then we can see from the variational principle that:

$$E_{HK}[n_0] = \langle \Psi_0 | \hat{H} | \Psi_0 \rangle < \langle \Psi' | \hat{H} | \Psi' \rangle = E_{HK}[n'], \tag{2.40}$$

so we conclude that the value of the Hohenberg-Kohn energy functional is greater than the ground-state energy for any density other than the ground state energy, which is achieved at the ground state density. Minimising the Hohenberg-Kohn energy functional with respect to the electron density thus results in the ground-state energy, and the density that produces this minimum value is the ground-state density.[1]

[1] In varying the ground state density, we must maintain the total number of electrons given by the density, $N = \int d^3\vec{r}\; n(\vec{r})$. This is achieved through a Lagrange multiplier, so that $E_{HK}[n] - \mu\left(\int d^3\vec{r}\; n(\vec{r}) - N\right)$ is the quantity that is minimised in the variational method.

An alternative formulation of the Hohenberg-Kohn approach is provided in the work of Levy and Lieb, known as the *constrained search* formulation [10–15]. This involves a two-step minimisation procedure. Working from the wavefunction formulation for the total energy of the system, E:

$$E = \langle\Psi|\hat{H}|\Psi\rangle = \langle\Psi|\hat{T}_e|\Psi\rangle + \langle\Psi|\hat{V}_{int}|\Psi\rangle + \int d^3\vec{r}\, V_{ext}(\vec{r})\, n(\vec{r}) + E_{N-N}, \quad (2.41)$$

the Levy-Lieb energy functional, E_{LL}, is defined as a functional of the density by minimising (2.41) with respect to all wavefunctions Ψ that correspond to the density $n(\vec{r})$:

$$\begin{aligned} E_{LL}[n] &= \min_{\Psi\to n(\vec{r})} \left[\langle\Psi|\hat{T}_e|\Psi\rangle + \langle\Psi|\hat{V}_{int}|\Psi\rangle \right] + \int d^3\vec{r}\, V_{ext}(\vec{r})\, n(\vec{r}) \;+\; E_{N-N} \\ &= F_{LL}[n] + \int d^3\vec{r}\, V_{ext}(\vec{r})\, n(\vec{r}) \;+\; E_{N-N}. \end{aligned} \quad (2.42)$$

$F_{LL}[n]$ is the equivalent of the Hohenberg-Kohn functional $F_{HK}[n]$ within the Levy-Lieb formulation. Equation (2.42) defines the energy functional of the density for all "N-representable" densities – that is, all densities that correspond to an antisymmetric N-electron wavefunction. This is a relaxation of the requirement of the Hohenberg-Kohn formulation that we consider only "V-representable" densities – densities that are the ground state density for some V_{ext}. We can now minimise the density functional defined in (2.42) with respect to the density to obtain the ground state energy and the corresponding density. At this minimum the Levy-Lieb energy functional is equal to the Hohenberg-Kohn energy functional: $E_{LL}[n_0(\vec{r})] = E_{HK}[n_0(\vec{r})]$. There is also no restriction on there being degenerate ground states.

2.3.2 The Kohn-Sham Equations

The Hohenberg-Kohn theorems establish that the total electron density, rather than the many-electron wavefunction Ψ, may be used in the calculation of physical properties. However, they only establish this *in principle* – they do not provide an actual practical method for carrying out calculations. In the year after the Hohenberg-Kohn theorems were published, Kohn and Sham proposed such a method [16], which shall now be outlined here.

The essence of the Kohn-Sham approach is to replace the true problem of solving the Hamiltonian of an interacting many-body system (equation (2.15)) with a different

problem, which approximates the original problem while being much easier to solve. The replacement system, known as the *auxiliary system*, is a *non-interacting* many-body system. At the heart of this is the assumption, originally made by Kohn and Sham, that one can construct an auxiliary non-interacting many-body system whose ground state density is the same as the ground state density of the actual system.

The starting point is the second Hohenberg-Kohn theorem, which allows us to express the system energy (2.25) as a functional of the ground state electron density. The Hohenberg-Kohn energy functional in equation (2.38) can be re-written as:

$$E_{HK} = T_s[n] + E_H[n] + \int d^3\vec{r}\, V_{ext}\; n(\vec{r}) + E_{N-N} + (T[n] - T_s[n] + E_{int}[n] - E_H[n])\,, \tag{2.43}$$

where $T_s[n]$ is a functional for the independent-particle kinetic energy, and $E_H[n]$ is a functional for the classical Hartree energy defined in equation (2.26). The Kohn-Sham approach treats the auxiliary system as being composed of independent particles, so that a total N-electron wavefunction Ψ may be constructed using products of single-particle wavefunctions ψ:

$$\Psi(\vec{r}_1, \vec{r}_2, \ldots, \vec{r}_N) = \prod_{i=1}^{N} \psi_i(\vec{r}_i). \tag{2.44}$$

Such a wavefunction, known as a Hartree product, is not guaranteed to obey exchange symmetry, so in fact we represent the total wavefunction using a Slater determinant, which results in a linear superposition of Hartree-like products:

$$\Psi(\vec{r}_1, \vec{r}_2, \ldots, \vec{r}_N) = \frac{1}{\sqrt{N!}} \begin{vmatrix} \psi_1(\vec{r}_1) & \psi_2(\vec{r}_1) & \cdots & \psi_N(\vec{r}_1) \\ \psi_1(\vec{r}_2) & \psi_2(\vec{r}_2) & \cdots & \psi_N(\vec{r}_2) \\ \vdots & \vdots & \ddots & \vdots \\ \psi_1(\vec{r}_N) & \psi_2(\vec{r}_N) & \cdots & \psi_N(\vec{r}_N) \end{vmatrix} := \langle \{\vec{r}_i\} | \psi_1 \psi_2 \ldots \psi_N \rangle\,. \tag{2.45}$$

The total electron density $n(\vec{r})$ now takes the simple form

$$n(\vec{r}) = \sum_{i=1}^{N} |\psi_i(\vec{r})|^2\,. \tag{2.46}$$

The independent-particle kinetic energy for the system, T_s, is

$$T_s = -\frac{1}{2}\sum_{i=1}^{N} \langle \psi_i | \nabla^2 | \psi_i \rangle = \frac{1}{2}\sum_{i=1}^{N} \int\; d^3\vec{r}\, |\nabla \psi_i(\vec{r})|^2. \tag{2.47}$$

This form makes it clear that T_s is an explicit functional of the single-particle wavefunctions, and so only an implicit functional of the density (applying the Hohenberg-Kohn theorems to the Kohn-Sham system).

We now collect the final four terms of equation (2.43) together to form the *exchange-correlation (xc) functional*:

$$E_{xc}[n] = F[n] - T_s[n] - E_H = \langle \hat{V}_{int} \rangle - E_H + \langle \hat{T}_e \rangle - T_s[n], \tag{2.48}$$

to yield the total energy functional in the Kohn-Sham approach:

$$E[n] = T_s[n] + E_H[n] + \int d^3\vec{r}\, V_{ext}(\vec{r})\; n(\vec{r}) + E_{N-N} + E_{xc}[n]. \tag{2.49}$$

We can see from the form of E_{xc} that the exchange-correlation functional represents the difference between the energy of the real system and that of the independent-particle system where the particle Coulomb interactions are replaced by a continuous charge distribution with the same density as the real system. The exchange-correlation functional thus contains all of the complexity relating to the effects of correlation and exchange, leaving all the other terms well-defined.

The final stage for getting to an equation we can actually solve is minimising the energy defined in equation (2.49). We do this by taking the functional derivative with respect to the conjugate of the wavefunction:

$$\frac{\delta E}{\delta \psi_i^*(\vec{r})} = \frac{\delta T_s}{\delta \psi_i^*(\vec{r})} + \left[\frac{\delta E_{ext}}{\delta n(\vec{r})} + \frac{\delta E_H}{\delta n(\vec{r})} + \frac{\delta E_{xc}}{\delta n(\vec{r})} \right] \frac{\delta n(\vec{r})}{\delta \psi_i^*(\vec{r})} = 0. \tag{2.50}$$

Using (2.45) as well as equation (2.47) and ensuring conservation of electron number constraints using Lagrange multipliers, we get a Schrödinger-like equation for each non-interacting electron:

$$\hat{H}_{KS}\psi_i(\vec{r}) = \epsilon_i \psi_i(\vec{r}). \tag{2.51}$$

$\hat{H}_{KS}$ acts as a Hamiltonian, defined as:

$$H_{KS}(\vec{r}) = -\frac{1}{2}\nabla^2 + V_{KS}(\vec{r}). \tag{2.52}$$

Here, V_{KS} is an effective potential, made up of the several different potentials in the system, which are the functional derivatives of the equivalent energy terms:

$$V_{KS}(\vec{r}) = V_{ext}(\vec{r}) + V_H(\vec{r}) + V_{xc}(\vec{r}). \tag{2.53}$$

It is important to remember that the equations above are for the non-interacting Kohn-Sham auxiliary system, which is related to the physical interacting system in that their ground state electron densities are taken to be identical. The wavefunction (2.45) will not necessarily be a good approximation to the true wavefunction: all we can say is that the non-interacting ground state electron density defined by (2.46) should be the same as the interacting ground state density defined by (2.24). It should also be noted that the Kohn-Sham eigenvalues ϵ_i do not correspond to physical electron energies, and so do not give the energy for adding or removing electrons from the system in general. However, it can be shown that the highest occupied energy level is equal to minus the first ionisation energy in a finite system, or to the Fermi energy in a metal [17]. It should also be noted that the total energy of the physical system is *not* equal to the sum of the Kohn-Sham eigenvalues. Instead the total energy is given by:

$$E = \sum_{i=1}^{N} \epsilon_i - \frac{e^2}{2} \int d^3\vec{r} \int d^3\vec{r}' \frac{n(\vec{r})\, n(\vec{r'})}{\left|\vec{r} - \vec{r'}\right|} - \int n(\vec{r}) V_{xc}(\vec{r}) d^3\vec{r} + E_{xc}[n(\vec{r})]. \tag{2.54}$$

Equations (2.51) – (2.53) form a set of equations we actually have some hope of being able to solve. Later sections will cover the methods for solving these equations, but first we must consider the exchange-correlation functional.

2.3.3 The Exchange-Correlation Functional

The exchange-correlation functional contains all the effects related to exchange and correlation in the interacting system [1]. The derivation of the Kohn-Sham equations outlined in the previous section provides a formal definition of the exchange-correlation functional as the difference between the interacting and Kohn-Sham kinetic energies, and the difference between the true electron-electron interaction energy and the Hartree energy for the Kohn-Sham system. This definition provides us with no particular insight as to the form of the functional, which in principle we could expect to be complicated and non-local. However, we are able to approximate the exchange-correlation functional using relatively simple functional forms that reproduce the physics of many systems to a good level of accuracy. In this section, several of these functional forms will be described; their known shortcomings will be briefly discussed, and corrections for these shortcomings described.

A useful aspect of the exchange-correlation functional is that it can often be well approximated as a local or semi-local functional of the density. Such an approximation greatly reduces the computational complexity of evaluating the functional. For simplicity, the theory laid out in this section is for non-spin-polarised systems. In the spin-polarised theory, the single density function is replaced with densities for each spin component, $n_\uparrow$ and $n_\downarrow$, which are dealt with separately, and the exchange-correlation (xc) functional becomes a functional of the densities of each spin channel.

The local density approximation

One of the most straightforward approaches to obtaining a form for the xc functional is the local density approximation (LDA) [1], in which the exchange-correlation energy of the system at a point is taken to be the same as the exchange-correlation energy of a homogeneous electron gas (HEG) with the same density as the local density of the system:

$$E_{xc} = \int d^3\vec{r}\; n(\vec{r})\; \epsilon_{xc}^{hom}(n(\vec{r})). \tag{2.55}$$

The exchange energy of the HEG can be found analytically as [17]:

$$\epsilon_x^{hom}(n(\vec{r})) = -\frac{3}{4}\left(\frac{3}{\pi}n(\vec{r})\right)^{\frac{1}{3}}. \tag{2.56}$$

The correlation energy cannot be found analytically in the same way, although it can be analytically parameterised in the low- and high-density case of the HEG. Ceperley and Alder [18] calculated the correlation energy of the HEG at a range of intermediate electron densities to a high level of accuracy using Quantum Monte Carlo (QMC) methods. Several analytic parameterisations of these data have been subsequently developed to interpolate the correlation energy of the HEG to all densities, such as the PZ81 parameterisation, due to Perdew and Zunger [19].

The LDA is a simple approximation, but one that produces good results in a variety of systems [16]. Part of the reason for the success of the LDA is that it obeys the sum rule for the exchange-correlation hole [3]:

$$\int d^3\vec{r'}\, n(\vec{r'})\left(g(\vec{r},\vec{r'}) - 1\right) = -1, \tag{2.57}$$

where $g(\vec{r},\vec{r'})$ is the pair correlation function, which can be thought of as the normalised probability of finding an electron at position $\vec{r'}$ given that there is an electron at

position $\vec{r}$. In other words, the presence of an electron displaces exactly one other electron from its vicinity.

However, the LDA is known to over-bind (calculate interatomic bonds to be stronger than they are) because it favours more uniform charge densities [3]. This motivated efforts to go beyond the LDA by taking the gradient of the density into account when constructing the xc functional.

The generalised gradient approximation

More sophisticated approaches for the xc functional are semi-local functionals, which are functionals not only of the value of the density at the point of evaluation, but also of the gradient of the density (thus giving some information about the neighbouring environment):

$$E_{xc}^{GGA} = \int d^3\vec{r}\; n(\vec{r})\; \epsilon_{xc}^{GGA}(n(\vec{r}), |\vec{\nabla} n(\vec{r})|) \tag{2.58}$$

$$= \int d^3\vec{r}\; n(\vec{r})\; \epsilon_{x}^{hom}(n(\vec{r}))\; F_{xc}^{GGA}(n(\vec{r}), |\vec{\nabla} n(\vec{r})|), \tag{2.59}$$

where $\epsilon_x^{hom}(n(\vec{r}))$ is the exchange energy density of the HEG and F_{xc}^{GGA} is a dimensionless quantity known as the *enhancement factor* [20]. The enhancement factor is usually defined in terms of a dimensionless gradient quantity s_1:

$$s_1 = \frac{|\vec{\nabla} n(\vec{r})|}{2k_F\; n(\vec{r})}, \tag{2.60}$$

where k_F is the local Fermi wavevector, $k_F = (3\pi^2\, n(\vec{r}))^{\frac{1}{3}}$.

These types of functionals are known as generalised gradient approximations (GGAs). Various forms for the GGA enhancement factors have been put forward, such as the PW91 [21, 22], WC [23] and PBE [24] functionals. The last of these functionals is one of the most commonly used in condensed-matter studies today, due to its respectable all-round accuracy for a range of properties. It has demonstrated a good level of accuracy over a variety of systems, although – in contrast to the LDA – it tends to overestimate volumes (under-bind) [3]. There exist two variants of the original PBE functional: the revised PBE (*RevPBE*) functional [25], which is intended to produce more accurate surface binding (adsorption) energies, and the PBE for solids (*PBEsol*) functional [26], which is designed to produce a more accurate description of equilibrium bond lengths and lattice parameters in solids. There are various physical conditions that the functionals should satisfy, which help to determine the forms of the function-

als, such as the local Lieb-Oxford limit [27]; these are discussed further by Martin [1] and Kohanoff [3]. Different formulations for F_{xc}^{GGA} make different choices on which of the conditions to obey and which to relax, leading to a variety of GGA xc functionals.

The idea behind the GGA can be extended further, in a process that Perdew described as part of a "Jacob's Ladder" of exchange-correlation functionals [28]. So-called *meta-GGAs* are integrals of the electron density over a local energy function, which takes as its inputs not only the value of the electron density and the gradient of the electron density at a point, but also the second derivative (Laplacian) of the density, or the kinetic energy density. Such functionals are also semi-local in nature.

Hybrid functionals

One well-known problem [29] with LDA and GGA functionals is that they fail to reproduce the known property of the non-vanishing discontinuity in the derivative of the xc energy with respect to the density upon passing through an integer number of particles in the system:

$$\lim_{\delta \to 0} \left[\left. \frac{\delta E_{xc}}{\delta n(\vec{r})} \right|_{N+\delta} - \left. \frac{\delta E_{xc}}{\delta n(\vec{r})} \right|_{N-\delta} \right] = C, \tag{2.61}$$

for integer particle number N, where C is a constant [30]. This leads to the band-gap problem, in which the band gaps of semi-conductors and insulators are under-predicted by a system-dependent constant amount of energy, C, which can typically represent $\sim$40% of the experimentally observed band gap [31].

Hybrid functionals are one approach to predicting more accurate band gaps. Such functionals mix a local or semi-local xc functional with the Hartree-Fock exchange energy, which is known to overestimate band gaps [3]. The HF exchange energy is computed in terms of wavefunctions, so hybrid density functionals are implicit rather than explicit functionals of the electron density. Hybrid functionals may differ both in the choice of (semi-)local functional and the method of mixing with the exact exchange energy from Hartree-Fock theory. Hybrid functionals commonly used in condensed matter physics include PBE0 [32] and HSE06 [33, 34]. The former straightforwardly mixes the PBE and Hartree-Fock exchange energies in a ratio fixed at 3:1, along with the PBE correlation energy. HSE06 is a more sophisticated functional, taking the form:

$$E_{xc}^{\omega PBEh} = aE_x^{HF,SR}(\omega) + (1-a)E_x^{PBE,SR}(\omega) + E_x^{PBE,LR}(\omega) + E_c^{PBE}. \tag{2.62}$$

SR and LR indicate short-range and long-range interactions respectively, the two ranges being delineated using a screening error function. Thus the correlation energy is simply that from PBE, and the exchange energy is the same as for PBE for long range interactions, and a mixture of PBE and HF exchange energies at short ranges, with the parameter ω determining the range of the short- and long-range interactions, and the parameter a determining the ratio of the exchange energy mixing for short-range interactions. The mixing and range parameters that mix the two theories – semi-local DFT and HF – are usually chosen to reproduce known results for a wide range of systems, so that hybrid functionals can no longer be considered a fully *ab initio* approach.

For a comparison of the performance of different xc functionals in various systems, see references 20 and 35. The choice of xc functional is usually determined by the system and properties of interest, so that well-converged calculations reproduce known properties of interest in the system under consideration. This agreement may be related to how important the conditions that are and aren't satisfied by the xc functional are to the system and properties under consideration.

Dispersion corrections

A second known failure of xc functionals is an inability to reproduce van der Waals (vdW) interactions. In order to ameliorate this problem in systems where vdW interactions are believed to play a significant role, such as molecular crystals or layered systems with interlayer interactions, an additional energy term can be applied to the DFT energy, so that the dispersion-corrected total energy E_{DFT-D} is given by [36]:

$$E_{DFT-D} = E_{DFT} + E_{vdW}. \tag{2.63}$$

These corrections are known as *semi-empirical dispersion corrections* (SEDCs). SEDCs use a functional form for pairwise interactions between atoms, for which the parameterisation is set to reproduce known results. Popular SEDC schemes such as G06 [36] and TS [37] use an r^{-6} functional form for the vdW energy between pairs of atoms, suppressed at short range:

$$E_{vdW} = -\frac{1}{2}\, s_6 \sum_i \sum_{j \neq i} \sum_{\vec{L}} f_{damp}(r_{ij}, R_i, R_j)\, \frac{C_{6,ij}}{r_{ij}^6}, \tag{2.64}$$

where s_6 is an xc functional-dependent overall energy scaling, i and j label atoms in the unit cell, the vectors $\vec{L}$ are the translation vectors to all unit cells within the periodic structure, r_{ij} is the separation between atoms i and j, R_i and R_j are the

vdW radii of atoms i and j, $C_{6,ij}$ is a constant describing the strength of the vdW interaction between the species of atoms i and j, and $f_{damp}(r_{ij}, R_i, R_j)$ is a damping function that prevents the r_{ij}^{-6} term diverging at small separations and to allow DFT to describe chemical bonding[2]:

$$f_{damp}(r_{ij}, R_i, R_j) = \left[1 + exp\left(-d\left(\frac{r_{ij}}{s_R(R_i + R_j)} - 1\right)\right)\right]^{-1}. \tag{2.65}$$

The r_{ij}^{-6} term means that very long-range interactions make little contribution to E_{vdW}, so that the summation in practice can be truncated to medium-range interactions.

In the G06 scheme, the atomic-pair dispersion constant $C_{6,ij}$ is defined as the geometric mean of constants for each atomic species:

$$C_{6,ij} = \sqrt{C_{6,i}\, C_{6,j}}. \tag{2.66}$$

$C_{6,i}$ and $C_{6,j}$ are constants for each atomic species, determined by fitting to known results for a large range of systems. The TS scheme is designed to be somewhat less empirical, though still not entirely *ab initio*, by taking the calculated electronic structure into account when determining the $C_{6,ij}$ constants. This is done by using effective $C_{6,ij}$ constants, modified from default values by comparing the Hirshfeld volume [38] around each atom to a pre-determined free atomic volume. The need to calculate Hirshfeld volumes can be problematic in small unit cells.

The G06 and TS schemes have both been shown to be effective in systems where vdW interactions are important, with the TS scheme having a better performance [39] overall.

2.3.4 Solving the Kohn-Sham Equations

The independent-particle Kohn-Sham problem defined in equations (2.51) – (2.53) now has to be solved. A self-consistent field approach is taken [1]. As the density can be used to generate the effective potential in equation (2.53), from an initial guess of the density we are able to calculate the effective potential, V_{KS}, of the Kohn-Sham single-particle Schrödinger-like equations. We can then solve the Kohn-Sham non-interacting Schrödinger-like equation to obtain the wavefunctions, from which we can calculate the density. Only when this calculated density is equal to the original density has self-consistency been achieved.

[2]The dispersion energy still diverges for extremely small interatomic separations, but the very high DFT energy cost of such small separations prevents this region from being reached in practice.

If the calculation is not self-consistent, then we can mix together the inputted and outputted densities to form a new density function, which can be used as the input to another iteration of the procedure described above. There are various schemes for mixing the density, such as the Broyden [40] and Pulay [41] mixing schemes. In this way we can improve our density function until the result of the iterative procedure is self-consistent (in practice, to within some tolerance in the calculated energy and forces). From this solution of the density we can construct the wavefunctions and then any property of the system we desire (for example, the total energy or the band structure).

This self-consistent-field procedure is summarised in the flow chart in Fig. 2.2, adapted from Martin [1]; f_i is the Fermi-Dirac function, $f_i = \left[1 + exp\left(-\frac{E-\mu}{k_B T}\right)\right]^{-1}$, where μ is the chemical potential.

Solving the Kohn-Sham equations takes up most of the computational effort of DFT calculations, particularly in ensuring that the solutions labelled by band index i are orthogonal to each other. There are alternative approaches to solving the Kohn-Sham equations, such as ensemble density functional theory (EDFT) [42], which is generally more robust than density mixing but more computationally expensive. EDFT is variational with respect to the total energy of the system, unlike many density mixing implementations, which utilise the Harris functional [43], and not the Kohn-Sham energy functional. These two functionals are equivalent when self-consistency has been achieved.

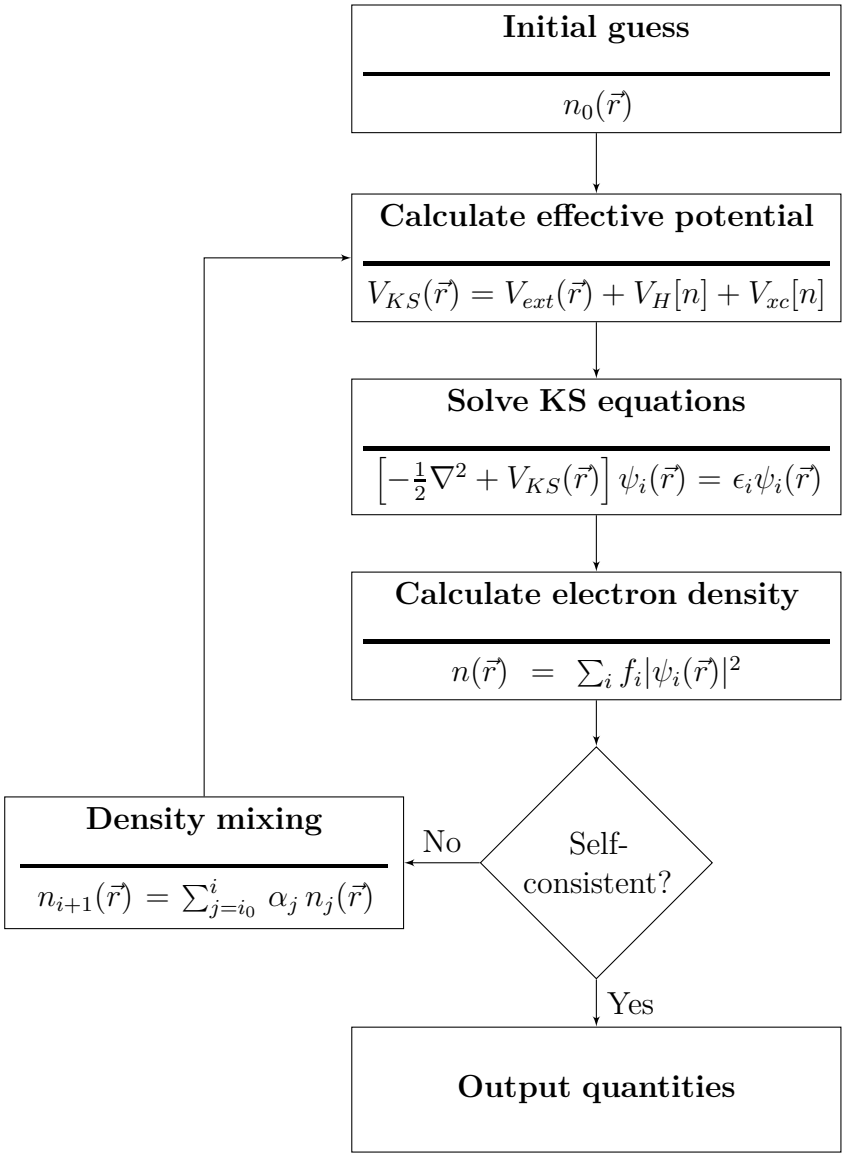

Fig. 2.2 Schematic of the density mixing approach to solving the Kohn-Sham equations.

2.3.5 Plane-Wave Basis Sets

The usual approach to solving the Kohn-Sham Schrödinger-like equations defined in equation (2.51) is to express the Kohn-Sham wavefunctions $\psi_i(\vec{r})$ in terms of a convenient basis set [3]. There are many choices that may be taken, depending on the system of interest, for example Gaussian basis set for molecular systems. For periodic crystals, the obvious choice of basis set is plane waves (PW): a PW basis set can easily be constructed to satisfy the periodic boundary conditions of a crystal system. Components of the plane wave basis set denoted by general wavevector $\vec{q}$, $|\vec{q}\rangle$, have the position representation:

$$\langle\vec{r}|\vec{q}\rangle = \phi_{\vec{q}}(\vec{r}) = \frac{1}{\sqrt{V_{cell}}}\, e^{i\vec{q}\cdot\vec{r}}. \tag{2.67}$$

We express the Kohn-Sham eigenfunctions and the periodic potential in terms of these Fourier components,

$$\psi_i(\vec{r}) = \sum_{\vec{q}} \alpha_{i,\vec{q}}\ \phi_{\vec{q}}(\vec{r}), \tag{2.68}$$

with the $\alpha_{i,\vec{q}}$ being the coefficients of the wavefunction in the plane-wave basis. Bloch's theorem [44] states that the eigenfunctions of the Hamiltonian of a periodic crystal system can be expressed as:

$$\psi_{\vec{k}}(\vec{r}) = e^{i\vec{k}\cdot\vec{r}} u_{\vec{k}}(\vec{r}), \tag{2.69}$$

with $u_{\vec{k}}(\vec{r})$ being a periodic function with the same periodicity as the crystal, satisfying $u_{\vec{k}}(\vec{r}+\vec{L}) = u_{\vec{k}}(\vec{r})$ for general lattice vectors $\vec{L} = n_a\vec{a} + n_b\vec{b} + n_c\vec{c}$; $\vec{a}$, $\vec{b}$ and $\vec{c}$ are the lattice vectors defining the unit cell, and n_a, n_b, $n_c \in \mathbb{Z}$. By considering $u_{\vec{k}}(\vec{r})$ in terms of its Fourier-transformed representation in reciprocal space:

$$u_{\vec{k}}(\vec{r}) = \int d\vec{g}\, \widetilde{u}_{\vec{k}}(\vec{g})\, e^{i\vec{g}\cdot\vec{r}}, \tag{2.70}$$

we can see from

$$u_{\vec{k}}(\vec{r}+\vec{L}) = \int d\vec{g}\, \widetilde{u}_{\vec{k}}(\vec{g})\, e^{i\vec{g}\cdot(\vec{r}+\vec{L})} \tag{2.71}$$

$$= e^{i\vec{g}\cdot\vec{L}} u_{\vec{k}}(\vec{r}) \tag{2.72}$$

that the only wavevectors $\vec{g}$ that need to be considered in the Fourier transform in equation (2.70) are those satisfying $\vec{g}\cdot\vec{L} = 2\pi n$ for integer n. This condition means

that we can re-express equation (2.70) as a sum over general reciprocal lattice vectors $\vec{G} = n_{\tilde{a}}\vec{\tilde{a}} + n_{\tilde{b}}\vec{\tilde{b}} + n_{\tilde{c}}\vec{\tilde{c}}$, where $\vec{\tilde{a}}$, $\vec{\tilde{b}}$ and $\vec{\tilde{c}}$ are the reciprocal lattice vectors of the crystal, and $n_{\tilde{a}}$, $n_{\tilde{b}}$, $n_{\tilde{c}} \in \mathbb{Z}$:

$$u_{\vec{k}}(\vec{r}) = \sum_{\vec{G}} \widetilde{u}_{\vec{k}}(\vec{G})\, e^{i\vec{G}\cdot\vec{r}}. \tag{2.73}$$

If we now represent general wavevectors $\vec{q}$ as the sum of a wavevector, $\vec{k}$, in the first Brillouin zone (henceforth referred to simply as BZ), and a general lattice vector $\vec{G}$: $\vec{q} = \vec{k} + \vec{G}$, then equation (2.68) can be expressed as

$$\psi_i(\vec{r}) = \int_{BZ} d\vec{k}\ \phi_{i,\vec{k}}(\vec{r})\ e^{i\vec{k}\cdot\vec{r}}, \tag{2.74}$$

where

$$\phi_{i,\vec{k}}(\vec{r}) = \frac{1}{\sqrt{V_{cell}}} \sum_{\vec{G}} C_{i,\vec{k}}(\vec{G}) e^{i\vec{G}\cdot\vec{r}}. \tag{2.75}$$

In practice, we do not calculate the integral in equation (2.74). Instead the integral is approximated using numerical integration methods by sampling the BZ at specific k-points. In this thesis the sampling is carried out using the Monkhorst-Pack scheme [45], a computationally-efficient scheme for generating a regular $N_1 \times N_2 \times N_3$ grid in reciprocal space.

$$\vec{k}(n_1, n_2, n_3) = \sum_{i=1}^{3} \frac{2n_i - N_i - 1}{2N_i} \widetilde{a}_i, \tag{2.76}$$

where the n_i are integers running between 0 and N_i, and the $\widetilde{a}_i$ correspond to the reciprocal basis vectors of the crystal. The size of the grid is chosen to accurately approximate the true integral over the BZ.

The Kohn-Sham potential can also be represented in reciprocal space through

$$V_{KS}(\vec{r}) = \sum_{\vec{G}} \widetilde{V}_{KS}(\vec{G})\, e^{i\vec{G}.\vec{r}}. \tag{2.77}$$

Substituting these expressions into the Kohn-Sham Schrödinger-like equations (2.51), we obtain the following equation for the components α_i:

$$\sum_{\vec{G}'} H_{\vec{G},\vec{G}'}(\vec{k})\ \alpha_{i,\vec{G}'}(\vec{k}) = \epsilon_i(\vec{k})\ \alpha_{i,\vec{G}}(\vec{k}), \tag{2.78}$$

where

$$H_{\vec{G},\vec{G'}} = \langle \vec{k} + \vec{G} | \hat{H}_{KS} | \vec{k} + \vec{G'} \rangle \tag{2.79}$$

$$= \frac{1}{2} |\vec{k} + \vec{G}|^2 \delta_{\vec{G},\vec{G'}} + \widetilde{V}_{KS}(\vec{G} - \vec{G'}) \tag{2.80}$$

It is these equations for the Fourier components that we then solve computationally. When reconstructing the new electron density from these components, the straightforward approach is simply to add the modulus-squared of the Fourier components and integrate over all k-points to construct the density. However, it is more computationally efficient to use fast Fourier transforms (FFTs) [46] to transform the Fourier components into a real-space representation, and construct a density in real space. The FFTs are carried out in $\mathcal{O}(N\,lnN)$, whereas the first approach is carried out in $\mathcal{O}(N^2)$. FFTs are can also be used to construct the Hamiltonian, transforming between reciprocal space, in which the kinetic energy term is diagonal, and real space, in which V_{KS} is usually local.

In principle the transformation into the plane wave basis set requires an infinite number of wavevectors to be complete. In practice, however, it is acceptable and indeed necessary to truncate the wavevectors at a certain point, the energy equivalent of which is called the cutoff energy: $E_{cut} = \frac{1}{2}|\vec{k}+\vec{G}_{max}|^2$ in atomic units. The G vectors to be included in the sum in equation (2.75) can be envisioned as those contained within a sphere in reciprocal space of radius G_{max}, centred on the Γ point. It is physically reasonable to do so as we expect the components $C_{i,\vec{k}}(\vec{G})$ corresponding to very high-energy plane waves to be small [3]. Extrapolative techniques can be used to correct for errors introduced by using a finite basis set [47]. Calculations can be run at a range of cutoff energies to determine the point at which the calculation is well converged with respect to E_{cut} in the calculated properties of interest.

When constructing the density, $n(\vec{r}) = \sum_i^N |\psi_i(\vec{r})|^2$, we need in principal to take G-vector components up to $2\,G_{max}$. However, in practice the largest of these components are often insignificant, so the FFT grid is often truncated at some size multiple of the cut-off sphere less than 2, for example 1.75. Truncating the summation in equation (2.75) to G vectors $|\vec{G}| \leq G_{max}$ introduces a limit on how accurately wavefunctions can be described in real space. The smallest meaningful separation between points in real space, Δx, scales as $\Delta x \sim E_{cut}^{-\frac{1}{2}}$ [3].

2.3.6 Pseudopotentials

When working with plane wave basis sets, it is desirable to minimise the number of plane waves required to describe the wavefunction of the system. This motivates the pseudopotential approach [48], in which an atom's electrons can be divided into *core* electrons, which are closely bound to the nucleus, and outer or *valence* electrons, which are less tightly bound to the nucleus and are relatively free to take part in bonding. [1]. In some atoms, there also exist 'semi-core' electrons, which are still highly localised to the atom but which nonetheless can have an indirect effect on the chemical bonding. These atoms may have to be treated as valence atoms to achieve accurate results, depending on the conditions under which the pseudopotential is being used.

Pseudopotentials remove the core electrons from the calculation and instead incorporate them within the potentials generated by the nuclei. The external potentials felt by the electrons, which are generated by the nuclei, are thus modified from a bare Coulomb potential to become *pseudopotentials*, taking into account the effect of the core electrons. The form of the pseudopotentials can be generated from first principles, so DFT using pseudopotentials can still be considered *ab initio*.

The atomic wavefunctions undergo rapid fluctuations close to the nucleus as a result of the orthogonality requirement on eigenfunctions of the Hamiltonian. As more rapid fluctuations require more Fourier components to map accurately into reciprocal space, the computational effort required to describe these wavefunctions becomes great. Instead, the real atomic potentials are replaced by a pseudopotential. This pseudopotential is constructed such that the wavefunctions corresponding to the pseudopotential, $\psi_{ps}(\vec{r})$, match the wavefunctions of the real all-electron potential, $\psi_{AE}(\vec{r})$, outside of some cut-off radius r_{cut}, but are much smoother than those of the real potential inside the cut-off radius. Additionally, the pseudopotential should be constructed such that the logarithmic derivatives of pseudowavefunction and the all-electron wavefunction, and the first energy derivatives of these, match at the cut-off radius; and such that the real and pseudo valence eigenvalues agree for a chosen electronic configuration [49]. We set the cut-off radius such that electronic wavefunctions are minimally affected by the external potential inside the cut-off radius. In this way we can preserve accuracy while reducing the computational effort substantially. Pseudopotentials must be tested to make sure that they reproduce the results of an all-electron calculation to the desired level of accuracy in the range of chemical environments that they will be used, in a property known as *transferability*. An example of the effect of pseudisation on a wavefunction is shown in Fig. 2.3.

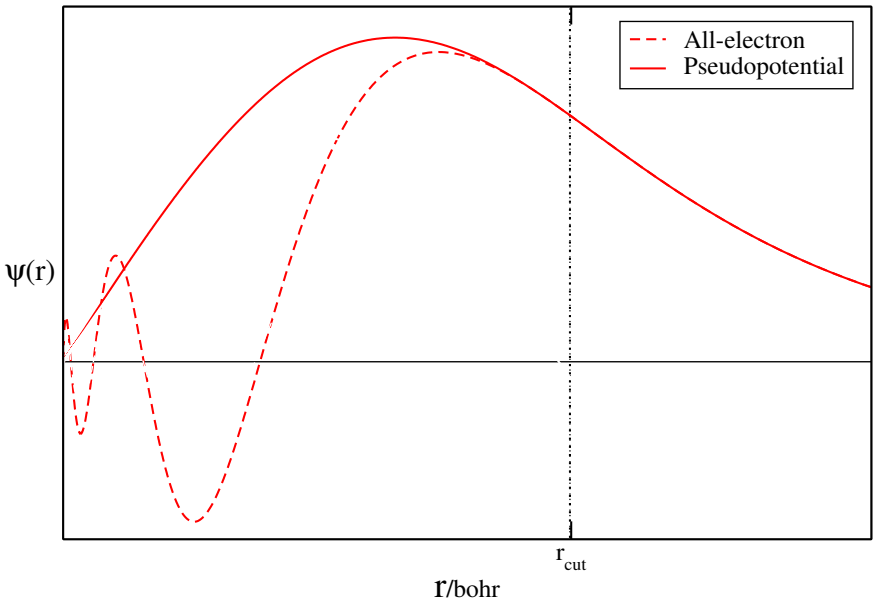

Fig. 2.3 The real and pseudised wavefunctions for the O 2*s* orbital. The all-electron wavefunction is represented by the dashed red line. The smoother wavefunction, arising from the pseudopotential, is in solid red. It is the same as the all electron wavefunction beyond the cut-off radius.

Ab initio pseudopotentials come in several varieties, including *norm-conserving*, *ultrasoft* [50] and *projector augmented wave* (PAW) [51] pseudopotentials. Norm-conserving pseudopotentials have the requirement that the norm of the pseudowavefunctions (wavefunction corresponding to the pseudopotential) inside the cutoff radius has the same value as for the true all-electron calculation. Physically, this means that the total charge inside the cutoff radius is the same for the pseudopotential calculation as for the all-electron calculation.

Ultrasoft pseudopotentials relax this requirement in order to create even smoother functions within the cutoff radius, thus lowering the required cut-off energy even further. The charge missing from inside the cut-off radius is replaced by an 'augmentation charge', $Q(\vec{r})$, so that the total density under the ultrasoft pseudopotential description becomes

$$n(\vec{r}) = \sum_{i}^{N} |\psi_i(\vec{r})|^2 + Q(\vec{r}). \tag{2.81}$$

The augmentation charge is itself pseudised, and is described in real space on a grid that usually needs to be finer than the grid that describes the charge density arising from the wavefunctions. The introduction of the augmentation charge generally

requires considerably more programming effort to implement, but is justified by the lower cut-off energies that can be used with the smoother ultrasoft pseudopotentials.

Several methods for generating pseudopotentials exist, such as the Troullier-Martins [52] and Vanderbilt [50] schemes. Such schemes usually decompose the pseudopotential into local and angular-momentum dependent potentials [1]:

$$\hat{V}_{ps} = V_{local}(\vec{r}) + \sum_{l,m} |Y_{l,m}\rangle \, V_l(\vec{r}) \, \langle Y_{l,m}| \,, \tag{2.82}$$

where $|Y_{l,m}\rangle$ are the spherical harmonic states, so that the external potential experienced by the valence electrons is no longer truly local, though is considered to be 'semi-local' as each angular momentum channel is local within $V_l(\vec{r})$ [1].

Projector augmented wave pseudopotentials use a linear transformation to transform the rapidly-varying core electron wavefunctions into smoother pseudowavefunctions [1, 51]. This transformation can be used to recover the core wavefunctions for calculating properties; PAW pseudopotentials are particularly useful when calculating properties that depend on the wavefunctions of the core electrons [53].

2.3.7 Geometry Optimisation

The previous sections have detailed how the Kohn-Sham system of density functional theory can be solved to obtain the ground-state electron density and the total energy. We are often interested in more than just the total energy, but many properties of interest can be related to the differential of the energy of the system with respect to some change. In this section, one such property shall be considered: the forces on each atom in the system. These are significant for vibrational properties of the crystal such as phonon frequencies, and are required to carry out geometry optimisation of a crystal structure, as described later in this section.

There is a straightforward way of calculating force F_I on an atom with position R_I if we know the total energy of the system, E:

$$\vec{F_I} = -\frac{\partial E}{\partial \vec{R_I}}. \tag{2.83}$$

Using the Hellmann-Feynman theorem [54]:

$$\frac{\partial E}{\partial \vec{R}} = \int d^3\vec{r} \, \psi^*(\vec{R}) \frac{d\hat{H}}{d\vec{R}} \psi(\vec{R}), \tag{2.84}$$

as well as using the form of (2.25), we can obtain from (2.83)

$$\vec{F}_I = -\int d^3\vec{r}\; n(\vec{r})\; \frac{\partial V_{ext}(\vec{r})}{\partial \vec{R}_I} - \frac{\partial E_{N-N}}{\partial \vec{R}_I} \tag{2.85}$$

This expression can be used to calculate the forces on the nuclei. By taking derivatives of the energy with respect to the strain tensor, the stresses on the unit cell can also be calculated [1].

Once we are able to calculate the forces and stresses arising from a given crystal structure, non-linear optimisation methods can be used to adjust the nuclear positions and unit cell parameters to relax a structure to a local minimum in enthalpy, a procedure known as *geometry optimisation*. The system parameters are varied by a small step in directions determined by the optimisation method chosen, and the forces and stresses are recalculated. This procedure is followed until the forces on the nuclei are sufficiently close to zero and the stresses on the unit cell are matched by any external pressure. At this point the system has been relaxed to an enthalpy minimum.

A variety of optimisation methods exist. One such method, which is used in the work in this thesis, is the quasi-Newton BFGS method [55], which is more robust than some other optimisation methods such as steepest descent, and its limited-memory variant, L-BFGS [56].

2.3.8 CASTEP

In this thesis I have used the CASTEP code for implementing DFT using plane-wave basis sets and grids [57]. CASTEP parallelises calculations in a highly efficient way by $\vec{k}$ point (requiring little inter-process communication), and less efficiently by $\vec{G}$ vector (in which many-to-many communications are required between processes to carry out Fourier transformations between real and reciprocal space). The computational cost of a calculation with a local or semi-local *xc* functional in CASTEP scales with the number of calculated electronic states N as $\sim N^3$. CASTEP can generate pseudopotentials 'on the fly', by default using the Vanderbilt scheme [50] to generate ultrasoft pseudopotentials. CASTEP can automatically determine symmetries in crystal structures and use them to reduce the computational cost of a calculation. Convergence testing was carried out to obtain suitably well-converged parameters for the plane-wave cutoff energy, k-point sampling density and grid scales, with regard to the total energy and other properties of interest, such as forces and stresses.

2.4 Stable Crystal Structures

2.4.1 Stability

The concept of crystal structure was introduced in Section 2.1. Knowledge of a crystal's atomic structure is essential for understanding and predicting the properties of that material. Often the structure of a crystalline material can be determined using experimental techniques such as X-ray or neutron diffraction. However, sometimes experimental determination of crystal structure is not possible or practical. There are several reasons for this. If the conditions of interest involve extremes of pressure and/or temperature, then they may be beyond the accessible range of experimental technologies such as diamond anvil cells, or else experimental data may be insufficiently clear to make an unambiguous determination of crystal structure. Furthermore, experiments are expensive; recent attempts to *design* materials for specific purposes are much more cost-effective if some of the screening of potential materials can be done theoretically, rather than through experimental synthesis. This further motivates the development of theoretical methods for crystal structure prediction.

For many years, such a method for predicting theoretically which crystal structures will emerge in nature, given a particular mix of elements and a set of conditions such as pressure and temperature, has been desired but not achieved. As recently as 1988, John Maddox – then the editor of *Nature* – said [58]:

> *One of the continuing scandals in the physical sciences is that it remains in general impossible to predict the structure of even the simplest crystalline solids from a knowledge of their chemical composition. Who, for example, would guess that graphite, not diamond, is the thermodynamically stable allotrope of carbon at ordinary temperature and pressure? Solids such as crystalline water (ice) are still thought to lie beyond mortals' ken.*

In recent years, however, and with the exponential growth of computational power available to scientists, *crystal structure prediction* has become feasible. There still does not exist any 'handle-turning' method of proceeding from a set of elements and environmental conditions directly and with certainty to the crystal structures that are adopted in nature, but a variety of methods have been developed that all work by exploring a range of possible crystal structures and comparing them to predict which will be found in nature. These methods shall be introduced later; first we must consider how we determine whether or not a given crystal structure will be adopted.

Thermodynamically, spontaneous changes in closed systems will act to increase the entropy of the system. This can be reformulated by saying that spontaneous changes in a system will act to decrease the thermodynamic free energy of the crystal. If we consider a crystal of volume V to be at constant temperature T and pressure P, then spontaneous changes to the crystal structure will be those for which the Gibbs free energy, G:

$$G = H - TS \tag{2.86}$$

is reduced. H denotes the enthalpy of the system:

$$H = U + PV. \tag{2.87}$$

U denotes the internal energy of the system – the total energy of the system in isolation, consisting of the kinetic and potential energies of the atoms that make up the crystal. In searching for crystal structures, we usually consider the crystal system to be at zero temperature, and neglect the quantum-mechanical zero-point motion, a simplification known as a *static lattice* treatment. Finite-temperature effects can then be calculated for the most promising static lattice structures found in the search, if desired. At $T = 0$, the Gibbs free energy thus reduces to the enthalpy, H, which itself reduces to the internal energy U in the absence of pressure.

Spontaneous changes to crystal structures will be those that reduce the free energy – or in the static lattice approximation, which shall be assumed henceforth, the enthalpy – of the system. If there is a structure such that any infinitesimal perturbation to the crystal's lattice parameters or atomic positions increases the enthalpy, then that structure is *locally* stable. Of all the locally stable structures, the one with the lowest enthalpy is termed *globally* stable. Any structure other than the globally stable one will be liable to undergo a spontaneous transition to a lower-enthalpy structure, ultimately down to the globally stable structure. As such, the structure corresponding to the global minimum of the enthalpy is the one we are usually most interested in. However, other locally stable structures, whose enthalpies are relatively low, may be regarded as *metastable* if spontaneous transitions or reactions to lower-enthalpy structures are energetically improbable, meaning that such structures may be found in nature. As such, these structures may be of interest. A prominent example of a metastable structure is the diamond allotrope of carbon – under ambient conditions it has a higher free energy than graphite, but the energy barrier for the transition between the two

structures is sufficiently high to make such a spontaneous transformation extremely improbable.

To examine the properties of minima of the enthalpy of a system more deeply, we shall introduce the concept of the potential energy surface.

2.4.2 The Potential Energy Surface

We have seen in Section 2.1 that the structure of a periodic crystal can be described by using a unit cell, and that a unit cell containing N independently-placed atoms has $3(N-1)$ atomic and 6 lattice degrees of freedom, i.e. can be fully described using $3N+3$ parameters. We can now consider functions of these $3N+3$ variables. These functions form a hypersurface in $3N+4$ dimensional space. It is easiest to visualise what this means conceptually by reducing the number of free variables to one or two. An example function of a single variable is plotted in Fig. 2.4. The point denoted 'A' is the global minimum of the function within the plotted range. The points denoted 'B' are local minima. If the function plotted was the enthalpy of a system parameterised by this single variable, then the structure corresponding to 'A' would be globally stable, and structures corresponding to the points 'B' would be locally stable – and potentially metastable. We can extend this treatment to a function of two variables, which is plotted in Fig. 2.5, with the variables plotted on the x and y axes, and the value of the function on the (vertical) z axis. The height of the surface thus represents the value of the function at that point. The point at which this value is lowest – the global minimum in the plotted range – is marked 'A'. There are several local minima, with one such minimum marked with 'B'. Again, if the function plotted was the enthalpy of a system parameterised by two variables, then the point 'A' would correspond to the globally stable structure, and the structure represented by point 'B' would be locally stable and potentially metastable. These concepts can be extended to functions of an arbitrary number of variables – in our case, $3N+3$.

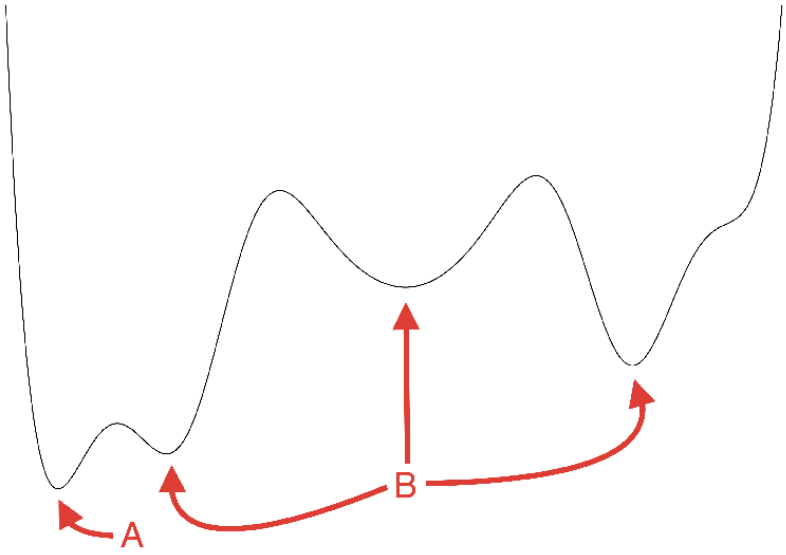

Fig. 2.4 Example of a function of one variable. 'A' marks the global minimum in the region under examination, and 'B' marks local minima.

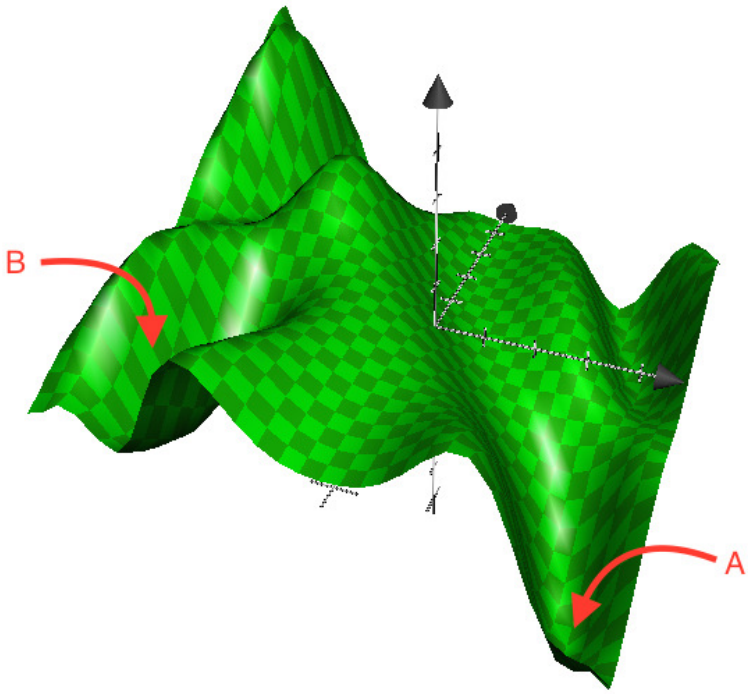

Plot of a function of two variables, with the value of the function plotted on the vertical axis.

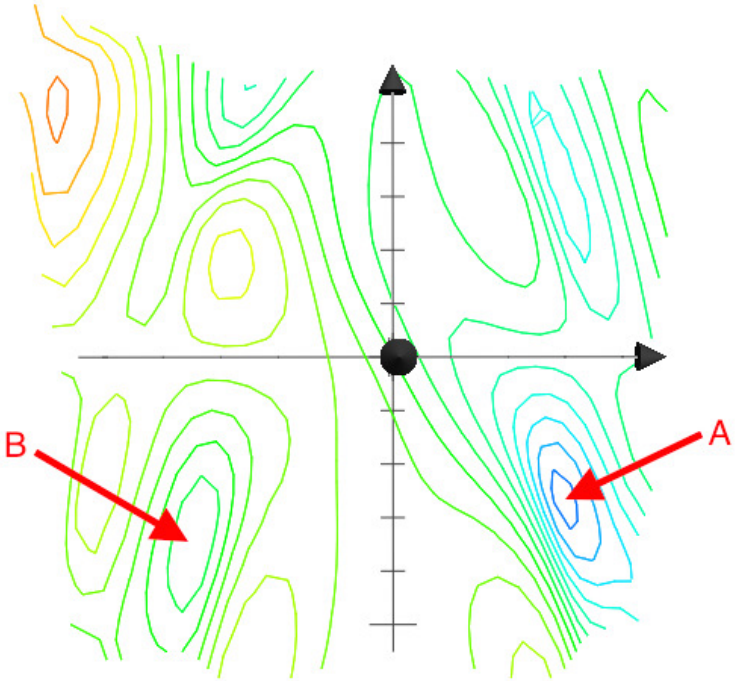

Contour map of the same function of two variables. Blue colours denote lower values of the function, and red colours denote higher values; green colours are intermediate values.

Fig. 2.5 Plots of an example function of two variables. Point 'A' denotes the global minimum of the function in the region plotted. Point 'B' denotes a local minimum of the function.

The functions that we are interested in are those that yield the thermodynamic potentials mentioned in the previous section – enthalpy or, at zero pressure, internal energy. The surface formed by the function corresponding to the internal energy in the space of crystal configurations is the Born-Oppenheimer energy surface, also called the *potential energy surface* (PES). This is a concept that can be generalised to other thermodynamic functions in crystal configuration space, such as to an enthalpy surface. In the rest of this thesis, PES shall denote the surface corresponding to whichever thermodynamic function is relevant – internal energy at zero pressure and temperature, and enthalpy at non-zero pressure but zero temperature.

Density functional theory can be used in a wide variety of systems to find the enthalpy or internal energy of a crystal system at zero temperature to a good degree of accuracy, requiring only the positions of the atoms and lattice parameters as inputs. We wish to find the lowest-lying minima of the enthalpy – corresponding to the deep wells in the two-variable function of Fig. 2.5. Several general properties of potential energy surfaces are worth considering:

- The number of local minima in the PES tends to grow exponentially with the number of atoms in the unit cell, N, for large values of N:

$$n_{minima} \sim e^{\alpha N}. \tag{2.88}$$

  This rapid growth in the number of minima suggests that the time required to sample all the minima will grow rapidly with system size, limiting our ability to predict structures for materials with a large number of atoms in their unit cells. The derivation of equation (2.88) makes no suggestion of clear relationships between the potential minima that could be used to ameliorate the exponential dependence, and no method has been put forward that reliably reduces the dependence of the number of minima on N [59].

- Around each local minimum is a 'basin'. All atomic configurations that lie in these basins relax to the basin's local minimum, so that the minimum may be representative of a large area of the PES. Every point on the surface is either a local extremum or lies in the basin of a local minimum.

- It has been demonstrated that the lowest-lying minima tend to have the largest basins, although this is not always true [60, 61]. Indeed, it has been demonstrated that the distribution of basin areas on the PES in model calculations follows a power-law relationship, and that the area of a basin grows exponentially with

its maximum depth [62]. This distribution is analogous to the distribution of volumes in high-dimensional Apollonian packing [63]; a two-dimensional example of which is illustrated in Fig. 2.6.

- Low-lying minima tend to cluster together, close to each other on the potential energy surface. This leads to the concept of 'funnels' – large areas of the PES in which very low-lying minima lie [64]. Of course, there may be multiple, disconnected, funnels in the PES, each of which contain low-lying minima. Furthermore, the energy barrier between low-lying basins tends to be small, making it relatively easy for a crystal to change between the two structures that the minima represent. This is related to the Bell-Evans-Polanyi principle, which holds that the more exothermic a reaction is, the smaller its activation energy will be [65, 66].

- Large areas of the potential energy surface have only high-lying minima. These areas usually correspond to pairs of atoms being very close to each other, leading to very high Coulomb energies [64].

- Low-lying minima of the PES tend to correspond to structures with high symmetry [67, 68].

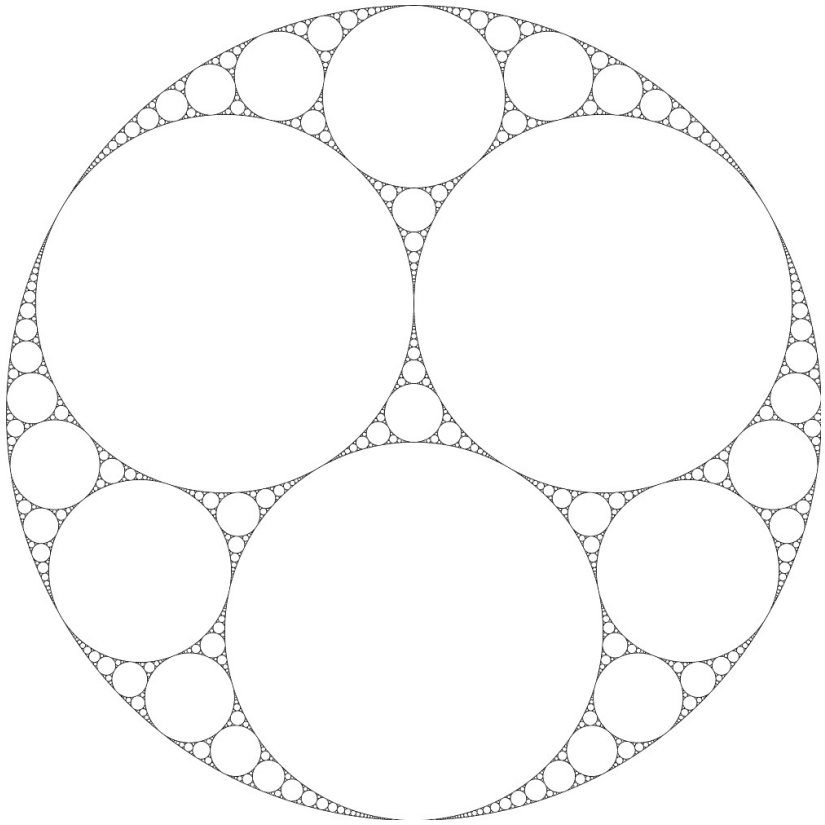

Fig. 2.6 Two-dimensional example of Apollonian packing of circles. Note how most of the total area is taken up by a small number of very large circles, with the rest of the area taken up by a very large number of small circles. Potential energy surfaces have shown analogous properties, so that despite the exponential growth of the number of basins with the number of atoms in the unit cell (equation (2.88)), much of the area of the PES is nevertheless taken up by a small number of the lowest-lying minima. Figure taken from Wikimedia Commons.

2.4.3 Methods for Crystal Structure Prediction

The theoretical task in predicting crystal structure is therefore to find the low-lying minima of the PES. There are multiple approaches to this problem, which are all fundamentally based on evaluating a range of possible structures and evaluating their enthalpies. Methods differ on how the structures are generated. Wolpert and Macready's "no free lunch" theorems for optimisation [69] suggest that no method will be consistently better than any other over a wide range of systems [64]. Techniques for finding the local minima of a PES include data mining techniques, simulated annealing, genetic algorithms, particle swarm optimisation and purely stochastic methods. A brief

overview of these methods is provided here; further information can be found in references 70 and 71.

Data mining approaches do not attempt to predict entirely novel crystal structures; instead, they attempt to reuse knowledge of known crystal structures. The general approach is as follows. First, a large number of existing crystal structures are obtained from one or more databases of crystal structures. The crystal structures selected are often restricted to those with some similarity to the system of interest – containing elements from the same groups as the species in the system of interest, for example. Next, the atoms in the database structures are appropriately replaced – anion for anion, and cation for cation – with atoms of the species in the system being studied. The unit cells are rescaled to an appropriate volume and the resulting structure relaxed to the local minimum in enthalpy. In this way a number of candidate structures are generated.

Such data mining techniques often produce competitive structures relatively cheaply, but are limited in their predictive power as they can only consider crystal structures that have already been observed before. Their ability to predict new structures is therefore limited, and there is nothing in the methodology that leads us to believe that the PES is well sampled. Nonetheless, data mining methods can be a good first step, before more powerful predictive techniques are used to produce competitive structures at low computational cost.

Simulated annealing is an optimisation technique inspired by physical annealing in metals [72]. An initial crystal structure is generated at random and its enthalpy is evaluated. The structure is then perturbed using either a Monte Carlo scheme or molecular dynamics, and the enthalpy of the new structure is evaluated. The change is either accepted (the new structure becomes the 'current' structure) or rejected (the original structure remains 'current') based on the Metropolis algorithm [73], in which the probability of a structural perturbation with enthalpy change ΔH being accepted is 1 if $\Delta H \leqslant 0$ and a random number between 0 and 1, ξ, if $\Delta H > 0$:

$$e^{-\frac{\Delta H}{k_B T}} - \xi \begin{cases} \geqslant 0 & \text{Accept} \\ < 0 & \text{Reject.} \end{cases} \tag{2.89}$$

T serves as a simulated temperature. At the beginning of the process, T is chosen to be large, in order to enable the structure to hop over large energy barriers, but its value gradually decreases as the perturbation and accept/reject steps are repeated. This is intended to settle the structure down to the global optimum, or at least, the optimum in the region of configuration space the structure began in. To try to ensure

that all the PES is sampled, the procedure is repeated multiple times with different initial structures chosen at random.

A related technique is a 'basin hopping' method developed by Wales and Doye [74] and initially applied to Lennard-Jones clusters. The technique is similar to simulated annealing except that each time a structure is perturbed, it is relaxed to the local minimum of enthalpy, and this enthalpy is then used in the Metropolis algorithm. A high simulated temperature is used and kept constant, allowing high energy barriers between basins in the PES to be crossed, and so enabling the technique to explore a large area of the PES.

Genetic algorithms are a class of evolutionary algorithms that take their inspiration from Darwinian or Lamarckian evolution [75]. An initial generation of structures are generated at random. A new generation of structures is then formed from the previous generation using operations of selection (removing from consideration structures considered poor, based either on enthalpy or some other 'cost function'), 'mutation' (randomly perturbing an existing structure) and 'crossover' (combining structural motifs from existing structures). New random structures may also be generated in order to promote a diversity of structures. This process continues for a number of generations. Many genetic algorithms exist, varying in how they select which structures survive to the next generation, and how the crossover and mutation operations are carried out. An example of a genetic algorithm is the USPEX code [76], which has been successfully applied to systems such as elemental boron [77].

Particle swarm optimisation (PSO) is an evolutionary method for crystal structure prediction that avoids the use of the mutation and crossover operations of genetic algorithms. An initial generation of randomly-generated structures are relaxed to their local minimum in enthalpy, and a new generation formed using an algorithm that gives each structure a 'velocity' in configuration space that is updated based not only on that particle's 'history', but also on the location in configuration space of the lowest-enthalpy particle in the 'swarm'. The procedure is repeated for a number of generations. In each generation repeated structures are removed and new randomly-generated structures are introduced, in order to try to promote diversity in the swarm. A PSO method, CALYPSO, has been applied to systems such as the Xe-Fe and Xe-Ni binary systems at high pressure [78].

All of the techniques described here, with the exception of data mining, have some stochastic elements to them (for example, the generation of a random set of initial structures). However, there also exist purely stochastic methods for crystal structure prediction that are based solely on the generation of structures at random, though

usually subject to constraints. These methods have been successfully applied to a wide variety of systems, such as silane [79] and high-pressure hydrogen [80]. This is the class of method that has been used in this thesis, and the particular implementation used, *ab initio* random structure searching, shall now be described and discussed.

2.5 *Ab initio* Random Structure Searching

2.5.1 Overview

Ab initio random structure searching [64] (AIRSS) is conceptually a very simple technique. It can be summarised as follows:

1. Generate a random structure: choose random values for each of the $3N + 3$ parameters, within the allowed ranges for each parameter. The restrictions on the parameters are such that the lengths of the cell axes are positive, unit cell angles are between 60° and 120° (all unit cells with other angles are equivalent to a unit cell with angles in this range [64]), and all atoms lie within the unit cell. In practice, we always put constraints on the unit cell parameters, so that we start with a physically reasonable unit cell volume. We intuitively realise that unit cells with volumes far removed from any found experimentally are very unlikely to correspond to low-lying minima of the enthalpy. Additional constraints can be placed on the structures we randomly generate. These will be discussed in the next section.

2. Calculate the forces and stresses on the structure. Relax the structure until the forces are zero and the stresses in the crystal are matched by any externally applied pressures (in practice, this is to within some tolerance). The structure has now relaxed into the local minimum of the basin the structure began in.

3. Calculate the total enthalpy of the system for this relaxed structure.

4. Repeat this procedure many times. As more and more structures are randomly generated, an increasingly large portion of the PES is sampled. When we start to see the same local minima appearing multiple times, we can be reasonably confident that we have sampled all the lower-lying minima. This can require the generation of thousands of structures.

5. The local minima that have been found can then be ranked in terms of their enthalpy. The structure that has the lowest enthalpy is presumed to correspond to

the global minimum of the PES, and so is the most stable structure. Metastable structures can also be identified by looking at other low-enthalpy structures.

In order to reduce computational cost, the initial optimisation and evaluation of the random structures is carried out using a 'rough' set of computational parameters. Although this reduces the accuracy of the calculated structures and enthalpies, the rough calculations should be good enough to distinguish between a small number of low-enthalpy candidate structures, which can be re-optimised using high-precision calculations, and the rest, on which further computational expense need not be wasted.

An additional type of stochastic search can be carried out on the lowest-enthalpy structures, known as *relax and shake* (RASH). In this, the lattice parameters and atomic displacements are given a small, random perturbation from the values for a relaxed low-enthalpy structure, and the resulting structure relaxed. Repetition of this procedure increases the chance of finding nearby local minima, which may be lower in enthalpy than the initial structure.

The AIRSS method is summarised in the flow chart of Fig. 2.7.

Several questions immediately arise:

i. *How do we relax the structures and calculate the enthalpy?*

   The AIRSS method is independent of the physical description of the system used – any approximation to quantum mechanics may be used, from empirical potentials to quantum Monte Carlo, provided that the method is capable of calculating forces, stresses and energies of the system. In practice, density functional theory is usually found to offer the best balance between accuracy and computational cost.

ii. *Which atoms should be put into the unit cell?*

   So far, we have dealt with unit cells containing N atoms, but *which* atoms? Clearly, the species of atoms to be used depend on the system we wish to study. But how many atoms should be inserted in total, and how many of each species? If we are interested in elemental systems, then the latter question is not relevant, but in binary, ternary, etc., systems, we have a choice of stoichiometric ratios. Sometimes we may be interested in a particular stoichiometry only, but in general we must search over as wide a range of stoichiometries as is feasible. This can be done by selecting the number of atoms of each species at random, subject to the constraint that there are N atoms in total. The lowest-enthalpy structures

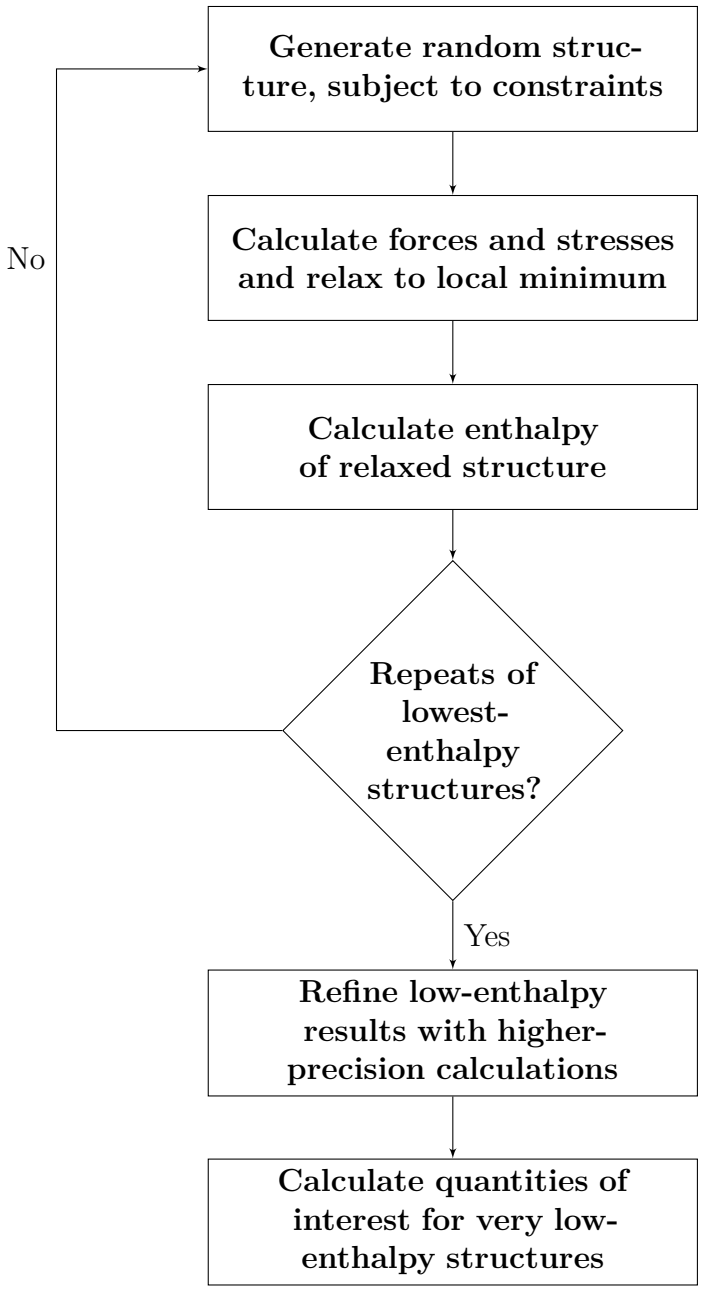

Fig. 2.7 Schematic of the *ab initio* random structure searching (AIRSS) method for crystal structure prediction.

at each stoichiometry can be compared by means of a *convex hull plot* (Maxwell construction) [81]. The total number of atoms in the unit cell, N, can in principal take any value. We may begin at small values of N, for which searches can be completed quickly, and then progressively increase N. In practice we must stop when the computational resources required for the search become unfeasible.

iii. *Is there any way of reducing the search space?*

We can apply chemical intuition to conclude that large areas of the PES are unlikely to contain low-lying enthalpy minima. We can apply additional constraints to the structures that we generate, to avoid sampling these areas of the PES [64]. This can save a considerable amount of computational effort, at the cost of having a less complete survey of the surface. The sorts of constraints that might be applied are discussed in the next section.

iv. *How do we know when we have done enough sampling of the surface?*

There is no way to be absolutely sure that we have found every minimum of the PES. We are, after all, only sampling the surface, not attempting to find an analytic form for it or carry out a complete mapping. Nonetheless, when we start to find multiple random structures relaxing into the same minimum, we know that there are basins that have been sampled multiple times. As the number of repeats we find increases, the likelihood that there is a minimum whose basin has not been sampled at all decreases. This is particularly true for the lowest-enthalpy minima (the ones we are most interested in), as these tend to have the largest basins, as discussed in the previous section. Thus, four to six repeats of the lowest-enthalpy structures and several repeats of higher-enthalpy structures usually means that the system has been adequately searched. Nevertheless, some basins – even those of low-lying enthalpies – can be much smaller than others, which means that we may sometimes finish searching when some minima have only a couple of repeats, if other minima have many more repeats. Looking for 'marker' structures that are known to exist is also a good check for making sure the PES has been well sampled – if such structures are absent, it could indicate that more searching should be performed. Ref. [64] discusses these issues in greater depth.

It should be noted that the PES of a system under external pressure changes as the pressure is varied. The results of searching the PES at a given pressure are therefore only exactly valid at that pressure. However, it is possible to extrapolate how the

enthalpies of the minima will change as the pressure is changed by a small amount, ΔP, from the searching pressure P_0 by considering the Taylor expansion of the enthalpy [64] at pressure $P = P_0 + \Delta P$:

$$\begin{aligned} H(P) &= H(P_0) + \left.\frac{dH}{dP}\right|_{P_0} \Delta P + \frac{1}{2}\left.\frac{d^2H}{dP^2}\right|_{P_0} (\Delta P)^2 + \dots \\ &= H(P_0) + V_0\,\Delta P - \frac{1}{2}\frac{V_0}{B_0}(\Delta P)^2 + \dots \\ &\simeq H(P_0) + V_0\,\Delta P, \end{aligned} \tag{2.90}$$

where V_0 and B_0 are respectively the volume and bulk modulus of the structure at the reference pressure, and the final line assumes that ΔP is small. As the volume of the structures at a searching pressure is known, equation (2.90) provides a cheap and convenient way of extrapolating the results of a structure search to other pressures.

2.5.2 Constraining the Search

Constraining the search by imposing a physically reasonable range for the unit cell volume – typically within 25% of the sum of the atomic volumes under the relevant conditions – has already been discussed. If this is the only condition imposed on the random structures then we will have to generate and relax a large number of random structures in order to be able to sample all of the potential energy surface corresponding to reasonable unit cell volume. Bearing in mind the exponential growth in the number of local minima with system cell size, this could rapidly lead to the computational time required to conduct a thorough survey of the potential energy surface becoming impractically large.

As a result, it is desirable to reduce the area of the PES that we actually search over. We can do this by utilising known properties of potential energy surfaces. We know that large areas of the PES, corresponding to atomic configurations in which pairs of atoms are very close together, are very unlikely to contain low-lying minima. Therefore a restriction can be imposed on the random structures that we generate, requiring a minimum separation between atoms. This minimum separation can be defined pairwise by species to generate structures in which certain pairs of species are more likely to be close together than others. This can be used to find structures in which atoms of different species bond with each other, for example.

We know also that the low-lying minima tend to correspond to high-symmetry structures [67], so we can impose a certain minimum amount of symmetry upon the

structures that we generate. Imposing symmetry on the random structures is particularly useful if we have experimental evidence that a crystal of unknown structure belongs to a certain space group. This is an example of using the available experimental evidence to restrict our search.

Another example of using experimental evidence to restrict searches is by imposing restrictions on unit cell dimensions or atomic positions, which can be deduced from diffractometry or other experimental techniques. Only structures that are compatible with these experimentally-imposed restrictions will be generated.

The effective dimensionality of the problem can be reduced by inserting pre-formed molecular units, such as water or ammonia molecules, into the unit cell, rather than individual atoms. This is useful when searching for molecular crystals; in such cases we are only interested in those structures containing the molecular building blocks.

These constraints on the random structures mean that we are sampling less of the PES. While this reduces the number of random structures required for a thorough search, it comes at the expense of potentially missing low-lying minima in the areas of the surface that we have restricted ourselves from searching. Such restrictions should therefore only be imposed when we are confident from physical and chemical intuition that the areas of the PES being ignored will not contain low-lying minima. The imposition of such restrictions means that generated structures are no longer randomly distributed over the whole potential energy surface, but rather only over those parts of the surface that we think stable structures might exist in.

2.6 Vibrations in Solids

In dealing with crystal structure in the previous sections, the nuclei have been treated semi-classically – as having fixed, definite positions – equivalent to the nuclear wavefunctions within the Born-Oppenheimer (BO) approximation (equation (2.14)) being infinitely localised to a point. This is usually a reasonable treatment for crystal structure prediction. Once a structure has been determined, however, nuclear motion has a significant impact on a material's properties. Various methods for determining nuclear vibrational properties have been developed. We shall here consider two approaches: the harmonic approximation (HA) and the vibrational self-consistent field method developed by Monserrat *et al.* [82].

2.6.1 Overview

The treatment of nuclear motion requires knowledge of the nuclear part of the total wavefunction of equation (2.14). In thermal equilibrium, this wavefunction can be constructed from the eigenvalues and eigenfunctions of the nuclear Hamiltonian, $\hat{H}_{nucl}$, of equation (2.18). Under the BO approximation this consists of the nuclear kinetic energy term of equation (2.1) and the total electronic energy arising from the solution of the electronic Hamiltonian of equation (2.15), $\epsilon_{el}(\vec{R})$,

$$\hat{H}_{nucl} = \sum_I -\frac{1}{2m_I}\nabla^2 + \epsilon_{el}(\vec{R}), \tag{2.91}$$

where $\vec{R}$ is a $3N$-dimensional collective position vector for the nuclei; $\vec{R} = (\vec{R_1}, \vec{R_2}, \ldots, \vec{R_N})$, and M_I is the mass of nucleus I.

Solving this Hamiltonian is not easy: to solve exactly – or rather, to within the accuracy of the electronic structure method used to solve the electronic Hamiltonian and determine $\epsilon_{el}(\vec{R})$ – the BO surface must be calculated as a function of many variables, with every point requiring a computationally demanding calculation. A straightforward approach to greatly simplifying this problem – which yields good results in a wide range of systems – is the harmonic approximation, which shall now be discussed.

2.6.2 The Harmonic Approximation

The harmonic approximation (HA) was developed on the assumption that typical nuclear displacements from their equilibrium (static lattice) positions are small, due to the large mass of the nuclei relative to electrons.

Let us label the unit cells of a periodic crystal by p, with translation vectors from a reference point labelled $\vec{L}_p$, and with the atoms within one unit cell labelled by α. Although we should in principle consider every atom within the crystal, in practice we will later find that we only need to explicitly consider atoms lying within a small number of unit cells, due to the relatively short range of inter-atomic interactions. We begin by defining displacement co-ordinates $\vec{u}_{p,\alpha}$ for each nucleus, relative to $\vec{r}^{\,0}_{p,\alpha}$, the equilibrium positions for each nucleus: $\vec{u}_{p,\alpha} = \vec{r}_{p,\alpha} - \vec{r}^{\,0}_{p,\alpha}$. Let the unsubscripted vectors $\vec{r}$, $\vec{r}^{\,0}$ and $\vec{u}$ denote the all-atom collective vectors for their relevant coordinates, e.g. $\vec{r}^{\,0} = (\vec{r}^{\,0}_{1,1}, \ldots, \vec{r}^{\,0}_{1,N_\alpha}, \vec{r}^{\,0}_{2,1}, \ldots, \vec{r}^{\,0}_{N_p,N_\alpha})$, where N_p is the number of unit cells and N_α is

the number of atoms in each unit cell. With these new co-ordinates, we can use a Taylor expansion for $\epsilon_{el}(\vec{r})$ to rewrite the nuclear Hamiltonian (2.91) as:

$$\hat{H}_{nucl} = \sum_{\vec{L}_{p},\alpha} -\frac{1}{2M_{\alpha}}\nabla^{2}_{p,\alpha} + \epsilon_{el}(\vec{r}^{0}) + \frac{1}{2}\sum_{\substack{\vec{L}_{p},\alpha,i \\ \vec{L}_{p'},\alpha',j}} \left.\frac{\partial^{2}\epsilon_{el}(\vec{r})}{\partial u_{p,\alpha;i}\,\partial u_{p',\alpha';j}}\right|_{\vec{r}^{0}} \hat{u}_{p,\alpha;i}\,\hat{u}_{p',\alpha';j} \;+\; \mathcal{O}(u^{3}). \tag{2.92}$$

The Latin indices i and j label the Cartesian directions x, y and z. Equation (2.92) uses the fact that, at equilibrium, the first-order derivatives of the BO energy ϵ_{el} are all zero, as they are proportional to the forces on the nuclei, which at equilibrium must be zero:

$$\left.\frac{\partial\epsilon_{el}(\vec{r})}{\partial u_{p,\alpha;i}}\right|_{\vec{r}^{0}} = 0 \qquad \forall \quad p,\alpha,i. \tag{2.93}$$

The harmonic approximation is obtained by truncating (2.92) at terms of $\mathcal{O}(u^{2})$, with higher-order terms being dropped. As we shall see, this approximation can enormously simplify the problem of nuclear motion. At this stage we also define $\epsilon_{el}(\vec{u}) = \epsilon_{el}(\vec{r}) - \epsilon_{el}(\vec{r}^{0})$, and drop the constant-energy term $\epsilon_{el}(\vec{r}^{0})$ so that under the HA equation (2.92) becomes

$$\hat{H}_{nucl} \simeq \sum_{\vec{L}_{p},\alpha,i} -\frac{1}{2M_{\alpha}}\nabla^{2}_{p,\alpha} + \sum_{\substack{\vec{L}_{p},\alpha,i \\ \vec{L}_{p'},\alpha',j}} \left.\frac{\partial^{2}\epsilon_{el}(\vec{u})}{\partial u_{p,\alpha;i}\,\partial u_{p',\alpha';j}}\right|_{\vec{u}=\vec{0}} \hat{u}_{p,\alpha;i}\,\hat{u}_{p',\alpha';j}. \tag{2.94}$$

The second-order partial derivatives can be expressed as a matrix, which is called the *matrix of force constants*, $\Phi_{\alpha,i;\alpha',j}(\vec{L}_{p},\vec{L}_{p'})$:

$$\Phi_{\alpha,i;\alpha',j}(\vec{L}_{p},\vec{L}_{p'}) = \left.\frac{\partial^{2}\epsilon(\vec{u})}{\partial u_{p,\alpha;i}\,\partial u_{p',\alpha';j}}\right|_{\vec{u}=\vec{0}}, \tag{2.95}$$

so that the nuclear Hamiltonian can finally be written as

$$\hat{H}_{nucl} = \sum_{\vec{L}_{p},\alpha,i} -\frac{1}{2M_{\alpha}}\nabla^{2}_{p,\alpha} + \sum_{\substack{\vec{L}_{p},\alpha,i \\ \vec{L}_{p'},\alpha',j}} \Phi_{\alpha,i;\alpha',j}(\vec{L}_{p},\vec{L}_{p'})\hat{u}_{p,\alpha;i}\,\hat{u}_{p',\alpha';j}. \tag{2.96}$$

It is convenient to consider the reciprocal space representation of the matrix of force constants, $D_{\alpha,i;\alpha',j}(\vec{k})$, defined as

$$D_{\alpha,i;\alpha',j}(\vec{k}) = \frac{1}{N_p\sqrt{M_\alpha M_{\alpha'}}} \sum_{\vec{L}_p,\vec{L}_{p'}} \Phi_{\alpha,i;\alpha',j}(\vec{L}_p,\vec{L}_{p'})\, e^{-i\vec{k}\cdot(\vec{L}_p-\vec{L}_{p'})}, \tag{2.97}$$

where N_p is the number of unit cells. $D_{\alpha,i;\alpha',j}(\vec{k})$ is called the *dynamical matrix*, and as we shall see it is a very useful way of thinking about nuclear vibrational motion under the HA. The dynamical matrix arises from the *ansatz* of plane-wave solutions to the nuclear Hamiltonian in equation (2.96):

$$u_{n,\vec{k};\alpha,p;i} = \frac{1}{\sqrt{M_\alpha}}\, \eta_{n,\vec{k};\alpha,i}\, e^{i(\vec{k}\cdot\vec{L}_p-\omega_{n,\vec{k}}t)}, \tag{2.98}$$

in which $\vec{\eta}_{n,\vec{k}}$ is the collective polarisation vector for atoms within the reference unit cell, and $\vec{k}$ is a wave-vector, commensurate with the boundary conditions, lying within the BZ. Note that the translational symmetry of the unit cell means that any wavevector lying outside the BZ is equivalent to one inside it [83]. The trial solution of equation (2.98) solves the semi-classical equations of motion for atomic motion under the HA:

$$M_\alpha \frac{\partial^2 u_{\alpha,p;i}}{\partial t^2} = -\frac{\partial \epsilon(\vec{u})}{\partial u_{\alpha,p;i}}, \tag{2.99}$$

if the eigenvalue equation

$$\sum_{\alpha',j} D_{\alpha,i;\alpha',j}(\vec{k})\, \eta_{n,\vec{k};\alpha',j} = \omega^2_{n,\vec{k}}\, \eta_{n,\vec{k};\alpha,i} \tag{2.100}$$

is satisfied. Here n is the *mode index*, with dimensionality $3N_\alpha$. It is convenient when considering collective atomic motion to define phonon coordinates $q'_{n,\vec{k}}$, as amplitudes of the $3N_\alpha$ allowed oscillations of the plane-wave solutions defined in equation (2.98):

$$\begin{aligned} u_{\alpha,p;i} &= \frac{1}{\sqrt{N_p}} \sum_{n,\vec{k}} q'_{n,\vec{k}}\, u_{n;\alpha,p;i}(\vec{k}) \\ &= \frac{1}{\sqrt{N_p M_\alpha}} \sum_{n,\vec{k}} q'_{n,\vec{k}}\, e^{i\vec{k}\cdot\vec{L}_p}\, \eta_{n,\vec{k};\alpha,i}, \end{aligned} \tag{2.101}$$

from which can be obtained an explicit form for the phonon co-ordinates:

$$q'_{n,\vec{k}} = \frac{1}{\sqrt{N_p}} \sum_{\vec{L}_p,\alpha,i} \sqrt{M_\alpha}\, u_{\alpha,p;i}\, e^{-i\vec{k}\cdot\vec{L}_p}\, \eta_{n,-\vec{k};\alpha,i}. \tag{2.102}$$

These phonon normal coordinates, q', are, in general, complex. We can exploit the Hermitian nature of the dynamical matrix defined in (2.97) to conclude that $\eta_{n,\vec{k};i,\alpha} = \eta^*_{n,-\vec{k};i,\alpha}$. Using this property, combinations of these normal coordinates corresponding to opposite wavevector values can be taken to form a set of real coordinates:

$$\begin{aligned} q_{n,\vec{k}} &= \frac{1}{\sqrt{2}}\left(q'_{n,\vec{k}} + q'_{n,-\vec{k}}\right), \\ q_{n,-\vec{k}} &= \frac{i}{\sqrt{2}}\left(q'_{n,\vec{k}} - q'_{n,-\vec{k}}\right). \end{aligned} \tag{2.103}$$

In terms of these new, real coordinates, the harmonic Hamiltonian (2.94) becomes

$$\hat{H}_{nucl} = \sum_{n,\vec{k}} \left[-\frac{1}{2}\frac{\partial^2}{\partial q^2_{n,\vec{k}}} + \frac{1}{2}\omega^2_{n,\vec{k}}\, q^2_{n,\vec{k}} \right]. \tag{2.104}$$

The form of equation (2.104) is of $3N_\alpha$ independent quantum harmonic oscillators (HO) for each of the N_k k-points in the BZ. The eigenfunctions of each HO are well known and have the real-space representation:

$$\langle x|\varphi^s\rangle = \varphi^s(\vec{x}) = \frac{1}{\sqrt{2^s\, s!}}\left(\frac{m\omega}{\pi}\right)^{\frac{1}{4}} H_s\left(\sqrt{m\omega}x\right) e^{-\frac{m\omega}{2}x^2}, \tag{2.105}$$

where m is the mass of the nuclear and H_s is the s^{th} physicists' Hermite polynomial, defined as

$$H_s(y) = (-1)^s\, e^{y^2}\frac{d^s}{dy^s}e^{-y^2}, \tag{2.106}$$

with the s^{th} eigenfunction solution having energy

$$E_s = \left(s + \frac{1}{2}\right)\omega. \tag{2.107}$$

Each independent HO in equation (2.104) can be in state $s_{n,\vec{k}}$. The total nuclear wavefunction can be formed as the Hartree-like product of the individual HO wavefunctions:

$$|\Phi^{\vec{S}}\rangle = \prod_{n,\vec{k}} |\varphi^{s_{n,\vec{k}}}_{n,\vec{k}}\rangle, \tag{2.108}$$

where $\vec{S}$ is a total state vector for the system, whose components are the excitation states of the individual HOs: $\vec{S} = \left(s_{1,\vec{k}_1}, \ldots, s_{3N_\alpha,\vec{k}_{N_k}}\right)$. A Hartree product, rather

than the Slater determinant (2.29) used in the electronic structure problem, is permissible because there is no requirement for the wavefunction to be antisymmetric. A state vector $\vec{S}$ has total energy $E^{\vec{S}}$ given by

$$E^{\vec{S}} = \sum_{n,\vec{k}} \left(s_{n,\vec{k}} + \frac{1}{2} \right) \omega_{n,\vec{k}}. \tag{2.109}$$

In thermal equilibrium, the probability of the systems being in state $\vec{S}$ is proportional to $\exp\left(-\frac{E^{\vec{S}}}{k_B T}\right)$. The partition function, $\mathcal{Z}$, for the system is given by

$$\begin{aligned} \mathcal{Z} &= \sum_{\vec{S}} e^{-\beta E^{\vec{S}}} \\ &= \prod_{n,\vec{k}} \sum_{s_{n,\vec{k}}} e^{-\beta\left(s_{n,\vec{k}}+\frac{1}{2}\right)\omega_{n,\vec{k}}} \\ &= \prod_{n,\vec{k}} \mathcal{Z}_{n,\vec{k}} \\ &= \prod_{n,\vec{k}} \tfrac{1}{2} \left[\sinh\left(\tfrac{1}{2}\beta\omega_{n,\vec{k}}\right) \right]^{-1}, \end{aligned} \tag{2.110}$$

where $\beta = \frac{1}{k_B T}$ is the inverse temperature and $Z_{n,\vec{k}}$ is the partition function for the individual mode with index n and wavevector $\vec{k}$. The free energy F of the system is given by

$$\begin{aligned} F &= -\frac{1}{\beta} \ln \mathcal{Z} \\ &= -\frac{1}{\beta} \sum_{n,\vec{k}} \ln \mathcal{Z}_{n,\vec{k}} \\ &= \sum_{n,\vec{k}} F_{n,\vec{k}} \\ &= \sum_{n,\vec{k}} \frac{1}{\beta} \ln\left[2 \sinh\left(\tfrac{1}{2}\beta\omega_{n,\vec{k}}\right) \right]. \end{aligned} \tag{2.111}$$

Finally, we note that if a collection of harmonic oscillators are in thermal equilibrium, such that the probability of being in a state $\vec{S}$ with energy $E^{\vec{S}}$ is proportional to $\exp(-\beta E^{\vec{S}})$, then the probability density function of the system, given by the modulus-square of the wavefunction, $|\Phi(\vec{q},\beta)|^2$, is [84]

$$
\begin{aligned}
|\Phi(\vec{q},\beta)|^2 =& \frac{1}{\mathcal{Z}} \sum_{\vec{S}} e^{-\beta E_{\vec{S}}} \; |\Phi^{\vec{S}}|^2 \\
=& \prod_{n,\vec{k}} \frac{1}{\sqrt{2\pi \, w_{n,\vec{k}}(\beta)}} \exp\left(-\frac{q^2_{n,\vec{k}}}{2 \, w_{n,\vec{k}}(\beta)} \right),
\end{aligned}
\tag{2.112}
$$

where the distribution width $w_{n,\vec{k}}(\beta)$ is defined as

$$
w_{n,\vec{k}}(\beta) = \frac{1}{2 \, \omega_{n,\vec{k}}} \coth\left(\tfrac{1}{2} \beta \omega_{n,\vec{k}} \right). \tag{2.113}
$$

There are two principal methods for carrying out vibrational calculations within the HA in practice. The first of these is *density functional perturbation theory* (DFPT) [85], in which the dynamical matrix is directly calculated using linear response perturbation theory at specified k points. Provided the k point sampling with exact DFPT calculations is sufficiently dense, properties at other k points can be calculated through Fourier interpolation, in which the dynamical matrices at the exact k points are Fourier-transformed to construct the effective force constant matrix, which can then be Fourier transformed back into reciprocal space to yield an approximate dynamical matrix at any given k point.

The second principal method for calculating vibrational properties is known as the *finite displacement* method. In this method, the dynamical matrix is calculated using equation (2.97) through knowledge of the matrix of force constants. The force constant matrix is calculated by making small perturbations to each atomic position from their equilibrium positions and calculating the resulting forces. Using the relation between atomic forces and the curvature of the Born-Oppenheimer surface:

$$
F^{\alpha',p';j} = \frac{\partial \epsilon(\vec{u})}{\partial u_{\alpha',p';j}}, \tag{2.114}
$$

the matrix of force constants can then be constructed as

$$
\Phi_{\alpha,i;\alpha',j}(\vec{L}_p, \vec{L}_{p'}) = \frac{\partial^2 \epsilon(\vec{u})}{\partial u_{\alpha,p;i} \, \partial u_{\alpha',p';j}} = \frac{\partial F^{\alpha',p';j}_{\alpha,p;i}}{\partial u_{\alpha,p;i}} \simeq \frac{\delta F^{\alpha',p';j}_{\alpha,p;i}}{\delta u_{\alpha,p;i}}, \tag{2.115}
$$

where $\delta u_{\alpha,p;i}$ is a small displacement to atom α in unit cell $\vec{L}_p$ in direction i, and $\delta F^{\alpha',p';j}_{\alpha,p;i}$ is the force in direction j on atom α' in unit cell $\vec{L}_{p'}$ arising as a result of this displacement. In the basic version of the scheme, calculations can be carried

out at the vibrational Γ point only. The derivatives of the forces with respect to an atomic displacement, due both to that displacement and all the periodic repeats of the displacement, yield directly the dynamical matrix of equation (2.97) at $\vec{k} = 0$. Other wavevectors can be calculated only by use of a supercell commensurate with that wavevector, such that the wavevector is equivalent to the Γ point of the supercell. If a sufficiently dense sampling of the vibrational BZ is performed, then the vibrational properties at any given wavevector can be calculated using Fourier interpolation, as for DFPT. The finite displacement scheme can also be extended beyond the Γ point using the *direct* or *supercell* scheme [86]. In this approach, a supercell is used for the finite displacement force calculations of sufficient size to ensure that the periodic repeats of a displaced atom do not have a significant impact on the calculated force constants. The matrix of force constants can thus be directly calculated and the dynamical matrix constructed from it. The use of larger supercells in finite displacement calculations is equivalent to denser k-point sampling under DFPT.

In this thesis, the finite displacement method is used, with implementation through CASTEP, and the LTE code developed by Neil Drummond, with modifications by Bartomeu Monserrat.

2.6.3 Anharmonicity

While the HA works well in many systems, in some systems the approximation is not sufficiently accurate. This occurs when the $\mathcal{O}(u^3)$ – or, in phonon coordinates, $\mathcal{O}(q^3)$ – and higher terms in the expansion of equation (2.92) become too large, relative to the second-order terms, to ignore. Such deviation from the $\epsilon(q) \sim q^2$ harmonic approximation is called *anharmonicity*. Consideration of anharmonicity tends to be important in systems with light atoms or at high temperature, due to the large amplitudes of oscillation in such systems; or in systems with highly anisotropic atomic environments [82].

Many schemes for introducing anharmonic corrections to vibrational calculations exist, which usually take the HA as a starting point. Many methods are based on the self-consistent harmonic approximation 'effective phonon' approach developed by Hooton [87]. In this thesis, a new approach developed by Monserrat *et al.* [82] is used, and shall now be discussed.

2.7 Vibrational Self-Consistent Field Approach to Anharmonicity

The *vibrational self-consistent field* (VSCF) approach to treating anharmonicities in crystals starts by expressing the full BO energy surface using the harmonic phonon modes as a convenient coordinate system.

2.7.1 The Principal Axis Approximation

The *principal axis approximation* (PAA) describes any point around a local minimum of the BO surface as a series of terms, which are functions of an increasing number of coupled harmonic phonon modes, thus:

$$\epsilon^{el}_{\mathrm{PAA}}(\vec{q}) = \epsilon^{el}(\vec{0}) + \sum_{n,\vec{k}} V_{n,\vec{k}}(q_{n,\vec{k}}) + \frac{1}{2!}\sum_{n,\vec{k}}\sum_{n',\vec{k}'}{}' V_{n,\vec{k};n',\vec{k}'}(q_{n,\vec{k}}, q_{n',\vec{k}'}) + \ldots, \tag{2.116}$$

with subsequent terms being functions of 3,4,..., $N_{modes}N_k$ of phonon coordinates. The final term is thus a function of all phonon coordinates. The prime on the summation symbol indicates that the sum does not include $(n', \vec{k}') = (n, \vec{k})$. The potential terms V are defined as

$$V_{n,\vec{k}}(q_{n,\vec{k}}) = \epsilon^{el}(0, \ldots, q_{n,\vec{k}}, \ldots, 0) - \epsilon^{el}(\vec{0}), \tag{2.117}$$

and

$$\begin{aligned} V_{n,\vec{k};n',\vec{k}'}(q_{n,\vec{k}}, q_{n',\vec{k}'}) =& \epsilon^{el}(0, \ldots, q_{n,\vec{k}}, \ldots, q_{n',\vec{k}'}, \ldots, 0) \\ & - V_{n,\vec{k}}(q_{n,\vec{k}}) - V_{n',\vec{k}'}(q_{n',\vec{k}'}) - \epsilon^{el}(\vec{0}), \end{aligned} \tag{2.118}$$

with higher terms defined similarly. Each potential term is thus defined as a *correction* to the description of the BO surface afforded by lower-order terms. If the full series is used, then the PAA is an exact description of the BO surface. However, such a complete mapping of the surface is an enormous computational expense: if each direction is mapped using N_m points, then a full mapping requires $N_m^{(3N_\alpha N_k - 3)}$ points to be calculated on the BO surface. The PAA amounts to truncating the expansion in equation (2.116); typically at either the first (requiring mapping of $\mathcal{O}(N_\alpha N_k N_m)$ configurations) or second non-constant term (requiring mapping of $\mathcal{O}(N_\alpha^2 N_k^2 N_m^2)$ configurations).

In this thesis, only the terms in one phonon coordinate (independent mode) are used, though in some systems the effect of the term in two phonon coordinates (pairwise coupled modes) is significant [82].

The PAA is a reasonable approximation because under the HA, different phonon modes are exactly non-interacting – that is, the V terms in more than one phonon mode are zero. Each additional term therefore adds an additional level of accuracy to the description of the BO energy surface beyond that afforded by the harmonic approximation.

The electronic energy at a given configuration may be calculated using any electronic structure methodology, although DFT has been used in most applications of the methodology [88–90], as it generally offers the best balance between accuracy and computational affordability. The mapping can be carried out in any electronic state, which under the BO approximation is taken to remain adiabatically the same under the nuclear motion. Typically either the ground state or a thermal (Fermi-Dirac) occupation distribution is used; if the material has a band gap substantially larger than the thermal energy $\beta^{-1} = k_B T$ then it makes little difference to the results.

2.7.2 Vibrational Self-Consistent Field Equations

Expressing the electronic BO energy $\epsilon^{el}(\vec{q})$ with the PAA, the Hamiltonian (2.104) becomes

$$\hat{H}_{nucl} = \sum_{n,\vec{k}} -\frac{1}{2}\frac{\partial^2}{\partial q_{n,\vec{k}}^2} + \epsilon_{\mathrm{PAA}}(\vec{q}). \tag{2.119}$$

We construct now a trial nuclear wavefunction, $|\Phi\rangle$, as a Hartree product of individual-mode nuclear wavefunctions $|\varphi_{n,\vec{k}}\rangle$,

$$|\Phi(\vec{q})\rangle = \prod_{n,\vec{k}} |\varphi_{n,\vec{k}}(q_{n,\vec{k}})\rangle \,. \tag{2.120}$$

A Slater determinant is not required as there is no requirement for the bosonic phonon wavefunctions to satisfy antisymmetry.

Substituting this trial wavefunction into the time-independent Schrödinger equation with the Hamiltonian of equation (2.119), and multiplying from the left by

$\langle \prod'_{n',\vec{k}'} \varphi_{n',\vec{k}'}(q_{n',\vec{k}'})|$, yields a set of mean-field equations for the individual-mode wavefunctions:

$$\left(-\frac{1}{2}\frac{\partial^2}{\partial q_{n,\vec{k}}^2} + \bar{V}_{n,\vec{k}}\right)|\varphi_{n,\vec{k}}(q_{n,\vec{k}})\rangle = E_{vib}\,|\varphi_{n,\vec{k}}(q_{n,\vec{k}})\rangle\,, \tag{2.121}$$

where

$$\bar{V}_{n,\vec{k}} = \left\langle \prod_{n,\vec{k}}{}' \varphi_{n,\vec{k}}(q_{n,\vec{k}}) \middle| \epsilon_{\mathrm{PAA}}(\vec{q}) \middle| \prod_{n,\vec{k}}{}' \varphi_{n,\vec{k}}(q_{n,\vec{k}}) \right\rangle \tag{2.122}$$

is the mean-field potential felt by the mode $\left(n,\vec{k}\right)$, and E_{vib} is the total vibrational energy.

In evaluating $\bar{V}_{n,\vec{k}}(q_{n,\vec{k}})$, it is useful to re-write the BO energy under the PAA, ϵ_{PAA}, by separating the terms that are a function of $q_{n,\vec{k}}$ and those that aren't:

$$\begin{aligned}\epsilon_{\mathrm{PAA}}(\vec{q}) = & \underbrace{V_{n,\vec{k}}(q_{n,\vec{k}}) + 2\cdot\frac{1}{2!}\sum_{\substack{n'',\vec{k}''\\ \neq(n,\vec{k})}} V_{n,\vec{k};n'',\vec{k}''}(q_{n,\vec{k}}, q_{n'',\vec{k}''}) + \ldots}_{q_{n,\vec{k}}\text{ dependent terms}} \\ & + \underbrace{\epsilon(\vec{0}) + \sum_{\substack{n',\vec{k}'\\ \neq(n,\vec{k})}} \left[V_{n',\vec{k}'}(q_{n',\vec{k}'}) + \frac{1}{2!}\sum_{\substack{n'',\vec{k}''\\ \neq(n,\vec{k})}}{}' V_{n',\vec{k}';n'',\vec{k}''}(q_{n',\vec{k}'}, q_{n'',\vec{k}''}) + \ldots \right]}_{\text{non-}q_{n,\vec{k}}\text{ dependent terms}},\end{aligned} \tag{2.123}$$

where we have used the fact that $V_{n'',\vec{k}'';n,\vec{k}}(q_{n'',\vec{k}''}, q_{n,\vec{k}}) = V_{n,\vec{k};n'',\vec{k}''}(q_{n,\vec{k}}, q_{n'',\vec{k}''})$ to collect together each coupled term that is a function of $q_{n,\vec{k}}$. A term with N_c coupled modes will have N_c such terms appearing in the first grouping. When the expectation value with respect to the state $|\prod'_{n',\vec{k}'} \varphi_{n',\vec{k}'}(q_{n',\vec{k}'})\rangle$ is taken to form $\bar{V}_{n,\vec{k}}\,(q_{n,\vec{k}})$, the first set of terms will give a function of $q_{n,\vec{k}}$, which is denoted by $\bar{V}'_{n,\vec{k}}(q_{n,\vec{k}})$, while the second will produce a constant energy, denoted $\bar{V}^{\mathrm{const}}_{n,\vec{k}}$. Thus:

$$\bar{V}_{n,\vec{k}}(\vec{q}_{n,\vec{k}}) = \bar{V}'_{n,\vec{k}}(\vec{q}_{n,\vec{k}}) + \bar{V}^{\mathrm{const}}_{n,\vec{k}}. \tag{2.124}$$

We can then define individual-mode eigenvalues $\lambda_{n,\vec{k}}$ as

$$\lambda_{n,\vec{k}} = E_{\text{vib}} - \bar{V}^{\text{const}}_{n,\vec{k}}, \tag{2.125}$$

so that equation (2.121) can be re-expressed as

$$\left(-\frac{1}{2}\frac{\partial^2}{\partial q^2_{n,\vec{k}}} + \bar{V}'_{n,\vec{k}}\right)|\varphi_{n,\vec{k}}(q_{n,\vec{k}})\rangle = \lambda_{n,\vec{k}}\,|\varphi_{n,\vec{k}}(q_{n,\vec{k}})\rangle\,. \tag{2.126}$$

This set of coupled mean-field equations is solved by self-consistently minimising the energy with respect to the individual mode wavefunctions $\left\{|q_{n,\vec{k}}(q_{n,\vec{k}})\rangle\right\}$. We can also obtain individual-mode excited states, which must be orthogonal to lower-energy solutions. The total vibrational energy E_{vib} is not simply a sum of the individual-mode eigenvalues, but rather is given by

$$E_{\text{vib}} = \sum_{n,\vec{k}} \lambda_{n,\vec{k}} \;+\; \left\langle \prod_{n,\vec{k}} \varphi_{n,\vec{k}}(q_{n,\vec{k}}) \middle| \epsilon_{\text{PAA}}(\vec{q}) - \sum_{n,\vec{k}} \bar{V}'_{n,\vec{k}} \middle| \prod_{n,\vec{k}} \varphi_{n,\vec{k}}(q_{n,\vec{k}}) \right\rangle. \tag{2.127}$$

The second term on the right hand side of the equation is a correction for multiple-counting of mode energies under the mean-field approach. Note that it equals zero in the case of independent modes.

When dealing with excited states, an excited state wavefunction analogous to that of equation (2.108) may be used:

$$|\Phi^{\vec{S}}(\vec{q})\rangle = \prod_{n,\vec{k}} |\varphi^{S_{n,\vec{k}}}_{n,\vec{k}}(q_{n,\vec{k}})\rangle\,. \tag{2.128}$$

A Møller-Plesset MP2-type perturbation theory can be implemented [91] to provide a correction to the mean-field energy, given by

$$E^{(2),\vec{S}}_{nucl} = \sum_{\vec{S}\neq\vec{S}'} \frac{1}{E_{\vec{S}} - E_{\vec{S}'}} \left| \left\langle \prod_{n,\vec{k}} \varphi^{S'_{n,\vec{k}}}_{n,\vec{k}}(q_{n,\vec{k}}) \middle| \epsilon_{\text{PAA}}(\vec{q}) - \sum_{n,\vec{k}} \bar{V}'_{n,\vec{k}} \middle| \prod_{n,\vec{k}} \varphi^{S_{n,\vec{k}}}_{n,\vec{k}}(q_{n,\vec{k}}) \right\rangle \right|^2. \tag{2.129}$$

Again, for independent modes this quantity equals zero. For coupled modes, the size of this correction gives some indication of the validity of the mean-field approach.

The partition function $\mathcal{Z}$ and free energy F are still given by the first lines of equations (2.110) and (2.111) respectively, but the state energies $E_{\vec{S}}$ are now those

determined from the VSCF calculations, rather than under the harmonic approximation.

2.7.3 Implementation

The work relating to anharmonic vibrational calculations in this thesis was carried out using a set of scripts originally authored by Bartomeu Monserrat, with modifications and further development by the author of this thesis. As the PAA is built upon the harmonic normal modes, a harmonic-level vibrational calculation must first be carried out. This also sets a baseline for comparison with the anharmonic treatment, to determine the extent of anharmonicity in a system of interest. The harmonic calculations were carried out using the finite displacement method implemented by the LTE code, with force constants derived from DFT calculations using the CASTEP program.

The eigenvectors and frequencies calculated at the harmonic level serve as inputs to the mapping of the BO energy surface. For the work in this thesis, mapping is carried out along each normal mode direction independently. An even number of equally-spaced data points are calculated, split evenly each side of the equilibrium configuration, in addition to the equilibrium configuration. The mapping is taken out to some multiple, typically five, of the square root of the harmonic expectation value of $q^2_{n,\vec{k}}$, given by

$$\left\langle q^2_{n,\vec{k}} \right\rangle = \frac{1}{\omega_{n,\vec{k}}} \left[\frac{1}{e^{\beta\omega_{n,\vec{k}}} - 1} \; + \; \frac{1}{2} \right]. \tag{2.130}$$

For soft modes, in which the harmonic frequency gives a poor approximation to the shape of the potential to be mapped, a different multiple of $\sqrt{\left\langle q^2_{n,\vec{k}} \right\rangle}$ is used to ensure a sensible sampling of the BO surface along that mode direction. A cubic spline is then fitted to the mapping data to produce a continuous BO surface for each mode. Examples of BO surfaces of modes demonstrating anharmonicity are shown in Fig. 2.8.

The VSCF calculation is then carried out using the mapping data. The single-mode wavefunctions $|\varphi_{n,\vec{k}}(q_{n,\vec{k}})\rangle$ are expanded in terms of a basis of quantum harmonic oscillator eigenstates, $\left\{|\phi^{\omega}_i(q_{n,\vec{k}})\rangle\right\}$,

$$|\varphi_{n,\vec{k}}(q_{n,\vec{k}})\rangle = \sum_{i=0}^{N_b} \alpha_{n,\vec{k};i} \, |\phi^{\omega}_i(q_{n,\vec{k}})\rangle \, , \tag{2.131}$$

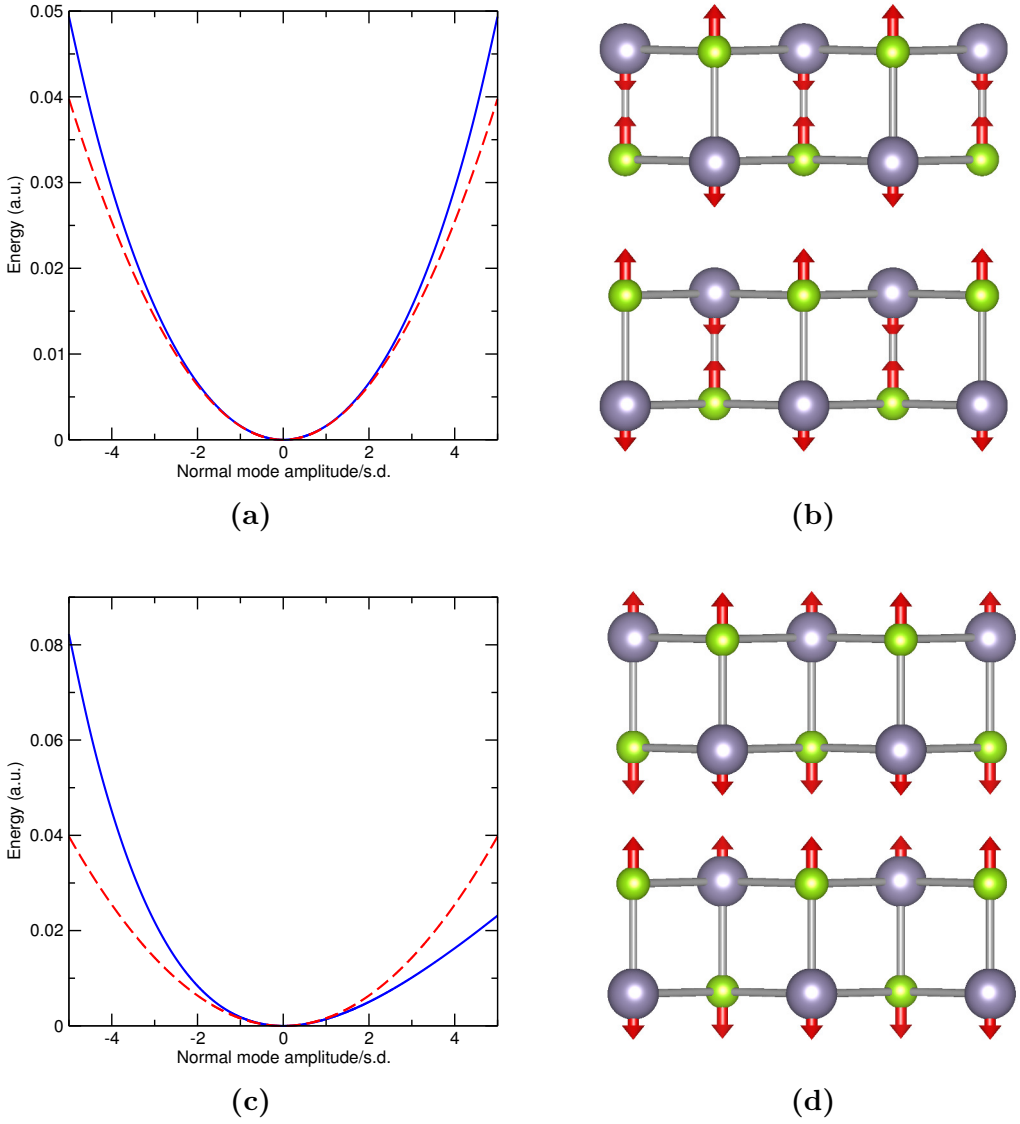

Fig. 2.8 Examples of Born-Oppenheimer energy surfaces along individual mode directions in the $Cmcm$ phase of SnSe. Subfigures (a) and (c) show the Born-Oppenheimer energy surface as a function of normal mode amplitude (expressed relative to $\sqrt{\langle q^2_{n,\vec{k}} \rangle}$) for two modes: (a) demonstrates a quartic-type anharmonicity, while (c) demonstrates a strong cubic-type anharmonicity. The solid blue lines show the cubic spline fit to the mapped BO potential, and the dashed red lines show the HA potential. Note that the BO surface and the harmonic potential agree well for small amplitudes, but diverge at larger amplitudes. Subfigures (b) and (d) depict the movement of the atoms for the modes plotted in (a) and (c), respectively.

where i denotes the excitation level of the harmonic eigenstate, ω is the frequency of the harmonic oscillator, and N_b is the number of basis functions used. The $\alpha_{n,\vec{k};i}$ coefficients are subject to the normalisation condition $\sum_i^{N_b} \alpha^2_{n,\vec{k};i} = 1$. In the limit of an infinite number of harmonic oscillator eigenfunctions, the basis is complete, though in practice the basis must be truncated at some finite N_b. The number of basis functions used is tested for convergence. The harmonic frequency of the basis functions, ω, is determined through a harmonic fit to the mapping data.

In the limit of infinite crystal size, the summation over all allowed wavevectors $\vec{k}$ becomes an integration over the BZ. This integration can be approximated by sampling the BZ on an $n_1 \times n_2 \times n_3$ grid, the size of which must be tested for convergence. In order to carry out mapping at a given k vector, a unit cell commensurate with vibrations with that k vector must be used. An $n_1 \times n_2 \times n_3$ sampling grid for BZ integration can be calculated by using a $n_1 \times n_2 \times n_3$ supercell, which is commensurate with all sampled k vectors. However, with plane-wave DFT, where the computational expense increases as the cube of the system size, this can rapidly become computationally unaffordable. For example, the computational cost of *each atomic configuration* for an $n \times n \times n$ sampling of the BZ grows as n^9.

The *non-diagonal supercell method* developed by Lloyd-Williams *et al.* [92] provides a way of greatly reducing this computational expense. A supercell matrix $\mathbf{S}$ can be used to construct a supercell with lattice vectors $\vec{a}_s$, $\vec{b}_s$ and $\vec{c}_s$ from a primitive cell with lattice vectors $\vec{a}_p$, $\vec{b}_p$ and $\vec{c}_p$ as follows:

$$\begin{pmatrix} \vec{a}_s \\ \vec{b}_s \\ \vec{c}_s \end{pmatrix} = \underbrace{\begin{pmatrix} S_{11} & S_{12} & S_{13} \\ S_{21} & S_{22} & S_{23} \\ S_{31} & S_{32} & S_{33} \end{pmatrix}}_{\mathbf{S}} \begin{pmatrix} \vec{a}_p \\ \vec{b}_p \\ \vec{c}_p \end{pmatrix}. \tag{2.132}$$

By allowing the off-diagonal elements of $\mathbf{S}$ to be non-zero, a non-diagonal supercell commensurate with a given vibrational k vector can be created – that is, the atomic displacements associated with the normal modes at the k vector can be represented within the periodic supercell. If the k vector can be represented in irreducible fractional coordinates within the BZ as

$$\vec{k} = \begin{pmatrix} \frac{m_1}{n_1} \\ \frac{m_2}{n_2} \\ \frac{m_3}{n_3} \end{pmatrix}, \tag{2.133}$$

then displacements corresponding to $\vec{k}$ can be represented within a non-diagonal supercell containing a number of primitive unit cells $N_{\text{p.c.}}$ equal to the least common multiple (LCM) of n_1, n_2 and n_3:

$$N_{\text{p.c.}} = \text{LCM}(n_1, n_2, n_3). \tag{2.134}$$

For the example of the $n \times n \times n$ grid, this means that each atomic configuration used as part of the mapping of the BO energy surface can be represented within a supercell containing n, rather than n^3 primitive cells, with a computational cost within plane-wave DFT scaling as n^3, rather than n^9, a saving of six powers of n. This clearly allows calculations to be performed that would be infeasible using diagonal supercells only.

Two examples of non-diagonal supercells are depicted in Fig. 2.9. A primitive cell and two non-diagonal supercells are depicted for the *Cmcm* phase of SnSe. The two supercells are generated by supercell matrices $\mathbf{S}_1$ and $\mathbf{S}_2$ to be commensurate with k-vectors given (in fractional coordinates) by $\vec{k}_1 = (0, 0, \frac{1}{3})$ and $\vec{k}_2 = (0, \frac{1}{3}, -\frac{1}{3})$. The supercell matrices are

$$\mathbf{S}_1 = \begin{pmatrix} 1 & 0 & 0 \\ 0 & 1 & 0 \\ 0 & 1 & -3 \end{pmatrix} \qquad \mathbf{S}_2 = \begin{pmatrix} 1 & 0 & 0 \\ 0 & 1 & 1 \\ 0 & 2 & -1 \end{pmatrix}$$

It should be noted that the definitions for atomic displacements and normal coordinates of equations (2.101) and (2.102) are not size-consistent within the supercell-based PAA. Instead, an alternative Fourier convention for these quantities is taken to ensure size-consistency within supercells:

$$u_{\alpha,p;i} \;=\; \frac{1}{\sqrt{M_\alpha}} \sum_{n,\vec{k}} q'_{n,\vec{k}}\, e^{\vec{k}\cdot\vec{L}_p}\, \eta_{n,\vec{k};\alpha,i}, \tag{2.135}$$

and

$$q'_{n,\vec{k}} = \frac{1}{N_p} \sum_{\vec{L}_p,\alpha,i} \sqrt{M_\alpha}\, u_{\alpha,p;i}\, e^{-i\vec{k}\cdot\vec{L}_p}\, \eta_{n,-\vec{k};\alpha,i}. \tag{2.136}$$

The non-diagonal supercell and VSCF calculations were carried out using programs authored by Jonathan Lloyd-Williams and Bartomeu Monserrat, with modifications by the author of this thesis.

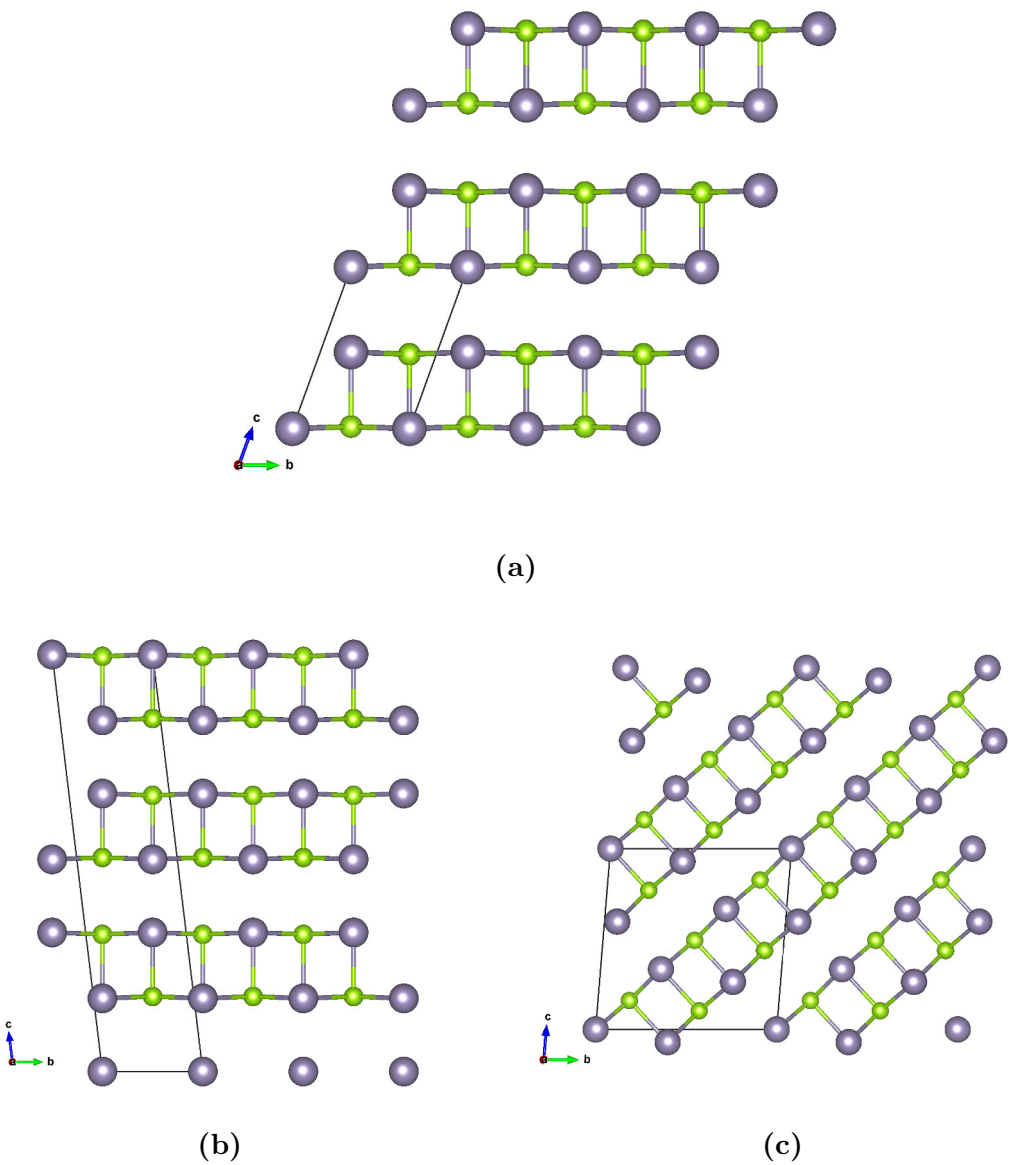

Fig. 2.9 Examples of non-diagonal supercells in the *Cmcm* phase of SnSe. In each case, several cells are depicted, with the boundary of one cell shown as black lines. (a) The primitive cell; (b) a supercell generated by supercell matrix $\mathbf{S}_1$ to be commensurate with k point $\vec{k}_1$; (c) a supercell generated by supercell matrix $\mathbf{S}_2$ to be commensurate with k point $\vec{k}_2$.

2.8 Expectation Values of Observables

The basic VSCF approach yields nuclear vibrational energies and free energies, but it also yields the anharmonic nuclear wavefunctions $|\Phi^{\vec{S}}\rangle$, which are the nuclear part of the wavefunction within the BO approximation, and therefore fully characterise the vibrational motion of the system. If the behaviour of some general physical observable can be characterised as a function of atomic configuration, then the wavefunction can be used to calculate an expectation value for that observable, renormalised over the atomic motion. This section describes the different approaches that can be taken to calculate these renormalised expectation values, and then proceeds to look in particular at the renormalisation of the stress experienced by a system, and the consequences for thermal expansion (which is an inherently anharmonic effect [93]); and the renormalisation of electronic structure due to nuclear motion (electron-phonon coupling).

2.8.1 Renormalisation of Observables

A physical observable may be denoted by an operator $\hat{\mathcal{O}}$. Let us suppose the observable may be uniquely determined by the atomic configuration $\vec{q}$, so that $\hat{\mathcal{O}} = \hat{\mathcal{O}}(\vec{q})$. We shall assume that we are able to calculate the value of the observable at any given nuclear configuration. The expectation value of the observable at in a statistical ensemble at inverse temperature β, $\left\langle \hat{\mathcal{O}} \right\rangle_\beta$, is given by

$$\left\langle \hat{\mathcal{O}} \right\rangle_\beta = \langle \Phi | \hat{\mathcal{O}} | \Phi \rangle \,, \tag{2.137}$$

where $|\Phi\rangle$ is the total vibrational wavefunction of the system. We may consider the total wavefunction $|\Phi\rangle$ in terms of the energy eigenfunctions defined in equation (2.128), $|\Phi^{\vec{S}}(\vec{q})\rangle$; equation (2.137) becomes:

$$\left\langle \hat{\mathcal{O}} \right\rangle_\beta = \sum_{\vec{S}} p_{\vec{S}} \left\langle \Phi^{\vec{S}} \middle| \hat{\mathcal{O}} \middle| \Phi^{\vec{S}} \right\rangle , \tag{2.138}$$

where $p_{\vec{S}}$ is the fraction of the ensemble found in state $\vec{S}$.

In thermal equilibrium, the fraction of the ensemble being in state $\vec{S}$ with energy $E_{\vec{S}}$ is determined by the Boltzmann distribution, so that $p_{\vec{S}} \propto e^{-\beta E_{\vec{S}}}$. Thus, at thermal equilibrium,

$$\begin{aligned}\left\langle \hat{\mathcal{O}} \right\rangle_\beta =& \frac{1}{\mathcal{Z}} \sum_{\vec{S}} e^{-\beta E_{\vec{S}}} \left\langle \Phi^{\vec{S}}(\vec{q}) \middle| \hat{\mathcal{O}}(\vec{q}) \middle| \Phi^{\vec{S}}(\vec{q}) \right\rangle \\ =& \frac{1}{\mathcal{Z}} \sum_{\vec{S}} e^{-\beta E_{\vec{S}}} \int d\vec{q} \, |\Phi^{\vec{S}}(\vec{q})|^2 \mathcal{O}(\vec{q}) \\ =& \int d\vec{q} \, |\Phi(\vec{q})|^2 \mathcal{O}(\vec{q}),\end{aligned} \tag{2.139}$$

defining $|\Phi(\vec{q})|^2 = \frac{1}{\mathcal{Z}} \sum_{\vec{S}} e^{-\beta E_{\vec{S}}} |\Phi^{\vec{S}}(\vec{q})|^2$. The evaluation of (2.139) can be tricky. Although we can produce $|\Phi^{\vec{S}}(\vec{q}, \beta)|^2$ through the VSCF approach, finding $\mathcal{O}(\vec{q})$ is not necessarily straightforward.

A few approaches to evaluating equation (2.139) will now be discussed.

Monte Carlo integration

One of the most direct approaches to the evaluation of equation (2.139) is *Monte Carlo integration*. In this method, the observable is evaluated at a finite number, N, of nuclear configurations, denoted $\{\vec{q}_i\}$, generated such that the probability of a configuration being generated is proportional to the amplitude-square of the thermally-averaged nuclear wavefunction evaluated at that configuration, i.e. $\{\vec{q}_i\} \sim |\Phi(\vec{q}, \beta)|^2$. The expectation value of the observable is then determined through standard numerical integration as

$$\left\langle \hat{\mathcal{O}} \right\rangle_\beta \simeq \frac{1}{N} \sum_{i=1}^{N} \hat{\mathcal{O}}(\vec{q}_i). \tag{2.140}$$

The Monte Carlo integration approach has several advantages. Firstly, the scheme allows for the evaluation of $\hat{\mathcal{O}}(\vec{q})$ across the complete range of nuclear configurations, without restricting configurations to only a certain number of coupled modes. However, this generally rules out use of the non-diagonal supercell method, as a supercell commensurate with all sampled $\vec{k}$ points is required. Secondly, the statistical variance of the expectation value, $\sigma^2_{\langle \mathcal{O} \rangle_\beta}$, which can be estimated as

$$\sigma^2_{\langle \mathcal{O} \rangle_\beta} \simeq \frac{1}{N(N-1)} \sum_{i=1}^{N} \left(\mathcal{O}(\vec{q}_i) - \frac{1}{N} \sum_{j=1}^{N} \mathcal{O}(\vec{q}_j) \right)^2, \tag{2.141}$$

is reduced simply by increasing the number of sampling points, without dependence on the dimensionality of the integral. This makes Monte Carlo integration especially

attractive for the evaluation of expectation values in large systems. Finally, from a computational point of view each sampling point $\vec{q}_i$ is essentially independent from all other points, so that the evaluation of (2.140) is trivially parallelisable. The principal disadvantage of the Monte Carlo integration approach is that the number of sampling points required for an accurate evaluation of the integral in equation (2.139) tends to be rather large. For high-dimensional systems, the dimensionality independence of the number of sampling points is attractive, but for lower-dimensional systems, other methods tend to be less computationally expensive.

The main difficulty in the implementation of the Monte Carlo method lies in the generation of the points $\{\vec{q}_i\}$. The computation of random numbers distributed according to an arbitrary distribution function is not a straightforward problem. However, in the present case we can make use of the known form of $|\Phi(\vec{q},\beta)|^2$ within the harmonic approximation, given in equations (2.112) and (2.113). Random numbers may be generated according to a Gaussian distribution straightforwardly using the Box-Muller transformation [94], and all that is required in the harmonic case is a temperature-dependent rescaling of the standard deviation (and corresponding normalisation) of the generated numbers. Provided the full anharmonic wavefunction is not very dissimilar from the harmonic wavefunction, we can go beyond the HA while still making use of the simplicity of generating Gaussian-distributed random numbers by rewriting equation (2.139) as

$$\begin{aligned}\left\langle\hat{\mathcal{O}}\right\rangle &= \int d\vec{q}\,\frac{|\Phi_{\mathrm{anh}}(\vec{q},\beta)|^2}{|\Phi_{\mathrm{har}}(\vec{q},\beta)|^2}|\Phi_{\mathrm{har}}(\vec{q},\beta)|^2\,\hat{\mathcal{O}}(\vec{q}) \\ &\simeq \frac{1}{N}\sum_{i=1}^{N}\frac{|\Phi_{\mathrm{anh}}(\vec{q}_i,\beta)|^2}{|\Phi_{\mathrm{har}}(\vec{q}_i,\beta)|^2}\,\hat{\mathcal{O}}(\vec{q}_i).\end{aligned} \tag{2.142}$$

The nuclear configurations $\{\vec{q}_i\}$ of the second line are again generated according to the harmonic distribution, $\{\vec{q}_i\} \sim |\Phi_{\mathrm{har}}(\vec{q},\beta)|^2$. The only difference to the harmonic case then becomes the additional weighting factor given by the ratio of the amplitude-squares of the anharmonic and harmonic wavefunctions. The variance of this approach is given by

$$\sigma^2_{\langle\mathcal{O}\rangle_\beta} \simeq \frac{1}{N(N-1)}\sum_{i=1}^{N}\left(\frac{|\Phi_{\mathrm{anh}}(\vec{q}_i,\beta)|^2}{|\Phi_{\mathrm{har}}(\vec{q}_i,\beta)|^2}\mathcal{O}(\vec{q}_i) - \frac{1}{N}\sum_{j=1}^{N}\frac{|\Phi_{\mathrm{anh}}(\vec{q}_i,\beta)|^2}{|\Phi_{\mathrm{har}}(\vec{q}_i,\beta)|^2}\mathcal{O}(\vec{q}_j)\right)^2. \tag{2.143}$$

Anharmonic wavefunctions that are substantially different from their harmonic equivalents may not be suited to this approach; instead, a Metropolis-Hastings algorithm-based approach [73, 95] may be better. However, the Metropolis-Hastings algorithm requires knowledge of the history of previously generated configurations, and so is much less suited to calculations in parallel.

Quadratic approximation

Another approach to the evaluation of equation (2.139) is to expand $\mathcal{O}(\vec{q})$ as a power series in the $q_{n,\vec{k}}$ about $\vec{q} = \vec{0}$:

$$\hat{\mathcal{O}}(\vec{q}) = \hat{\mathcal{O}}(\vec{0}) + \sum_{n,\vec{k}} c^{(1)}_{n,\vec{k}}\, q_{n,\vec{k}} + \sum_{n,\vec{k};n',\vec{k}'} c^{(2)}_{n,\vec{k};n',\vec{k}'}\, q_{n,\vec{k}}\, q_{n',\vec{k}'} + \ldots, \tag{2.144}$$

where the $c^{(i)}_{n,\vec{k};\ldots}$ are coupling constants of the observable to the relevant term in the power expansion. These may be obtained by fitting a functional form to the observable mapped along relevant modes.

In the case of a harmonic wavefunction, the evenness of the wavefunction about $\vec{q} = \vec{0}$ leads to all the terms in an odd power of q evaluating to zero, leaving only the even-powered terms. Furthermore, at $\mathcal{O}(q^2)$, terms corresponding to different modes or k-points also evaluate to zero in the expectation value. Thus, in the case of the harmonic wavefunction, the expectation value of equation (2.144) evaluates to

$$\left\langle \hat{\mathcal{O}} \right\rangle = \hat{\mathcal{O}}(\vec{0}) + \frac{1}{\mathcal{Z}} \sum_{n,\vec{k}} \sum_{\vec{S}_{n,\vec{k}}} c^{(2)}_{n,\vec{k};n,\vec{k}} \left\langle \phi^{S_{n,\vec{k}}}_{\mathrm{har}}(q_{n,\vec{k}}) \middle| q^2_{n,\vec{k}} \middle| \phi^{S_{n,\vec{k}}}_{\mathrm{har}}(q_{n,\vec{k}}) \right\rangle e^{-\beta E_{S_{n,\vec{k}}}} + \mathcal{O}(q^4), \tag{2.145}$$

which can be further simplified to

$$\left\langle \hat{\mathcal{O}} \right\rangle \simeq \hat{\mathcal{O}}(\vec{0}) + \sum_{n,\vec{k}} \frac{c^{(2)}_{n,\vec{k};n,\vec{k}}}{2\,\omega_{n,\vec{k}}} \left[1 + 2n_B(\omega_{n,\vec{k}}, \beta)\right], \tag{2.146}$$

where n_B is the Bose-Einstein occupation, $n_B(\omega_{n,\vec{k}}, \beta) = \left[\exp\left(\beta\omega_{n,\vec{k}}\right) - 1\right]^{-1}$. The terms in q^4 and higher have been dropped here; the assumption that these terms are small compared to the lower-order terms is not always true, as has been demonstrated in one recent study [88].

In the more general case of an anharmonic wavefunction, we may no longer consider the evaluation of terms in odd powers of q to be small, or that terms with $(n', \vec{k}') \neq (n, \vec{k})$ will evaluate to zero in the second-order term. We should instead evaluate

the full expression in (2.144). An alternative approximation that can be made when evaluating the expectation value of the expansion is to neglect coupled modes, so only coupling constants of the form $c^{(i)}_{n,\vec{k};n,\vec{k};\ldots}$ are considered to be non-zero. This is the approach used in this thesis.

Although the quadratic approximation is not as exact as the Monte Carlo integration method, it is usually less computationally intensive, particularly for lower-dimensional systems, and like Monte Carlo integration is easily parallelised. It also allows for physical insight into the renormalisation of physical properties through examination of the individual terms in the expansion; this is not possible in Monte Carlo integration, which simply produces the renormalised expectation value without physical insight. However, while a reasonable approximation in some systems, the quadratic approximation has been found to be inadequate in others, such as molecular crystals [88].

An extension to the quadratic approximation based on estimating a mean-value nuclear configuration for a property, known as the *thermal lines* method, has also been proposed [96, 97].

Dynamical approaches

A final class of methods for evaluating the integral equation (2.139) is based on dynamical methods, such as classical molecular dynamics (MD) [98, 99] and path integral molecular dynamics (PIMD) [100, 101].

In these methods, the nuclear configurations at which the observable is sampled are generated by propagating the system in discrete time steps according to forces calculated by quantum mechanical methods. In MD, the nuclei are treated classically, but with forces calculated through quantum-mechanical methods such as DFT. As a result the quantum-mechanical effect of zero-point motion is not included. PIMD is based on the path-integral formulation of quantum mechanics and does include zero-point effects.

When propagated for a sufficiently long time, these dynamical methods end up generating configurations according to $|\Phi(\vec{q},\beta)|^2$ indirectly through the quantum-mechanical forces used, rather than the direct generation of configurations according to $|\Phi(\vec{q},\beta)|^2$ employed in the Monte Carlo integration technique.

The principal drawback to such dynamical techniques is that the next configuration can only be generated following a computationally intensive electronic structure calculation based on the previous configuration. These techniques are therefore serial in

nature, as opposed to the easily parallelisable Monte Carlo integration and quadratic approximation methods, and so less well suited to high-throughput calculations.

2.8.2 Specific Cases of Renormalised Observables

Particular attention will now be turned to the principal observables studied in this thesis (other than energies): stress and electronic band gaps. The thermal expansion that results from the vibrational stress will also be discussed.

Stress and thermal expansion

Under the HA, nuclear vibrations do not lead to any thermal expansion. However, when anharmonicities are treated, nuclear motion gives rise to a vibrational correction to the stress tensor σ of the system, which determines the thermal expansion of the system.

For systems with only a very small number – typically not more than two – degrees of freedom, an established method for studying thermal expansion is the *quasi-harmonic method* [83]. In this method, the HA is used, but the vibrational frequencies are taken to be dependent on the lattice parameters of the system. For example, in the case of a system with a single lattice parameter, a, such as diamond, $\omega_{n,\vec{k}} = \omega_{n,\vec{k}}(a)$. Phonon calculations at the harmonic level are carried out at a range of lattice parameters, and the total free energy of the system is calculated. Energies are generated for intermediate values of the lattice parameter by interpolation. The thermally-expanded lattice parameter is then the one that minimises the total free energy of the system. The quasi-harmonic approximation is an effective technique in systems with only a very small number of degrees of freedom, but in other systems the global minimisation of the free energy as a function of many variables becomes a computationally expensive task. It is therefore desirable to be able to study thermal expansion through the full anharmonic vibrational renormalisation of the stress tensor.

Nielsen and Martin [102] derived the internal stress tensor σ for a quantum mechanical system as

$$\sigma_{ij} = \frac{1}{V} \frac{\partial \langle \Psi | \hat{H} | \Psi \rangle}{\partial \epsilon_{ij}}, \tag{2.147}$$

where V is the volume, $\hat{H}$ is the Hamiltonian of the system, and ϵ_{ij} is the strain tensor; i and j label Cartesian directions. Following the Hamiltonian of equation (2.18), we may decompose the Hamiltonian $\hat{H}$ into nuclear kinetic and electronic potential parts

– $\sigma^{\text{vib,kin}}$ and $\sigma^{\text{vib,pot}}$, respectively – and examine the contribution of each to the total stress [82]. The kinetic contribution to the stress tensor is given by

$$\sigma_{ij}^{\text{vib,kin}} = \frac{1}{\mathcal{Z}} \sum_{\vec{S}} -\frac{1}{V} \left\langle \Phi^{\vec{S}} \middle| \sum_{\vec{L}_p,\alpha} m_\alpha \hat{\dot{u}}_{p,\alpha;i} \hat{\dot{u}}_{p,\alpha;j} \middle| \Phi^{\vec{S}} \right\rangle e^{-\beta E_{\vec{S}}}, \tag{2.148}$$

where the dots indicate time derivatives. Using $m_\alpha \hat{\dot{u}}_{p,\alpha;i} = \hat{p}_{p,\alpha;i} = -i\frac{\partial}{\partial \hat{x}_{p,\alpha;i}}$, where $\hat{p}$ is the momentum operator, we can see that these time derivatives can be calculated from the gradient of the wavefunction, which can be easily obtained for the anharmonic wavefunction when using a basis of harmonic wavefunctions.

The electronic stress σ^{el} experienced by the system is a function of the nuclear configuration, and can be calculated using DFT methods. The potential contribution to the stress tensor then arises from a vibrational renormalisation of the electronic stress within the system. In accordance with equation (2.139), the potential contribution to the stress is

$$\sigma_{ij}^{\text{vib,pot}} = \frac{1}{\mathcal{Z}} \sum_{\vec{S}} \left\langle \Phi^{\vec{S}}(\vec{q}) \middle| \sigma_{ij}^{el} \middle| \Phi^{\vec{S}}(\vec{q}) \right\rangle e^{-\beta E_{\vec{S}}}, \tag{2.149}$$

which may be evaluated using the methods described in the previous section. The total vibrational correction to the internal stress of the system is then simply $\sigma^{\text{vib}} = \sigma^{\text{vib,kin}} + \sigma^{\text{vib,pot}}$.

Thermal expansion

We shall now see the role the vibrational stress tensor plays in thermal expansion. Indeed, as well as thermal expansion, the vibrational stress tensor includes quantum-mechanical zero-point effects, which will also be included in the expansion described here.

The expanded system will be the one in which the Gibbs free energy, G, is minimised, so that the differential Gibbs free energy dG, given by [103]

$$dG = dF_{el} + dF_{vib} - V \sum_{i,j} \sigma_{ij}^{\text{ext}} d\epsilon_{ij}, \tag{2.150}$$

is zero. F is the Helmholtz free energy, decomposed into electronic and nuclear vibrational parts, and σ^{ext} is the external stress tensor acting upon the system. The

vibrational stress tensor can be related to the differential of the vibrational Helmholtz free energy with respect to strain:

$$\sigma_{ij}^{\text{vib}} = -\frac{1}{V}\frac{\partial F_{vib}}{\partial \epsilon_{ij}}. \tag{2.151}$$

By defining an effective total stress tensor $\sigma^{\text{eff}} = \sigma^{\text{vib}} + \sigma^{\text{ext}}$, we can use equation (2.151) to re-write equation (2.150) as

$$dG = dF_{el} - V\sigma_{ij}^{\text{eff}}\, d\epsilon_{ij}. \tag{2.152}$$

Electronic structure codes such as CASTEP are capable of performing such a minimisation of the Gibbs free energy with respect to lattice parameters and atomic positions, so that the thermally-expanded unit cell and atomic coordinates can be obtained by use of this effective stress tensor.

It should be noted that thermal expansion modifies the BO energy surface mapped by the phonon normal modes, and so changes σ^{vib}. Therefore, to obtain the correct thermally-expanded structure, the BO mapping and thermal expansion processes may have to be repeated until the calculated effective stress tensor is self-consistent with the stress tensor used to generate the static lattice. In practice the vibrational stress tensor does not vary very much during thermal expansion and so only a relatively small number of iterations are usually required.

Carrying out thermal expansion of a system at a range of temperatures allows for the calculation of properties such as coefficients of expansion – for example, the volume coefficient of expansion, $\alpha_V(T)$, defined as

$$\alpha_V(T) = \frac{1}{V}\frac{dV}{dT}. \tag{2.153}$$

Band Gaps

The coupling of nuclear vibrational motion to electronic structure, often referred to as electron-phonon coupling, is a property of interest. Solving the electronic Hamiltonian $\hat{H}_{el}$ at each nuclear configuration yields the electronic band structure. Let the energy for band s at position $\vec{r}$ in reciprocal space be denoted by $\epsilon_{s,\vec{r}}$. Then, following equation (2.139), the expectation value for this band energy will be

$$\langle \epsilon_{s,\vec{r}} \rangle = \frac{1}{\mathcal{Z}} \left\langle \Phi^{\vec{S}}(\vec{q}) \middle| \epsilon_{s,\vec{r}}(\vec{q}) \middle| \Phi^{\vec{S}}(\vec{q}) \right\rangle e^{-\beta E_{\vec{S}}}, \tag{2.154}$$

which may be evaluated using the methods described in the previous section. This allows the entire renormalised band structure to be calculated.

In general, a single band energy is not of much interest, as the energy scale is arbitrary. However, the difference between two bands is not. Of particular interest in non-metals is the band gap – the difference in energy between the highest-energy valence band and the lowest-energy conduction band – which is of considerable importance to the properties of many materials. For example, the vibrational renormalisation of the band gap of helium at terapascal pressures indicates that helium does not metallise until higher pressures than are predicted using static-lattice calculations, leading to revised estimates of the age of white dwarf stars [104]. The band gap should be calculated at each nuclear configuration and vibrationally averaged, as interactions involving electronic transitions happen over a timescale much shorter than nuclear motion.

Finally, it should be noted that the thermal expansion described in the previous section affects the electronic energy bands, and so is also an important factor in calculating electron-phonon coupling.

The renormalisation calculations described in this thesis were carried out using programs authored by Bartomeu Monserrat, Jonathan Lloyd-Williams and the author of this thesis.

2.9 Summary

Within the density functional theory approach to determining the properties of quantum-mechanical systems, we have described a methodology, AIRSS, for conducting global explorations of the Born-Oppenheimer energy landscape, to identify stable and metastable structures. We also have a methodology, the VSCF approach, to explore the local shape of the Born-Oppenheimer energy surface around such local minima, and to obtain renormalisations for physical observables as a result of nuclear motion through this local energy landscape. The application of these methodologies to several systems of interest shall now be described.

Chapter 3

Defects in Graphene

In this chapter, a random structure searching method is applied to search for new vacancy and adatom defects in the two-dimensional carbon allotrope graphene. The atoms in a region of a graphene supercell are randomly disrupted to generate defect structures, whose formation energy is then calculated. Several possible new defect types are identified, with almost all known point defects of the types studied also appearing in the searches.

3.1 Introduction

3.1.1 Graphene

Graphene is a two-dimensional allotrope of carbon consisting of a flat layer of threefold-coordinated carbon atoms forming tessellating hexagons, as illustrated in Fig. 3.1. Graphene belongs to the hexagonal $P6/mmm$ space group. The C–C bonding consists of sp^2 hybridisation of the carbon s, p_x and p_y orbitals to form σ bonds, with a bond length of about 1.42 Å. The p_z orbitals hybridise to form half-filled π bands, which are the source of many of graphene's electronic properties [105, 106]. The common three-dimensional carbon allotrope graphite consists of weakly-bound layers of graphene, which are alternately offset from one another. Isolation of a single layer of graphene leads to remarkable properties not observed in bulk graphite.

Although theoretical work has been carried out on the graphene structure for many decades [106], it was only as recently as 2004 that Konstantin Novoselov and Andre Geim were able to isolate and study single layers of graphene experimentally [107], an achievement that won them the 2010 Nobel Prize in Physics. Since that time, there has been a great deal of experimental and theoretical interest in graphene for its

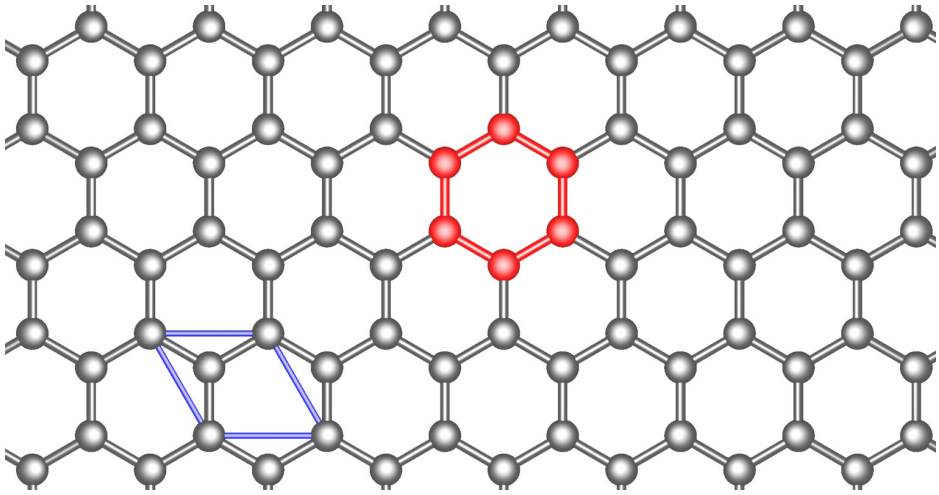

Fig. 3.1 Structure of pristine (undefected) graphene. The blue lines denote the primitive unit cell. The threefold-coordinated carbon atoms form tessellating hexagons, one of which is highlighted in red. The carbon atoms lie in a single plane of the c direction, which is perpendicular to the page.

extraordinary physical and electronic properties and its potential practical applications [108], some of which will now be summarised.

Graphene possesses enormous mechanical strength, with a tensile strength measured at 130 GPa and a Young's modulus of 1 TPa [109]. Being made up of light atoms that are tightly bound in the plane of the layer gives graphene a very high sound velocity, and consequentially a high thermal conductivity [105]. The thermal conductivity of graphene has been measured to be between 600 and 5,300 $\mathrm{Wm^{-1}K^{-1}}$ [110, 111]. Graphene also possesses remarkable electronic properties. Graphene is a zero band-gap semiconductor with a linear dispersion relation at the K and K′ points in the Brillouin zone (BZ), at which the valence and conduction bands meet at the Fermi energy. The electronic band structure along a high-symmetry path in the BZ is shown in Fig. 3.2. The points K and K′ are known as *Dirac points*, so called because the linear dispersion relation about these points corresponds to that of the massless Dirac equation, with the Fermi velocity v_F taking the place of the speed of light. In graphene, $v_F/c \simeq 0.01$. Electrons with wave vectors in the vicinity of K and K′ – i.e. near the Fermi level – thus behave relativistically [105, 106].

Graphene possesses exceptionally high carrier mobilities μ, with values of $\mu = 15{,}000\ \mathrm{cm^2V^{-1}m^{-1}}$ reported, which are only weakly dependent on temperature [108], and which remain high even when graphene is heavily doped. This yields very high electrical conductivity, including a minimum electrical conductivity when the carrier

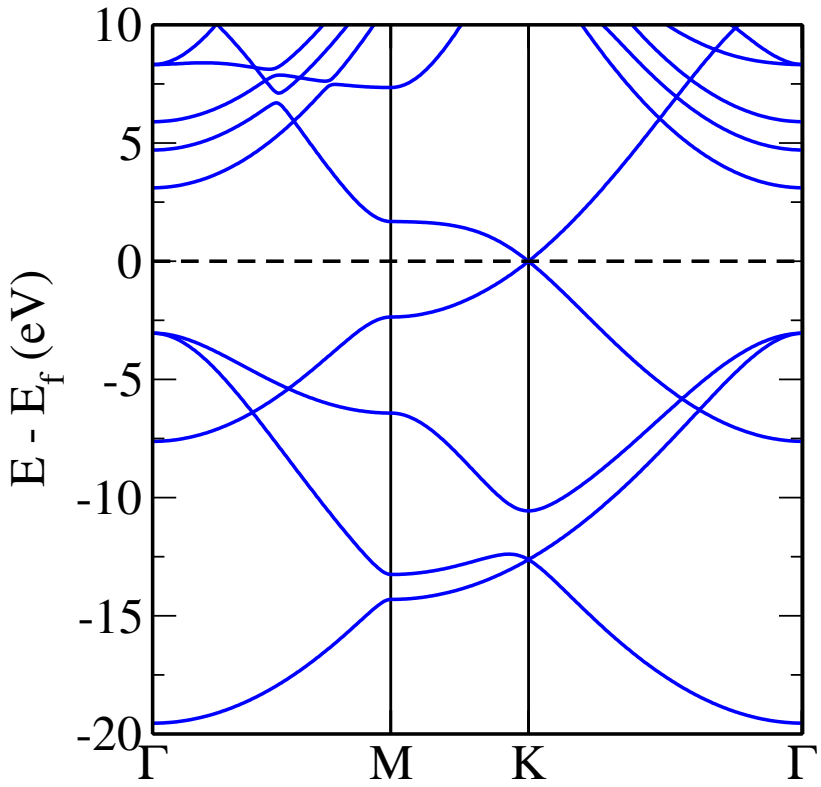

Fig. 3.2 Band structure of pristine graphene along a high-symmetry path through the first Brillouin Zone, calculated using DFT with the PBE [24] *xc* functional. Note that the conduction and valence bands meet at the K point, with zero band gap, and that the dispersion relation around this point is linear.

concentration tends towards zero [105]. Other electronic properties of graphene are discussed in the review of Castro Neto *et al.* [106].

The π bands in graphene open up the possibility of bonding and adsorption [106]. One notable example of graphene reactivity is with hydrogen. One hydrogen atom can bond to each carbon atom in graphene, with hydrogen atoms bonding to neighbouring carbon atoms being on opposite sides of the graphene sheet, to form a material known as *graphane*. Chemically, the carbon atoms transform from sp^2 to sp^3 hybridisation, with the π band disappearing [112]. This introduces a direct band gap of about 5.4 eV [113]. The presence of defects in the graphene structure is known to increase the reactivity of the defect site [114].

Various methods of synthesising graphene have been developed, such as mechanical exfoliation from graphite, the thermal decomposition of SiC, and molecular beam deposition on a substrate. The carrier mobility of graphene is highly dependent on the substrate [105].

The unique electronic and mechanical properties of graphene has led to a great deal of interest in the material over recent years. It is hoped that graphene will one day be used in a wide variety of applications, such as in battery applications and in hydrogen storage [108], that take advantage of its properties. The most longed-for potential application for graphene is in electronics, as a replacement to silicon chips, on account of graphene's very high carrier mobility [108]. However, such an application is a long way off, and will require us to be able to engineer a band gap of about 0.4 eV in graphene [105].

3.1.2 Defects in Graphene

Most theoretical studies consider only 'pristine' graphene, represented by an infinitely-repeated two-atom unit cell. However real graphene, like every material, may pick up defects in the 'pristine' material structure. This can occur naturally during graphene synthesis, particularly if carried out at low temperatures. Defects may also be deliberately induced through particle irradiation (requiring an energy of 15–20 eV to be transferred to a carbon atom to prevent immediate recombination [115]) or chemical reactions such as with an oxidising acid like H_2SO_4 [116]. Various types of defects in graphene have been studied both theoretically and experimentally, with many having been directly observed using high-resolution transmission electron microscopy (HRTEM) techniques [117–120].

The presence of defects in graphene modifies the local electronic and chemical properties in the vicinity of the defect. This may be undesirable, impairing pris-

tine graphene's remarkable properties, but it may also be desired. For example, for graphene-based electronic devices to become a reality, a method of introducing a small band gap in graphene is required, and inducing defects at particular sites on a graphene sheet could potentially offer a way of doing so [108]. The chemical reactivity also increases in the vicinity of graphene defects, opening up the possibility of local functionalisation of graphene sheets, for example to create electrical "contacts" with other materials [116, 121].

Graphene defects can be characterised as either 0-dimensional *point defects*, or 1-dimensional *line defects*. Line defects are reconstructions of the graphene structure occurring as a result of dislocations, at the interface of two graphene sheets and at the edges of graphene layers [116]. These types of defect are not the focus of this study; instead, we will focus on point defects of graphene.

The point defects of graphene can be considered to be of one of the following types:

1) Reconstructions of the graphene sheet;

2) Vacancies due to the loss of one or more carbon atoms;

3) The addition of carbon adatoms;

4) Foreign adatoms;

5) Substitutions of carbon atoms for foreign (non-carbon) atoms.

When vacancies, substitutions or adatoms occur, a reconstruction of the graphene layer usually occurs, which often maintains threefold carbon coordination through the formation of non-hexagonal groups of carbon atoms, such as pentagons and heptagons. The known point defects of graphene layers, falling into one of the above classes, shall now be briefly summarised. In the following discussion, the *defect formation energy* E_f is defined as

$$E_f = E_d - \sum_s N_s \, \mu_s, \tag{3.1}$$

where E_d is the total energy of the defected graphene structure, s labels the atomic species that constitute the defected structure, N_s is the number of atoms of species s in the structure, and μ_s is the chemical potential for species s. The chemical potential for carbon is the energy per atom of pristine graphene; for nitrogen, oxygen, hydrogen etc. it is the energy per atom of their diatomic gases. The defect *migration energy* is the minimum energy barrier that must be overcome for a defect to move from one site on the graphene layer to another.

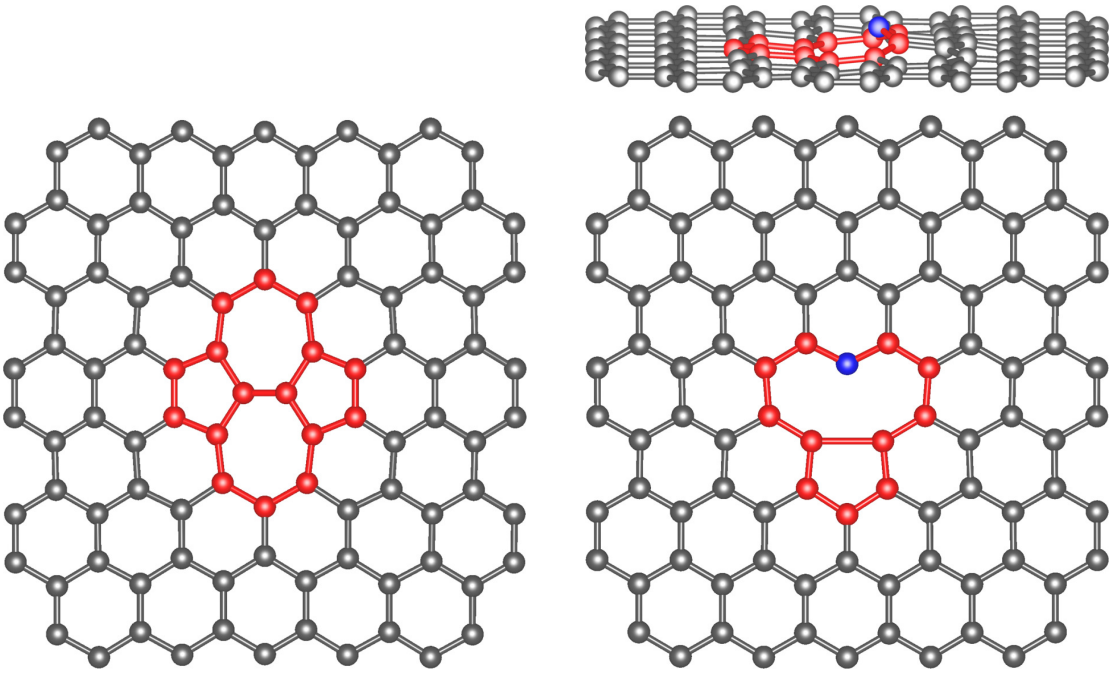

(a) SW(55–77)

(b) V_1(5–9)

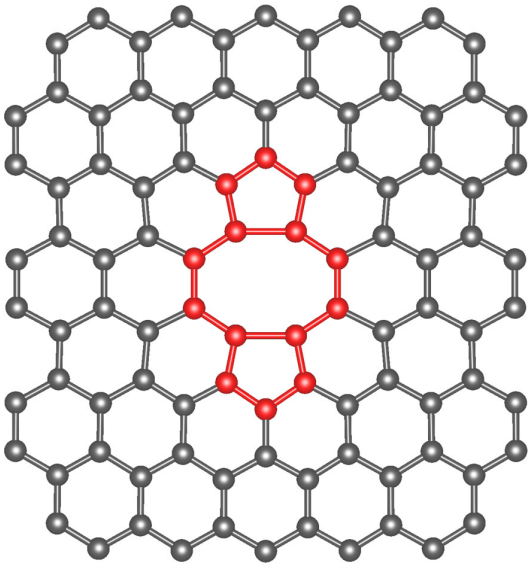

(c) V_2(5–8–5)

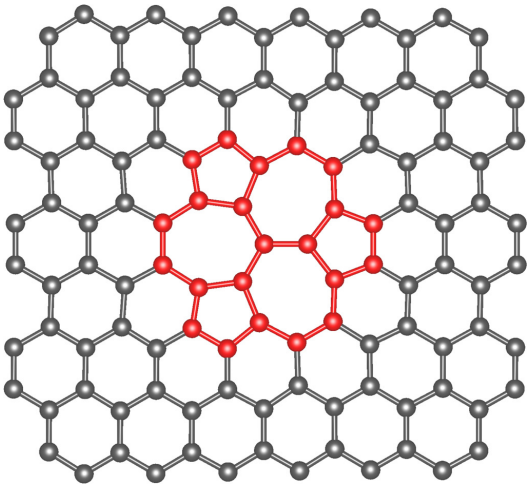

(d) V_2(555–777)

Fig. 3.3 Points defects in graphene. (a) Stone-Wales reconstruction SW(55–77); (b) single vacancy V_1(5–9); (c) double vacancy V_2(5–8–5); (d) double vacancy reconstruction V_2(555–777). In each case, the defect is highlighted in red. The single vacancy defect leaves an undercoordinated carbon atom, highlighted in blue, with dangling bonds that substantially increase the site reactivity. This atom is raised up slightly out of the plane. A slight 'ripple' in the sheet is observed for the Stone-Wales defect; the double vacancy defects do not produce any out-of-plane distortion in the graphene layer.

Reconstructions of pristine graphene: the Stone-Wales defect

The rotation by 90° of a C–C bond in the pristine graphene structure can lead to a point defect known as the Stone-Wales defect, SW(55–77) [122]. This leads to the formation of two pentagonal and two heptagonal arrangements of carbon atoms, in place of four hexagons, accompanied by an out-of-plane 'rippling' of the graphene sheet in the region around the defect [123]. The Stone-Wales defect is depicted in Fig. 3.3a. The energy barrier for formation of a Stone-Wales defect has been calculated to be about 9.2 eV [124], indicating that Stone-Wales defects are unlikely to form spontaneously at equilibrium under ambient conditions [116]. However, once formed, for example through particle beam irradiation, an energy barrier of about 4.4 eV for the reverse transformation keeps the Stone-Wales defect stable under ambient conditions [116, 124]. The formation energy of the Stone-Wales defect has been calculated to be about 5 eV [123]. Although the Stone-Wales defect leaves all carbon atoms fully coordinated, with no dangling bonds, the disruption to the π electrons results in an increase in the chemical reactivity of the defect site [116].

Vacancies

The loss of a carbon atom from graphene leads to a local reconstruction around the vacancy site, leaving a pentagonal and a nonagonal structure, denoted V_1(5–9) and depicted in Fig. 3.3b. The reconstruction takes the form of a Jahn-Teller distortion [125]. One atom in the nonagonal structure is only two-fold coordinated, leaving that carbon atom with dangling bonds that substantially increase the site reactivity, opening up the possibility of functionalisation at this site. The dangling bonds result in the under-coordinated atom sitting slightly above the graphene plane. The formation energy of the single vacancy defect is high, calculated theoretically to be 7.4–7.7 eV [125, 126] and experimentally estimated at 7.0±0.5 eV [127], due to the presence of the dangling bond, though the migration energy is smaller, at 1.4–1.7 eV [125, 126].

If two vacancies occur in the same location on the graphene sheet, either through direct double vacancy formation or through the migration of two single vacancies, then a reconstruction of the carbon atoms occurs, which results in a fully connected sp^2 network with no dangling bonds. There are three known reconstructions, which are denoted V_2(5–8–5), V_2(555–777) and V_2(5555–6–7777) and are depicted in Figs 3.3c, 3.3d and 3.4a, respectively. The V_2(5–8–5) defect consists of an octagon with two pentagons either side of it, taking the place of four hexagons in pristine graphene. Calculations have estimated the formation energy of V_2(5–8–5) to be 7.5–8.0 eV [128].

The transformation of a V_2(5–8–5) into a V_2(555–777) has been found by theoretical calculations to be energetically favourable, as the formation energy of V_2(555–777) is about 0.9 eV lower than that of V_2(5–8–5) [129]. The energy barrier for this transformation has been calculated to be about 5 eV, a substantially smaller barrier than that required for the Stone-Wales bond rotation [129].

The V_2(555–777) structure can be formed from the V_2(5–8–5) defect through a bond rotation, and consists of three heptagons, which all share a carbon atom, and three pentagons, each one adjacent to two of the heptagons. A further bond rotation leads to the formation of the V_2(5555–6–7777) defect, consisting of a central hexagon that is surrounded by four heptagons and two pentagons. A pentagon is also located adjacent to each of two pairs of heptagons. The V_2(5555–6–7777) formation energy is about 0.3 eV smaller than that of V_2(5–8–5), and so is intermediate between the formation energies of V_2(5–8–5) and V_2(555–777) [128].

The migration energy of these double defects is about 6–7 eV [116, 125], making them essentially immobile under ambient conditions.

Carbon Adatoms

The addition of a single carbon adatom can take several known forms, such as the "*bridge*" and "*dumbbell*" configurations [130]. These are depicted in Figs 3.4b and 3.4c, respectively. In no known form does the additional carbon atom sit within the graphene layer, as this would require a very high energy to achieve [116].

In the "bridge" configuration, which is lower in energy by about 0.22–0.5 eV than the metastable "dumbbell" configuration [130, 131], the carbon adatom sits above the graphene layer, equidistant between two neighbouring carbon atoms and bonded to both. These two atoms in the graphene layer are pulled slightly out of the graphene plane by the adatom [132]. The binding energy E_b of the carbon adatom in the "bridge" configuration to the graphene sheet has been calculated to be 1.4–1.8 eV [132, 133], corresponding to a formation energy of about 6–7 eV [116] [1] The migration energy of the carbon adatom in the "bridge" configuration is low, at 0.4–0.5 eV [131, 133, 134].

The "dumbbell" configuration consists of two carbon atoms – the adatom and one of the atoms of the graphene layer – 'sharing' a site on the graphene later, one below the graphene plane and the other above. The two site-sharing carbon atoms each bond to the three nearest neighbours in the graphene sheet [116, 131].

[1] The formation energy E_f can be calculated as $E_f = E_b + \mu_C$, where μ_C, the chemical potential for a carbon atom, is the atomisation energy per atom of pristine graphene.

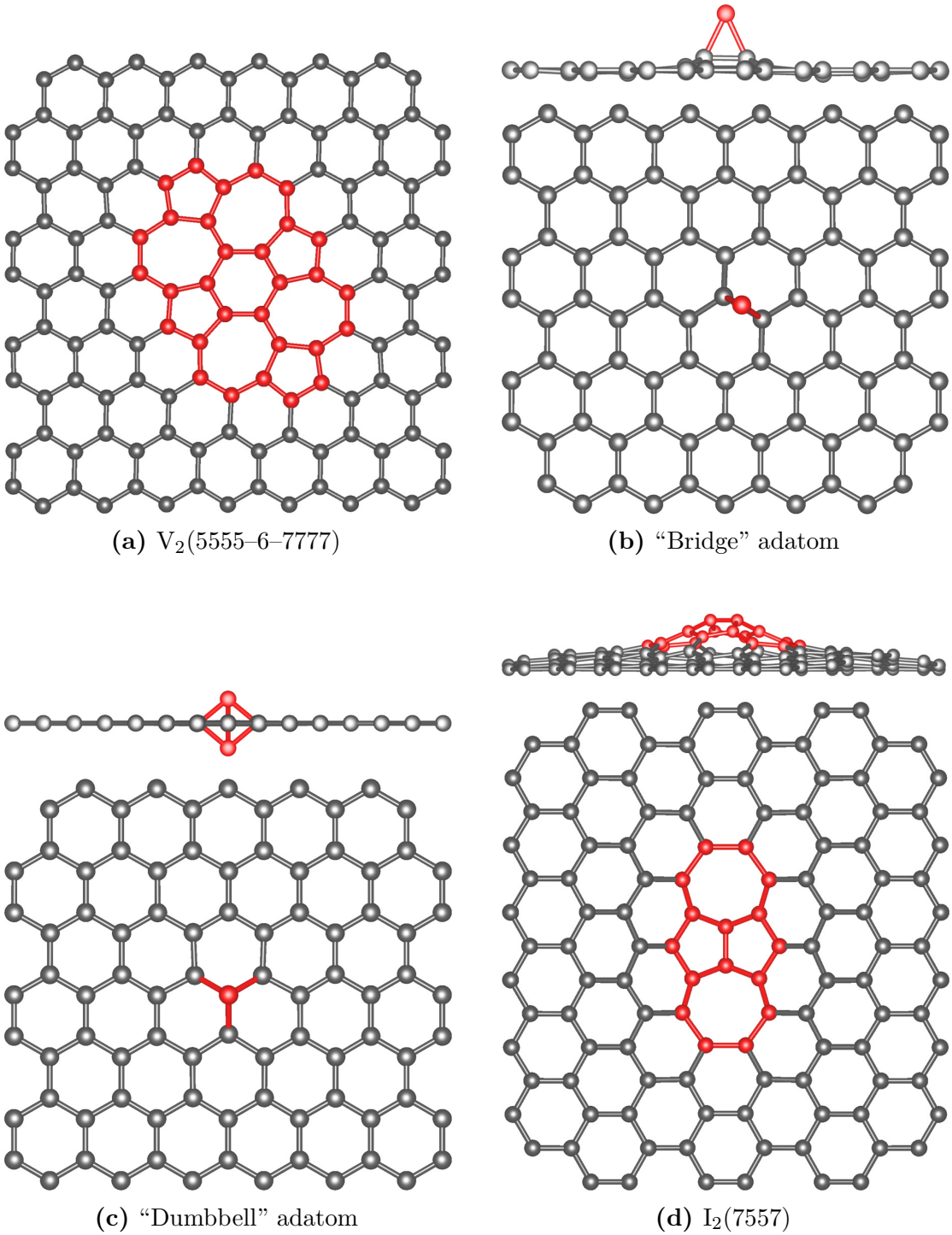

(a) V_2(5555–6–7777) **(b)** "Bridge" adatom

(c) "Dumbbell" adatom **(d)** I_2(7557)

Fig. 3.4 (a) Double vacancy reconstruction V_2(5555–6–7777); (b) carbon adatom in the "bridge" configuration; (c) carbon adatom in the "dumbbell" configuration; (d) double carbon adatom reconstruction I_2(7557), known as the inverse Stone-Wales defect. The out-of-plane effects of each defect are displayed above the in-plane structures of each defect. The inverse Stone-Wales defect leads to a 'bulging' out of the plane, while the V_2(5555–6–7777) defect does not protrude from the plane.

Two carbon adatoms may migrate across the surface of the graphene layer and combine to form a single defect, or *adatom dimer*, of which there are several known structures [130]. One such structure, which is formed of a pair of pentagons and a pair of heptagons, is known as the *inverse Stone-Wales* defect, denoted $I_2(7557)$ and depicted in Fig. 3.4d. This structure is considered to be an important building block in the synthesis of nano-engineered graphene [135]. In contrast to the Stone-Wales defect, the pentagons are in direct contact and the heptagons are separated. The inverse Stone-Wales defect allows an sp^2 bonded network to be restored, though at the cost of introducing a 'buckling' of the graphene layer out of the plane. The formation energy of an inverse Stone-Wales defect, which is calculated to be 6.2 eV [134, 135], is substantially less than twice the formation energy of an isolated adatom defect, and so it is energetically favourable for two single adatoms to combine into a single defect structure. The inverse Stone-Wales defect is not mobile at ambient temperature [116, 130].

Other adatom dimer structures exist, such as the defect blister $I_2(555\text{–}6\text{–}777)$ [134], which consists of three pentagons and three heptagons alternately surrounding a central hexagon ring and which is related to the inverse Stone-Wales defect through a bond rotation, as well as further such structures related to the $I_2(7557)$ and $I_2(555\text{–}6\text{–}777)$ defects through additional bond rotations [130, 136, 137]. The formation energy of the $I_2(555\text{–}6\text{–}777)$ defect has been calculated to be 6.07 eV [134], comparable to the inverse Stone-Wales defect. An $I_2(7\text{–}4\text{–}7)$ defect featuring two heptagons and two hexagons surrounding a square of carbon atoms raised above the graphene plane has also been investigated and found to have a formation energy 1.09 eV higher than $I_2(7557)$. As with the inverse Stone-Wales defect, these defect structures all involve a reconstruction of the graphene sheet to avoid dangling bonds, at the cost of introducing a buckling of the graphene sheet.

An extension to the single adatom "bridge" defect has also been studied, which features a second carbon adatom bonded to the "bridge" atoms, leading to a two-atom protrusion from the graphene plane, with a formation energy 1.03 eV higher than that of the inverse Stone-Wales defect [130]. The $I_2(555\text{–}6\text{–}777)$, $I_2(7\text{–}4\text{–}7)$ and two-atom protrusion adatom dimer structures are displayed in Figs 3.5a, 3.5b and 3.5c, respectively.

Non-carbon Adatoms

Non-carbon, or *foreign*, adatoms may bond to a layer of pristine graphene. Foreign adatoms sit above the plane of the graphene layer in high-symmetry sites such as above

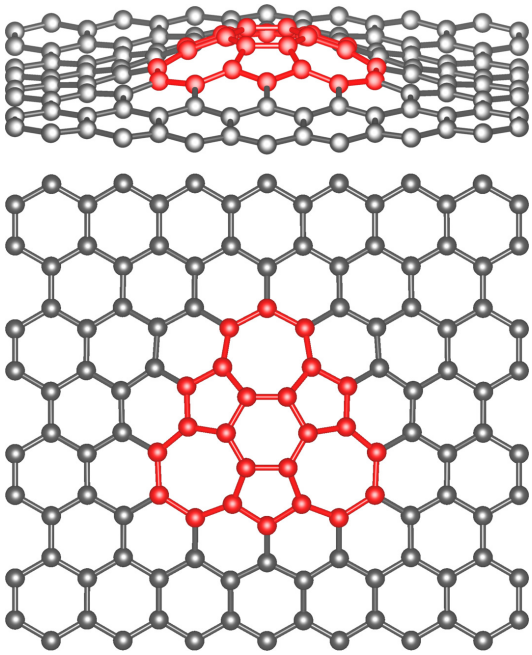

(a) I_2(555–6–777)

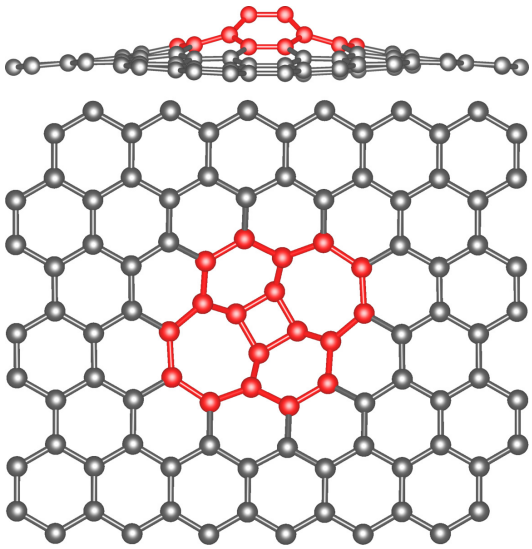

(b) I_2(7–4–7)

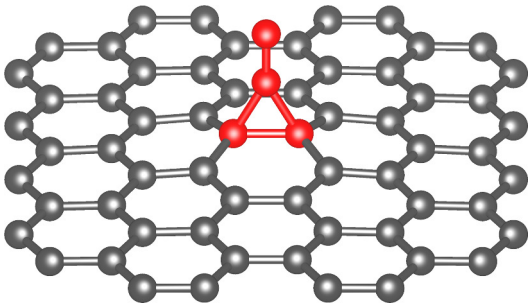

(c) Two-atom protrusion

Fig. 3.5 (a) double carbon adatom reconstruction I_2(555–6–777); (b) double carbon adatom reconstruction I_2(7–4–7); (c) double carbon adatom in the two-atom protrusion configuration. Out-of-plane effects of each defect are displayed above the in-plane structures of relevant defects.

the centre of a hexagon, above a carbon atom, or in the "bridge" position occupied by carbon adatoms [138]. Many foreign adatoms will only undergo physisorption with the graphene layer with van der Waals bonding, but some species such as Au, W and Pt may form stronger covalent bonds and undergo chemisorption, with binding energies typically less than 1 eV [116, 117, 139, 140]. The relatively weak bonding strength of foreign adatoms allows the adatoms to migrate across the graphene surface under ambient conditions [139].

Other defects of graphene may result in a substantial increase in local reactivity, enabling a stronger bonding between a foreign adatom and a graphene layer [140, 141]. The Stone-Wales and inverse Stone-Wales defects result in a significant increase in local reactivity [116], while the dangling bonds of the under-coordinated carbon atom in the V_1(5–9) defect substantially increases the site reactivity. One study found that the reconstructed V_2(777–555) defect has a binding energy of about 2 eV with a range of metal adatoms. This was ascribed to a distortion to the π bands due to the defect [117].

Substitutional Defects

Foreign atoms may also enter into the graphene structure itself through substitutional defects, in which one or more carbon atoms is replaced by a foreign atom – essentially the combination of a vacancy defect and a foreign adatom.

Boron and nitrogen are commonly found as substitutional atoms, as they are of a very similar size to carbon, while possessing respectively one fewer and one more electron [116]. Larger atoms such as transition metals may also be substituted in for carbon atoms, and are capable of replacing one or two carbon atoms, with strong binding energies for W atoms of –8.6 eV and –8.9 eV for unreconstructed single and double vacancies, respectively [117]. The, in general, longer bond lengths between carbon and foreign substitutional atoms compared with the C–C bond length means that the substitutional atom usually sits slightly above the graphene layer [141].

The presence of substitutional impurities such as B and N alters the local electronic structure of the graphene sheet [121, 142], and increases the chemical reactivity of the defect site [121, 143]. Transition metal impurities are able to inject additional charge into graphene sheets [144]. As such substitutional defects may offer pathways for the functionalisation of graphene for electronics applications [121].

Summary of Defect Energies

The formation energies E_f for some types of graphene defects, which have been calculated by previous studies and that have been referred to in this section, are summarised in Table 3.1.

Defect type	**Specification**	$\mathbf{E_f}$**/eV**
Stone-Wales	SW(55–77)	5
Single vacancy	V_1(5–9)	7.4–7.7
Double vacancy	V_2(5–8–5)	7.5–8.0
	V_2(555–777)	6.6–7.1
	V_2(5555–6–7777)	7.2–7.7
C adatom	"Bridge"	6–7
	"Dumbbell"	6.2–7.5
Double C adatom	I_2(7557)	6.2

Table 3.1 Graphene defect formation energies E_f from previous theoretical studies.

In this thesis, an *ab initio* random structure searching method was applied to find point defect structures in graphene, involving reconstructions, vacancies and carbon adatoms, as well as nitrogen, oxygen and hydrogen adatoms. The discovery of known defect structures is intended to demonstrate the validity of the approach. The formation energies of several potentially viable new defect structures are calculated.

3.2 Methodology

Novel and known graphene point defects were searched for using a set of scripts developed by the author of this thesis, which implemented the *ab initio* random structure searching method for graphene. 4×4×1 and 5×5×1 supercells of pristine graphene were generated, and the atoms lying within a central section of each supercell were removed, and then replaced in randomly-generated positions within the central area. Depending on the nature of the defect type under investigation, carbon atoms could be removed, and carbon or foreign adatoms added, during the randomisation process.

The resulting randomly-generated structure was then relaxed until the forces on the atoms were close to zero, and the procedure repeated until multiple repeats of defect structures were obtained. Relatively low-energy structures, which could correspond to defects with relatively low formation energies, were then set within larger graphene supercells (between 7×7×1 and 9×9×1), in order to increase the separation between a defect and its periodic repeats, as is illustrated in Fig. 3.6. This reduces the effect of spurious defect-defect interactions, so that in the limit of increasing supercell size the true single defect formation energy is obtained from the calculations. The size of the supercell was increased until the formation energy was converged to within 0.1 eV.

The separation between the graphene layer and its periodic repeats was kept fixed at 8 Å during the initial searches and at 10 Å in the refined calculations using the larger supercells.

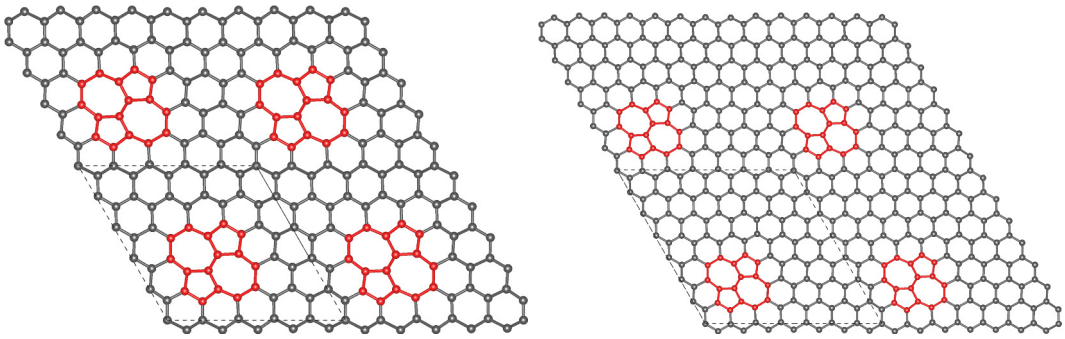

(a) 5×5 supercell **(b)** 7×7 supercell

Fig. 3.6 Illustration of supercell size convergence with graphene defects. A Stone-Wales defect SW(55–77) is shown, highlighted in red, set within an (a) 5×5 and (b) 7×7 graphene supercell, with the unit cell in each case denoted by the black dashed lines. Increasing the supercell size also increases the separation between the periodic repeats of the defect, thus reducing undesirable defect-defect interactions.

Electronic structure calculations were carried out using the CASTEP code [57]. The PBE functional [24] was used to approximate the effects of exchange and correlation. For the final converged (large-supercell) results, a plane-wave cut-off energy of 600 eV was used for calculations involving only carbon atoms, while a higher cut-off energy of 850 eV was used for calculations involving hydrogen and oxygen. In calculations of the formation energy E_f defined in equation (3.1), the chemical potentials μ were calculated using the same cut-off energy as the defect structure. A $3\times3\times1$ Monkhorst-Pack grid was used to sample the Brillouin zones of the defect structures, equivalent to a k-point spacing of $2\pi\times0.025$ Å^{-1} for k-vectors within the graphene layer. These

parameters were tested to ensure total energy convergence of 1 meV/atom and convergence of calculated forces to within 1 meV/Å. Lower cut-off energies and a less dense k-point grid were used for the initial searches.

Ultrasoft pseudopotentials generated on-the-fly by the CASTEP code were used to describe the nuclei and core electrons of the atoms. The default pseudopotentials for CASTEP version 8 were used, which treated explicitly the $2s^2$ and the $2p$ electrons for C, O and N. The H pseudopotential is simply a Coulomb potential that is softened within the core radius.

The chemical potential of carbon was set to be the energy per atom of carbon in pristine graphene. The chemical potentials of H, O and N were taken to be the energies per atom of their respective diatomic molecules, calculated using a $10\times11\times12$ Å periodic unit cell containing one diatomic H_2, O_2 or N_2 molecule, with spin-polarised calculations and sampling of the Brillouin zone at the gamma point only.

3.3 Results

Searches over double carbon vacancies, single carbon vacancies, graphene sheet reconstructions, single carbon adatoms and double carbon adatoms produced all known defects for these types, with the exception of a very large I_2(755–6776–557) defect [137], which is related to the I_2(777–6–555) defect through a bond rotation. This defect was too large to be found with the randomised section of the graphene sheet used.

Specifically, the Stone-Wales, single vacancy, V_2(5–8–5), V_2(555–777), V_2(5555–6–7777) double vacancy, "bridge" and "dumbbell" single carbon adatom and I_2(7557) (inverse Stone-Wales), I_2(777–6–555), I_2(7–4–7) and "two-atom protrusion" double carbon adatom vacancies were all found in searches, validating the approach taken. The calculated formation energies E_f and supercell sizes used for the converged calculations are given for each of these defects in Table 3.2. They largely compare very well to the previously-calculated formation energies of Table 3.1.

Searches involving N, O and H substitutions and adatoms also confirmed:

1. that N and O can substitute in for a C atom to form a low-energy defect structure;

2. that an OH group can stably bond in the "atom" position directly above a carbon atom in the graphene layer; and

3. that O atoms can exist in the "bridge" position as an adatom.

Defect type	Specification	E_f/eV	Supercell size
Double C vacancy	V_2(5–8–5)	7.51	9×9
Double C vacancy	V_2(555–777)	6.63	8×8
Double C vacancy	V_2(5555–6–7777)	7.03	9×9
Single C vacancy	V_1(5–9)	7.84	8×8
Reconstruction	SW(55–77)	4.81	8×8
Single C adatom	"Bridge"	6.49	8×8
Single C adatom	"Dumbbell"	6.89	8×8
Double C adatom	I_2(7557)	6.27	8×8
Double C adatom	I_2(777–6–555)	6.61	8×8
Double C adatom	I_2(7–4–7)	7.12	8×8
Double C adatom	"Two-atom protrusion"	6.99	8×8

Table 3.2 Formation energies of known defects from structure searching calculations, along with the supercell size used for the converged calculation of the formation energy.

In addition to finding a wide range of known defect structures, the structure searching calculations also revealed two new defects that it may be possible to engineer in graphene: a double carbon vacancy structure, V_2(77784555), and a double O adatom defect, which features an O atom substitution for a C atom. This results in a broken bond with a neighbouring C atom, as the O atom is only two-fold coordinated. This neighbouring C atom then bonds with a C–O projection out of the plane of the graphene layer. The two defects are depicted in Fig. 3.7.

The formation energy for the V_2(77784555) is calculated to be relatively high, at 10.50 eV, so its formation is less probable than other V_2 double vacancy defects. The formation energy for the double O adatom defect is just 0.16 eV, suggesting that such an arrangement may be a metastable configuration resulting from the reaction of an O_2 molecule and a graphene sheet. The defect formation energies for these two structures are summarised in Table 3.3.

3.4 Summary and Conclusions

A random structure searching scheme has been used to look at several types of defects in graphene layers on a theoretical basis. This method predicted all the defect types that the searching parameters could have found, and then predicted the formation en-

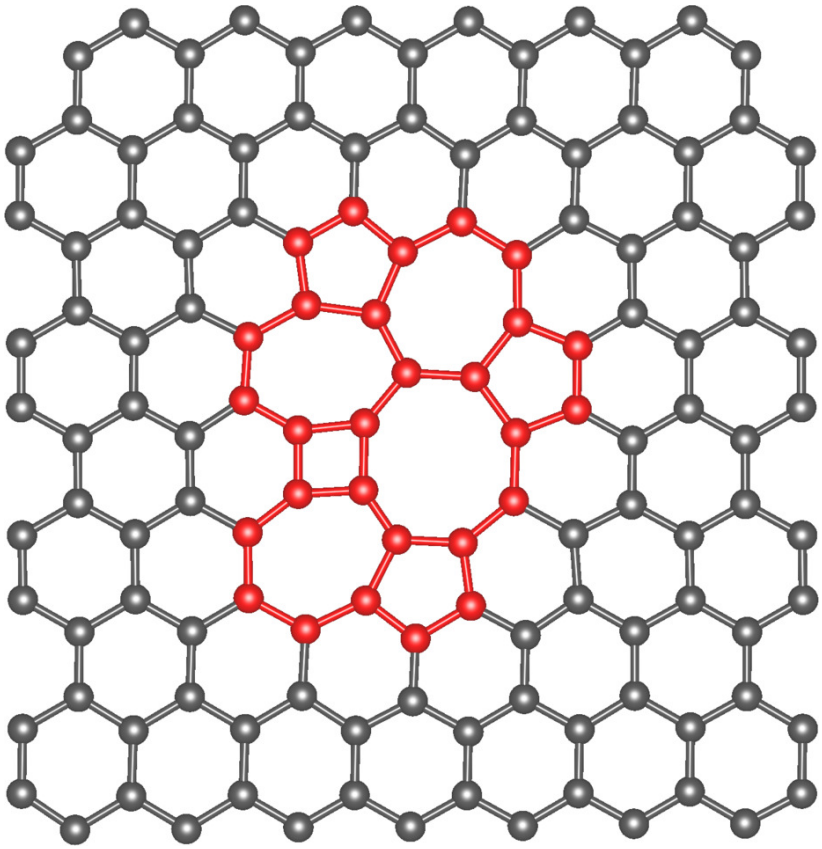

(a) $V_2(77784555)$

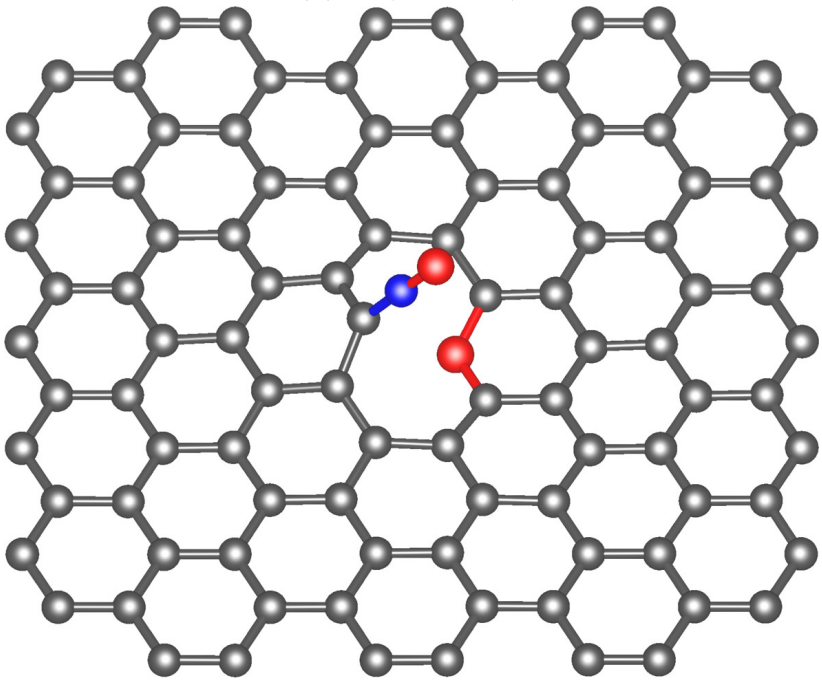

(b) Double O adatom defect

Fig. 3.7 Illustration of novel graphene defect structures. (a) $V_2(77784555)$ double vacancy defect, with the defect atoms highlighted in red. (b) double O adatom defect, with an O atom substituting for a carbon atom and a C–O projection. In (b), the O atoms are highlighted in red, and the C atom in the C–O projection is highlighted in blue.

Defect type	Specification	E_f/eV	Supercell size
Double vacancy	$V_2(77784555)$	10.50	9×9
Double O adatom	Substitution and projection	0.16	7×7

Table 3.3 Formation energies of novel defects from structure searching calculations, along with the supercell size used for the converged calculation of the formation energy.

ergies of these known defects in good agreement with previous studies, thus validating the approach taken.

The structure searching method also predicted two graphene defect structures that have not previously been described: a $V_2(77784555)$ double vacancy structure and a double O adatom structure featuring an O atom substitution and a C–O projection from the graphene layer. The formation energies of these structures have been calculated. As these structures have positive formation energies, they can be at most metastable. Whether these structures are likely to be found in nature depends on the size of the energy barrier for transformations to a lower-energy structure. This energy barrier could be calculated computationally using a transition state search.

Chapter 4

Xenon Oxides Under Pressure

In this chapter we explore the chemistry of the noble gas xenon under high pressures, of the order found in the Earth's mantle. The xenon-oxygen binary system is examined using *ab initio* random structure searching, and stable structures are characterised. Density functional theory methods are used for both the searches and the characterisation. The work is conducted in collaboration with experimentalists, and the results from the structure searching and theoretical characterisation are compared with the experimental results.

4.1 Introduction

The noble gases were for a long time considered to be chemically inert, so that they would not under any circumstances form chemical bonds with other species, due to their full outer (valence) electron shells. However, the binding strength of these valence electrons to the ionic core decreases with increasing atomic number as the outermost electrons exist further away from the nucleus, opening up the possibility of oxidation and chemical bonding for the heavier elements. The heaviest known noble gas, radon, is unstable to radioactive decay for all known isotopes, but the next-heaviest element, xenon, has stable isotopes. In 1962, Neil Bartlett synthesised the first compound of xenon, which he identified as $Xe^{+}[PtF_6]^{-}$ [145].

Since this discovery, more compounds of xenon have been synthesised, many of them oxides, featuring xenon in oxidation states of +2, +4, +6 and +8 [146], consistent with each xenon atom bonding to an integer number of oxygen atoms, or an even number of fluorine atoms. These compounds include molecular crystal XeF_2 [147, 148], XeO_3 [149] and XeO_4 [150]. A new xenon oxide, XeO_2, has recently been synthesised, in which Xe-O bonds form an extended disordered network of XeO_4 squares, with

the squares connected through shared oxygen atoms at the corners [151]. Xenon has also recently been incorporated into a double perovskite structure [152], again under ambient conditions.

Under ambient conditions, all known xenon oxides are thermodynamically unstable to decomposition and are synthesised indirectly using xenon fluorides as reactants. At moderate pressures, xenon has been shown to form weakly-bonded compounds, such as with H_2O at about 1 GPa [153], and with O_2 at about 3 GPa [154, 155]. However, the properties of xenon change significantly as the pressure is further increased.

Xenon itself undergoes a sluggish martensitic transformation between 3 and 80 GPa from a face-centred cubic (fcc) to a hexagonal close packed (hcp) structure [156–158]. The hcp structure becomes metallic around 135 GPa [159], although this pressure is reduced substantially by the presence of a small amount of oxygen impurities [154], to just 49 GPa for a Xe-0.6 mol.% O_2 mixture.

Recently, theoretical proposals and experimental evidence have appeared for the formation of strongly bonded and stable xenon compounds under pressure. A recent theoretical study has proposed Xe-Ni and Xe-Fe structures, and found them to be stable against decomposition under conditions found in the Earth's inner core [78]. Xenon has been incorporated in quartz at pressures of a few GPa and high temperatures [160]; it is proposed that xenon atoms replace silicon atoms in this structure. The experimental synthesis of a compound of xenon, oxygen and hydrogen was reported recently at around 50 GPa [161].

The formation of xenon oxides in the Mbar range has been predicted using an evolutionary structure searching algorithm [76] and DFT methods [162–164]. In Refs. 162 and 163, only the simple stoichiometries XeO, XeO_2, XeO_3 and XeO_4 suggested by low-pressure experimental observations were considered. Hermann and Schwerdtfeger found a Xe_3O_2 structure in theoretical searches and predicted it to be stable above 75 GPa [164], as well as a Xe_2O structure stable at higher pressures and a Xe_7O_2 structure that they predicted to be metastable. However, experimental data for xenon oxides have not been reported at the high pressures at which they might become stable.

Studies of xenon chemistry [78, 151, 160–164] have been performed in part to help in explaining the anomalously low xenon content of the Earth's atmosphere [165–167] in comparison with chondrites (stony meteorites). Various resolutions to this so-called "missing xenon paradox" have been put forward, including loss of atmospheric xenon into outer space, and a range of proposals for xenon storage within the Earth. One proposal for resolving the "paradox" is storage in the deep Earth – the mantle or core – thus motivating a better understanding of the chemistry of xenon under geological

pressures of up to 350 GPa, the pressure at the centre of the Earth.

Oxygen is both highly reactive and the most abundant element in the Earth's mantle. As such, it is a natural focus for investigation as a reagent for xenon at high pressures of tens to hundreds of gigapascals. To further the understanding of the high pressure xenon-oxygen binary system, we have conducted a theoretical search for stable compounds of xenon and oxygen in the pressure range 83–200 GPa. This involved a structure search using AIRSS over a wide range of stoichiometries, with subsequent theoretical characterisation of the stable structures, both within a DFT framework. The searches were conducted by the author of this thesis and by Chris Pickard, and the theoretical characterisation by the author.

The theoretical searches were conducted in collaboration with experimentalists, principally Agnès Dewaele, with contributions from Sakura Pascarelli, Olivier Mathon, Mohamed Mazouar and Tetsuo Irifune. This experimental work involved synthesis of xenon oxides using laser-heated diamond anvil cells (DACs) loaded with a mixture of xenon and oxygen in a range of stoichiometries, and subsequent experimental characterisation. The theoretical and experimental components of this research were conducted in close collaboration, with the results of each feeding into the other. Consequently the experimental methods and results will be described in this chapter; however, no experimental work was conducted by the author. Descriptions of the experimental methods and results are edited versions of summaries written by Agnès Dewaele.

4.2 Methodology

4.2.1 Structure Searches and Theoretical Characterisation

The AIRSS methodology [64], implemented using a set of programs and scripts authored by Chris Pickard, was used to conduct the structure searches for xenon oxides. Earlier studies [163, 164] had used a restricted range of stoichiometries: Ref. 163 considered only stoichiometries corresponding to simple oxidation states (even positive integers) for Xe, while Ref. 164 focussed on xenon suboxides (compounds containing more xenon atoms than oxygen by number). In this study, a wide range of stoichiometries were considered. In addition to Xe and O, 17 stoichiometries were investigated: Xe_7O_2, Xe_3O, Xe_5O_2, Xe_2O, Xe_3O_2, Xe_4O_3, XeO, Xe_4O_5, Xe_3O_4, Xe_2O_3, XeO_2, Xe_2O_5, XeO_3, XeO_4, Xe_2O_9, XeO_5 and XeO_{11}. Up to 28 atoms per unit cell were considered;

beyond this number the Born-Oppenheimer (BO) surface becomes unfeasible to survey.

Searches were restricted to those parts of the BO surface likely to contain low-enthalpy structures by the imposition of several constraints. The volumes of the randomly-generated unit cells were restricted to being within 25% of a target volume, which was determined by the pure-species atomic volumes of the contents of the unit cells at the target pressure. The random atomic positions were subject to a minimum separation constraint, which was specified separately for each pair of atomic species. The minimum separation was higher for Xe-Xe and O-O atomic pairs than for Xe-O pairs, in order to encourage inter-species bonding. Various symmetry constraints were imposed on the structures, by generating structures belonging to a range of space groups possessing between 4 and 48 symmetry operations. In addition to these 'stand-alone' searches, additional searches with the constraint of the unit cell volume suggested by experimental measurements were also conducted. The stoichiometries used for these experimentally-constrained searches were those consistent with this experimental volume, based on the volumes of low-enthalpy structures from the stand-alone searches.

In addition to AIRSS, a data mining technique was used to generate low-enthalpy stoichiometries for comparison with the results from AIRSS. Sets of known structures for a range of species, which were consistent with the stoichiometries searched for using AIRSS, were downloaded from the Inorganic Crystal Structure Database (ICSD) [1]; the atomic species were then exchanged as appropriate for Xe and O, the unit cell volume rescaled and the resulting structure relaxed to the minimum of enthalpy in the same manner as structures generated using AIRSS.

Electronic structure calculations, including geometry optimisations, phonon and Raman spectroscopy calculations and band structure calculations, were carried out using the plane-wave DFT code CASTEP [57], with ultrasoft pseudopotentials [50] being used for most calculations; norm-conserving pseudopotentials were used for calculations involving Raman intensities or hybrid functionals, as these calculations are not currently implemented for ultrasoft pseudopotentials in CASTEP. The PBE-GGA *xc* functional [24] was used for all calculations except for one band gap calculation, for which the HSE06 functional [33] was used. The pseudopotential for the O ion was the default CASTEP pseudopotential generated 'on-the-fly', with $2s^2$ and $2p^4$ electrons treated as valence. The pseudopotential for Xe was also generated on-the-fly

[1] URL: https://icsd.fiz-karlsruhe.de/search/index.xhtml. Access provided through the National Chemical Database Service (CDS) run by the Royal Society of Chemistry, URL: http://cds.rsc.org/

by CASTEP, but differed from the default CASTEP pseudopotential by the explicit treatment of the Xe $4d$ electrons; more details are in the next subsection.

A plane-wave energy cutoff of 400 eV was used for the initial structure searches, with a higher cutoff energy of 700 eV being used for the final converged results. Monkhorst-Pack grids [45] were used to sample the BZ, with a maximum spacing between k points of $2\pi\times0.07\,\text{Å}^{-1}$ for the initial searches and $2\pi\times0.03\,\text{Å}^{-1}$ for the final converged results.

4.2.2 Pseudopotential Description of Xenon

Previous theoretical studies of high-pressure xenon chemistry have generally used a pseudopotential description of xenon in which only the $5s^2$ and $5p^6$ electrons are treated explicitly within DFT, with xenon's $4d^{10}$ electrons being described as core electrons by the pseudopotential [163, 164]. This has been verified to be a good description at low pressures [168]. To investigate whether the implicit treatment of the Xe $4d$ electrons is an adequate description of xenon at high pressures, we tested the default CASTEP ultrasoft pseudopotential for xenon (henceforth referred to as the $5s5p$ pseudopotential) against an ultrasoft pseudopotential that does pseudise and explicitly calculate the $4d^{10}$ electrons (henceforth referred to as the $4d5s5p$ pseudopotential), which had been developed by Chris Pickard as part of a separate study of xenon's high-pressure chemistry with Fe and Ni [78]. To further test the accuracy of the Xe pseudopotential, a pseudopotential that provided for the explicit treatment of the Xe $4s^2$ and $4p^6$ electrons was also used (referred to as the $4s4p4d5s5p$ pseudopotential). The pseudopotential was generated by Chris Pickard and tested by the author.

The pseudopotentials were tested against each other in two ways. The first comparison was for the equation of state for Xe in the hcp structure. The hcp Xe structure was relaxed at a large number of external pressures in the range 20–265 GPa with each pseudopotential. The pressure-volume curves for each pseudopotential are shown in Fig. 4.1.

At lower pressures, up to about 40GPa, the difference in the calculated unit cell volume between the pseudopotentials is negligible. At higher pressures, however, the calculated volume with the $5s5p$ pseudopotential diverges from those with the $4d5s5p$ and $4s4p4d5s5p$ pseudopotentials. By 270 GPa the divergence is substantial, the atomic volume being approximately 4% smaller with the $4d5s5p$ and $4s4p4d5s5p$ pseudopotentials compared with the $5s5p$ pseudopotential. However, the $4d5s5p$ and $4s4p4d5s5p$ pseudopotentials produce almost indistinguishable results throughout this pressure range. It is possible they may begin to diverge at higher pressures yet, but such pressures are beyond the scope of this study.

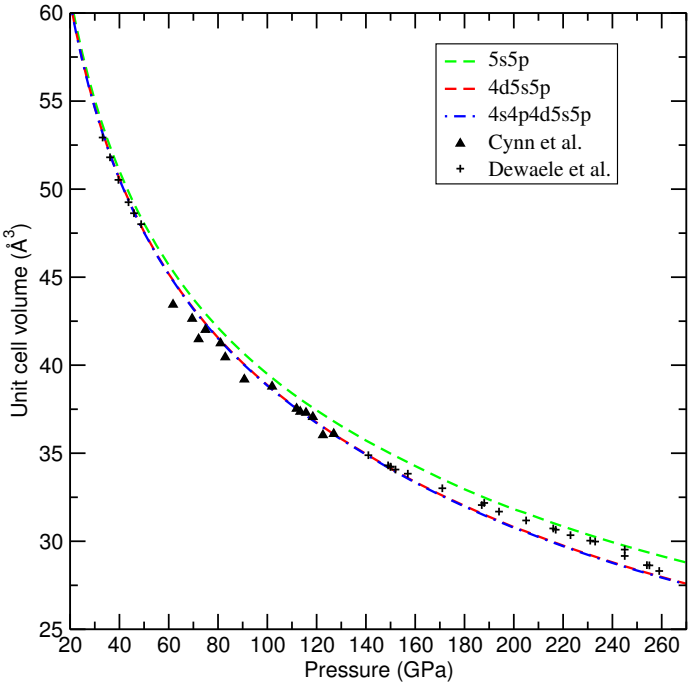

Fig. 4.1 Pressure-volume curve for hcp Xe using three different pseudopotentials and data from two experimental studies. The pseudopotentials treat explicitly the $5s5p$ electrons (green curve); the $4d5s5p$ electrons (red curve); and the $4s4p4d5s5p$ electrons (blue curve). The $4d5s5p$ pseudopotential was used in the main calculations. Experimental data points are included for reference [154, 157]. The equation of state (EoS) obtained with the $4d5s5p$ and $4s4p4d5s5p$ pseudopotentials are almost identical, but the EoS for the $5s5p$ pseudopotential is significantly different.

To further examine the importance of the choice of pseudopotential, the $5s5p$ and $4d5s5p$ pseudopotentials were also compared following structure searching by relaxing the lowest-enthalpy structures from a search at 83 GPa using each pseudopotential. The resulting enthalpies of formation per atom, $\Delta\mathrm{H}_f$, were then compared. For a compound with stoichiometry $\mathrm{Xe}_m\mathrm{O}_n$, $\Delta\mathrm{H}_f$ is defined as

$$\Delta H_f(\mathrm{Xe}_m\mathrm{O}_n) = [H(\mathrm{Xe}_m\mathrm{O}_n) - (mH(\mathrm{Xe}) + nH(\mathrm{O}))]/(m + n), \qquad (4.1)$$

where H denotes the enthalpy of each formula unit under the relevant pressure. Fig. 4.2 displays the results of this comparison for the most stable (according to the $4d5s5p$ pseudopotential) structure for each stoichiometry at 83 GPa.

As can be seen in the figure, there is a substantial – typically well over 100 meV/atom – difference in enthalpy of formation for all stoichiometries between these two pseudopotentials, with the $4d5s5p$ pseudopotential consistently predicting lower enthalpies of formation. The difference in enthalpy of formation between the two pseudopotentials

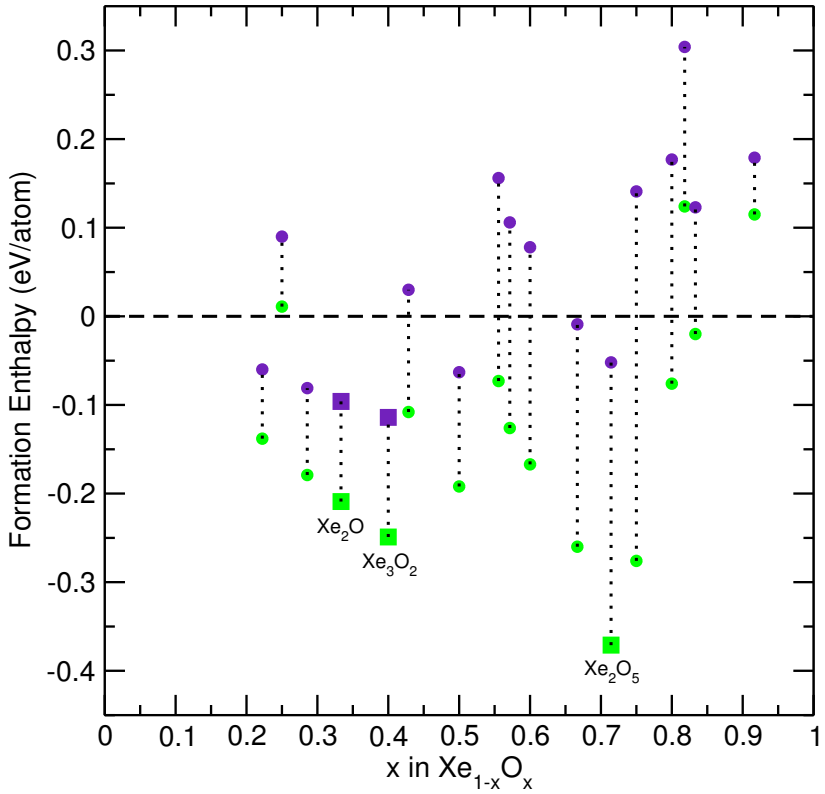

Fig. 4.2 Diagram showing calculated enthalpies of formation per atom from the elements for xenon oxides at 83 GPa, calculated both with and without explicit treatment of the *d*-electrons. The lowest-enthalpy structures for each stoichiometry, according to calculations with the 4*d* electrons calculated explicitly, are shown. Green points denote formation enthalpies calculated with an explicit treatment of the *d* electrons (4*d*5*s*5*p* pseudopotential), and purple points denote formation enthalpies without the explicit treatment of the *d* electrons (5*s*5*p* pseudopotential). Points marked with squares represent structures stable against decomposition into other structures; structures unstable to decomposition are marked with circles. $x = 0$ corresponds to pure xenon and $x = 1$ to pure oxygen.

also varies substantially over the different structures, from about 100 meV/atom to about 400 meV/atom. These differences alter both the relative and absolute stabilities of structures. For example, calculations in which the $4d$ electrons are explicitly calculated predict that lowest-enthalpy structure with Xe_2O_5 stoichiometry will be stable to decomposition at 83 GPa, with an enthalpy of formation of -0.37 eV per atom, but unstable to decomposition into other xenon oxide stoichiometries, with an enthalpy of formation of only -0.05 eV per atom, when the $4d$ orbitals are described by the pseudopotential. In contrast, minimal differences in enthalpy of formation between the $4d5s5p$ and $4s4p4d5s5p$ pseudopotentials were calculated.

Inspection of the orbital wavefunctions of the Xe atom, which are depicted in Fig. 4.3, suggests a reason for the increasing importance of the Xe $4d$ orbitals with pressure. There is a substantial overlap of the $4d$ orbitals with the outer $5s$ and $5p$ orbitals, suggesting that the 'semi-core' $4d$ orbitals will impact on the chemical bonding effected by the $5s$ and $5p$ valence electrons. As atoms are forced closer together under increasing pressure, the overlap with the bonding region of the $5s$ and $5p$ electrons becomes greater and so the effect of the $4d$ orbitals on the bonding becomes more significant.

Comparison of the results of the three pseudopotentials tested, the $5s5p$, $4d5s5p$ and $4s4p4d5s5p$ pseudopotentials, indicates that the Xe $4d^{10}$ electrons must be explicitly treated within DFT for accurate calculations at high pressures. However, there is no cost to accuracy of incorporating the $4s$ and $4p$ orbitals into the pseudopotential. Allowing the $4d$ orbitals to relax within their chemical environment, rather than enforcing the 'frozen core' approximation, permits the xenon atoms so described to reconfigure their electronic structure to achieve a tighter packing of atoms. Under high pressures, this results in a reduction in enthalpy, and so greater stability at high pressures.

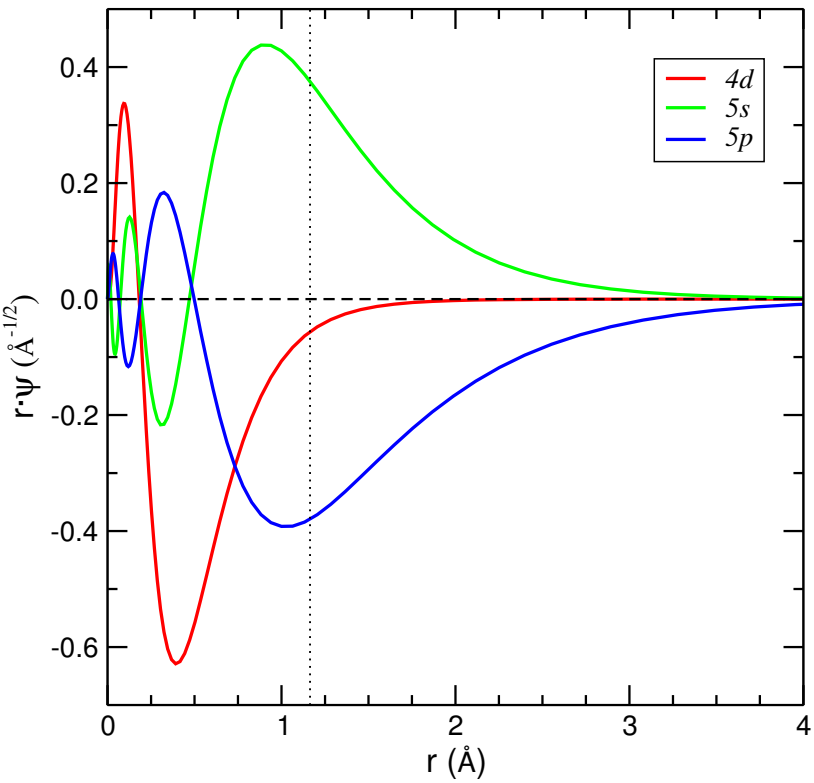

Fig. 4.3 Hartree-Fock orbitals for an isolated Xe atom. The cut-off radius of the pseudopotential used is shown with the dotted vertical line. There is a significant extension of the 4*d* orbital beyond the cut-off radius of the pseudopotential. The Hartree Fock data were generated by John Trail.

4.2.3 Experimental Methodology

Membrane DACs were loaded at room temperature with xenon-oxygen mixtures (with a composition determined using O_2 [169] and Xe [170] equations of state) in a high-pressure vessel. The mixtures were homogenised in the vessel over ∼12 hours before loading. After loading, the pressure was increased to ∼10 GPa and the sample was characterised with Raman spectroscopy. The crystallisation of Xe-O_2 mixtures under pressure leads to three different solid phases (Xe with O_2 impurities, a $Xe(O_2)_2$ Laves phase [155] and pure O_2). The diamond anvil cell was heated at 420 K for several hours to reduce compositional heterogeneities in the sample chamber. The pressure was then increased to the required value, and the sample was laser-heated for a few minutes at the centre of the sample chamber, on one or both sides. The temperature was estimated to be above 2000 K. The sample was characterised before and after heating with powder X-ray diffraction (PXRD), X-ray absorption spectroscopy (XAS) and/or Raman spectroscopy. The reacted zone was detected by mapping PXRD or XAS spectra. In one run, the rhenium gasket was isolated from the sample chamber by a gold ring in order to verify that rhenium did not participate in the chemical reactions.

PXRD experiments were performed on the ID27 beamline of the European synchrotron Radiation Facility, ESRF (λ=0.3738 Å). PXRD spectra were treated using the Fit2d software [171]. XAS experiments were performed on the BM23 beamline of the ESRF [172], at the K-edge of xenon (34.561 keV), calibrated using gaseous xenon. Nano-polycrystalline diamond anvils [173], which do not create any XAS parasitic signal due to Bragg diffraction, were used. A high quality spectrum was recorded in a wide range in the reciprocal space ($k_{\max} = 18\text{Å}^{-1}$), which enabled a detailed quantitative analysis of the near-neighbour shells of Xe in the direct space. The XAS spectra were analysed with the Athena and Artemis softwares [174] to determine the local structure around xenon atoms. PXRD was also performed on BM23. On ID27 and BM23, the pressure was measured using the PXRD signal from unreacted xenon or a gold pressure marker placed at the edge of the sample chamber, and their ambient temperature equations of state [154, 175] were checked with the rhenium gasket PXRD signal and equation of state [176]. The pressure was obtained from the high-frequency Raman edge of the diamond anvil [177] in the Raman spectrum measurements.

4.3 Results

4.3.1 Structure Searching at 83 GPa

Ab initio random structure searching was carried out on the Xe-O system at a pressure of 83 GPa as described in the Methodology section. Structures were also generated by data mining using the ICSD. The most promising structures were re-relaxed using the more accurate DFT parameters.

The results of the structure searching are displayed in Fig. 4.4. Here, the enthalpies of formation per atom from the elements (defined in equation (4.1)) for xenon oxide structures are plotted against the stoichiometric ratio of the structure. A convex hull is formed; structures lying on the hull are stable against decomposition into other structures lying on the hull. The xenon oxides that are predicted to form depend on the stoichiometric ratio of the xenon and oxygen reactants: if the reactant stoichiometry corresponds to a stable structure, then this will be the only reaction product predicted. If not, then the two structures on the convex hull with stoichiometric ratios either side of the reactants' stoichiometry on the hull will form.

Note that the pure elements, xenon and oxygen, are always present on the hull. Structure searching was also carried out on the pure elements. The results of this searching were in agreement with the accepted structures for Xe and O at this pressure: the hcp structure for xenon [156, 178] and the ϵ-O phase for oxygen [179, 180].

The results presented here are for static-lattice calculations: neither thermal nor zero-point effects are included. A previous study [163] and our own calculations on the structures predicted to be stable by the static lattice calculations (discussed later in this chapter) suggest that these effects are unlikely to alter the relative stability of the compounds significantly.

The convex hull at 83 GPa suggests that three structures are stable to decomposition in the binary system: an oxygen-rich Xe_2O_5 structure belonging to the $P4/ncc$ space group, and two oxygen-poor structures, Xe_3O_2 and Xe_2O, belonging to the $Immm$ and $C2/m$ space groups, respectively. The Xe_2O_5 structure had not been predicted previously; the Xe_3O_2 was independently predicted to be stable by Hermann and Schwerdtfeger [164], who also originally predicted the stability of the Xe_2O structure and investigated its properties; as such, the Xe_2O structure will not be described in detail in this thesis.

The structures of Xe_2O_5 and Xe_3O_2 are illustrated in Fig. 4.5. The Xe_2O_5 structure is a complex structure incorporating local geometries of both XeO_4 rectangles (almost squares), with oxygen atoms forming the corners, and XeO_5 'pyramids'. In these

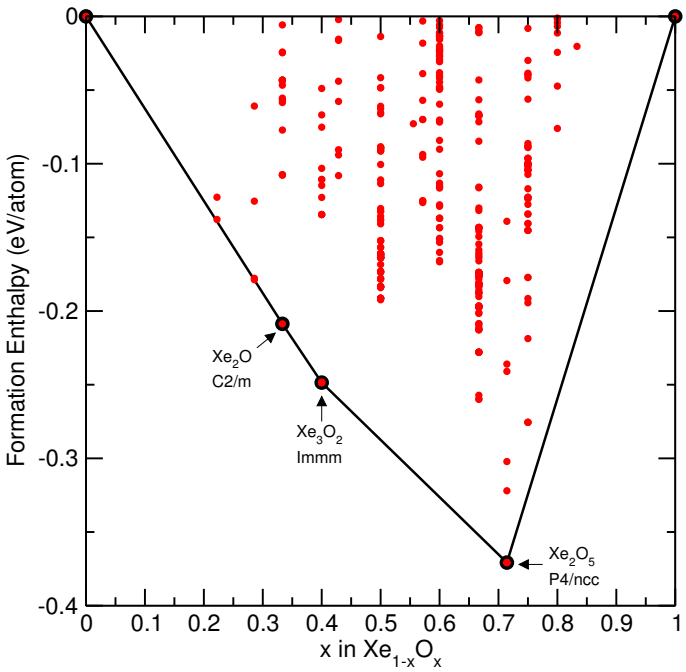

Fig. 4.4 Convex hull plot for the xenon oxygen binary system at 83 GPa. Black circles with red centres lying on the convex hull represent structures stable to decomposition. These are labelled with their stoichiometry and space group. Red dots denote structures generated by AIRSS that are either higher in enthalpy than other structures of the same stoichiometry, or unstable to decomposition into structures of other stoichiometries. The black lines connecting the stable structures denote the convex hull.

pyramids, the base is formed of XeO_4 in another almost-square arrangement, but in this case the Xe atom is slightly displaced below the plane of the oxygen atoms. The apex of the pyramids are formed by the fifth O atom, which is bonded to the Xe atom only. The length of the bond between the fifth O atom and the Xe atom is just 1.83 Å, compared with Xe-O bond lengths of 1.97–1.98 Å in the rest of the structure (see Table 4.6), suggesting that this bond is particularly strong. All other O atoms are additionally bonded to other Xe atoms, connecting the local geometries. These local geometries suggest a +4 oxidation state for the Xe atoms in the XeO_4 local geometry, and +6 for those in the XeO_5 local geometry. Xe_2O_5 forms a layered structure, with each layer being three Xe atoms thick.

Local geometries incorporating XeO_4 units have been identified in the XeO_2 structure described by Brock and Schrobilgen [151], while XeO_5 local geometries have been identified previously in $[XeF_5]^+[PtF_6]^-$ [181].

Xe atoms connected to each other via an oxygen atom have different oxidation states. The shortest distance between a Xe^{6+} ion and the four nearest oxygen atoms not bonded to it is only 2.29 Å (in contrast, for Xe^{4+} this distance is 2.49 Å). This small interatomic separation suggests a weak inter-layer attraction between these atoms, as in $[XeF_5]^+[PtF_6]^-$ [181].

The structure of Xe_3O_2 is simpler than that of Xe_2O_5; it consists of planar chains along the b axis of XeO_2 stoichiometry formed of XeO_4 'squares' with oxygen-sharing corners, in a similar manner to the structure proposed by Brock and Schrobilgen for XeO_2 [151]. This suggests a +4 oxidation state for the xenon atoms in the chains. These chains are intercalated by free xenon atoms. The minimum distances between free xenon atoms, and between a free xenon atom and the xenon atoms of the chains, are both comparable to the Xe-Xe distance in pure xenon (3.03 Å) at the same pressure [154].

The structure of Xe_2O is displayed in Fig. 4.6, along with the structures of two oxides lying very close to the convex hull at 83 GPa – Xe_5O_2 with a $C2/m$ space group, and Xe_7O_2 with an $Immm$ space group (predicted by Hermann and Schwerdtfeger [164]). Each of these xenon-rich oxides possess a great deal of chemical similarity with Xe_3O_2, consisting of long chains of XeO_2 stoichiometry intercalated by increasing numbers of unbonded xenon atoms. These structures – Xe_3O_2, Xe_2O, Xe_5O_2 and Xe_7O_2 – can all be thought of structurally as $(XeO_2) \cdot Xe_n$, where $\frac{n}{n+1}$ is the fraction of unbonded xenon present in the structure.

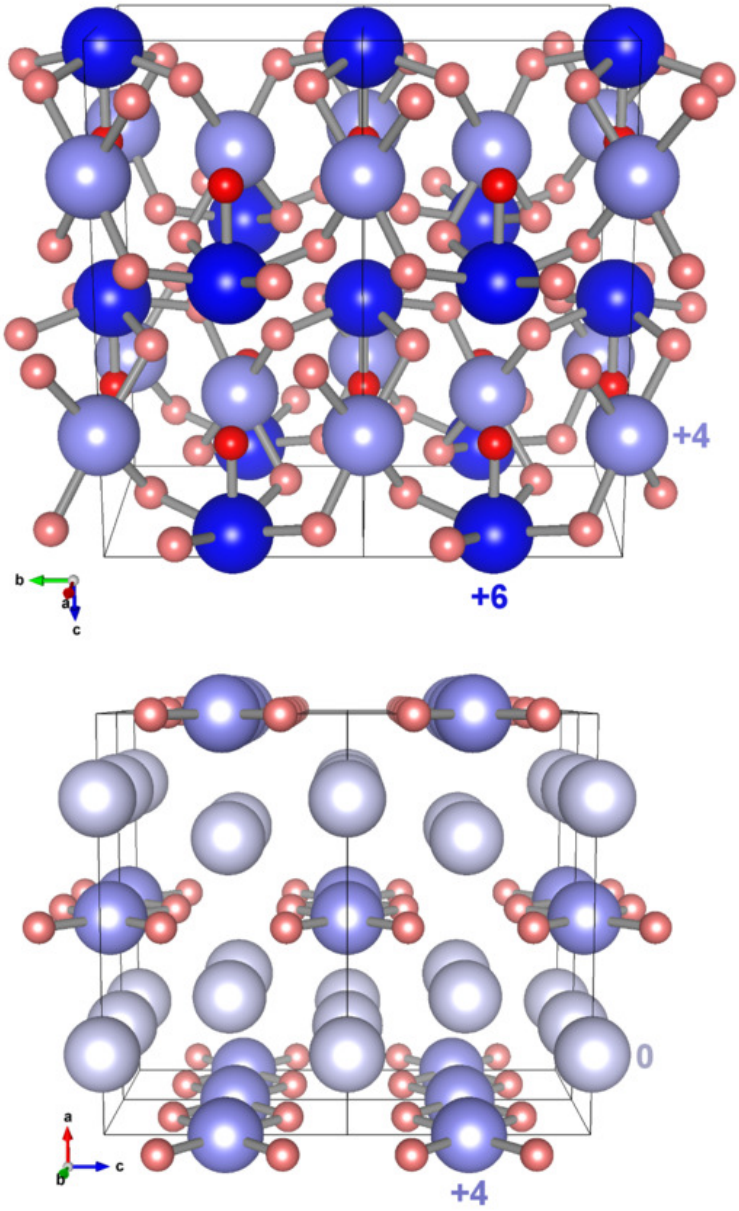

Fig. 4.5 Structures of stable xenon oxides at 83 GPa. Top: Xe_2O_5; bottom: Xe_3O_2. Xenon atoms are shown in blue shades and oxygen atoms in red shades. The oxygen atoms have an oxidation state of -2, and the darker shade of red denotes an oxygen atom that bonds only to one xenon atom. The oxidation states of the xenon atoms are indicated by different shades of blue. The lightest blue indicates 0 oxidation state, the darker shade +4 and the darkest blue the +6 oxidation state. The xenon atoms in Xe_2O_5 and Xe_3O_2 exist in two different oxidation states within each structure, +4 and +6 in Xe_2O_5 and 0 and +4 in Xe_3O_2.

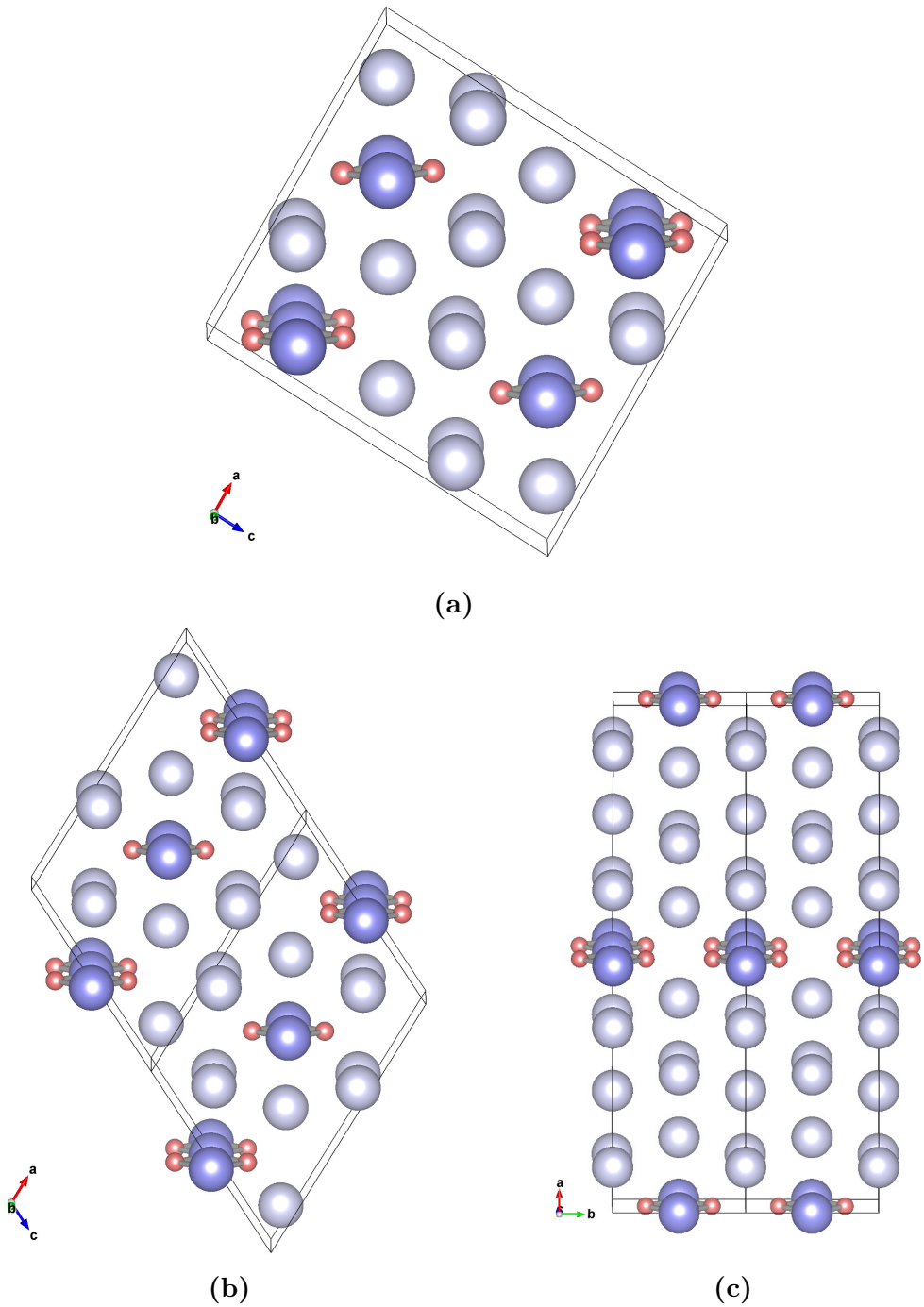

Fig. 4.6 Xenon suboxides at 83 GPa. Top: Xe_2O-$C2/m$; bottom left: Xe_5O_2-$C2/m$; bottom right: Xe_7O_2-$Immm$. The unit cells are rotated in order to emphasise the structural similarities. Xenon atoms are in blue: the darker hue indicates the bonded Xe atoms in the +4 oxidation state, and the lighter hue the unbonded Xe atoms in the 0 oxidation state. Oxygen atoms are in red.

The structural parameters for the xenon oxides predicted to be stable at 83 GPa are provided in Table 4.1. The lattice parameters are provided in minimal form for the space group, and the atomic positions are provided in terms of the given Wyckoff positions.

Stoichiometry	Space group	Lattice parameters	Atomic co-ordinates
Xe_2O_5	$P4/ncc$	a=4.983 Å c=9.955 Å	Xe (4a) 0.000 0.000 0.250 Xe (4c) 0.000 0.500 0.450 O (4c) 0.000 0.500 0.266 O (16g) 0.334 0.311 0.403
Xe_3O_2	$Immm$	a=8.536 Å b=3.217 Å c=4.964 Å	Xe (2c) 0.500 0.500 0.000 Xe (4e) 0.196 0.000 0.000 O (4j) 0.500 0.000 0.246
Xe_2O	$C2/m$	a=10.001 Å b = 3.206 Å c=11.081 Å β=93.32°	Xe (4i) 0.643 0.000 0.923 Xe (4i) 0.083 0.000 0.688 Xe (4i) 0.634 0.000 0.458 Xe (4i) 0.638 0.000 0.193 O (4i) 0.207 0.000 0.290 O (4i) 0.069 0.000 0.099

Table 4.1 Structural information for stable xenon oxides at 83 GPa. Atomic sites are given in terms of Wyckoff positions and in fractional co-ordinates.

Xe_2O_5, Xe_3O_2 and Xe_2O all feature Xe atoms in mixed oxidation states. Xe_2O_5 has an equal number of atoms in the +4 and +6 oxidation states, while Xe_3O_2 and Xe_2O possess a mixture of oxidised Xe atoms with a +4 oxidation state and unoxidised Xe atoms. The ratio of unoxidised to oxidised Xe atoms is 2:1 in Xe_3O_2 and 3:1 in Xe_2O. The unoxidised Xe atoms in Xe_3O_2 and Xe_2O demonstrate a small transfer of charge to the XeO_2 chains, particularly at higher pressures when the unbonded Xe atoms are forced closer to the chains.

These oxidation states are assigned on the basis of Hirshfeld [38], Bader [182] and Mulliken [183] charge analyses. The results of these analyses for Xe_2O_5 and Xe_3O_2 at 83 GPa are shown in Tables 4.2 and 4.3. The Bader and Mulliken charge density analyses would suggest an approximately 50% ionicity for the Xe-O bonding.

Species	Number	s	p	d	Charge (e)	Oxidation state
O1	16	1.92	5.05	0.00	-0.96	–2
O2	4	1.93	5.09	0.00	-1.02	–2
Xe1	4	1.73	3.30	10.00	2.98	+6
Xe2	4	2.15	3.96	10.00	1.89	+4

(a) Mulliken population analysis

Species	Number	Charge (e)	Oxidation state
O1	16	-0.27	–2
O2	4	-0.33	–2
Xe1	4	0.80	+6
Xe2	4	0.61	+4

(b) Hirshfeld charge analysis

Species	Number	Charge (e)	Oxidation state
O1	16	-1.00	–2
O2	4	-1.12	–2
Xe1	4	2.96	+6
Xe2	4	2.16	+4

(c) Bader charge analysis

Table 4.2 Atomic charges for Xe_2O_5, with assigned oxidation states.

Species	Number	s	p	d	Charge (e)	Oxidation state
O	4	1.93	5.10	0.00	-1.03	–2
Xe1	4	2.06	5.76	10.00	0.18	0
Xe2	2	1.92	4.38	10.00	1.71	+4

(a) Mulliken population analysis

Species	Number	Charge (e)	Oxidation state
O	4	-0.31	–2
Xe1	4	0.08	0
Xe2	2	0.46	+4

(b) Hirshfeld charge analysis

Species	Number	Charge (e)	Oxidation state
O	4	-1.00	–2
Xe1	4	0.22	0
Xe2	2	1.57	+4

(c) Bader charge analysis

Table 4.3 Atomic charges for Xe_3O_2, with assigned oxidation states.

Electronic structure

Density functional theory band structures using the PBE *xc* functional predict Xe_2O_5 to be an insulator with a minimum indirect (thermal) band gap of 1.48 eV at 83 GPa. The minimum direct (optical) band gap at this pressure is slightly larger, at 1.80 eV. As pressure increases, these band gaps become smaller. The thermal band gap reduces to 0.77 eV by 200 GPa, and the optical band gap to 1.55 eV. In contrast, DFT calculations with the PBE functional indicate that Xe_3O_2 is semi-metallic, with no band gap, but with a greatly reduced density of electronic states (eDoS) around the Fermi energy, across a wide range of pressures. The calculated minimum direct and indirect band gaps for Xe_2O_5 and Xe_3O_2 using the PBE functional at several pressures between 83 GPa and 200 GPa are shown in Table 4.4.

As the PBE functional is known to underestimate band gaps, the band structure of Xe_3O_2 was also calculated using the HSE06 *xc* functional [33], which usually yields larger and more accurate band gaps. With this functional, Xe_3O_2 is predicted to be a narrow band-gap semiconductor, with a band gap of 0.05 eV, in line with the calculations of Hermann and Schwerdtfeger [164].

Structure	Pressure (GPa)			
	83	100	150	200
Xe_2O_5-$P4/ncc$	1.48	1.38	1.04	0.77
Xe_3O_2-$Immm$	0.00	0.00	0.00	0.00

(a) Minimum band gap

Structure	Pressure (GPa)			
	83	100	150	200
Xe_2O_5-$P4/ncc$	1.80	1.76	1.65	1.55
Xe_3O_2-$Immm$	0.01	0.02	0.07	0.02

(b) Minimum direct band gap

Table 4.4 Minimum (thermal) and minimum direct (optical) band gaps in eV calculated with the PBE exchange-correlation functional [24].

Band structures along high-symmetry paths and partial electronic densities of states (PDoS), decomposed by angular momentum channel, are shown for Xe_2O_5 and Xe_3O_2 in Figs 4.7a and 4.7b, respectively. Figs 4.7c and 4.7d show the PDoS decomposed by both angular momentum channel and atomic species, for which the OptaDOS code [184–186] was used.

As can be seen from Figs 4.7a and 4.7c, the top of the valence band and the bottom of the conduction band for Xe_2O_5 is made up predominantly of Xe $5p$ and O $2p$ orbitals. The width of the occupied part of these bands is approximately 12 eV. The width of the p orbital bands lying above the Fermi level is about 3.5 eV, with an additional band gap above these bands. Lying immediately below the p-orbital bands in energy are the Xe $5s$ and O $2s$ levels, with a width of about 15 eV. A further $\sim$30 eV below the bottom of these bands lie the almost-dispersionless Xe $4d$ orbitals.

The band structure of Xe_3O_2 is similar to that of Xe_2O_5, with the principal differences being the lack of a band gap at the Fermi level – although the DoS is greatly reduced in the region of the Fermi energy – and the appearance of a small band gap between the lower-energy s and higher-energy p orbitals. Again, the bands corresponding to the p orbitals are partially unoccupied.

The PDoS for Xe_2O_5 shown in Fig. 4.7c demonstrates a very considerable depletion of the Xe p states below the Fermi level and a corresponding augmentation of the density of O p states. This suggests a hybridisation of the Xe and O p orbitals,

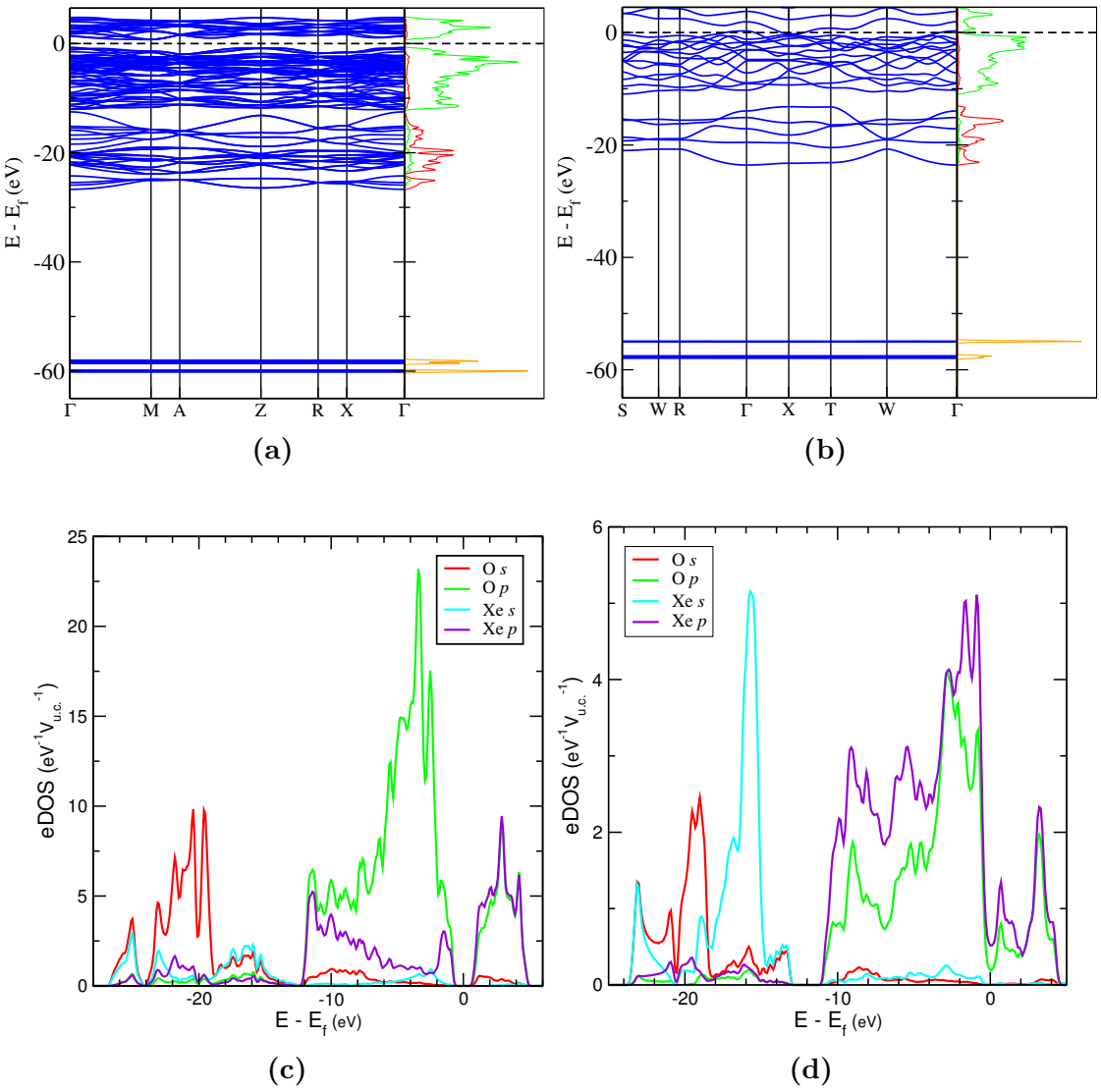

Fig. 4.7 Band structures and partial densities of states for Xe_2O_5 and Xe_3O_2. (a) and (b): band structures along high-symmetry paths and PDoS (resolved by angular momentum channel) for Xe_2O_5 and Xe_3O_2, respectively. The electronic bands are shown in blue and the Fermi level is shown as a horizontal black dashed line. The orange line shows the d electron density of states (rescaled to fit on the axes), the red shows the s density of states, and the green shows the p density of states. The s and p densities of states include contributions from both Xe and O.(c) and (d): PDoS (resolved by both atomic species and angular momentum channel; colour keys are in the figures) for Xe_2O_5 and Xe_3O_2, respectively. $V_{u.c.}$ denotes the unit cell volume.

resulting in a transfer of charge from the xenon atoms to the oxygen atoms, consistent with the charge transfer analysis (see Table 4.2).

The PDoS for Xe_3O_2 plotted in Fig. 4.7d also indicates a depletion of the Xe p states and corresponding augmentation of the O p states. This effect is less obvious in Xe_3O_2 than in Xe_2O_5, as only one xenon atom in three is involved in chemical bonding with oxygen atoms (the 'average' oxidation state for xenon in Xe_3O_2 is $\frac{4}{3}$, as opposed to 5 in Xe_2O_5). Again, the transfer of charge implied by the partial hybridisation of the Xe and O p orbitals is consistent with the charge transfer analysis summarised in Table 4.3.

Vibrational properties

The convex hull plot of Fig. 4.4 is calculated at the static-lattice level of theory, ignoring the effect of nuclear motion, both zero-point and thermal, on stability. For the structures predicted to be stable at 83 GPa at the static level, phonon calculations were performed at the harmonic level using the finite-displacement method within the supercell approach, as implemented in the CASTEP code. Supercell sizes were tested for convergence. Phonon free energies were evaluated using equation (2.111) and added to the enthalpies from the static-lattice calculations. The resulting free energies are plotted in Fig. 4.8.

As can be seen from Fig. 4.8, inclusion of phonon effects does not significantly alter the relative stability of the xenon oxide structures; although the free energies of the oxygen-poor structures decrease more than the oxygen-rich structures, the difference is modest compared with the static-lattice enthalpies of formation. The free energy change of formation from the elemental solids is reduced for all of the compounds, indicating that thermal effects increase the stability of the oxides. These conclusions are consistent with those of Zhu *et al.* [163].

Phonon dispersion curves and densities of states are plotted for Xe_2O_5 and Xe_3O_2 in Fig. 4.9. The vibrational density of states for Xe_2O_5 shows that vibrational states exist across the full range of frequencies up to almost 800 cm^{-1}, but with sharp reductions in the vibrational DoS at about 200, 400 and 700 cm^{-1}. The vibrational DoS for Xe_3O_2 is divided into four sections: a lower section, with frequencies up to about 300 cm^{-1}, has a high density of vibrational states, which demonstrate a high degree of dispersion. After a small gap, there is then a narrow band of low-dispersion states between about 330 and 400 cm^{-1}, followed by a wide band of high-dispersion states between 415 and 580 cm^{-1}. Finally, there is a narrow band of low-dispersion vibrational states between

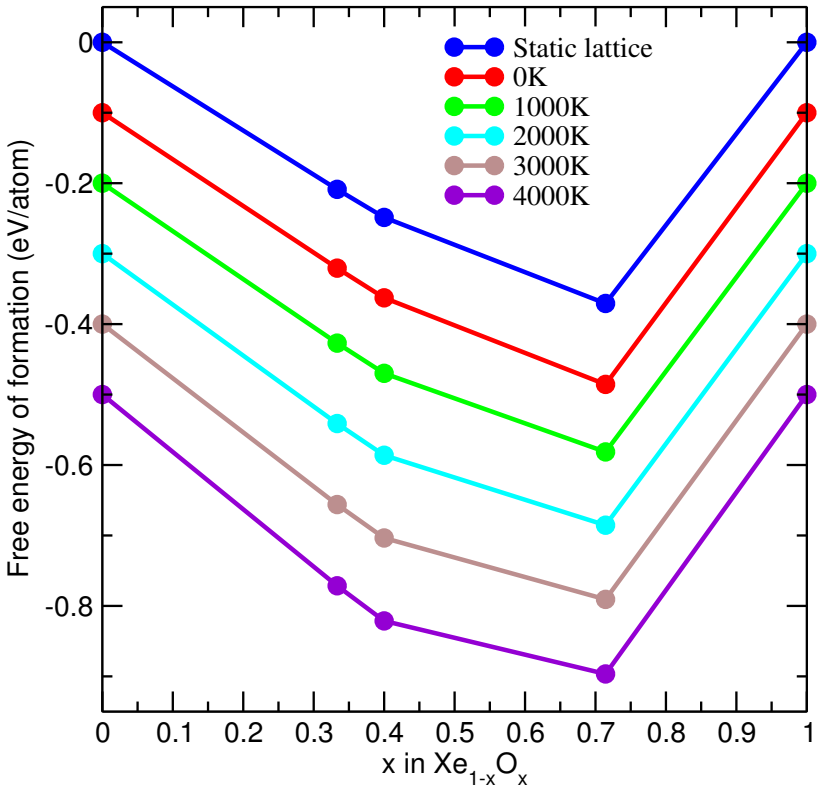

Fig. 4.8 Convex hull graph showing the free energies of formation from the elemental solids at 83 GPa for several temperatures up to 4000 K, as well as the static-lattice hull for comparison. The convex hull at 0 K includes zero-point effects. Each curve is shifted by -0.1 eV/atom from the previous curve for ease of visibility.

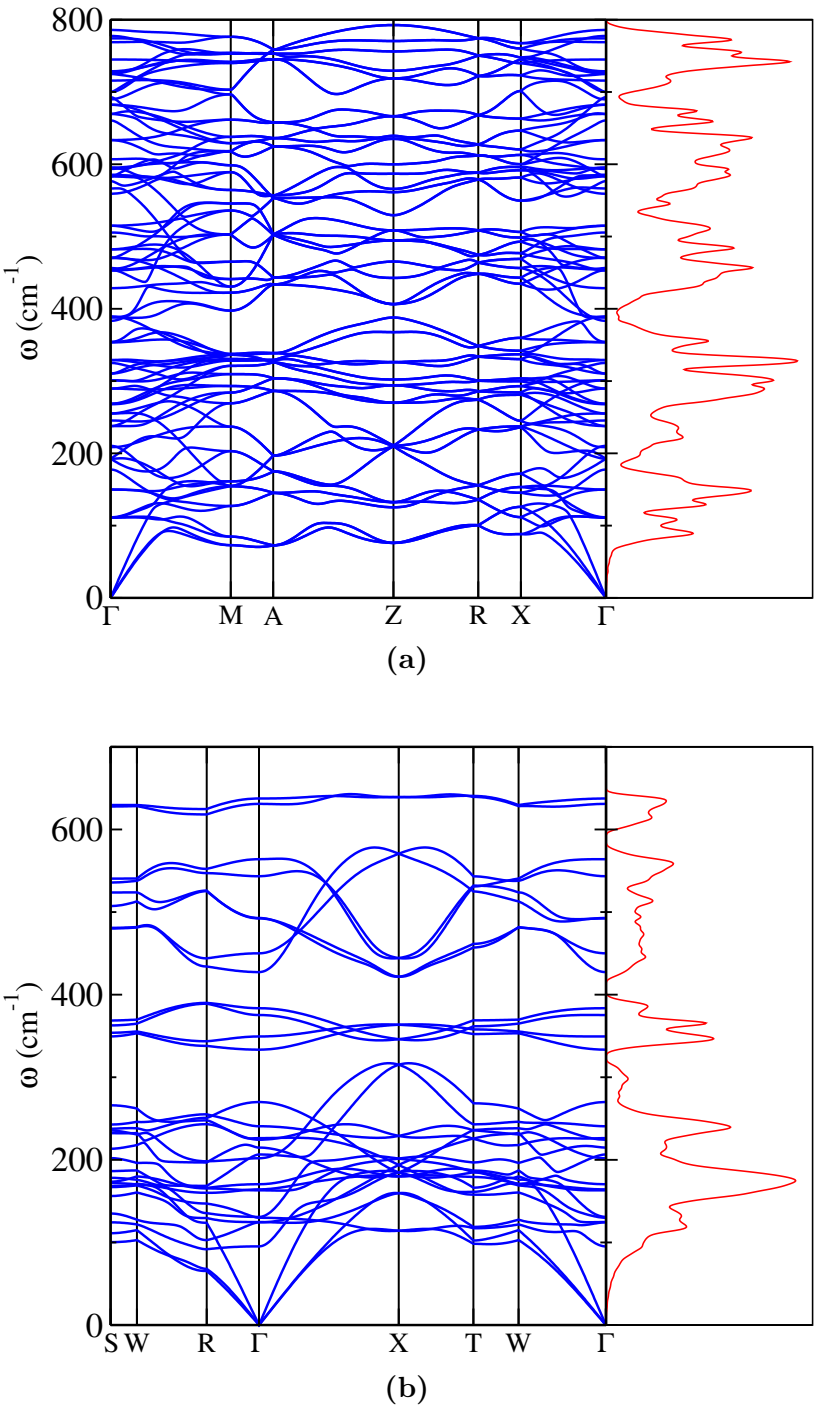

Fig. 4.9 Phonon dispersion curves along high-symmetry paths and vibrational densities of states for (a) Xe_2O_5 and (b) Xe_3O_2 at 83 GPa. Phonon curves are calculated at the harmonic level of theory using the finite displacement and supercell methods.

600 and 640 cm^{-1}. This maximum frequency is substantially lower than the maximum frequency in Xe_2O_5, consistent with weaker bonding in Xe_3O_2 than in Xe_2O_5.

The highest frequency vibrational modes in Xe_2O_5 consist of symmetric stretches of Xe-O bonds. The lowest-frequency modes in this structure involve motion of the xenon atoms, with the oxygen atoms barely moving; intermediate-frequency modes feature Xe-O torsional modes. The low-frequency modes in Xe_3O_2 involve the motion of the free xenon atoms, or of the XeO_2 chains collectively. The next band of phonon modes in Xe_3O_2 (with frequencies between 330 and 400 cm^{-1}) involve motions of the oxygen atoms out of the plane of the XeO_2 chains. The third band (frequencies between 415 and 580 cm^{-1}) demonstrate in-plane motions of oxygen atoms relative to the xenon atoms. Symmetric Xe-O stretches constitute the highest-frequency phonon modes, as in Xe_2O_5.

Comparison with experimental results

In parallel with the theoretical work, experimental collaborators laser-heated Xe-O mixtures with an O_2 content higher than 50 mol.% in a DAC under pressures of around 80-90 GPa, as described in section 4.2.3. This led to a reaction above ∼77 GPa with a single reaction product, which was characterised by powder X-ray diffraction, X-ray absorption and Raman spectroscopies. As a result of our prediction of the stability of Xe_3O_2 in this pressure range, additional experiments were later carried out using xenon-rich starting mixtures. The experiments that were conducted by our collaborators are summarised in Table 4.5.

Run number	Composition	Heating P	Measurements	Products
1	33 % Xe – 67 % O_2	83 GPa	PXRD + Raman	Xe_2O_5
2	40 % Xe – 60 % O_2	77 GPa	Raman	Xe_2O_5
3	49 % Xe – 51 % O_2	90 GPa	PXRD	Xe_2O_5
4	36 % Xe – 64 % O_2	82 GPa	PXRD + XAS	Xe_2O_5
5	75 % Xe – 25 % O_2	92 GPa	PXRD	Xe_3O_2 + Xe_2O_5
6	89 % Xe – 11 % O_2	95 GPa	PXRD + Raman	Xe_3O_2 + Xe_2O_5

Table 4.5 Synthesis conditions of the xenon oxides. The starting mixtures (composed of Xe with O_2 impurities, $Xe(O_2)_2$ and O_2) were laser-heated for several minutes at the specified pressure. Xe_2O_5 and Xe_3O_2 were the only products observed in the experiments, in co-existence with the reactants. During the second experiment, the sample was laser-heated on pressure increase, beginning at 40 GPa, with pressure steps of ∼5 GPa; the reaction was observed at 77 GPa.

The PXRD pattern of the product subsequently identified as Xe_2O_5, measured at around 83 GPa, could be indexed by a tetragonal unit cell of volume $V = 247.3\,Å^3$, with a small amount of unreacted xenon also observed in the spectrum. Although approximate atomic positions could be deduced from the PXRD pattern for the xenon atoms, the low atomic scattering power of oxygen relative to xenon meant that the number and positions of the oxygen atoms could not be determined. The PXRD data recorded at about 83 GPa following laser heating agree very well with the simulated PXRD pattern for the Xe_2O_5 structure, see Fig. 4.10.

In the experiments using mixtures with an O_2 content lower than 25 mol.%, PXRD data indicate the presence of a new phase consistent with the simulated diffraction pattern for Xe_3O_2, in agreement with the theoretical prediction. As can be seen in Fig. 4.10, Xe_3O_2 co-exists with Xe and Xe_2O_5 even for the mixture containing only 11% O_2, whereas a mixture containing only Xe_3O_2 and xenon would be expected from the convex hull. This may be due to the presence of the oxygen-rich $Xe(O_2)_2$ phase in the starting mixture and inhomogeneities in the mixture of reactants.

The equations of state (EoS) for Xe_2O_5 and Xe_3O_2 were derived both theoretically and experimentally from the pressure-volume curves for these structures. The Rydberg-Vinet equation of state [187] was used in both cases. Fig. 4.11 shows the pressure-volume curves with both theoretical and experimental data plotted for Xe_2O_5 and Xe_3O_2, along with theoretical and experimental data on the ratio of lattice parameters as a function of pressure. Parameters for the calculated EoS, as well as other structural data, for both structures are displayed in Table 4.6. The measured and calculated lattice parameters and atomic separations agree well for both Xe_2O_5 and Xe_3O_2.

The EoS for Xe_2O_5 predicted by DFT calculations agrees well with the experimental evidence. The bulk modulus of Xe_2O_5 at 83 GPa is about 50% higher than the bulk modulus of pure Xe at this pressure, indicating strong bonding in Xe_2O_5. The density of Xe_2O_5 is significantly higher (17% for DFT calculations, 14% for experimental measurements) than that of a mixture of xenon [154] and O_2 [188] with the same pressure and stoichiometry. Xe_2O_5 thus represents an efficient packing of xenon and oxygen atoms.

The EoS for Xe_3O_2 measured on pressure decrease is in good agreement with that predicted by DFT close to the synthesis pressure. The measured bulk moduli of Xe_3O_2 and Xe are similar at high pressures, which is consistent with the presence of large amounts of unoxidised xenon in the Xe_3O_2 structure. The bulk modulus of Xe_2O_5 at 83 GPa is approximately twice that of Xe_3O_2 at 97 GPa, consistent with stronger

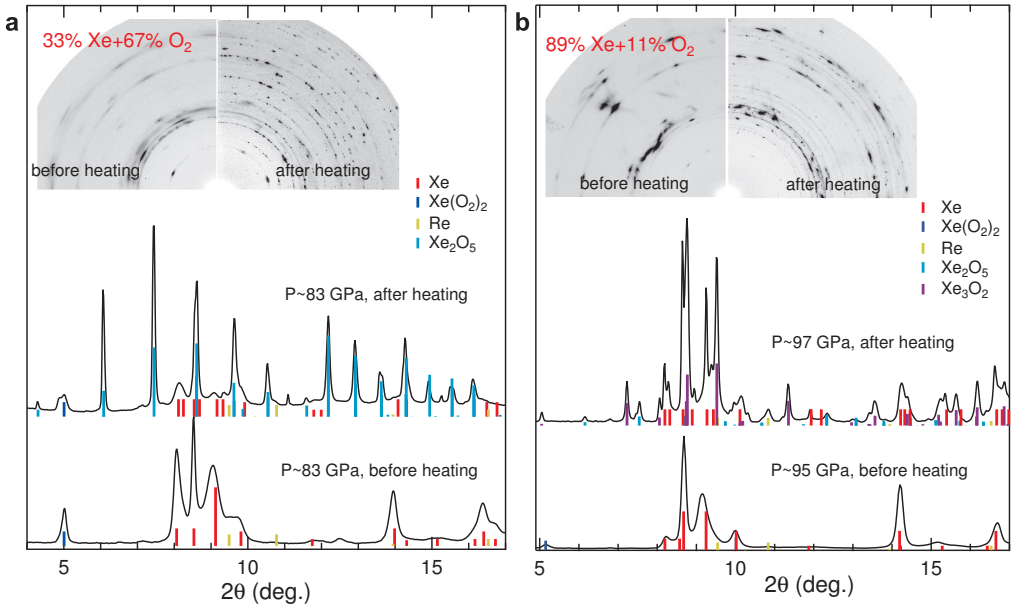

Fig. 4.10 Powder X-ray diffraction (PXRD) patterns of Xe–O_2 mixtures under pressure, before and after laser heating. (a) PXRD patterns of a 33% Xe–67% O_2 mixture at about 83 GPa; (b) PXRD patterns of an 89% Xe–11% O_2 mixture at about 97 GPa. The insets show the two-dimensional patterns before circular integration. Prior to laser-heating, in both mixtures the phases were Xe with O_2 impurities [154] and $Xe(O_2)_2$[155]. (a), After laser-heating, most of the reactant has transformed into Xe_2O_5. The light blue ticks indicate the positions and predicted relative intensities of the diffraction peaks of Xe_2O_5 (lattice parameters in Table 4.6). (b) After laser-heating, Xe_3O_2 and Xe_2O_5 appear, in addition to the reactants. The most intense xenon diffraction peaks were masked during the circular integration. The purple and light blue ticks indicate the positions and predicted relative intensities of the diffraction peaks of Xe_3O_2 (lattice parameters in Table 4.6) and Xe_2O_5. In both experiments, the Xe PXRD lines (red ticks) are split after laser-heating, which can be explained as arising from a variable content of O_2 impurities. Figures produced by Agnès Dewaele.

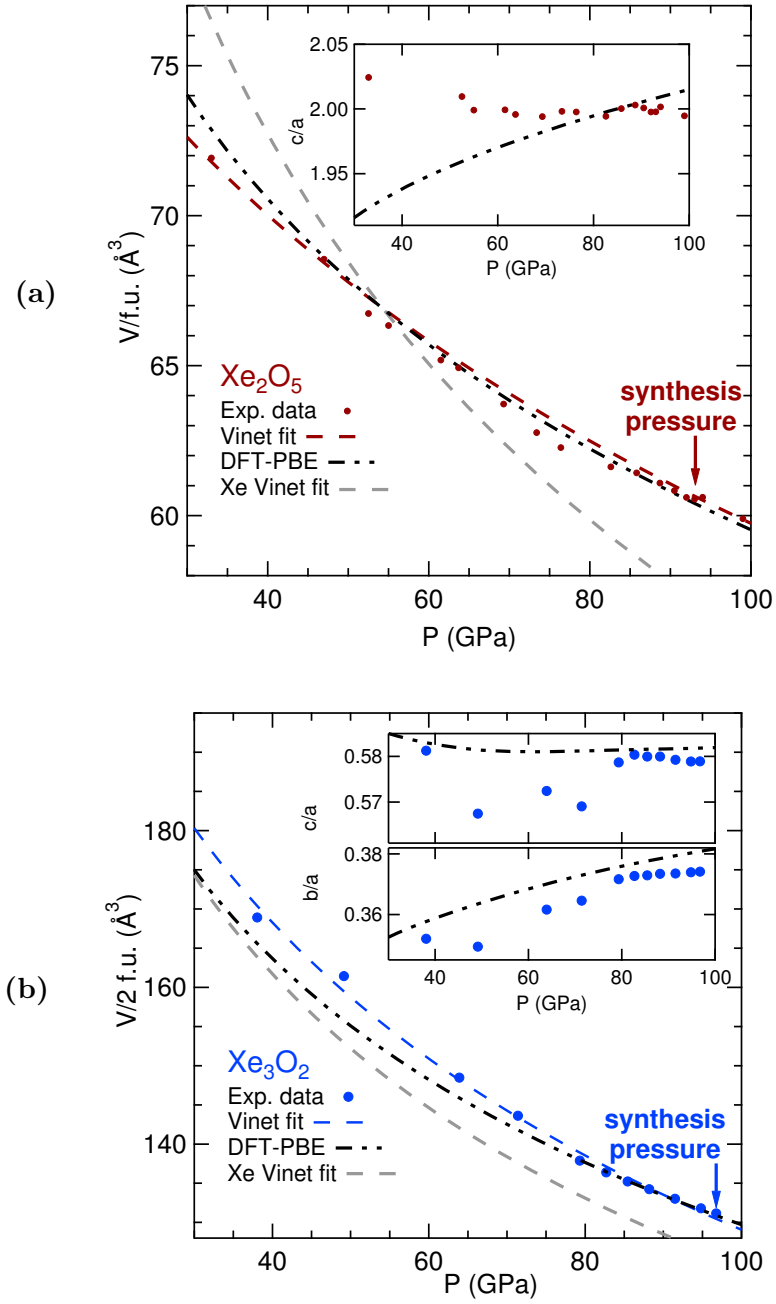

Fig. 4.11 Pressure-volume curves for (a) Xe_2O_5 and (b) Xe_3O_2 in the pressure range 30–100 GPa. The pressure-volume curve obtained from DFT calculations is depicted by the dash-dot black line. Experimental data points are depicted using red (Xe_2O_5) and blue (Xe_3O_2) filled circles, with the Rydberg-Vinet equation of state [187] fits to the experimental data shown as dashed lines with the corresponding colour. For comparison, the pressure-volume curves for pure xenon are also depicted, using a dashed grey line. Insets depict lattice parameter ratios for the two structures, with experimental data points indicated by filled circles and the lattice parameter ratios predicted by DFT calculations shown with dash-dot black lines. *f.u.* denotes formula unit. Graphs were produced by Agnès Dewaele with minor modifications by the author.

$\mathbf{Xe_2O_5}$	Experiment	Theory
Lattice parameter a (Å)	4.980	4.978
Lattice parameter c (Å)	9.970	9.951
Volume (Å^3/4 f.u.)	247.3	246.6
Xe^{6+} – O(1) bond length (Å)	1.83	1.83
Xe^{6+} – O(2) bond length (Å)	1.97	1.97
Xe^{4+} – O bond length (Å)	1.98	1.98
Xe^{6+} – Xe^{4+} bond length (Å)	3.19	3.19
Rydberg-Vinet V_0 (Å^3/4 f.u.)	337.2 ±6	332.8±2.4
Rydberg-Vinet K_0 (GPa)	150±20	161±6
Rydberg-Vinet K_0'	4 (fixed)	4 (fixed)
$\mathbf{Xe_3O_2}$	Experiment	Theory
Lattice parameter a (Å)	8.457	8.388
Lattice parameter b (Å)	3.166	3.195
Lattice parameter c (Å)	4.904	4.880
Volume (Å^3/2 f.u.)	131.3	130.8
Xe^{4+} – O bond length (Å)	1.99	2.01
Xe^{4+} – Xe^{4+} bond length (Å)	3.17	3.19
Xe^{0} – Xe^{0} bond length (Å)	3.06	3.05
Xe^{4+} – Xe^{0} bond length (Å)	2.96–3.01	2.95–3.00
Rydberg-Vinet V_0 (Å^3/2 f.u.)	262±15	217.8±2.4
Rydberg-Vinet K_0 (GPa)	37.2±8	74.5±4
Rydberg-Vinet K_0'	4 (fixed)	4 (fixed)

Table 4.6 Comparison of experimental and theoretical properties of Xe_2O_5 and Xe_3O_2. Experimental lattice constants were obtained from the PXRD data. Experimental interatomic distances were obtained using the structures from AIRSS and the experimental lattice constants. Lattice parameters and bond lengths are given at 83 GPa for Xe_2O_5 and at 97 GPa for Xe_3O_2. V_0 and K_0 denote the zero-pressure volume and bulk modulus obtained with a Rydberg-Vinet [187] fit of P–V data plotted in Fig. 4.11. The error bars represent a 95% confidence interval. The fitting of experimental and theoretical data was performed by Agnès Dewaele.

interatomic bonding in the extended Xe_2O_5 structure than in Xe_3O_2. As expected from the structure,the b axis parallel to the strong Xe-O chains is less compressible than the a and c axes. There is good agreement between the experimental and DFT values of the lattice parameters and interatomic distances of Xe_3O_2 at the experimental pressure of 97 GPa. The agreement diverges at lower pressures, as Xe_3O_2 is predicted to become unstable. The pressure distribution may also become heterogeneous during the release of pressure, which may be affecting the experimental measurements.

The density of Xe_3O_2 at 83 GPa is predicted to be 9% greater than the density of a stoichiometric mixture of the pure elements at the same pressure, therefore also indicating a more efficient packing of xenon and oxygen atoms in the oxide compared with the pure elements, although not to the same extent as for Xe_2O_5. The experimental density of Xe_3O_2 was estimated to be about 8% greater than a stoichiometric mixture of the elements under the same conditions.

XAS at the K-edge of xenon performed on Xe_2O_5 confirms the presence of Xe-O bonds. X-ray absorption near edge spectra of the sample compressed to 82 GPa are presented in Fig. 4.12a. Fig. 4.12b shows the extended X-ray absorption fine structure function oscillations due to the local environment around the Xe atoms, and Fig. 4.12c shows the Fourier transform of these oscillations for the heated sample. A simple two-shell model including just one Xe-O and one Xe-Xe coordination shell provides a good fit to the data (green dashed lines), with 3.0±0.5 oxygen atoms and 5.0±0.6 xenon atoms at separations of 1.93 Å and 3.165 Å, respectively. A second model, assuming the Xe_2O_5 structure, provided a very good fit to the experimental data. The fitting parameters for the two models are presented in Appendix B; the fits were performed by Agnès Dewaele and Sakura Pascarelli. There was no evidence for contamination of the XAS spectra by unreacted xenon; this was confirmed by PXRD data taken on the same spot. XAS was not performed on Xe_3O_2.

The Raman spectrum of Xe_2O_5 was collected at 88 GPa (Fig. 4.13). The Raman frequencies and intensities calculated at the experimental volume in Xe_2O_5 correctly reproduce the Raman spectrum, although all Raman frequencies are slightly (∼4%) underestimated, suggesting that the bond strength is slightly underestimated in the calculations. The Raman spectrum collected in Xe_3O_2 is in agreement with the predicted Raman frequencies, apart from one intense extraneous peak (Fig. 4.13).

The experimental evidence from the experimentally measured EoS, and the PXRD, X-ray absorption and Raman spectroscopies, supports the predictions from theoretical structure searching of a Xe_2O_5 structure being formed under oxygen-rich conditions, and a Xe_3O_2 structure being formed under oxygen-poor conditions.

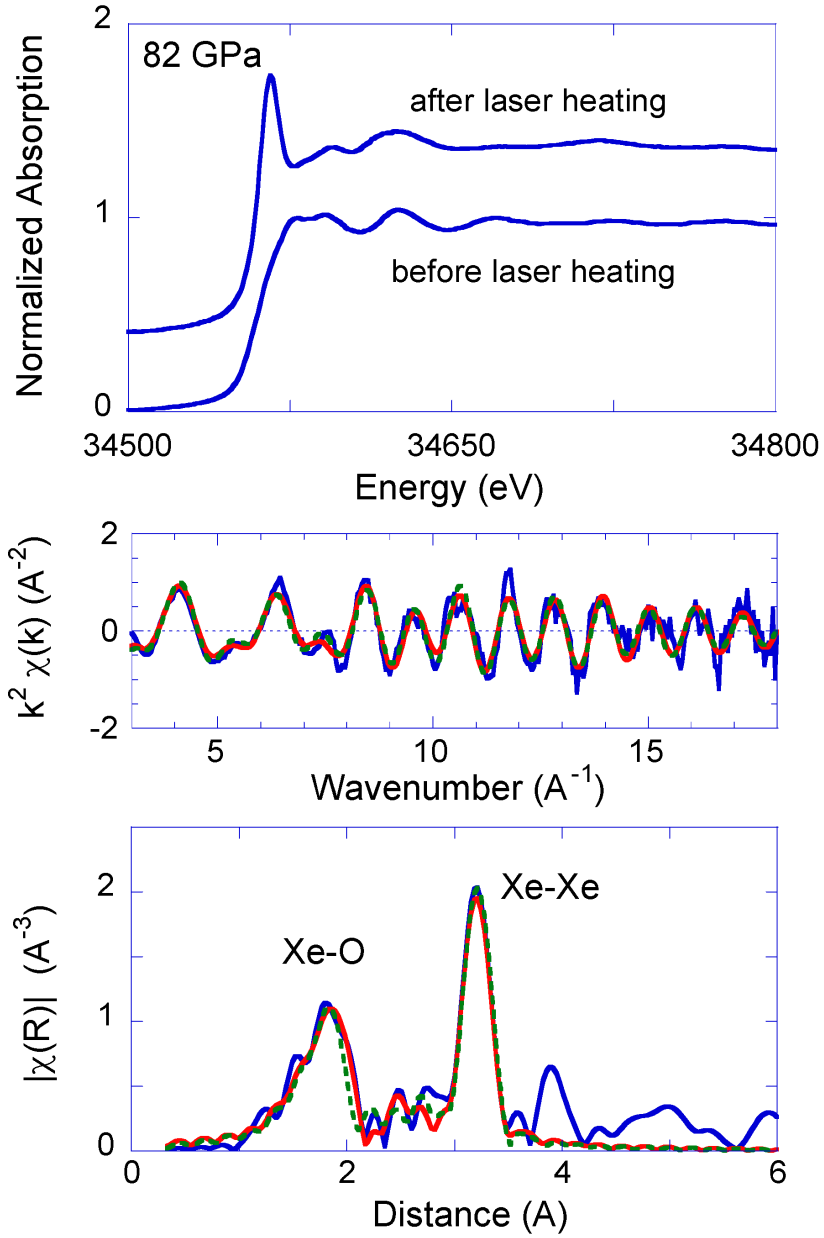

Fig. 4.12 X-ray absorption spectroscopy (XAS) taken at the Xe K-edge for Xe_2O_5. The top panel shows the raw spectra before and after laser heating. After laser heating, a strong absorption line appears at the Xe K-edge absorption onset (around 34.6 keV) at the centre of the laser-heated area, which indicates depletion due to oxidation of the $5p$ states of Xe just above the Fermi level. The middle panel shows the extended X-ray absorption fine-structure function $\chi(k)$, weighted by k^2 (where k is the photoelectron wavenumber), extracted from the X-ray absorption spectrum after laser heating (blue line: experimental data; dashed green: two-shell fit; red: fit assuming the Xe_2O_5 structure). The bottom panel shows the $|\chi(R)|(\text{Å}^{-3})$ amplitude of the Fourier transform of this function (with the same key as for the middle panel). The two intense peaks reflect the presence of two distinct distances for neighbours around xenon atoms. The abscissa is rigidly shifted by 0.33 Å to account for the photoelectron scattering phase shift. Figures produced by Agnès Dewaele.

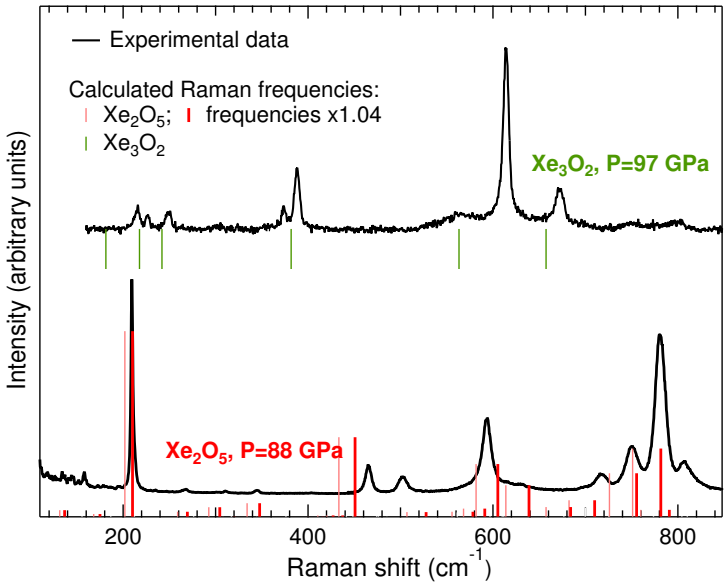

Fig. 4.13 Raman spectra of Xe_2O_5 and Xe_3O_2, measured at 88 GPa and 97 GPa, respectively. Peak frequencies were calculated for Xe_2O_5 and Xe_3O_2 at their experimental volumes and are plotted as red and green ticks, respectively. Peak intensities were also calculated for Xe_2O_5. When the frequencies calculated for Xe_2O_5 are increased by 4% (bold red ticks), they agree with the experimentally measured frequencies to within $\pm 15\,\mathrm{cm}^{-1}$. Figure produced by Agnès Dewaele.

However, no experimental evidence was recorded for the Xe_2O structure that is also predicted (originally by Hermann and Schwerdtfeger [164]) to form under oxygen-poor conditions, despite an experimental run with an O_2 content of just 11 mol.%. In Fig. 4.4, it is clear that Xe_2O only just lies on the convex hull; it is therefore possible that more accurate calculations – going beyond the DFT level of theory – might not predict Xe_2O to be stable.

4.3.2 Structure Searching at 150 GPa and 200 GPa

In order to investigate the evolution of the xenon-oxygen binary system with increasing pressure, structure searching using the AIRSS methodology combined with data mining techniques was also carried out at higher pressures of 150 and 200 GPa, using the same stoichiometries as at 83 GPa. No experiments were conducted at these higher pressures in the Xe-O binary system, so results are presented for theoretical calculations only.

Structure searching carried out on the pure elements confirmed that the xenon continues to take the hcp structure, whereas the structure of pure oxygen at these pressures is now the experimentally-known ζ-O phase [189, 190], related to ϵ-O by an isosymmetric phase transition.

The results of the structure searching at 150 and 200 GPa are presented as convex hull plots in Fig. 4.14. At 150 GPa, the Xe_2O_5 structure with $P4/ncc$ symmetry is still predicted to be stable to decomposition within the binary system under oxygen-rich conditions, as are Xe_3O_2 (with $Immm$ space group) and Xe_2O (with $C2/m$ space group) under oxygen-poor conditions. Additionally however, a XeO_3 structure with $P2_12_12_1$ symmetry is predicted to be stable under oxygen-rich conditions at this pressure.

As the pressure increases further, to 200 GPa, Xe_2O and Xe_2O_5 are no longer predicted to be stable, both structures lying just off the convex hull. Xe_3O_2 is still predicted to be stable under oxygen-poor conditions, and XeO_3-$P2_12_12_1$ remains stable to decomposition under oxygen-rich conditions. A new oxygen-rich phase, a XeO_2 structure belonging to the $Pnma$ space group, becomes stable by this pressure.

At 150 GPa, the XeO_3 structure is 17% denser than a stoichiometric mixture of the pure elements, and 5% denser than a stoichiometric mixture of Xe_2O_5 and ζ-O, suggesting that the origin of its stability at higher pressures is its high atomic packing density. At 200 GPa, the density of the XeO_2 structure is 12% greater than that of a stoichiometric mixture of the elements, and 3% greater than a mixture of Xe_2O_5 and Xe_3O_2. At this pressure, XeO_3 has a density 15% greater than a mixture of the pure

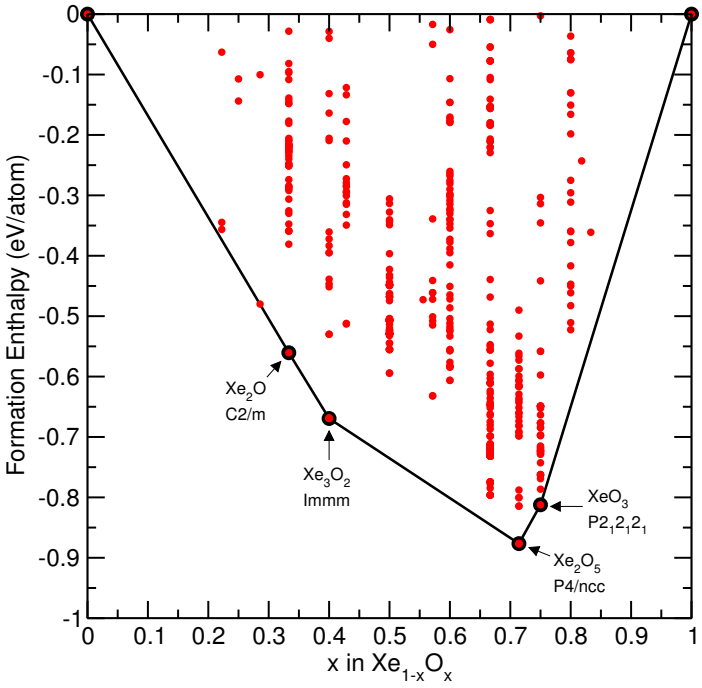

(a) 150 GPa

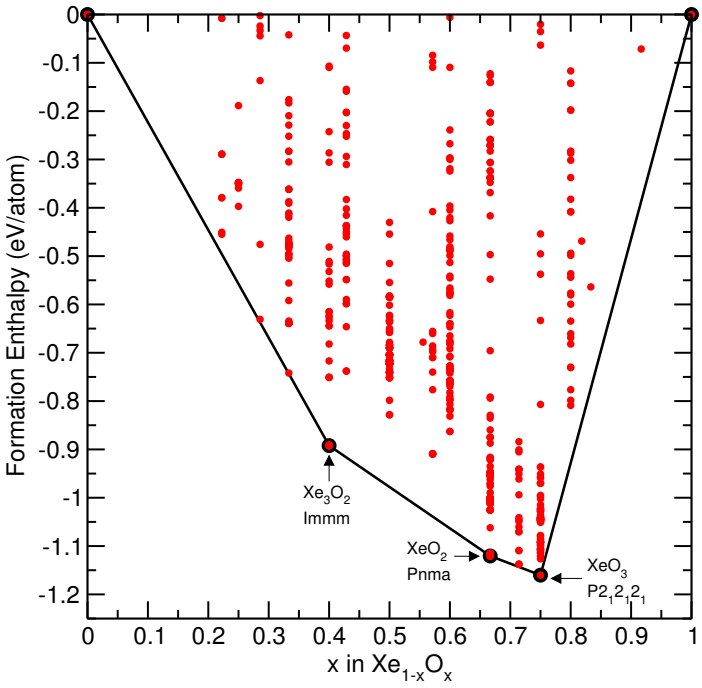

(b) 200 GPa

Fig. 4.14 Convex hull plots from structure searching at (a) 150 GPa and (b) 200 GPa. As for Fig. 4.4, red circles represent calculated structures, and the larger black circles represent structures stable to both phase changes to other structures with the same stoichiometry and to decomposition into a mixture of structures with different stoichiometries. These structures are labelled by stoichiometry and space group. The black lines connecting these structures denote the convex hull.

elements, and 6% greater than a mixture of Xe_2O_5 and ζ-O. These greater densities may explain why these two oxides have pushed Xe_2O_5 out of stability by this pressure.

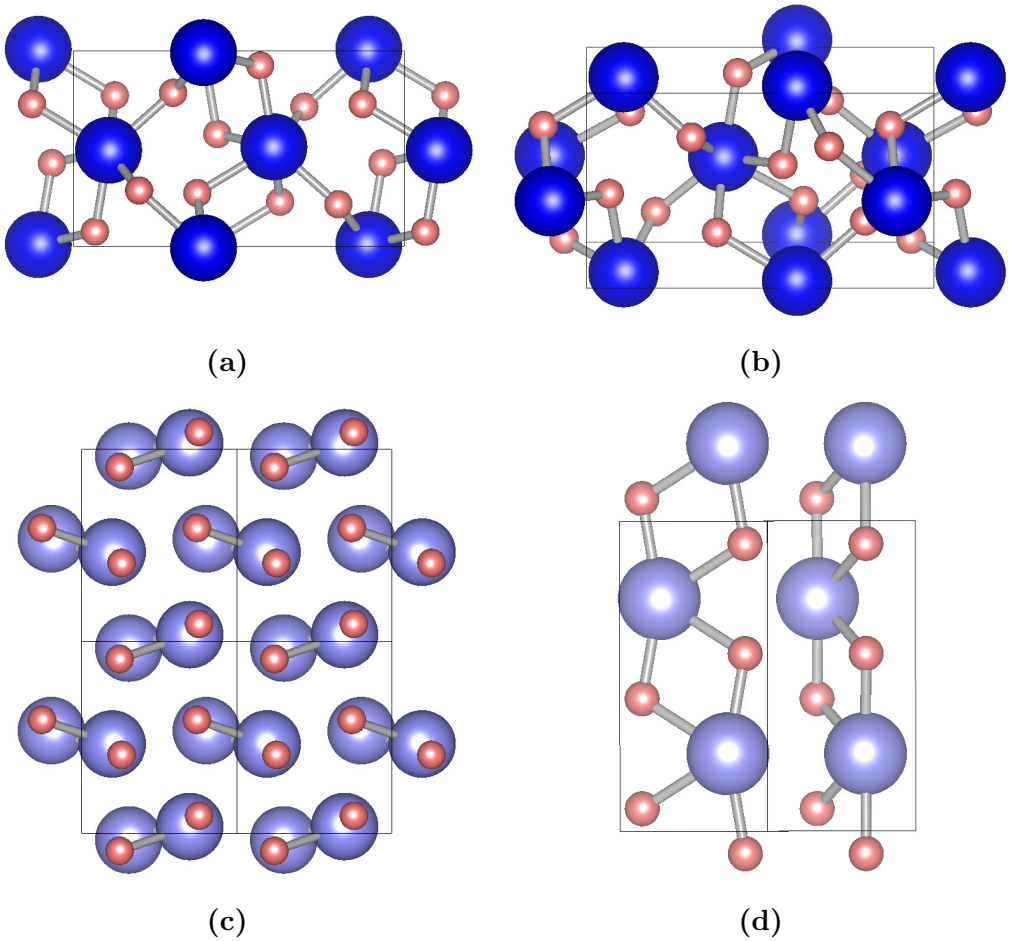

Fig. 4.15 Representative views of the structures of higher-pressure xenon oxides. (a), (b): XeO_3 with $P2_12_12_1$ symmetry (stable to decomposition at 150 and 200 GPa); (c), (d): XeO_2 with *Pnma* symmetry (stable to decomposition at 200 GPa).

The two new higher-pressure xenon oxides, XeO_3-$P2_12_12_1$ and XeO_2-*Pnma*, are depicted in Fig. 4.15. XeO_3 has a compact extended structure consisting of xenon atoms that bond to six oxygen atoms, each of which is shared with another xenon atom. XeO_2 consists of XeO_2 chains, with each xenon atom bonded to four oxygen atoms. Unlike in Xe_3O_2, in which the Xe atoms lie along straight lines, the Xe atoms zig-zag between two parallel lines along the direction of the chain. The XeO_2 chains form layers, with the chains in alternate layers offset from, and at an angle to, each other. The structural parameters for XeO_3 and XeO_2 are listed in Table 4.7.

Stoichiometry	Space group	Lattice parameters	Atomic co-ordinates
XeO_3	$P2_12_12_1$	a=7.654 Å b=3.289 Å c=4.528 Å	Xe (4a) 0.106 0.195 0.491 O (4a) 0.699 0.751 0.715 O (4a) 0.065 0.251 0.074 O (4a) 0.375 0.256 0.272
XeO_2	$Pnma$	a=3.561 Å b=5.799 Å c=4.405 Å	Xe (4c) 0.304 0.250 0.965 O (8d) 0.757 0.073 0.092

Table 4.7 Structural information (derived from DFT calculations) for the xenon oxides that become stable at higher pressures, XeO_3 and XeO_2. The structural parameters for XeO_3 are reported at 150 GPa, and for XeO_2 at 200 GPa. Atomic sites are given in terms of Wyckoff positions and in fractional co-ordinates.

To better understand the nature of the chemical bonding in the higher-pressure xenon oxides, several charge analyses were applied to the two phases: Mulliken population analysis, as well as the Bader and Hirshfeld charge analyses. The results of these analyses for XeO_3 and XeO_2 are displayed in Tables 4.8 and 4.9, respectively. The results of the charge analyses are consistent and suggest an ionicity of approximately 50% for the bonding in both oxides, with hybridisation of the Xe $5p$ and O $2p$ orbitals leading to a transfer of charge from the xenon atoms to the oxygen atoms, forming highly polar bonds, similar to those found in Xe_2O_5 and Xe_3O_2.

In the XeO_3 $P2_12_12_1$ phase, all xenon atoms assume a +6 oxidation state. This supports the structural interpretation of each xenon atom being bonded to six oxygen atoms, each of which are additionally bonded to a second xenon atom. The xenon atoms in the XeO_2 $Pnma$ phase each assume an oxidation state of +4, also supporting the structural interpretation of each xenon atom being bonded to four oxygen atoms, each of which are in turn bonded to a second xenon atom to form XeO_2 chains.

The electronic band structures along high-symmetry paths, along with electronic densities of states, are plotted for XeO_3 and XeO_2 in Fig. 4.16. The electronic band structures of the two structures are broadly similar to those of Xe_2O_5 and Xe_3O_2. PDOS calculations projected by angular momentum channel indicate that the states around the Fermi level are dominated by the p states of Xe and O, the conduction band portions of which have a width of approximately 13 eV in XeO_3 and 15 eV in XeO_2. Unoccupied p states extend immediately above the Fermi level, forming a conduction band with a width of approximately 6 eV in both structures. Directly below the p bands in energy are the s bands, which have a width of about 14 eV in both XeO_3

Species	Number	s	p	d	Charge (e)	Oxidation state
O1	4	1.91	5.05	0.00	-0.96	–2
O2	4	1.92	5.02	0.00	-0.94	–2
O3	4	1.91	5.04	0.00	-0.96	–2
Xe	4	1.92	3.22	10.00	2.86	+6

(a) Mulliken population analysis

Species	Number	Charge (e)	Oxidation state
O1	4	-0.27	–2
O2	4	-0.27	–2
O3	4	-0.26	–2
Xe	4	0.79	+6

(b) Hirshfeld charge analysis

Species	Number	Charge (e)	Oxidation state
O1	4	-1.02	–2
O2	4	-1.01	–2
O3	4	-0.99	–2
Xe	4	3.01	+6

(c) Bader charge analysis

Table 4.8 Atomic charges for XeO_3, with assigned oxidation states. Results for Mulliken population analysis (including populations for each angular momentum channel), Bader charge analysis and Hirshfeld charge analysis are presented.

Species	Number	s	p	d	Charge (e)	Oxidation state
O	8	1.90	5.18	0.00	-1.08	–2
Xe	4	1.94	3.89	10.00	2.16	+4

(a) Mulliken population analysis

Species	Number	Charge (e)	Oxidation state
O	8	-0.28	–2
Xe	4	0.57	+4

(b) Hirshfeld charge analysis

Species	Number	Charge (e)	Oxidation state
O	8	-1.10	–2
Xe	4	2.20	+4

(c) Bader charge analysis

Table 4.9 Atomic charges for XeO_2, with assigned oxidation states. Results for Mulliken population analysis (including populations for each angular momentum channel), Bader charge analysis and Hirshfeld charge analysis are presented.

and XeO_2. In both oxides, the almost-dispersionless d bands are some 30 eV below the bottom of the s bands.

The electronic band structure calculations using the PBE functional predict that XeO_3 is a semiconductor, with a minimum band gap of 0.31 eV and a minimum direct band gap of 0.66 eV at 150 GPa. Calculations at 100 and 200 eV indicate that this band gap opens up with increasing pressure, in contrast to the closing behaviour of the band gap of Xe_2O_5. XeO_2 has no band gap in this pressure range, with a greatly reduced eDoS around the Fermi level indicating that XeO_2 may be a semi-metal. However, the PBE functional is known to underestimate band gaps, and more accurate calculations may indicate that XeO_2 is a narrow band gap semiconductor, like Xe_3O_2.

Structure	Pressure (GPa)		
	100	150	200
XeO_3	0.26	0.31	0.64
XeO_2	0.00	0.00	0.00

(a) Minimum band gap

Structure	Pressure (GPa)		
	100	150	200
XeO_3	0.35	0.66	1.18
XeO_2	0.08	0.12	0.07

(b) Minimum direct band gap

Table 4.10 Minimum (thermal) and minimum direct (optical) band gaps in eV calculated with the PBE exchange-correlation functional for the high-pressure xenon oxides XeO_3 and XeO_2.

The experimental work that ran in parallel to the work of this thesis was not carried out at the higher pressures in the range 150–200 GPa that would be required to obtain experimental verification of these higher-pressure oxides, and of the continuing stability of Xe_2O_5 and Xe_3O_2. However, these higher-pressure predicted structures may be experimentally tested in the future.

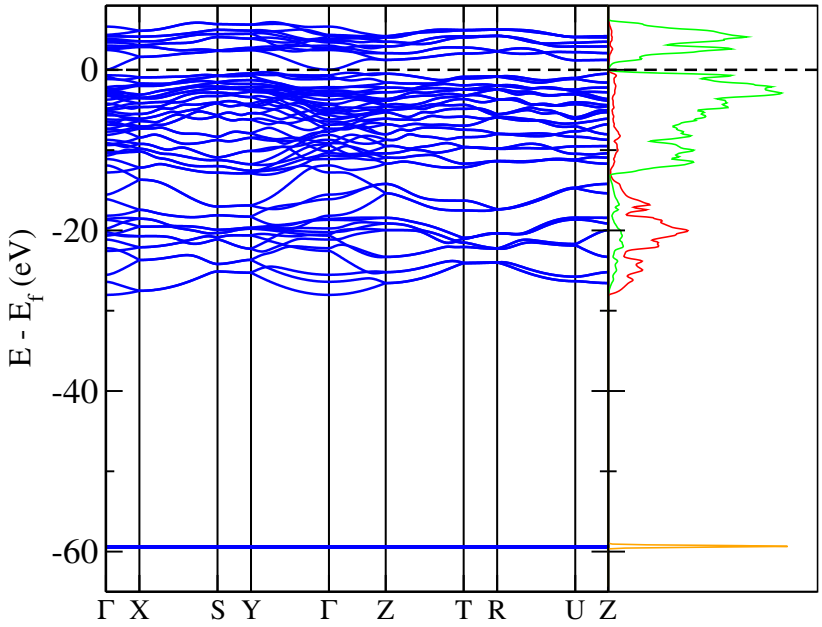

(a) XeO_3-$P2_12_12_1$

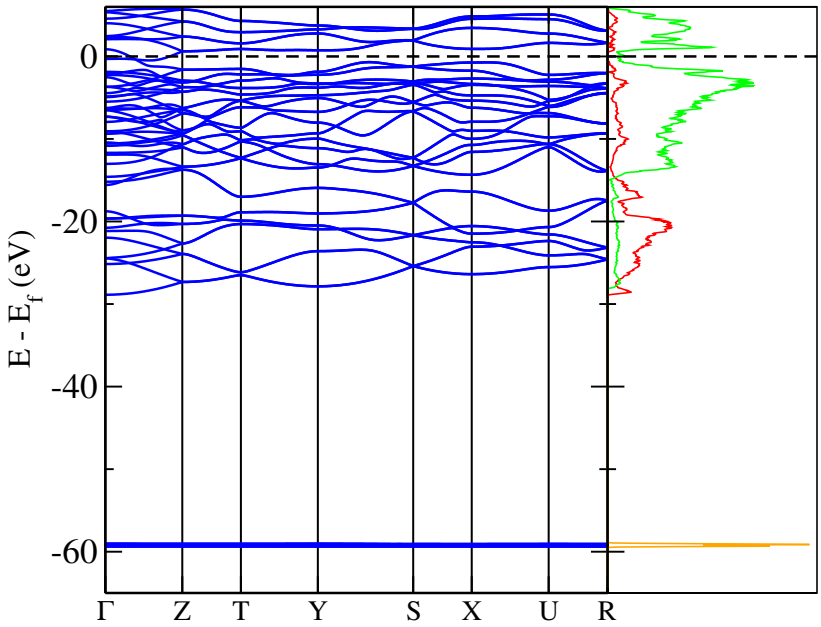

(b) XeO_2-*Pnma*

Fig. 4.16 Electronic band structures along high-symmetry paths and partial densities of electronic states (projected by angular momentum channel) for (a) XeO_3 with $P2_12_12_1$ symmetry and (b) XeO_2 with *Pnma* symmetry. The electronic bands are shown in blue and the Fermi level is shown as a horizontal black dashed line. The orange line shows the *d* electron density of states (rescaled to fit on the axes), the red shows the *s* density of states, and the green shows the *p* density of states. The *s* and *p* densities of states include contributions from both Xe and O.

4.4 Discussion

The evolution of the xenon-oxygen binary system with pressure is summarised by the convex hull of Fig. 4.17. There is a clear increase in the magnitude of the enthalpy of formation of stable xenon oxides as the external pressure increases. This can be readily understood in terms of the saving in volume that is achieved by oxides with Xe-O bonding compared with the pure elements. As the external pressure P increases, this saving in volume becomes more significant through the minimisation of the PV term in the enthalpy H (see equation (2.87)). This increasingly compensates for the Xe-O chemical bonding, which is less preferred energetically to isolated xenon atoms and diatomic oxygen molecules.

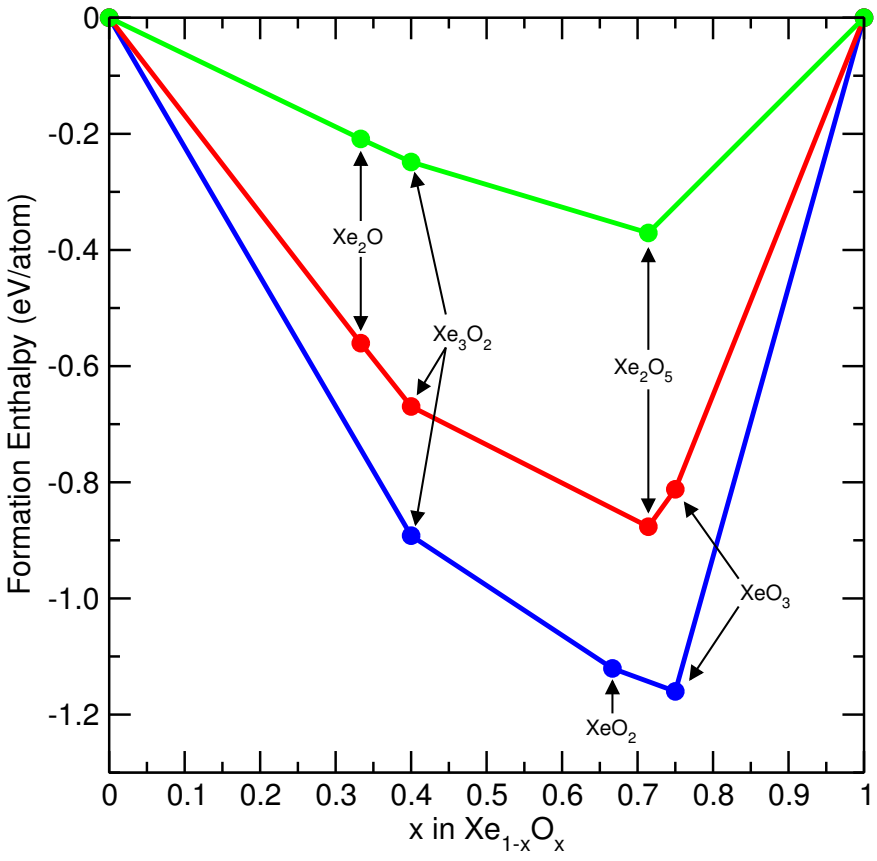

Fig. 4.17 Convex hull diagram for xenon oxides showing calculated enthalpies of formation per atom from the elements for the predicted stable phases. The enthalpy of formation per atom is given by equation (4.1). The three convex hulls shown are for 83 GPa (green), 150 GPa (red), and 200 GPa (blue). Each coloured circle denotes a structure that is stable against decomposition. The coloured lines joining the enthalpies of the stable structures denote the convex hull.

A comparison of the results of this theoretical study with the previous high-pressure *ab initio* studies of Zhu *et al.* [163] and Hermann and Schwerdtfeger [164] is presented in Fig. 4.18.

The substantial differences between the hull plots in Fig. 4.17 and those of Zhu *et al.* and Hermann and Schwerdtfger arise from two main sources. Firstly, this study searched over 17 stoichiometries to identify possible stable structures with up to 28 atoms in the primitive unit cell. This involved relaxing about 10^5 structures. In contrast, Zhu *et al.* considered only the four stoichiometries – XeO, XeO_2, XeO_3 and XeO_4 – consistent with all xenon atoms being in the oxidation states +2, +4, +6 and +8. For each of the structures predicted in that study, we have found either a lower-enthalpy structure, or that the structure was unstable to decomposition into compounds on the convex hull with other stoichiometries. The theoretical searches of Hermann and Schwerdtfeger were conducted over 8 stoichiometries, including Xe_3O_2, which they predicted to be stable, although they did not consider Xe_2O_5 as a stoichiometry [164]. Secondly, in the two previous theoretical studies, a pseudopotential was used to describe the Xe 4*d* orbitals. However, as discussed in section 4.2.2, although accurate at low pressures, at higher levels of compression this treatment is inaccurate for both xenon oxides and elemental xenon. Explicit treatment of the xenon 4*d* electrons results in a substantial re-ordering of relative stabilities, along with an overall increase in the magnitude of the enthalpy of formation from the elemental solids across the range of stoichiometries.

The newly predicted xenon oxides, together with the more accurate treatment of the semi-core 4*d* electrons of xenon, means that xenon oxides are predicted to become stable to decomposition into the elemental solids at a considerably lower pressure than previously thought. In their study, Zhu *et al.* predicted that no xenon oxide is stable against decomposition below 83 GPa [163], while Hermann and Schwerdtfeger predicted that 75 GPa is the lowest pressure at which xenon oxides may be stable.

In contrast, Xe_2O_5 is predicted to be stable to decomposition from 50 GPa, with Xe_2O predicted to be stable above 65 GPa and Xe_3O_2 above 66 GPa. XeO_3 and XeO_2 are predicted to be stable above 131 GPa and 186 GPa, respectively. At about 191 GPa, Xe_2O becomes unstable to decomposition into Xe_3O_2 and Xe, and above about 197 GPa, Xe_2O_5 becomes unstable to decomposition to XeO_2 and XeO_3. These ranges of stability are summarised in Table 4.11.

These pressures of initial stability were predicted using a combination of the linear projection of equation (2.90), along with explicit calculations at the pressures indicated by the application of this equation. A full structure search of the binary system was

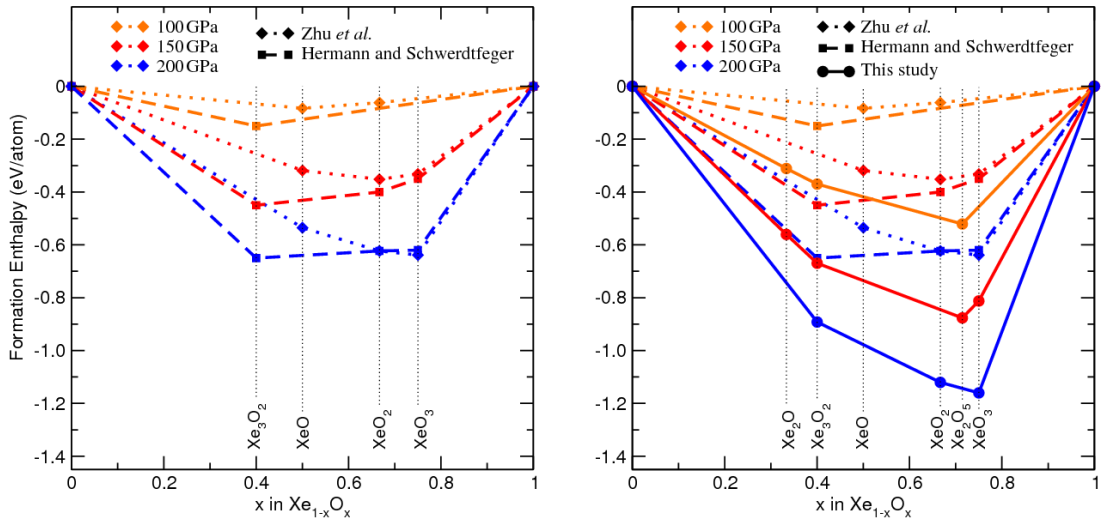

Fig. 4.18 Convex hull diagrams for xenon oxides showing the enthalpies of formation per atom from the elements calculated in Zhu *et al.* [163] and Hermann and Schwerdtfeger [164], and in the current work, at pressures of 100, 150 and 200 GPa. The different symbols and lines correspond to the different studies (dotted lines and diamonds: Zhu *et al.*, dashed lines and squares: Hermann and Schwerdtfeger, continuous lines and circles: the present work). The enthalpies calculated in Zhu *et al.* and Hermann and Schwerdtfeger agree with each other. The Xe_3O_2 and Xe_2O stoichiometries were considered by Hermann and Schwerdtfeger but not by Zhu *et al.* In contrast to the current work, neither Zhu *et al.* nor Hermann and Schwerdtfeger explicitly included the Xe 4*d* electrons in their calculations. Including the Xe 4*d* electrons results in lower enthalpies of formation (greater stability) for all xenon oxides and in changes to the relative stabilities of structures (see Fig. 4.2).

Stoichiometry	Space group	Pressure range (GPa)
Xe_2O_5	$P4/ncc$	50–197
Xe_3O_2	$Immm$	66–
Xe_2O	$C2/m$	65–191
XeO_3	$P2_12_12_1$	131–
XeO_2	$Pnma$	186–

Table 4.11 Summary of the predicted pressure ranges of stability to decomposition for xenon oxides. Open pressure ranges indicate that the structure is stable to at least 200 GPa.

not carried out at each pressure, so these pressures of initial stability serve as estimates rather than definitive predictions. Nevertheless it is clear that xenon oxides are stable at substantially lower pressures than has previously been predicted.

Experimentally, the Raman and XRD data show that the Xe_2O_5 crystal is metastable down to $\simeq$30 GPa, becoming amorphous at lower pressures. However, the Xe-O bonding can survive the complete release of pressure – a Raman mode with a frequency similar to metastable XeO_4 [191] or XeO_3 [192] was recorded at 0 GPa before the diamond anvil cell was opened. Xe_3O_2 was found to be metastable down to $\sim$38 GPa before amorphisation.

The requirement of laser heating in order to induce chemical reactions in the Xe-O_2 mixtures and the observation that Xe_2O_5 and Xe_3O_2 are metastable down to $\sim$30 GPa and $\sim$38 GPa, respectively, implies the existence of substantial kinetic barriers between phases.

4.5 Conclusions

Our searches for stable xenon oxides at high pressures have yielded a number of structures and have substantially enhanced our understanding of the Xe-O binary system in the pressure range 83–200 GPa. The DFT calculations, together with experimental evidence, indicates that xenon is much more reactive under pressure than was previously believed.

Working in collaboration with experimentalists, we have identified the structure of one xenon oxide, Xe_2O_5, and predicted the stability of a second structure, Xe_3O_2, which was subsequently confirmed by experiment. The band structures, bonding, phonon dispersion, thermal stability and Raman spectra of these two structures were calculated within DFT. Comparison of the theoretically predicted properties of both Xe_2O_5 and Xe_3O_2 with the experimental results for PXRD, XAS and Raman spectroscopy yields a good agreement.

Further xenon oxide structures, XeO_2 and XeO_3, are predicted to become stable to decomposition into their elements at higher pressures. These structures have also been characterised theoretically, but have yet to be searched for experimentally.

Our understanding of the chemistry of the binary xenon-oxygen system has been placed on a firmer foundation, advancing our knowledge of the chemistry of the xenon, a geologically intriguing element that was once believed to be entirely unreactive.

Chapter 5

Vibrational and Electronic Properties of the Thermoelectric Material SnSe

In this chapter, the promising thermoelectric material tin selenide (SnSe) is studied using first-principles methods. The Born-Oppenheimer energy surface around the nuclear equilibrium positions is mapped using density functional theory methods, and this mapping is used to calculate anharmonic nuclear wavefunctions. The thermal expansion is calculated using anharmonic methods and the vibrational and electronic band structures, important factors in the thermoelectric performance of a thermoelectric material, are renormalised with respect to vibrational effects.

5.1 Introduction

5.1.1 Thermoelectricity

The *thermoelectric effect* encompasses three related bulk effects: the *Seebeck*, *Peltier* and *Thomson* effects. Each effect is a manifestation of the different energies charge carriers possess in different materials when carrying a current, and are the results of this energy being transferred between the electrons and their environment.

The Seebeck effect was first observed by Thomas Seebeck in 1821 [193, 194], when he noted that if two different materials are joined and a temperature difference ΔT is applied between the junction of the materials and their ends, then a potential difference

ΔV is produced between the ends, with the potential difference being proportional to the temperature difference:

$$\Delta V = -S_{AB}\Delta T. \tag{5.1}$$

S_{AB} is known as the *relative* or *differential Seebeck coefficient*, or the *thermopower*, and is defined for a pair of joined materials labelled A and B as the difference between the *absolute* Seebeck coefficients of the materials, S_A and S_B:

$$S_{AB} = S_A - S_B. \tag{5.2}$$

The absolute Seebeck coefficients are intrinsic properties of a material, and can be thought of as the amount of entropy carried per unit charge by an electrical current running through the material [195]. It is clear that if the two materials that are joined together have the same Seebeck coefficient (e.g. because they are the same material), that the Seebeck effect will not be observed. The Seebeck effect was identified as a "thermoelectric" effect by Hans Christian Ørsted soon after its discovery [196].

The Peltier effect was first described shortly after the Seebeck effect, by Jean Peltier in 1834 [194, 197]. He observed that passing a current through a joined pair of different materials (a thermocouple) resulted in either heating or cooling at the junction, depending on the direction of the current, and the opposite – cooling or heating – at the two ends of the materials. The current also results in Joule heating, which can partially obscure the effect. The rate of heating or cooling, $\dot{q}$, is proportional to the current passed through the materials, I:

$$\dot{q} = \Pi_{AB} I, \tag{5.3}$$

Π_{AB} is the differential or relative *Peltier coefficient*, which is defined, in a similar manner to the differential Seebeck coefficient, as the difference between the (intrinsic) absolute Peltier coefficients of the two materials: $\Pi_{AB} = \Pi_A - \Pi_B$.

Despite the fact that the Seebeck and Peltier effects appear to be the inverse of each other, a connection between the two was not immediately recognised. The two effects were first connected by William Thomson (later, Lord Kelvin) [194, 198], who derived the Thomson relation between the Seebeck and Peltier coefficients for a pair of materials A and B:

$$\Pi_{AB} = S_{AB} T. \tag{5.4}$$

Thomson also described the third thermoelectric effect, known as the Thomson effect in his honour. This effect is observed when an electric current is passed through a homogeneous material, along which is a temperature gradient, as a result of which reversible heating or cooling occurs. The effect is related to the observation that the Seebeck coefficient is temperature dependent. The rate of heating, $\dot{q}$, is given by

$$\dot{q} = -\mathcal{K}\vec{J} \cdot \vec{\nabla} T, \tag{5.5}$$

where $\mathcal{K}$ is called the Thomson coefficient, and $\vec{J}$ is a current density. For two conductors, A and B, the difference in their Thomson coefficients is given by

$$\begin{aligned} \mathcal{K}_A - \mathcal{K}_B &= \frac{d\Pi_{AB}}{dT} - S_{AB} \\ &= T\frac{dS_{AB}}{dT}. \end{aligned} \tag{5.6}$$

Equation (5.6) constitutes the other Thomson relation; in the second line we have made use of equation (5.4). The Thomson relations of equations (5.4) and (5.6) relate the three thermoelectric coefficients, S, Π and $\mathcal{K}$, providing a clear connection between the three effects [194]. The relations allow us to characterise all three of the thermoelectric coefficients of a material by any one of them; typically, the Seebeck coefficient is used.

Although all pairs of materials with different thermoelectric coefficients may demonstrate thermoelectric effects, the term 'thermoelectric materials' is often used to refer to materials in which the effects are particularly prominent and may be utilised. Considerable effort has been put into developing devices that utilise thermoelectric effects, either to generate electricity (*thermoelectric generators, TEGs*), or to transfer heat (*thermoelectric refrigerators, TERs*). The basic design of these devices are discussed in the next subsection.

So far applications of such devices have been relatively limited. TEGs have been used in aerospace applications as radioisotope thermoelectric generators, and TERs have been used in small-scale cooling applications for which conventional cyclic vapour-compression refrigeration technologies cannot easily be scaled down [199, 200]. Small thermoelectric devices are currently available relatively cheaply, but the technology is scalable to a wide range of sizes [200]. Much research effort is being put in to improving the efficiency and power of thermoelectric devices to allow their use in a much wider range of situations, such as recovering energy from waste heat produced by car engines, providing a "green" way of producing electricity from the waste heat

that accounts for more than 60% of the energy use of the planet [201]. One estimate suggests that by the year 2026 the global market for TEGs will grow to over US$1 billion [202].

5.1.2 Thermoelectric Devices

The basic design of thermoelectric devices involves connecting two different materials, which have a large differential Seebeck or Peltier coefficient (TEGs and TERs respectively). In a TEG, a temperature difference is applied between the coupling point of the two materials and the two ends of the materials, across which an electrical circuit is completed in which a current results. In a TER, the setup is the same but an electrical current is passed through the circuit, resulting in transfer of thermal energy to or from the junction of the two materials, from or to the ends of the materials, depending on the direction of the current.

Generally, multiple such pairs of materials, known as *couples*, are connected together, in serial electrically, but in parallel thermally. Simplified designs of thermoelectric devices are shown in Fig. 5.1.

Most thermoelectric devices use a semiconducting material, with n and p doping used to produce oppositely-signed values of the Seebeck coefficient, helping to produce a large differential Seebeck coefficient [203]. In n-type semiconductors, the dominant charge carriers are electrons, whereas in p-type semiconductors, the dominant charge carriers are holes, i.e., the absence of an electron. An electrical conductor is used to join the different materials. More advanced designs for thermoelectric devices exist: for example, layers of thermoelectric devices such such as the one depicted in Fig. 5.1 may be stacked to form a 'cascade', in which the layers are connected thermally, but not electrically. Such devices can more efficiently deal with large differences in temperature between the heat source and the heat sink [194].

The discussion henceforth will focus upon thermoelectric generators, which are likely to find more areas of application in the future than thermoelectric refrigerators. A TEG is a form of heat engine, and so its efficiency is limited to that of a Carnot engine, η_{max}, given by

$$\begin{aligned} \eta_{\max} &= (T_1 - T_2)/T_1 \\ &= 1 - T_2/T_1, \end{aligned} \tag{5.7}$$

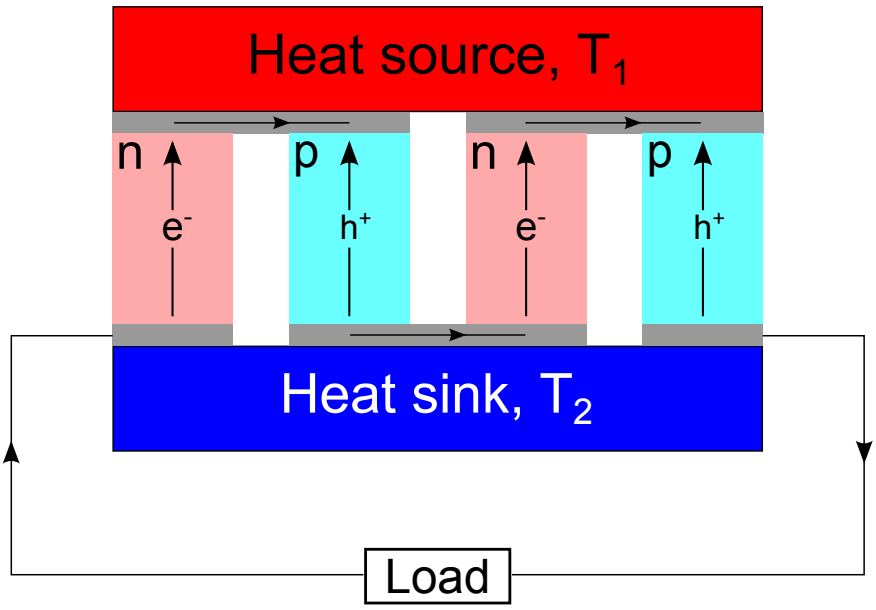

(a) Thermoelectric generator

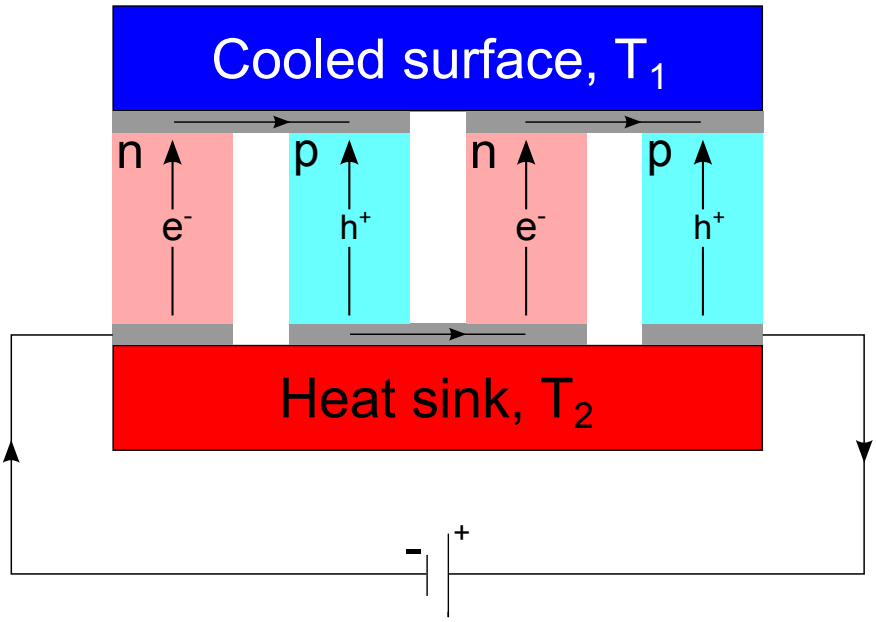

(b) Thermoelectric refrigerator

Fig. 5.1 Schematic representation of typical thermoelectric devices: (a) a thermoelectric generator; (b) a thermoelectric refrigerator. In the thermoelectric generator, a temperature gradient induces a potential difference, while in the refrigerator, an electrical current induces a temperature difference. Unlabelled arrows indicate the direction in which the electrons move through the circuit, rather than conventional current; n and p label respectively n-type and p-type semiconductors, and e^- and h^+ denote electrons and holes, respectively. In the generator, $T_1 > T_2$, while in the refrigerator, $T_1 < T_2$.

where T_1 and T_2 are the absolute temperatures of the heat source and heat sink, respectively (i.e., $T_1 > T_2$). However, real-world devices are not ideal Carnot engines, and the efficiency is reduced by irreversible heat losses [194]. A more realistic estimate of the efficiency η of a TEG is

$$\eta = \frac{(T_1 - T_2)}{T_1} \frac{\sqrt{1 + Z\bar{T}} - 1}{\sqrt{1 + Z\bar{T}} + T_2/T_1}, \tag{5.8}$$

where $\bar{T}$ is the mean temperature of the device. Here we make use of a dimensionless quantity called the *figure of merit*, $Z\bar{T}$ (henceforth referred to more simply as ZT), which is defined as

$$ZT = \frac{\sigma S^2 T}{\kappa}, \tag{5.9}$$

where σ is the electrical conductivity of the device, S its Seebeck coefficient, and κ its thermal conductivity [194]. The thermal conductivity can be broken down into electrical and lattice contributions, denoted κ_{el} and κ_L respectively:

$$\kappa = \kappa_{el} + \kappa_L. \tag{5.10}$$

It is clear from equation (5.8) that increasing the value of ZT makes the device more efficient. There is no upper limit to the value of ZT, but the best thermoelectric materials currently available yield a value of ZT on the order of unity. This means that current TEGs have a rather low efficiency. The value of ZT in most materials is highly temperature-dependent, so that most thermoelectric devices have a rather narrow range of operating temperatures over which they demonstrate good performance. An average ZT value of about 2 is thought to be required for TEGs to become viable for widespread use [200].

The quantity forming part of the numerator of equation (5.9) is known of the *power factor*, defined as

$$\text{Power factor} = \sigma S^2. \tag{5.11}$$

The power factor indicates the thermoelectric power that may be generated for a given ΔT by a TEG, and is the most important aspect of a thermoelectric device when generating as much electrical power as possible is more important than efficiency. The figure of merit is this power factor divided by the thermal conductivity, which indicates how rapidly thermal transport dissipates an initial temperature difference

across a device – such thermal dissipation constitutes a 'waste' of thermal energy from the point of view of a thermoelectric device.

Much of the effort that has been made over the last few decades to improve the performance of thermoelectric devices has been focussed on the choice of the thermoelectric materials used to create the devices [203]. We shall now review the progress that has been made in recent years to try to produce better thermoelectric materials through a range of means.

5.1.3 Thermoelectric Materials

Optimisation of the figure of merit ZT, defined in equation (5.9), is made difficult by the interrelationship between the thermopower S, the electrical conductivity σ and the electronic thermal conductivity κ_{el}. Attempts to optimise the power factor σS^2 usually result in a corresponding increase in κ_{el} that largely nullifies any potential improvement to ZT.

Although metals possess excellent electrical conductivity σ, the Wiederman-Franz law

$$\frac{\kappa_{el}}{\sigma} = LT, \tag{5.12}$$

where L is a material-specific constant, indicates that the impact of their high electrical conductivity on ZT is counteracted by the concomitant increase in the electrical contribution to the thermal contribution, which dominates the thermal conductivity in metals. Furthermore, metals possess relatively small Seebeck coefficients, on the order of a few μVK^{-1}, due to the continuous existence of conduction states around the Fermi level.

The very poor electrical conductivity of insulators also makes them unsuitable as thermoelectric materials. Instead, semiconductors have demonstrated the best performance as thermoelectric materials. Semiconductors are typically doped into n and p type semiconductors to maximise the differential Seebeck coefficient. Light doping levels maximise the Seebeck coefficient, but heavier doping is typically used to increase the electrical conductivity and so the power factor. This typically results in Seebeck coefficients of the order of hundreds of μVK^{-1}.

In addition to maximising the power factor, the figure of merit ZT can be optimised by minimising the thermal conductivity of the thermoelectric material. Although the electrical conductivity and the electrical contribution to the thermal conductivity are closely connected, in semiconductors a significant portion of the total thermal

conductivity comes from the lattice contribution to the thermal conductivity, κ_L. κ_L can be minimised more independently from σ and S than κ_{el}.

Three principle approaches have been used to try to minimise the lattice contribution to the thermal conductivity:

1) use of materials with heavy atoms, due to their low phonon frequencies;

2) use of materials with structural disorder, which acts to scatter phonons and reduce the thermal conductivity;

3) use of materials with strongly anharmonic phonons, which also act to increase phonon scattering and consequently reduce κ_L.

There now follows brief overviews outlining some of the most promising thermoelectric materials that have been studied to date.

Bismuth chalcogenides

Bismuth chalcogenides, with stoichiometries Bi_2X_3, where X is a chalcogenide, have demonstrated amongst the best bulk thermoelectric performances at room temperature, with values of ZT between 0.8 and 1.0, having been studied extensively since 1954 [204]. This makes these materials particularly viable for use in TERs, which operate at about room temperature. The most commonly used chalcogenides are tellurium and selenium.

The promising bulk properties of bismuth chalcogenides have lead to efforts to improve ZT by use of nanostructuring methods. In 2008, Cao *et al.* recorded a ZT value of 1.47 at about 438 K with a Bi_2Te_3/Sb_2Te_3 laminated nanostructure incorporating nanolayer thicknesses between 5 and 50 nm [205]. In the same year, Poudel *et al.* demonstrated a ZT value of about 1.4 for a nano-composite $Bi_xSb_{2-x}Te_3$ p-type bulk material at 373 K [206]. The following year, Zhao *et al.* synthesised a proof-of-concept Bi_2Te_3 structure using a variable-ratio mixture of coarse ($\sim 1\,\mu$m) and fine ($\sim$100 nm) grains, and achieved an optimised ZT ratio at a 3:2 fine:coarse grain ratio [207]. The addition of small amounts (0.2 vol%) of SiC nanoparticles to Bi_2Te_3 has been demonstrated to produce a 20% increase in the value of ZT, as well as improving the durability of the material [204]. Bi_2Te_3 nanowires have also been synthesised, but have so far demonstrated poorer performance than the bulk material [208].

Bulk Bi_2Te_3 has a small band gap of 0.13 eV, with the Fermi level close to the conduction band minimum, and so has a high intrinsic carrier concentration and a

significant minority carrier population when doping is light. Carrier concentrations are usually manipulated through the use of non-stoichiometric compositions (introducing excess bismuth during the fabrication process) or by dopant impurities such as halogens and group IV and V atoms [194].

Lead telluride

Lead telluride, PbTe, adopts a simple rocksalt structure yet has been demonstrated to possess excellent thermoelectric properties, due to strongly anharmonic phonons, which lead to high phonon scattering rates and consequently low lattice thermal conductivity. This phonon anharmonicity has been studied both experimentally and theoretically [209–213].

Improvements to the bulk thermoelectric performance of PbTe have been demonstrated through the use of band engineering and nanostructuring intended to reduce κ_L. In 2008, Heremans *et al.* demonstrated that thallium impurities can be used to distort the electronic density of states in PbTe, with the effect of approximately doubling the achievable value of ZT, reaching over 1.5 at 773 K in p-type PbTe [214]. The figure of merit is also improved through band convergence (increasing the electronic valley degeneracy), which occurs at temperatures above 700 K [215], and which can be promoted using nanostructuring [216].

Biswas *et al.* have demonstrated that a "panoscopic" approach to manipulating the small-scale structure of thermoelectric materials – that is, using different length scales of micro- and nano-structuring simultaneously [217] – can be used to produce a ZT value of 2.2 in p-type PbTe at 915 K [218].

Both Bi_2Te_3 and PbTe may be subject to thermal decomposition at the high temperatures they may be required to work at; furthermore, Bi, Pb and Te are all toxic. These factors limit the suitability of these two types of material for some operating conditions.

Silicon-germanium alloys

Alloys of silicon and germanium have been used as thermoelectric materials for several decades, notably in radioisotope thermoelectric generators in deep space missions, operating at temperatures between 600 and 1,000 K [219, 220]. Using two chemically similar elements minimises the scattering of charge carriers, which maintains a high electrical conductivity σ, with the thermal conductivity suppressed by the alloying.

ZT values have typically been around unity, but recently an n-type Si-Ge bulk alloy ($Si_{80}Ge_{20}$) featuring nanoscale grains has recorded a ZT value of 1.84 at 1073 K. Silicon nanowires have demonstrated a peak ZT value of about 1, at 200 K [221].

Complex crystalline structures

Thermoelectric materials featuring complex crystalline structures have shown good thermoelectric efficiency due to low lattice thermal conductivity. The most commonly-studied classes of these materials are types I and II clathrates and skutterudites. These materials contain large voids or 'cages', which can be partially occupied by loosely-bound atoms – typically rare-earth elements. These atoms undergo large-amplitude oscillations in an often highly anharmonic potential. These oscillations are often called 'rattler' modes, and they act to scatter phonons and so reduce thermal conductivity, but they do so without significantly affecting the electrical conductivity. This is a scenario that is sometimes referred to as 'phonon-glass electron-crystal' [222, 223]. A ZT value of 1.35 has been reported for the $Ba_8Ga_{16}Ge_{30}$ clathrate [224]. Skutterudite $CoSb_3$ with Ba, La and Yb fillers has demonstrated a ZT value of 1.7 at 850 K [225].

Oxide thermoelectrics

Several oxides have been investigated as potential thermoelectric materials, including layered cobaltates such as Na_xCoO_2 and $Ca_4Co_3O_9$. $Na_{0.8}CoO_2$ has been shown to have a thermal conductivity six times smaller than vacancy-free $NaCoO_2$, due to the sodium atoms moving in highly anharmonic 'rattler' modes within the vacancies [226], acting as a 'phonon-glass electron-crystal' type material [227]. Oxide thermoelectrics are an attractive proposition because they are more chemically stable in the high-temperature oxidising environments in which thermoelectric materials are often deployed than thermoelectrics such as bismuth chalcogenides and PbTe, and because they are mostly composed of abundant, light and non-toxic elements [228]. Other oxide thermoelectrics that have been studied include $Bi_2Sr_2Co_2O_9$, $CaMnO_3$ and $SrTiO_3$ based perovskites and doped ZnO [227, 229].

Half Heusler alloys

Half-Heusler alloys are a class of intermetallics with a particular periodic structure and stoichiometry XYZ, where X is a transition metal, a noble metal or a rare-earth element, Y is a transition metal or rare-earth element, and Z is a main group element. The most studied half-Heuslers are n-type XNiSn and p-type XCoSb, where X is one

of, or some combination of, the elements hafnium, zirconium and titanium [230]. Fu *et al.* have achieved a ZT of about 1.5 in p-type FeNbSb with Hf doping at 1,200 K [231]. The high Hf doping was found to both optimise the power factor and reduce κ_L through acting as phonon-scattering point defects.

Organic thermoelectrics

Some electrically-conductive organic materials have shown some promise as thermoelectrics, and have the potential to be both low cost and environmentally friendly. However, with demonstrated ZT values of under 0.5, more development is required for these types of materials to become competitive with other classes of thermoelectric materials. Small organic molecules and conducting polymers are of particular interest [232].

5.1.4 Tin Selenide

Tin Selenide, SnSe, is a stable crystalline solid that has demonstrated considerable promise as a thermoelectric material. At 1 atm, SnSe takes one of two crystal structures: a low-temperature *Pnma* phase and a high-temperature *Cmcm* phase, which possesses higher symmetry. The transition between the two phases is a reversible second-order process that occurs at about 750–800 K [233, 234]. Both the *Pnma* and *Cmcm* structures can be thought of as strong distortions of the rocksalt structure, and are both layered structures with a highly anisotropic crystal structure. The *Pnma* phase features an 'accordion-like' folding in one direction along the layers, which is not present in the *Cmcm* phase. The *Pnma* and *Cmcm* phases are depicted in Fig. 5.2. The *Cmcm* phase exists as a high-temperature 'averaged structure' over lower-energy *Pnma* structures [235].

The band gap of SnSe under ambient conditions, under which the *Pnma* structure is adopted, has been measured to be 0.86 eV [233]. Many-body perturbation calculations within the one-shot GW approximation carried out by Shi and Kioupakis were in good agreement with this experimental band gap, predicting an indirect band gap of 0.829 eV for the *Pnma* phase and a direct band gap of 0.464 eV for the *Cmcm* phase [234]. The same study found that in both phases there were multiple local band extrema lying near in energy to the global extrema, and that this had an impact on the thermoelectric properties of SnSe.

In a recent experimental study into undoped single-crystal SnSe, Zhao *et al.* reported an exceptionally high value of ZT, 2.6±0.3, at 923 K along one crystallographic

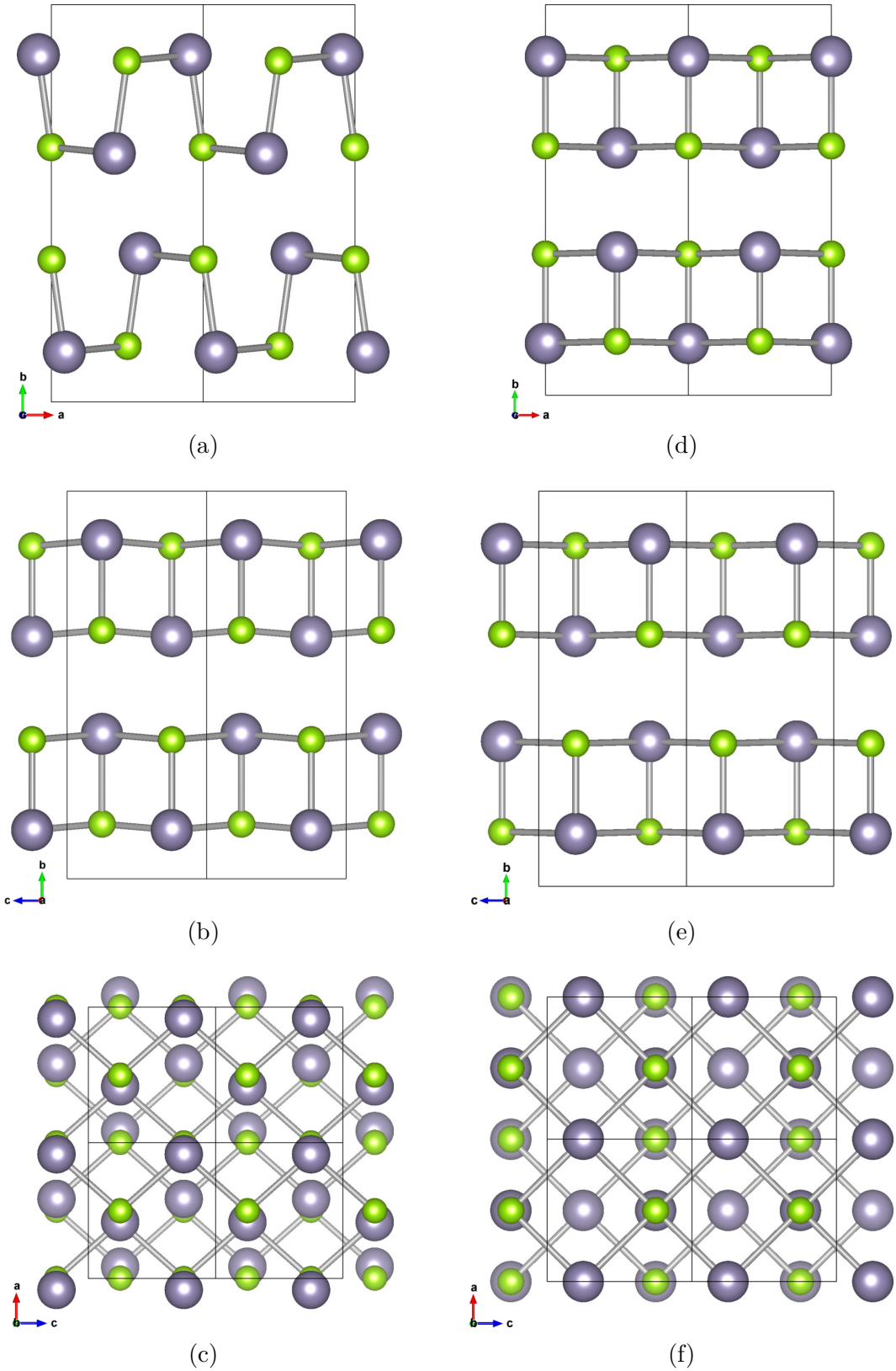

Fig. 5.2 Crystal structure of SnSe: (a)–(c) *Pnma* phase, (d)–(f) *Cmcm* phase. The *Cmcm* phase is shown in a conventional unit cell setting. The three figures for each phase are projections along (in sequence) the c, a and b crystallographic axes; the unit cell setting is such that the b axis is the inter-layer direction. Sn atoms are depicted in blue, Se atoms in green.

axis (the b axis of the room-temperature orthorhombic cell) [233]. This study reported a similarly large ZT of 2.3±0.3 along the c axis, but a very much lower ZT of 0.8±0.2 along the a axis. ZT was found to be strongly temperature dependent for all axes. There were low ZT values below about 700 K, above which ZT increased sharply with temperature, up to a peak value at about 923 K. At higher temperatures the ZT values begin to decrease. Zhao and his co-workers attributed the very high figure of merit to exceptionally low (0.23–0.34 $\mathrm{Wm^{-1}}$ at 973 K) lattice thermal conductivity in SnSe, which they in turn attributed to a high degree of anharmonicity in the structure. The achievement of a high ZT in a non-nanostructured material with a simple crystal structure has prompted a renewed consideration of materials with intrinsic anharmonicity as thermoelectric materials [236, 237].

Zhao *et al.* later hole-doped single-crystal SnSe with small amounts of Na, achieving a high ZT of 2.0 at 773 K [238]. Chen *et al.* doped polycrystalline SnSe with 1% of Ag, reaching a ZT value of 0.6 at 750 K [239]. Although much lower than the ZT achieved by Zhao *et al.*, this value is nonetheless double that achieved with undoped SnSe, indicating that polycrystalline SnSe has much poorer thermoelectric characteristics than single-crystal SnSe. This is supported by a study by Sassi *et al.*, who recorded a maximum ZT value of 0.5 at 823 K in polycrystalline p-type SnSe [240]. Serrano-Sánchez *et al.* nanostructured polycrystalline SnSe, which resulted in an exceptionally low thermal conductivity of less than $0.1\,\mathrm{Wm^{-1}K^{-1}}$ at room temperature and a high Seebeck coefficient of $668\,\mu\mathrm{VK^{-1}}$ at 380 K [241], suggesting that nanostructuring techniques in conjunction with the very high inherent anharmonicity in SnSe may result in very promising thermoelectric materials. The theoretical study of Shi and Kioupakis concluded that the optimum level of doping for thermoelectric performance in SnSe lies in the range of 10^{19} – $10^{20}\,\mathrm{cm^{-3}}$ [234], in agreement with the study of Chen *et al.* [239].

SnSe is attractive as a prospective thermoelectric materials partly because it is composed of elements of low toxicity that are abundant in the Earth, making it a viable material for widespread usage. However, some experiments [239, 240] suggest that the record-high thermoelectric performance of SnSe requires single crystals to realise, with polycrystalline SnSe demonstrating substantially poorer thermoelectric characteristics. This would be problematic for incorporating SnSe into practical thermoelectric devices, as single crystals tend to be brittle and expensive to synthesise.

A number of theoretical studies have been carried out to try to understand the origin of the extremely low thermal conductivity in SnSe. Carrete *et al.* investigated the thermal conductivity of the *Pnma* phase of SnSe using a Boltzmann transport

equation (BTE) formalism with second- and third-order force constants [242]. The results of this study were in agreement with the experimental work of Zhao *et al.*, in that they predicted SnSe to have an anisotropic but very low thermal conductivity. Li *et al.* carried out inelastic neutron scattering experiments on SnSe in conjunction with an *ab initio* study of the thermal conductivity of SnSe using the BTE formalism with up to third-order interatomic force constants, and mapping of certain phonon modes to study their anharmonicity [243]. Their results indicate that the phonons in SnSe demonstrate giant anharmonicity and are highly anisotropic, leading to very low thermal conductivity. They concluded that the origin of the anharmonicity is due to a resonant bonding network forming across the layers in SnSe between the Se $4p$-states and Sn $5s$ lone pairs [237]. Hong and Delaire reached similar conclusions, and determined that the lattice distortion between the *Cmcm* and *Pnma* phases is due to a Jahn-Teller instability in the resonant bonding network [244]. A similar resonant bonding network has been described in materials such as SnTe and Bi_2Te_3 [245]. Skelton *et al.* conducted a similar study, which concluded that the origin of the low high-temperature thermal conductivity was anharmonic damping, associated with modes relating to the phase transition, of the low-frequency phonon modes [235].

In this thesis, the structural, electronic and vibrational properties of SnSe are studied at a range of temperatures between 0 and 1,000 K. The VSCF methodology at the independent mode level of theory is used to calculate the thermal expansion, vibrational mode potentials and frequencies (including anharmonic effects), and the temperature dependence of the band gap, an important quantity for the thermoelectric properties of a material, for both *Pnma* and *Cmcm* phases of SnSe.

5.2 Methodology

Mapping of the Born-Oppenheimer energy surface for both the *Cmcm* and *Pnma* phases was carried out at the independent-mode level at several temperatures: 0, 300, 500, 800, 900 and 1000 K for the *Cmcm* phase, and 0, 300, 500 and 800 K for the *Pnma* phase.

The PBE *xc* functional [24] was used to describe the effects of exchange and correlation, along with a semi-empirical dispersion correction (SEDC) under the G06 scheme [36], which was intended to better describe inter-layer interactions. A variety of semi-

local *xc* functionals and SEDC schemes were tested, and this combination yielded the best match to the experimental lattice parameters, bearing in mind thermal expansion.

Pseudopotentials were generated on-the-fly using CASTEP. The Sn pseudopotential explicitly treated the $4d^{10}$, $5s^2$ and $5p^2$ electrons, with a core radius of 2.3 bohr, while the Se pseudopotential explicitly treated the $4s^2$ and $4p^4$ electrons, with a core radius of 1.6 bohr. Thermal (Fermi-Dirac) smearing was applied to the electronic states with the appropriate electronic temperature.

A plane-wave cutoff energy of 550 eV was used. The electronic Brillouin zone was sampled using a Monkhorst-Pack grid with a maximum spacing between k-points of $0.025\times2\pi$ Å^{-1}. These were tested for convergence such that the difference in energy at $q_{n,\Gamma} = \sqrt{\langle q_{n,\Gamma}^2 \rangle}$ between the highest- and lowest-frequency mode at the Γ point was converged for both phases to within 10^{-4} eV/atom. The calculated forces for these modes were converged to 1 meV/atom, and the stresses to within 10^{-2} GPa. At each nuclear configuration, the BO electronic energy was calculated to an SCF tolerance of 10^{-9} eV/atom, and the forces to within 10^{-5} eVÅ^{-1}.

A 5×5×5 grid size was used to sample the vibrational BZ of the *Cmcm* phase, and a 4×2×4 grid was used for the *Pnma* phase. This is equivalent to calculating the normal modes of 5×5×5 and 4×2×4 supercells for the *Cmcm* and *Pnma* phases, respectively.

At each temperature, the phonon normal modes under the harmonic approximation were calculated for each k-point on the vibrational grid using the finite-displacement method to calculate the harmonic phonon modes and frequencies. A Fourier interpolation scheme was used to obtain the matrix of force constants from the dynamical matrices at each calculated k-point. The matrix of force constants was then used to calculate harmonic properties such as vibrational densities of states by constructing the dynamical matrix at the required k-points in the vibrational BZ.

The BO surface was then mapped along each normal mode independently, with 10 evenly-spaced sampling points being taken each side of the static lattice configuration for the *Cmcm* structure, and 8 for the *Pnma* structure. Cubic splines were used to fit a curve to the BO surfaces. These potentials were used as inputs to the programs implementing the VSCF method, which yielded the anharmonic wavefunctions for each mode and k-point. The maximum mapping amplitude for the initial mapping at each temperature was chosen to be $5\times\sqrt{\langle q_{n,\vec{k}} \rangle}$ for each mode and k-point. As for some normal modes – especially soft modes – the calculated harmonic frequency was a poor descriptor of the shape of the BO surface, in subsequent iterations of mapping

each maximum normal mode amplitude was chosen to ensure that the anharmonic probability density became negligible by 80% of the maximum mapping amplitude.

In the VSCF calculations, numerical integrals were calculated using 3,000 integration points. The number of harmonic basis functions and anharmonic states to calculate were converged with respect to the anharmonic free energy, and ranged from 30 at 0 K to 140 at 1,000 K.

Stresses and band gaps were also calculated for each mapped atomic configuration, and the differences in stress and band gap between the static lattice structure and each configuration were fitted with a cubic spline. The stresses and band gaps were then renormalised using the anharmonic wavefunction from the VSCF procedure under the independent-mode approximation. The renormalised stresses were used to re-optimise the static lattice structures at each temperature, in an iterative procedure that continued until lattice parameters were converged to within 10^{-2}Å ($2\times\ 10^{-2}$ for the a axis of the $Pnma$ phase at 800 K).

The anharmonic energy eigenvalues were used to construct the anharmonic vibrational partition function, $\mathcal{Z}_{anh}$, for each mode. $\mathcal{Z}_{anh}$ is defined as

$$\mathcal{Z}_{anh} = \sum_{i=0}^{N_s-1} \exp(-\beta E_i), \tag{5.13}$$

where E_i are the anharmonic energy eigenvalues for the mode and k-point and N_s is the total number of anharmonic states calculated. The partition function was used to calculate the individual-mode vibrational free energy, $F_{vib} = -k_B T \ln \mathcal{Z}_{anh}$. The individual mode partition functions were also used to calculate temperature-dependent effective harmonic frequencies $\omega_{\text{eff}}(T)$ for each mode and k-point, determined such the harmonic partition function $\mathcal{Z}_{harm}$ of the effective frequency was equal to the anharmonic partition function $\mathcal{Z}_{anh}$ for each normal mode:

$$\begin{aligned} \mathcal{Z}_{harm}(\omega, \beta) &= \frac{1}{2\sinh\left(\frac{1}{2}\beta\omega\right)} \\ &= \mathcal{Z}_{anh}(\beta), \end{aligned} \tag{5.14}$$

which yields

$$\omega_{\text{eff}}(T) = 2k_B T \sinh^{-1}\left(\frac{1}{2\mathcal{Z}_{anh}}\right). \tag{5.15}$$

Note that $\omega_{\text{eff}}(T=0) = 2E_0$, where E_0 is the ground-state anharmonic energy for the mode and k-point.

These effective frequencies were recombined with the eigenvectors of the harmonic dynamical matrices to form effective dynamical matrices, which were used to calculate renormalised vibrational densities of state.

The calculations on the *Cmcm* phase utilised the four-atom primitive cell, rather than the 8 atom conventional cell, as it was more computationally efficient. The *Cmcm* primitive cell is shown in comparison to the conventional cell in Fig. 5.3. The lattice parameters and atomic positions for the calculated static lattice structures for the *Pnma* and *Cmcm* phases are shown in Table 5.1.

Phase	Lattice parameters	Atomic positions
Pnma	a=4.300 Å b=11.613 Å c=4.191 Å	Sn (4c) 0.057 0.128 0.250 Se (4c) 0.498 0.861 0.250
Cmcm	a=4.201 Å b=11.643 Å c=4.222 Å	Sn (4c) 0.000 0.870 0.250 Se (4c) 0.000 0.638 0.250

Table 5.1 Initial static lattice parameters and atomic positions at zero stress and zero temperature, prior to the application of vibrational stress, for the *Pnma* and *Cmcm* phases of SnSe. The *Cmcm* conventional cell is described here, but the primitive cell was used in the calculations.

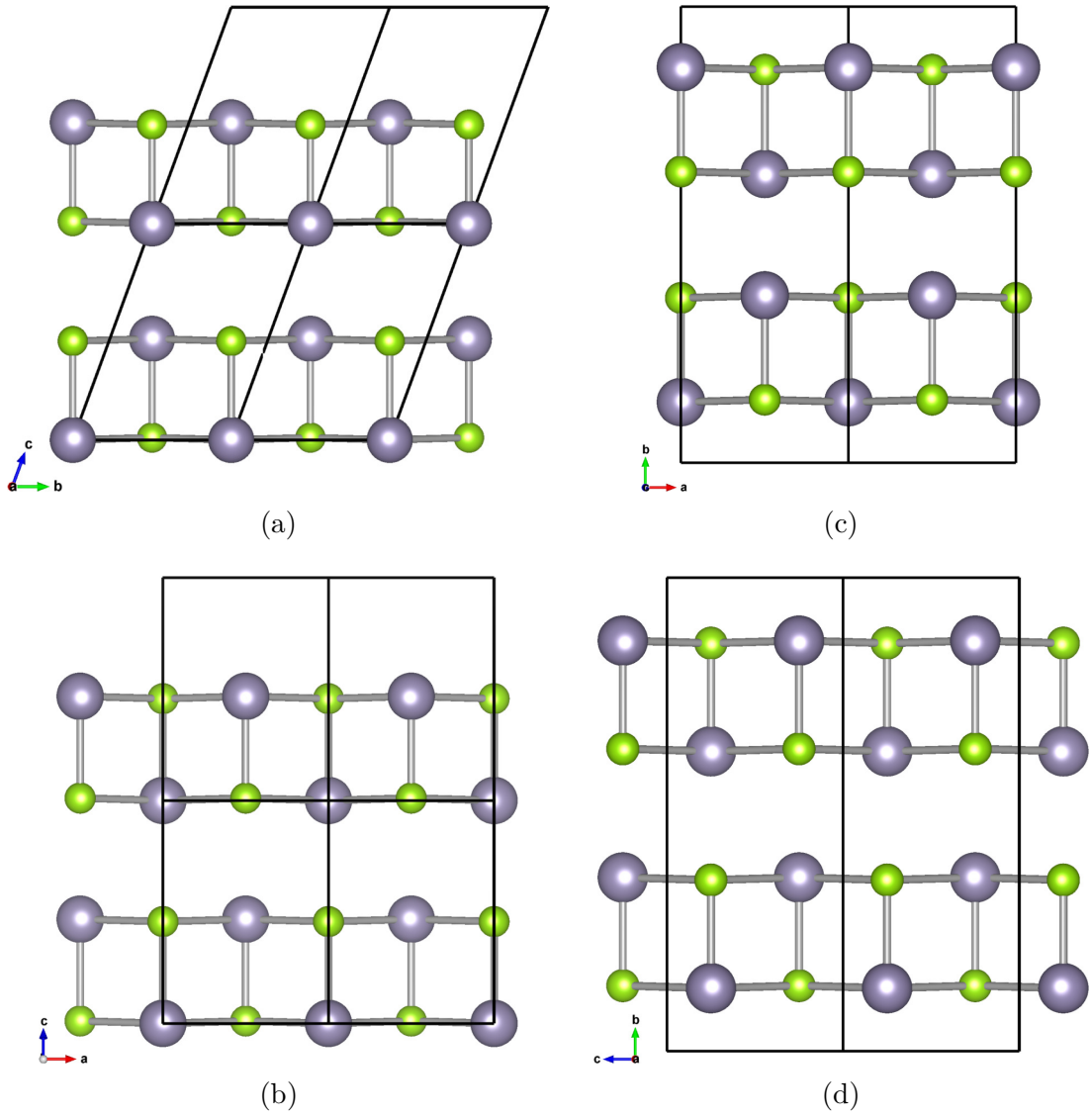

Fig. 5.3 Primitive and conventional cells for the *Cmcm* phase of SnSe along axes parallel to the layers. (a) and (b) depict the primitive cell settings, (c) and (d) the equivalent conventional cell setting. The black lines denote the unit cell boundaries.

5.3 Results

5.3.1 Thermal Expansion

The *Cmcm* phase of SnSe was expanded using the iterative procedure described in the Methodology section at 0, 300, 500, 800, 900 and 1000 K; the *Pnma* phase was expanded at temperatures of 0, 300, 500 and 800 K. The lattice parameters and unit cell volumes (in the case of the *Cmcm* phase, converted to the conventional cell setting) at these temperatures are plotted as blue circles in Figs 5.4 and 5.5 for the *Cmcm* and *Pnma* phases, respectively. A smoothed cubic spline fit was also applied to the data (plotted as blue lines), to generate a best-fit line in the presence of noise arising from the uncertainties in the data due to the iterative expansion process. Equation (2.153) and its linear equivalents were used to calculate the coefficients of expansion as functions of temperature, plotted in the insets to the figures.

At 0 K, the calculated unit cell volume of the *Pnma* phase is greater than that of the *Cmcm* phase, but the calculated unit cell volumes of the two phases converge at about 800 K, which is around the phase transition temperature [233].

Each lattice parameter in the *Cmcm* phase shows comparable expansion behaviour with temperature: an initially low rate of expansion, growing rapidly between 800 and 900 K, and then dropping rapidly as the temperature approaches 1000 K. The a and c lattice parameters have approximately twice the coefficient of expansion as the b lattice parameter. A very minor 'hump' in the coefficient of expansion at around 500 K is likely just an artefact of the uncertainties in the data.

By contrast, the a and c lattice parameters show different expansion behaviours as a function of temperature in the *Pnma* phase, with the a parameter showing more rapid expansion than the c parameter at low temperatures, but with this behaviour inverting at higher temperatures. As the temperature approaches 800 K, the difference between the a and c parameters reduces. The expansion of the b parameter is similar to the c parameter – smaller at lower temperatures, and increasing above 500 K. The overall volume expansion of the *Pnma* phase is fairly constant with temperature, and is in general smaller than the expansion of the unit cell volume of the *Cmcm* phase.

The appropriate thermally-expanded unit cells are used in the temperature-dependent calculations in the subsequent sections.

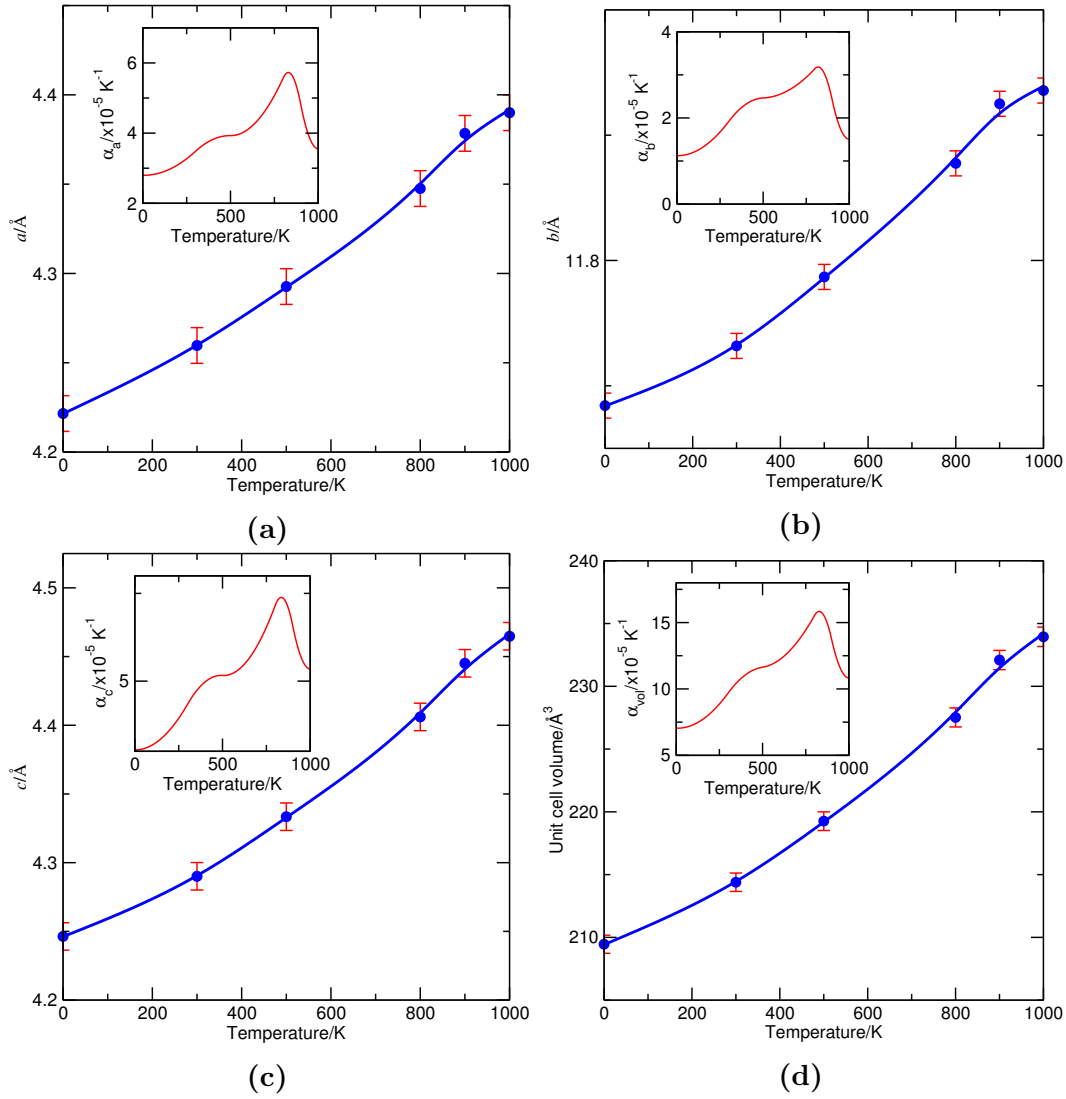

Fig. 5.4 Lattice parameters and unit cell volumes as a function of temperature for the *Cmcm* phase of SnSe, including error bars. (a), (b) and (c): lattice parameters for the a, b and c parameters, respectively; (d): unit cell volume. Insets show the coefficients of thermal expansion for the relevant quantities. Lattice parameters and volumes for the *Cmcm* phase are given in terms of the conventional (8 atom) unit cell. Calculated data points are represented by blue circles, while the blue line represents a smoothed cubic spline fit to these data points. The coefficients of expansion are calculated through numerical differentiation of the fitted data.

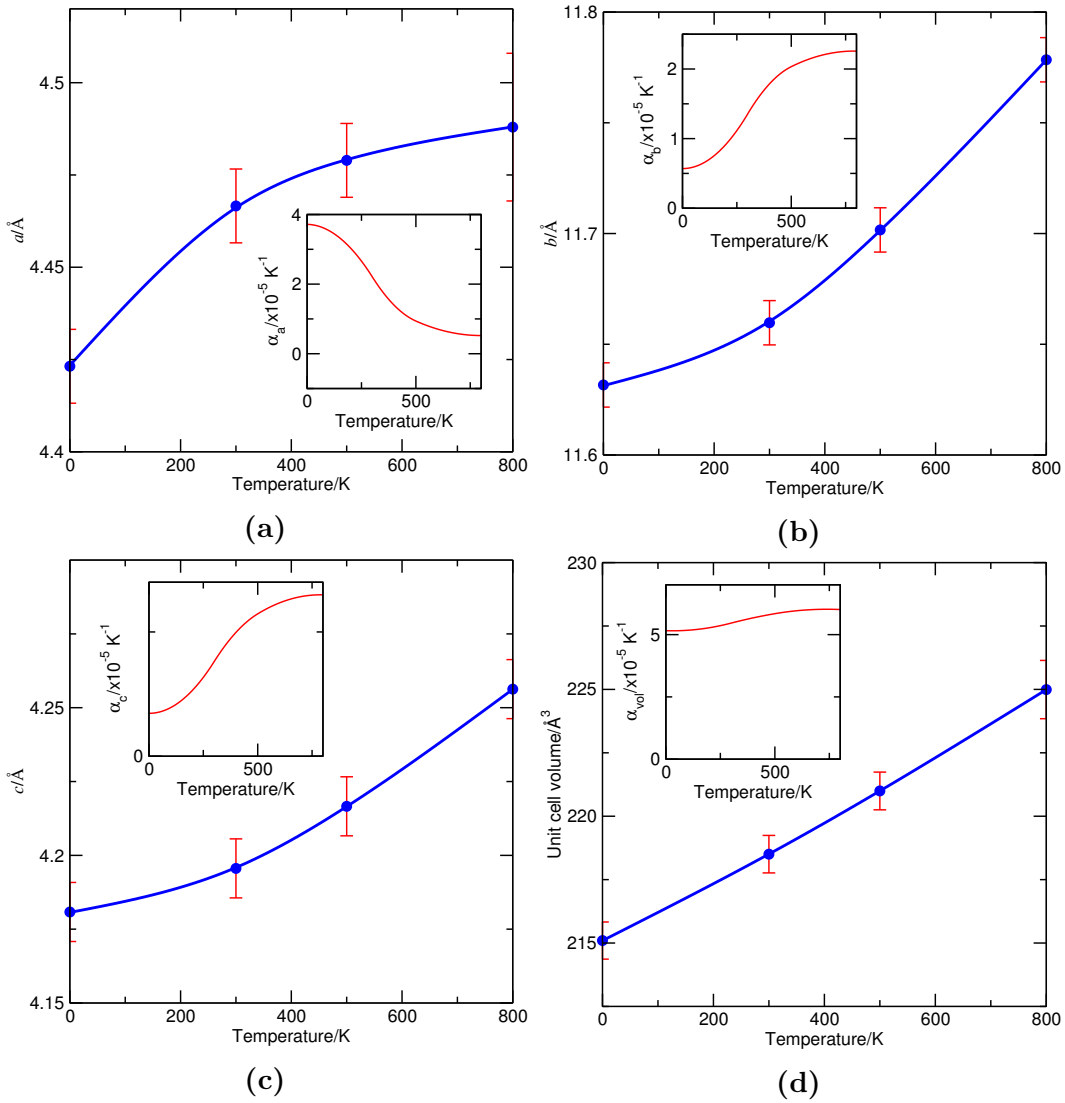

Fig. 5.5 Lattice parameters and unit cell volumes as a function of temperature for the *Pnma* phase of SnSe, including error bars. (a), (b) and (c): lattice parameters for the a, b and c parameters, respectively; (d): unit cell volume. Insets show the coefficients of thermal expansion for the relevant quantities. Calculated data points are represented by blue circles, while the blue line represents a smoothed cubic spline fit to these data. The coefficients of expansion are calculated through numerical differentiation of the fitted data.

5.3.2 Free Energies

The total Gibbs free energies per unit cell (including thermal expansion and vibrational effects) for the *Cmcm* and *Pnma* phases are plotted as a function of temperature in Fig. 5.6. As expected, the free energy of the *Pnma* phase is lower at low temperatures, and the free energy of the *Cmcm* phase is lower at high temperatures, consistent with the observed phase transition. In these calculations, the transition is expected to occur at about 410 K, lower than the experimentally-observed value of 750–800 K [233, 234]. The discrepancy may be due to coupled-mode effects. The anharmonic calculations are closer to the experimental observation than harmonic calculations, which predict a transition at about 250 K.

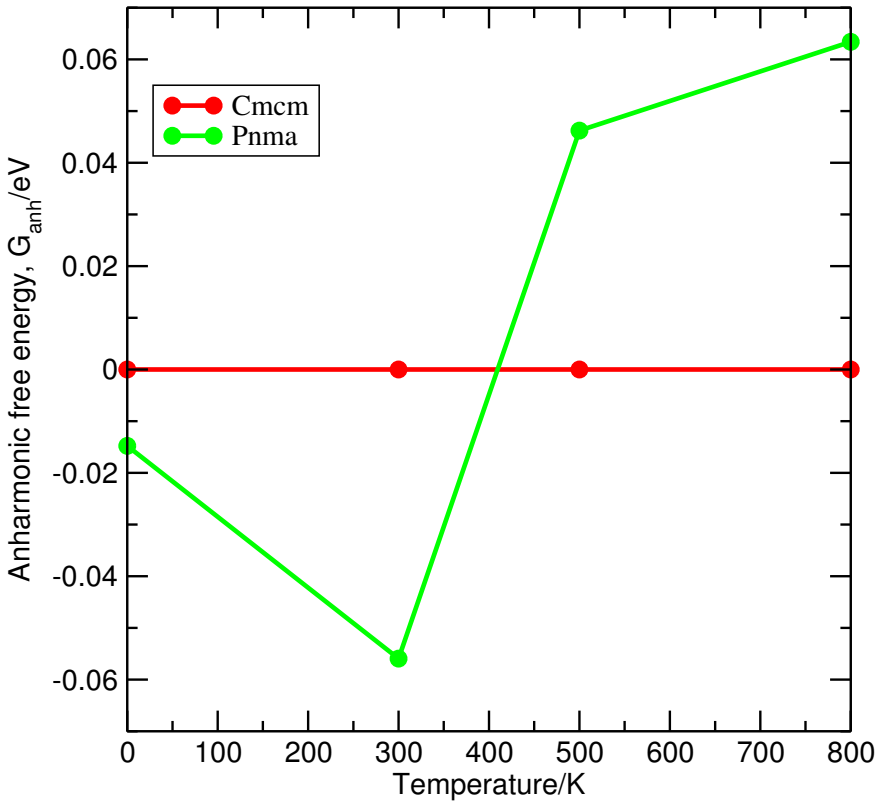

Fig. 5.6 Total Gibbs free energies of the *Cmcm* and *Pnma* phases of SnSe, including vibrational effects, plotted in red and green, respectively. The energies are plotted relative to the free energy of the *Cmcm* phase at each temperature. Energies are given per conventional unit cell. Note the crossover in the free energies of the phases at about 410 K.

5.3.3 Vibrational Properties

Vibrational densities of states (DoS) for both the *Pnma* and *Cmcm* phases were calculated at each temperature using both the harmonic approximation, as implemented in the LTE code, and the anharmonic renormalisation scheme described in the Methodology section. Some of these densities of states are shown in Fig. 5.7: illustrative vibrational densities of states using both schemes are shown for the *Cmcm* phase at 900 K. Additionally, the temperature evolution of the vibrational DoS is shown between 500 and 800 K for the *Pnma* phase using the harmonic approximation, and between 800 and 1000 K for the *Cmcm* phase using the renormalisation scheme, which is used particularly to deal with the soft phonon modes found in the *Cmcm* structure.

The vibrational DoS of the *Cmcm* phase at 900 K (Fig. 5.7a) contains a sharp peak of high-frequency modes between 5 and 6 THz, corresponding to vibrational modes involving stretches of the Se-Sn bonds perpendicular to the layers. These bonds are the shortest found in the structure, suggesting that they are particularly strong. The strength of these perpendicular Sn-Se bonds is also suggested by a charge density analysis, which indicates a particularly high electron density over the length of the bonds. This is consistent with a high vibrational frequency for stretches of these bonds.

The application of the anharmonic renormalisation scheme does not have a particularly strong effect across much of the vibrational spectrum in *Cmcm*, but it does increase the vibrational DoS over low-frequency modes between about 1 and 2 THz. This can be traced to the soft modes in the *Cmcm* structure, which do not appear in the spectrum under the HA, but which have a positive frequency under the renormalisation scheme.

As can be seen in Fig. 5.7b, an increase in temperature from 800 to 1000 K results in a small reduction in vibrational frequencies across much of the frequency range in the *Cmcm* phase, with the exception of the high-frequency modes above 5 THz. This can be explained by the thermal expansion stretching and so weakening the interatomic bonds in the structure, although the strong across-layer Sn-Se bonds are largely unaffected by this.

The *Pnma* vibrational DoS depicted in Fig. 5.7c features two distinct regions: a lower-frequency region up to about 3 THz, and a higher-frequency region above 3 THz, with a substantial reduction in the vibrational DoS inbetween the two regions. The higher-frequency region corresponds to Se-Sn bond stretches across the width of the layers, The lower-symmetry accordion-like folding in the *Pnma* structure results in a broader range of frequencies for these modes than in the *Cmcm* structure. The lower-

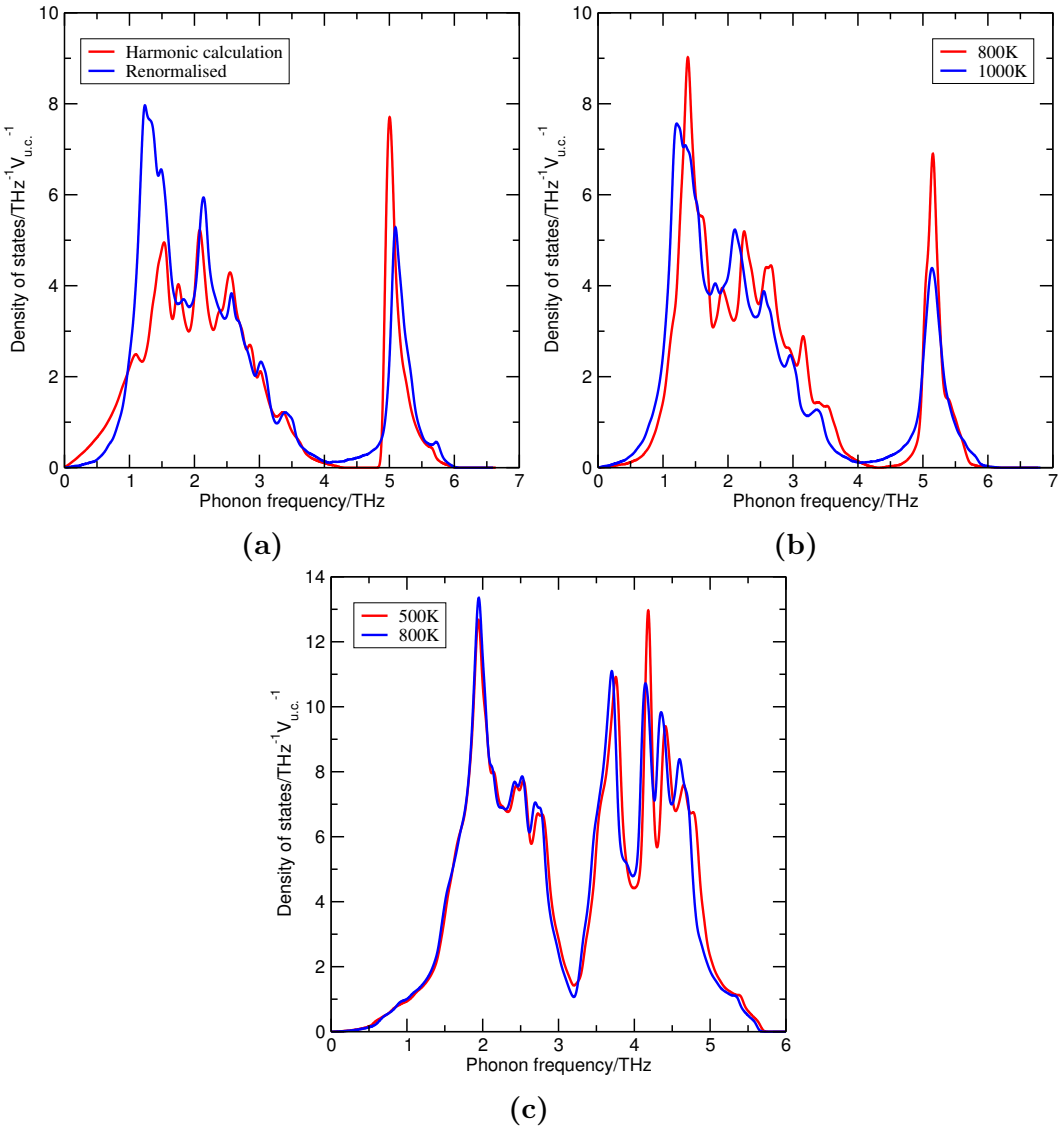

Fig. 5.7 Vibrational properties of SnSe. (a) and (b): *Cmcm* phase; (c): *Pnma* phase. (a): vibrational densities of states at 900 K calculated using the harmonic approximation and the anharmonic renormalisation scheme described in the Methodology section. (b): anharmonic renormalised vibrational density of states at temperatures of 800 and 1000 K. (c): vibrational density of states at 500 and 800 K calculated using the harmonic approximation.

frequency region is comprised of the other vibrational modes. Between 500 and 800 K, there is again a small shift across the frequency range to lower vibrational frequencies, which can be explained by the thermal expansion stretching and slightly weakening interatomic bonds.

5.3.4 Band Gaps

At each calculated temperature, the total renormalised minimum band gap of the *Pnma* and *Cmcm* phases was calculated as the sum of the equilibrium-configuration band gap for the thermally-expanded unit cell and the vibrational renormalisation to this equilibrium band gap. The temperature dependence of the equilibrium-configuration band gap, the vibrational renormalisation to this gap and the resulting overall band gap are plotted for *Pnma* and *Cmcm* in Figs 5.8a and 5.8b, respectively. The calculated unexpanded static-lattice band gap for each structure is also shown, for comparison. The static-lattice band structures for the *Pnma* and *Cmcm* phase are shown in Fig. 5.9, for reference.

From a 0 K band gap very close to the calculated static-lattice value of 0.77 eV, the band gap in *Pnma* initially decreases by 0.15 eV on temperature increase, up to 300 K, as the equilibrium-value band gap decreases slightly and a substantial vibrational renormalisation takes effect. On temperature increase above 300 K, the effect of thermal expansion begins to increase the equilibrium-value band gap, almost cancelling out the increase in the magnitude of the vibrational renormalisation, so that the total band gap decreases only slightly between 300 and 800 K, down to a value of 0.57 eV at 800 K.

In the *Cmcm* phase, the total band gap is initially 0.27 eV at 0 K, above the calculated static-lattice value of 0.22 eV. As the temperature increases, there is initially little change to the total band gap, up to about 800 K, as the effects of an increasing equilibrium band gap and an increasingly negative vibrational renormalisation largely cancel each other out. Above 800 K, however, the vibrational renormalisation increases in magnitude at a faster rate than the equilibrium lattice value increases, resulting in a decrease in the total band gap down to 0.19 eV at 900 K and 0.16 eV at 1000 K, both values being smaller than the static lattice band gap. At 800 K, the band gap of the *Cmcm* phase (0.24 eV) is significantly smaller than the band gap of the *Pnma* phase (0.57 eV), consistent with experimental observation. The size of the band gap in the *Cmcm* phase is important in determining the electronic and thermoelectric properties of SnSe at high temperatures.

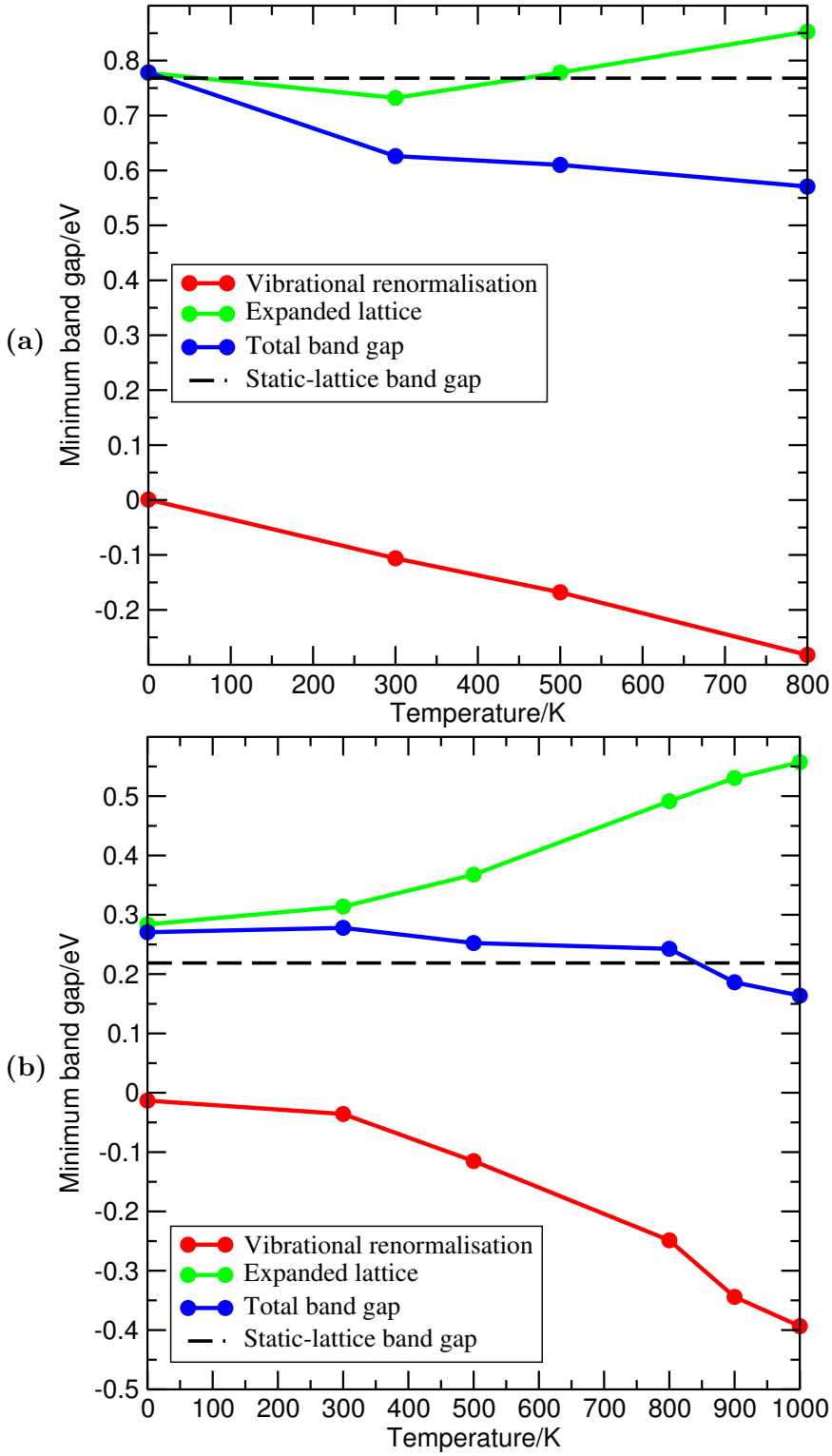

Fig. 5.8 Temperature dependence of band gaps in SnSe: (a) *Pnma* phase, (b) *Cmcm* phase. Band gaps are calculated using the PBE [24] *xc* functional. The expanded static-lattice band gap, the vibrational renormalisation to this gap, and the resulting total band gap are plotted in green, red and blue, respectively. The unexpanded static-lattice band gaps are shown as a black dashed line, for reference.

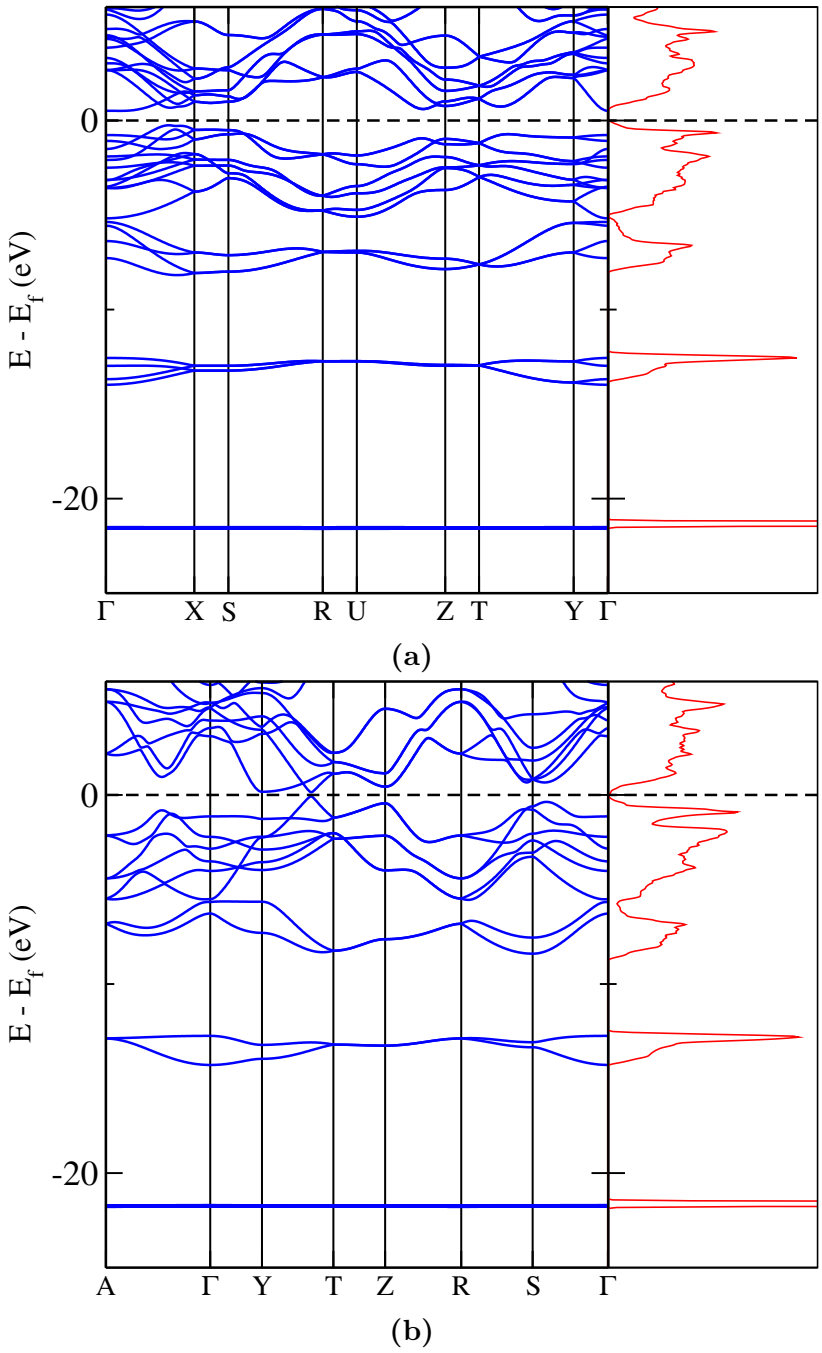

Fig. 5.9 Band structures along a high-symmetry path in the BZ of the *Pnma* and *Cmcm* phases of SnSe: (a): *Pnma*; (b): *Cmcm*. The electronic densities of states are shown alongside. Note the relatively small minimum band gaps for both structures, especially the *Cmcm* structure.

5.3.5 Vibrational Modes

Analysis of the vibrational modes of the *Cmcm* and *Pnma* phases confirms that they possess anharmonic phonon modes. Three BO potentials for modes at the Γ point in the *Cmcm* structure at 900 K are plotted in Fig. 5.10. These modes are selected to illustrate the three principal 'classes' of anharmonic modes found in the *Cmcm* phase: 'double-well', 'quartic' and 'cubic'. On the left hand side of the figure, the mapped and spline-fitted BO potentials are plotted, along with the BO potentials implied under the harmonic approximation. Also plotted on the same graph are the probability densities corresponding to both the anharmonic and harmonic energy surfaces. On the right hand side of the figure are displayed the atomic displacement patterns corresponding to each mode.

The first mode, depicted in Figs 5.10a and 5.10b, is a soft mode forming a double-well potential. This mode corresponds to a displacement of atoms in the planar direction, in the direction of a more 'accordion-like' folded structure, akin to the *Pnma* structure (though not actually the *Pnma* structure itself). As can be seen from the anharmonic probability density, there is a significant probability density across both wells, and in the central $q = 0$ configuration. This indicates that the *Cmcm* phase is a "thermally-averaged" structure, with an *average* atomic configuration (given by the configuration at $q = 0$) that is not *statically* stable. The negative-energy potential curve implied by the harmonic approximation is clearly inadequate to describing the atomic motion in this mode. The soft modes were determined to make a significant contribution to the vibrationally renormalised stress tensor and so to thermal expansion in the *Cmcm* phase.

The second mode, depicted in Figs 5.10c and 5.10d, is a symmetric 'quartic-type' anharmonicity. The mapped BO surface agrees well with the harmonic surface close to $q = 0$, but diverges from the harmonic curve further away from the equilibrium position. This results in an anharmonic probability density that is more tightly localised around $q = 0$ than the harmonic density. This mode arises from a symmetric alternating stretch of the Sn-Se bonds across the width of the layers.

The third mode, depicted in Figs 5.10e and 5.10f, is an asymmetric 'cubic-type' mode. For $q > 0$, the atoms at the top and bottom of each layer are pulled apart, and so closer to the atoms of the adjacent layer. The increase in bonding strength with the neighbouring layer partially compensate for the energy required to separate the atoms within each layer, so that the BO energy surface is shallower than would be expected under the harmonic approximation. By contrast, for $q < 0$, the Se-Sn bonds across the width of each layer are pushed closer together. These bonds are already strong, so

compressing them takes a lot of energy, resulting in a BO energy surface steeper than that predicted by the HA. As a result, the anharmonic probability density is greater than the harmonic density for $q > 0$, and less than the harmonic density for $q < 0$, particularly for large absolute values of q.

The *Pnma* phase demonstrates similar modes to the 'cubic-type' and 'quartic-type' modes of *Cmcm*. Two modes selected to illustrate these types of anharmonic potential are depicted in Fig. 5.11. In the case of the 'cubic-type' mode, the atomic motion for the softer $q > 0$ direction moves the atoms closer towards a *Cmcm*-type arrangement, while the motion for the harder $q < 0$ motion results in considerable compression of Sn-Se bonds along the plane of the layers.

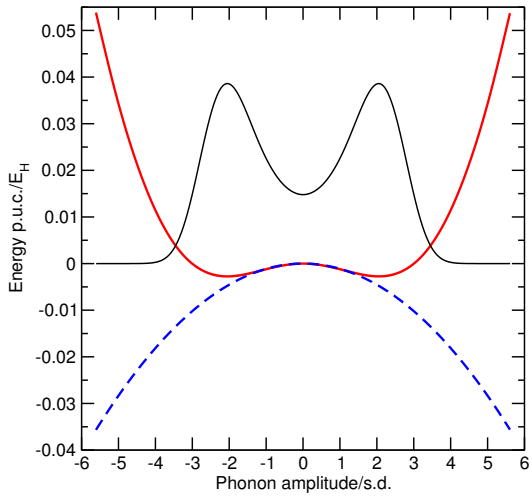
Energy p.u.c./E_H
0.05
0.04
0.03
0.02
0.01
0
-0.01
-0.02
-0.03
-0.04
-6 -5 -4 -3 -2 -1 0 1 2 3 4 5 6
Phonon amplitude/s.d.

(a)

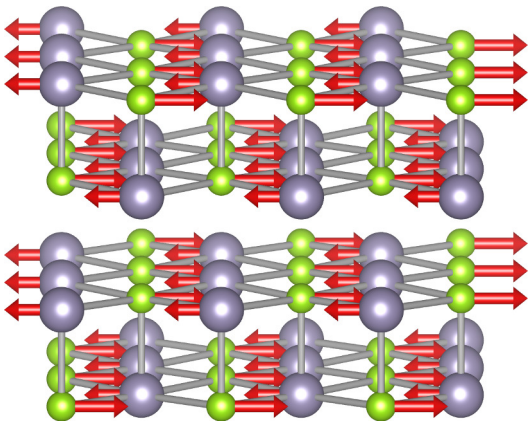

(b)

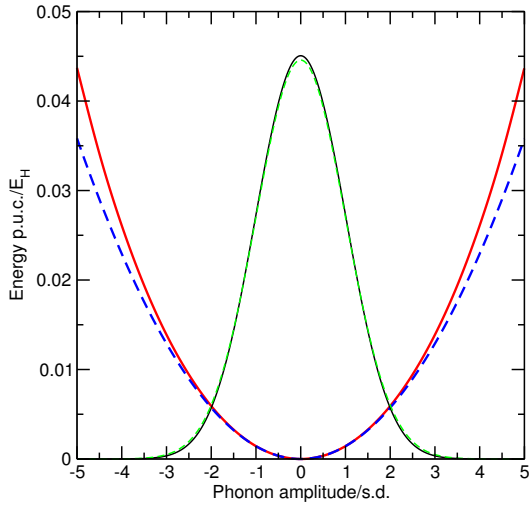
Energy p.u.c./E_H
0.05
0.04
0.03
0.02
0.01
0
-5 -4 -3 -2 -1 0 1 2 3 4 5
Phonon amplitude/s.d.

(c)

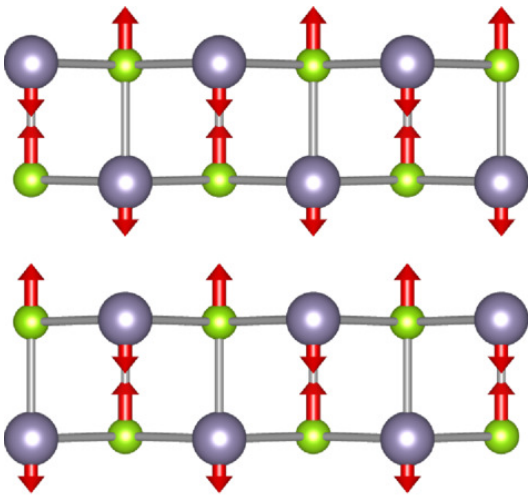

(d)

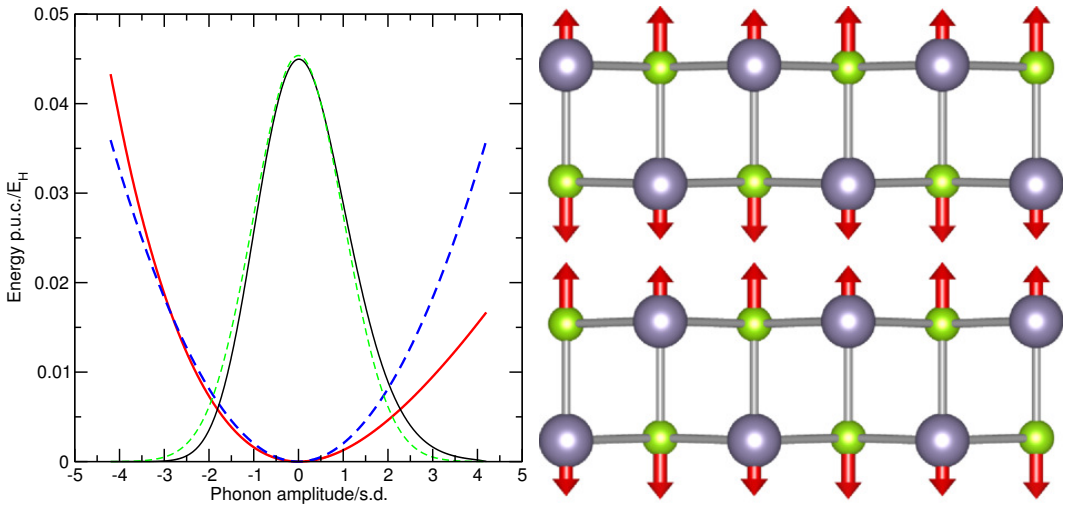

Fig. 5.10 Several illustrative anharmonic modes of SnSe, in the *Cmcm* phase at $\vec{k}$ = Γ. (a) and (b): a soft (negative curvature around $\vec{q} = 0$ "double well potential" mode corresponding to a *Pnma*-like atomic motion; (c) and (d): a 'quartic' type symmetric anharmonicity ($E^{\hbar\omega}_{\text{harm}} = 20.3\,\text{meV}$); (e) and (f) a 'cubic' type asymmetric anharmonicity ($E^{\hbar\omega}_{\text{harm}} = 20.7\,\text{meV}$). (a), (c) and (e): fitted anharmonic and harmonic potentials (solid red and dashed blue lines, respectively), along with the corresponding anharmonic and harmonic equilibrium probability densities (solid black and dashed green lines, respectively; there is no harmonic probability density in (a) due to the soft-mode harmonic potential). The y-axis scales refer to the BO surface energies per unit cell (p.u.c.) only; the probability densities are normalised to unity. The phonon coordinates used are multiples of the 'standard deviation' (s.d.), $\left\langle \sqrt{q^2_{n,\vec{k}}} \right\rangle$, see equation (2.130). (b), (d) and (f): depiction of the atomic displacement patterns for each mode.

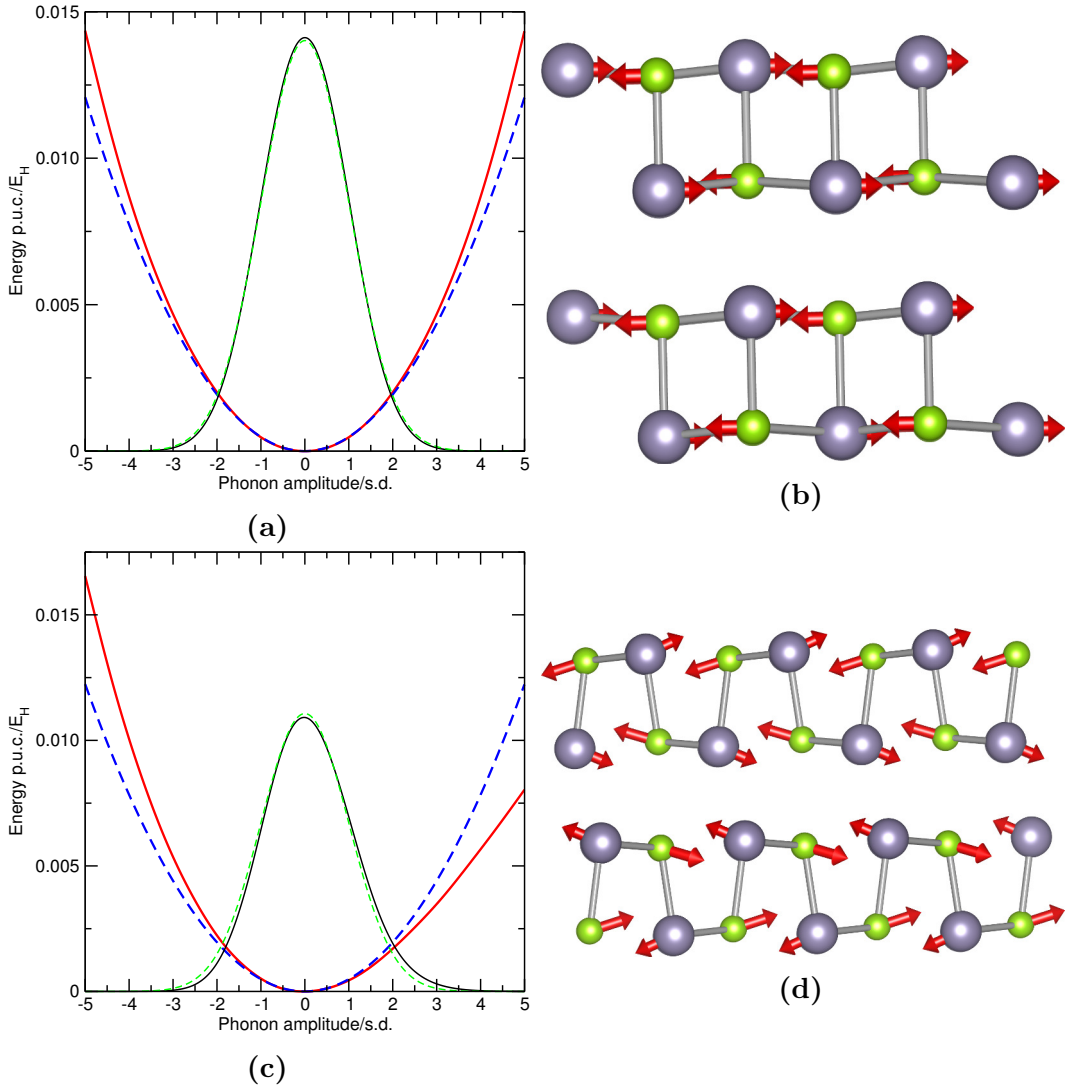

Fig. 5.11 Several illustrative anharmonic modes of SnSe, in the *Pnma* phase at $\vec{k} = \Gamma$. (a) and (b): a 'quartic' type symmetry anharmonicity ($E^{\hbar\omega}_{\text{harm}} = 11.9\,\text{meV}$); (c) and (d): a 'cubic' type asymmetric anharmonicity ($E^{\hbar\omega}_{\text{harm}} = 15.7\,\text{meV}$). (a) and (c): fitted anharmonic and harmonic potentials (solid red and dashed blue lines, respectively), along with the corresponding anharmonic and harmonic equilibrium probability densities (solid black and dashed green lines, respectively). The y-axis scales refer to the BO surface energies per unit cell (p.u.c.) only; the probability densities are normalised to unity. The phonon coordinates used are multiples of the 'standard deviation' (s.d.), $\left\langle \sqrt{q^2_{n,\vec{k}}} \right\rangle$, see equation (2.130). (b) and (d): depiction of the atomic displacement patterns for each mode.

The vibrational renormalisation of the band gap has contributions – mostly negative – from all the vibrational modes of the *Pnma* and *Cmcm* structures, but analysis of the contribution from each mode indicates that some vibrational modes contribute considerably more than others. Two vibrational modes in the *Cmcm* structure were found to contribute particularly strongly to the band gap vibrational renormalisation: the highest (harmonic) frequency mode at $\vec{k} = \left(0, 0, \frac{1}{5}\right)$, illustrated in Fig. 5.12a ($E^{\hbar\omega}_{\text{harm}}$ = 24.0 meV), and the third-highest-frequency mode at $\vec{k} = \left(\frac{1}{5}, 0, 0\right)$, illustrated in Fig. 5.12c ($E^{\hbar\omega}_{\text{harm}}$ = 15.3 meV). Both of these modes correspond to motion of pairs of Sn and Se atoms towards each other in a direction parallel to the plane of the SnSe layers.

The two highest-frequency modes at $\vec{k} = \left(0, \frac{1}{2}, 0\right)$ were the biggest contributors to the band gap renormalisation in the *Pnma* phase, although the impact of these modes is not so much greater than the average for all modes, compared with the illustrated *Cmcm* modes. One of these modes is depicted in Fig. 5.12b ($E^{\hbar\omega}_{\text{harm}}$ = 23.4 meV); the mode motion comprises bond stretching and compression in a direction perpendicular to the SnSe layers.

The soft "double-well" modes of the *Cmcm* phase, particularly those at reciprocal space points corresponding to small supercells – and especially at the Γ point, such as that shown in Fig. 5.10(a) and 5.10(b) – play a very significant role in the thermal expansion of the *Cmcm* phase, an intrinsically anharmonic property. These modes have very low effective mode energies (e.g. 2.1 meV for the mode depicted in Fig. 5.10(a) at 900 K), leading to very high occupancies. The very high degree of anharmonicity in these "double-well" modes makes them key to the highly anharmonic properties of the *Cmcm* phase, such as its thermal conductivity.

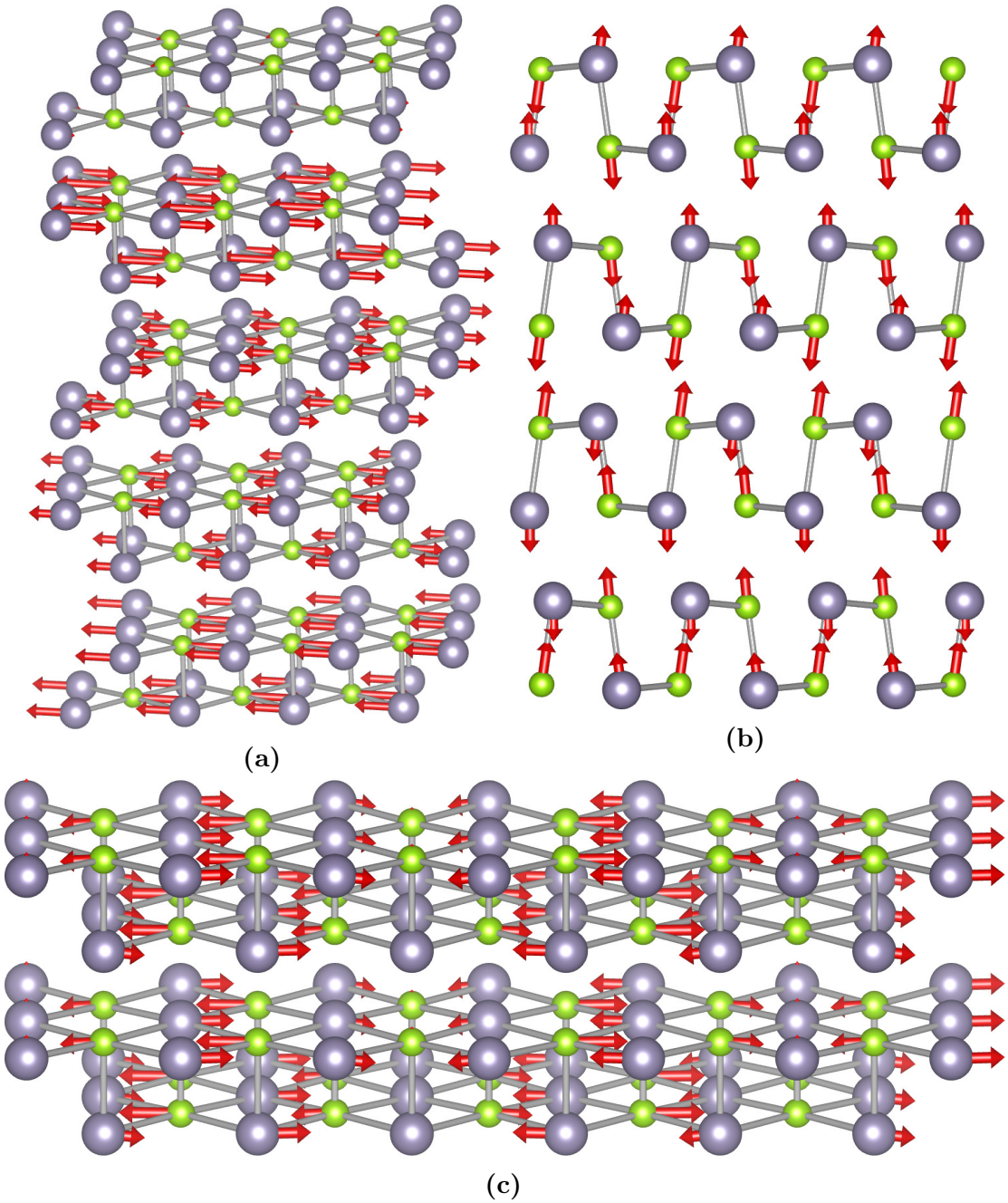

Fig. 5.12 Several illustrative modes of SnSe, resulting in significant vibrational renormalisation of the band gap. (a) and (c): *Cmcm* phase, (b): *Pnma* phase. (a): Highest-frequency mode at $\vec{k} = \left(0, 0, \frac{1}{5}\right)$, close to the Γ point; (b): second-highest-frequency mode at $\vec{k} = \left(0, \frac{1}{2}, 0\right)$ (the Y point in the BZ); (c): third-highest-frequency mode at $\vec{k} = \left(\frac{1}{5}, 0, 0\right)$, close to the Γ point. The modes depicted in (a) and (c) demonstrate movement of pairs of Sn and Se atoms towards each other within the planes of the layers. The mode depicted in (b) demonstrates Sn-Se bond stretching and compression perpendicular to the planes of the layers.

5.4 Conclusions

This study has investigated the vibrational properties of SnSe, a promising thermoelectric material of considerable interest. A first-principles approach to treating the considerable anharmonicity in SnSe has been applied to study the thermal expansion, and the temperature dependence of the electronic and vibrational properties of both the *Cmcm* and *Pnma* phases of the material, revealing a reduction in the size of the band gap in *Cmcm* at temperatures above 800 K – the region of interest for the thermoelectric properties of SnSe.

The origin of these anharmonic renormalisations has been explored, and traced to particular vibrational modes. The considerable anharmonicity in SnSe has been confirmed, and the role in thermal expansion of the statically unstable but thermally stabilised soft modes of the *Cmcm* phase has been identified. This work could be extended to consider further properties of relevance to thermoelectric materials. The VSCF method could be coupled with DFPT methods to calculate phonon linewidths, and hence thermal conductivity, which is a quantity relevant to the calculation of ZT.

Chapter 6

Conclusions and Outlook

6.1 Conclusions

In this thesis, we have explored two key problems in the investigation of materials in the solid state: the prediction of crystal structure under specified external conditions, and the calculation of the effects of nuclear motion, particularly when significant anharmonicity is present. In Chapter 2, the theoretical basis of these two problems was laid out, together with approaches for solving these problems. In particular, the *ab initio* random structure searching (AIRSS) method for crystal structure prediction, and the vibrational self-consistent field (VSCF) method for treating nuclear motion beyond the harmonic approximation, were described. The former method involves a global search of the Born-Oppenheimer energy surface to determine the low-energy crystal structures that are most likely to exist in nature; the latter involves a local exploration of the Born-Oppenheimer energy surface, to explore the potential that nuclei experience as they move about their equilibrium positions. In both cases, the Born-Oppenheimer energy surface was explored within density-functional theory, which was also outlined in this chapter.

In Chapter 3, a random structure seaching approach was applied to the investigation of point defects in graphene, and several novel defects predicted. Although the point defects are not themselves periodic, a scheme was descibed to predict and characterise them using periodic calculations. The prediction of previously described point defects confirmed the validity of the approach taken.

In Chapter 4, the AIRSS approach was applied to predict novel stable structures in the xenon-oxygen binary system at pressures of 83, 150 and 200 GPa. Five structures were identified as being stable within parts of this pressure range, and were characterised theoretically. Three of these structures were previously unreported. The work

was conducted in collaboration with experimentalists investigating the low end of the pressure range; comparison of the theoretical characterisation of the three xenon oxides predicted to be stable at 83 GPa with the results of the experiments confirmed the stability of two of the structures.

Finally, in Chapter 5, mapping of the local Born-Oppenheimer energy surface of two phases of SnSe was carried out to calculate the anharmonic vibrational wavefunction at a range of temperatures using the VSCF methodology. These wavefunctions and mapping data were used to calculate the thermal expansion and renormalised vibrational and electronic properties of SnSe. Finally, the physical origin of the anharmonic properties was explored.

In the rest of this chapter, future avenues of study will be briefly discussed.

6.2 Outlook

Further work could be carried out for the graphene point defects predicted in Chapter 3 by exploring possible ways the defects could be put to practical use, such as through chemical functionalisation. The random structure searching approach could also be extended to consider other types of defect, such as line defects. AIRSS has already been used to study point defects in three dimensional materials, such as silicon [246].

As outlined in Chapter 4, the chemistry of xenon under high pressure is of particular interest in part due to the "missing xenon paradox". The work in this thesis has provided a strong, experimentally-backed basis for our understanding of xenon chemistry with oxygen at pressures below 1 Mbar, and has made predictions for pressures up to 2 Mbar, which remain to be experimentally verified. Further progress could be made by considering the chemistry of xenon with other elements commonly found in the Earth's interior, such as magnesium, silicon, iron and nickel. Some such studies have already been conducted [78], but these have generally been searches in binary systems. Real progress will be made when searches in ternary and higher-order systems become computationally feasible: if xenon is trapped inside the Earth, then it will be in a chemical system of many elements, not just oxygen.

The work of Chapter 4 could also be extended by studying the oxides of other noble gases. The most obvious candidate for study is krypton, which is the next-largest noble gas after xenon, and so is likely to be the next most reactive noble gas [1]. One such theoretical study, on krypton oxides, has already been carried out, and

[1] excluding radon, which is unstable to radioactive decay for all its isotopes.

has predicted several thermodynamically stable Kr-O structures forming at pressures above about 300 GPa [247].

The study of anharmonicity in SnSe could be extended by going beyond the independent-modes approximation and considering the coupling of two or more modes in the mapping of the Born-Oppenheimer energy surface. There is some evidence to suggest this could have some impact on calculated vibrational properties [235]. At present, the computational expense of carrying out such a systematic mapping is too great, but may be feasible in the future with the growth of available computer power. The extension of the non-diagonal supercell approach to construct supercells periodically compatible with two or more phonon wavevectors is worthy of consideration, and could reduce the expense of a coupled-modes mapping.

The computational expense could also be significantly reduced if a computationally cheaper method of calculating the energy and desired properties at points on the Born-Oppenheimer surface with the required level of accuracy could be found. Gaussian approximation potentials are one such attempt to find an approximation to quantum mechanics with comparable accuracy to, but less cost than, density functional theory [248]. Consideration of coupled modes can be effected for all combinations of modes n and k-points $\vec{k}$ on a grid using Monte Carlo integration. This approach requires an $n_1 \times n_2 \times n_3$ supercell to be used for calculations on an $n_1 \times n_2 \times n_3$ grid in the vibrational Brillouin zone, which for the number of calculations required is currently computationally infeasible.

References

[1] R. M. Martin, *Electronic structure: basic theory and practical methods* (CUP, Cambridge, UK, 2010).

[2] M. Born and R. Oppenheimer, Zur Quantentheorie der Molekeln. *Ann. Phys.* **389**, 457 (1927), URL http://dx.doi.org/10.1002/andp.19273892002.

[3] J. Kohanoff, *Electronic structure calculations for solids and molecules* (CUP, Cambridge, UK, 2006).

[4] P. P. Ewald, Die Berechnung optischer und electrostatisher Gitterpotentiale. *Ann. der Physik* **64**, 253 (1921), URL http://dx.doi.org/10.1002/andp.19213690304.

[5] J. C. Slater, Atomic shielding constants. *Phys. Rev.* **36**, 57 (1930), URL http://dx.doi.org/10.1103/PhysRev.36.57.

[6] S. F. Boys, Electronic wave functions. I. A general method of calculation for the stationary states of any molecular system. *Proc. R. Soc. A* **200**, 542 (1950), URL http://dx.doi.org/10.1098/rspa.1950.0036.

[7] P. Hohenberg and W. Kohn, Inhomogeneous electron gas. *Phys. Rev.* **136**, B864 (1964), URL http://dx.doi.org/10.1103/PhysRev.136.B864.

[8] W. Kohn, Density functional theory: fundamentals and applications, in F. Bassani, F. Fumi, and M. P. Tosi (editors), *Highlights of Condensed Matter Theory*, pp. 1–15 (North-Holland, 1985).

[9] N. D. Mermin, Thermal properties of the inhomogeneous electron gas. *Phys. Rev.* **137**, A1441 (1965), URL http://dx.doi.org/10.1103/PhysRev.137.A1441.

[10] M. Levy, Universal variational functionals of electron densities, first-order density matrices, and natural spin-orbitals and solution of the v-representability problem. *Proc. Natl. Acad. Sci. U.S.A.* **76**, 6062 (1979), URL http://www.pnas.org/content/76/12/6062.abstract.

[11] M. Levy, Electron densities in search of Hamiltonians. *Phys. Rev. A* **26**, 1200 (1982), URL http://dx.doi.org/10.1103/PhysRevA.26.1200.

[12] E. Lieb, Density functionals for Coulomb systems, in A. Shimony and H. Feshbach (editors), *Physics as natural philosophy*, p. 111 (MIT Press, 1982).

[13] E. Lieb, Density functionals for Coulomb systems. *Int. J. Quant. Chem.* **24**, 243 (1983), URL http://dx.doi.org/10.1002/qua.560240302.

[14] M. Levy and J. P. Perdew, The constrained search formulation of density functional theory, in R. M. Dreizler and J. da Providencia (editors), *Density functional methods in physics* (Plenum Press, 1985).

[15] E. Lieb, Density functionals for Coulomb systems, in R. M. Dreizler and J. da Providencia (editors), *Density functional methods in physics* (Plenum Press, 1985).

[16] W. Kohn and L. J. Sham, Self-consistent equations including exchange and correlation effects. *Phys. Rev.* **140**, A1133 (1965), URL http://dx.doi.org/10.1103/PhysRev.140.A1133.

[17] G. F. Giuliani and G. Vignale, *Quantum Theory of the Electron Liquid* (CUP, Cambridge, UK, 2005).

[18] D. M. Ceperley and B. J. Alder, Ground state of the electron gas by a stochastic method. *Phys. Rev. Lett.* **45**, 566 (1980), URL http://dx.doi.org/10.1103/PhysRevLett.45.566.

[19] J. P. Perdew and A. Zunger, Self-interaction correction to density-functional approximations for many-electron systems. *Phys. Rev. B* **23**, 5048 (1981), URL http://dx.doi.org/10.1103/PhysRevB.23.5048.

[20] J. P. Perdew and K. Burke, Comparison shopping for a gradient-corrected density functional. *Int. J. Quantum Chem.* **57**, 309 (1996), URL http://dx.doi.org/10.1002/(SICI)1097-461X(1996)57:3<309::AID-QUA4>3.0.CO;2-1.

[21] J. P. Perdew, Unified theory of exchange and correlation beyond the local density approximation, in P. Ziescher and H. Eschrig (editors), *Electronic structure of solids '91*, pp. 11–20 (Akademie Verlag, 1991).

[22] J. P. Perdew and Y. Wang, Accurate and simple analytic representation of the electron-gas correlation energy. *Phys. Rev. B* **45**, 13244 (1992), URL http://dx.doi.org/10.1103/PhysRevB.45.13244.

[23] Z. Wu and R. E. Cohen, More accurate generalized gradient approximation for solids. *Phys. Rev. B* **73**, 235116 (2006), URL http://dx.doi.org/10.1103/PhysRevB.73.235116.

[24] J. P. Perdew, K. Burke, and M. Ernzerhof, Generalized gradient approximation made simple. *Phys. Rev. Lett.* **77**, 3865 (1996), URL http://dx.doi.org/10.1103/PhysRevLett.77.3865.

[25] Y. Zhang and W. Yang, Comment on "Generalized gradient approximation made simple". *Phys. Rev. Lett.* **80**, 890 (1998), URL http://dx.doi.org/10.1103/PhysRevLett.80.890.

[26] J. P. Perdew, A. Ruzsinszky, G. I. Csonka, O. A. Vydrov, G. E. Scuseria, *et al.*, Restoring the density-gradient expansion for exchange in solids and surfaces. *Phys. Rev. Lett.* **100**, 136406 (2008), URL http://dx.doi.org/10.1103/PhysRevLett.100.136406.

[27] E. H. Lieb and S. Oxford, Improved lower bound on the indirect Coulomb energy. *Int. J. Quant. Chem.* **19**, 427 (1981), URL http://dx.doi.org/10.1002/qua.560190306.

[28] J. P. Perdew and K. Schmidt, Jacob's ladder of density functional approximations for the exchange-correlation energy. *AIP Conf. Proc.* **577**, 1 (2001), URL http://dx.doi.org/10.1063/1.1390175.

[29] P. Mori-Sánchez and A. J. Cohen, The derivative discontinuity of the exchange-correlation functional. *Phys. Chem. Chem. Phys.* **16**, 14378 (2014), URL http://dx.doi.org/10.1039/c4cp01170h.

[30] J. P. Perdew, R. G. Parr, M. Levy, and J. L. Balduz, Jr., Density-functional theory for fractional particle number: derivative discontinuities of the energy. *Phys. Rev. Lett.* **49**, 1691 (1982), URL http://dx.doi.org/10.1103/PhysRevLett.49.1691.

[31] J. P. Perdew and M. Levy, Physical content of the exact Kohn-Sham orbital energies: band gaps and derivative discontinuities. *Phys. Rev. Lett.* **51**, 1884 (1983), URL http://dx.doi.org/10.1103/PhysRevLett.51.1884.

[32] C. Adamo and V. Barone, Toward reliable density functional methods without adjustable parameters: The PBE0 model. *J. Chem. Phys.* **110**, 6158 (1999), URL http://dx.doi.org/10.1063/1.478522.

[33] J. Heyd, G. E. Scuseria, and M. Ernzerhof, Hybrid functionals based on a screened Coulomb potential. *J. Chem. Phys.* **118**, 8207 (2003), URL http://dx.doi.org/10.1063/1.1564060.

[34] J. Heyd, G. E. Scuseria, and M. Ernzerhof, Erratum: Hybrid functionals based on a screened Coulomb potential. *J. Chem. Phys.* **124**, 219906 (2006), URL http://dx.doi.org/10.1063/1.2204597.

[35] K. Burke and J. P. Perdew, Real space analysis of the exchange-correlation energy. *Int. J. Quantum Chem.* **56**, 199 (1995), URL http://dx.doi.org/10.1002/qua.560560403.

[36] S. Grimme, Semiempirical GGA-type density functional constructed with a long-range dispersion correction. *J. Comput. Chem.* **27**, 1787 (2006), URL http://dx.doi.org/10.1002/jcc.20495.

[37] A. Tkatchenko and M. Scheffler, Accurate molecular van der Waals interactions from ground-state electron density and free-atom reference data. *Phys. Rev. Lett.* **102**, 073005 (2009), URL http://dx.doi.org/10.1103/PhysRevLett.102.073005.

[38] F. L. Hirshfeld, Bonded-atom fragments for describing molecular charge densities. *Theoret. Chim. Acta* **44**, 129 (1977), URL http://dx.doi.org/10.1007/BF00549096.

[39] J. Binns, M. R. Healy, S. Parsons, and C. A. Morrison, Assessing the performance of density functional theory in optimizing molecular crystal structure parameters. *Acta Cryst. B* **70**, 259 (2014), URL http://dx.doi.org/10.1107/S205252061303268X.

[40] G. P. Srivastava, Broyden's method for self-consistent field convergence acceleration. *J. Phys. A* **17**, L317 (1984), URL http://dx.doi.org/10.1088/0305-4470/17/6/002.

[41] P. Pulay, Convergence acceleration of iterative sequences. The case of SCF iteration. *Chem. Phys. Lett.* **73**, 393 (1980), URL http://dx.doi.org/10.1016/0009-2614(80)80396-4.

[42] N. Marzari, D. Vanderbilt, and M. C. Payne, Ensemble density-functional theory for *ab initio* molecular dynamics of metals and finite-temperature insulators. *Phys. Rev. Lett.* **79**, 1337 (1997), URL http://dx.doi.org/10.1103/PhysRevLett.79.1337.

[43] J. Harris, Simplified method for calculating the energy of weakly interacting fragments. *Phys. Rev. B* **31**, 1770 (1985), URL http://dx.doi.org/10.1103/PhysRevB.31.1770.

[44] N. W. Ashcroft and N. D. Mermin, *Solid state physics* (Brooks/Cole, USA, 1976).

[45] H. J. Monkhorst and J. D. Pack, Special points for Brillouin-zone integrations. *Phys. Rev. B* **13**, 5188 (1976), URL http://dx.doi.org/10.1103/PhysRevB.13.5188.

[46] J. C. Cooley and J. W. Tukey, An algorithm for the machine calculation of complex Fourier series. *Math. Comput.* **19**, 297 (1965), URL http://dx.doi.org/10.1090/S0025-5718-1965-0178586-1.

[47] G. P. Francis and M. C. Payne, Finite basis set corrections to total energy pseudopotential calculations. *J. Phys.: Condens. Matter* **2**, 4395 (1990), URL http://dx.doi.org/10.1088/0953-8984/2/19/007.

[48] M. H. Cohen and V. Heine, Cancellation of kinetic and potential energy in atoms, molecules, and solids. *Phys. Rev.* **122**, 1821 (1961), URL http://dx.doi.org/10.1103/PhysRev.122.1821.

[49] D. R. Hamann, M. Schlüter, and C. Chiang, Norm-conserving pseudopotentials. *Phys. Rev. Lett.* **43**, 1494 (1979), URL http://dx.doi.org/10.1103/PhysRevLett.43.1494.

[50] D. Vanderbilt, Soft self-consistent pseudopotentials in a generalized eigenvalue formalism. *Phys. Rev. B* **41**, 7892 (1990), URL http://dx.doi.org/10.1103/PhysRevB.41.7892.

[51] P. E. Blöchl, Projector augmented-wave method. *Phys. Rev. B* **50**, 17953 (1994), URL http://dx.doi.org/10.1103/PhysRevB.50.17953.

[52] N. Troullier and J. L. Martins, Efficient pseudopotentials for plane-wave calculations. *Phys. Rev. B* **43**, 1993 (1991), URL http://dx.doi.org/10.1103/PhysRevB.43.1993.

[53] B. Monserrat, R. J. Needs, and C. J. Pickard, Temperature effects in first-principles solid state calculations of the chemical shielding tensor made simple. *J. Chem. Phys.* **141**, 134113 (2014), URL http://dx.doi.org/10.1063/1.4897261.

[54] R. P. Feynman, Forces in molecules. *Phys. Rev.* **56**, 340 (1939), URL http://dx.doi.org/10.1103/PhysRev.56.340.

[55] C. G. Broyden, The convergence of a class of double-rank minimization algorithms 1. General considerations. *J. Inst. Math. Appl.* **6**, 76 (1970), URL http://dx.doi.org/10.1093/imamat/6.1.76.

[56] D. C. Liu and J. Nocedal, On the limited memory BFGS method for large scale optimization. *Math. Prog.* **45**, 503 (1989), URL http://dx.doi.org/10.1007/BF01589116.

[57] S. J. Clark, M. D. Segall, C. J. Pickard, P. J. Hasnip, M. I. J. Probert, *et al.*, First principles methods using CASTEP. *Z. Kristallogr.* **220**, 567 (2005), URL http://dx.doi.org/10.1524/zkri.220.5.567.65075.

[58] J. Maddox, Crystals from first principles. *Nature* **335**, 201 (1988), URL http://dx.doi.org/10.1038/335201a0.

[59] F. H. Stillinger, Exponential multiplicity of inherent structures. *Phys. Rev. E* **59**, 48 (1999), URL http://dx.doi.org/10.1103/PhysRevE.59.48.

[60] J. P. K. Doye, D. J. Wales, and M. A. Miller, Thermodynamics and the global optimization of Lennard-Jones clusters. *J. Chem. Phys.* **109**, 8143 (1998), URL http://dx.doi.org/10.1063/1.477477.

[61] J. P. K. Doye and C. P. Massen, Characterizing the network topology of the energy landscapes of atomic clusters. *J. Chem. Phys.* **122**, 084105 (2005), URL http://dx.doi.org/10.1063/1.1850468.

[62] C. P. Massen and J. P. K. Doye, Power-law distributions for the areas of the basins of attraction on a potential energy landscape. *Phys. Rev. E* **75**, 03101 (2007), URL http://dx.doi.org/10.1103/PhysRevE.75.037101.

[63] C. P. Massen, J. P. K. Doye, and R. W. Nash, Exploring the origins of the power-law properties of energy landscapes: An egg-box model. *Physica A* **382**, 683 (2007), URL http://dx.doi.org/10.1016/j.physa.2007.04.054.

[64] C. J. Pickard and R. J. Needs, *Ab initio* random structure searching. *J. Phys.: Condens. Matter* **23**, 053201 (2011), URL http://dx.doi.org/10.1088/0953-8984/23/5/053201.

[65] F. Jensen, *Introduction to Computational Chemistry* (Wiley, Chichester, UK, 2006).

[66] S. Roy, S. Goedecker, and V. Hellmann, Bell-Evans-Polanyi principle for molecular dynamics trajectories and its implications for global optimization. *Phys. Rev. E* **77**, 056707 (2008), URL http://dx.doi.org/10.1103/PhysRevE.77.056707.

[67] L. J. Pauling, The principles determining the structure of complex ionic crystals. *J. Am. Chem. Soc.* **51**, 1010 (1929), URL http://dx.doi.org/10.1021/ja01379a006.

[68] D. J. Wales, Symmetry, near-symmetry and energetics. *Chem. Phys. Lett.* **285**, 330 (1998), URL http://dx.doi.org/10.1016/S0009-2614(98)00044-X.

[69] D. H. Wolpert and W. G. Macready, No free lunch theorems for optimization. *IEEE Trans. Evo. Comput.* **1**, 67 (1997), URL http://dx.doi.org/10.1109/4235.585893.

[70] S. M. Woodley and R. Catlow, Crystal structure prediction from first principles. *Nature Materials* **7**, 937 (2008), URL http://dx.doi.org/10.1038/nmat2321.

[71] A. R. Oganov (editor), *Modern methods of crystal structure prediction* (Wiley-VCH, Weinheim, Germany, 2011).

[72] S. Kirkpatrick, J. C. D. Gelatt, and M. P. Vecchi, Optimization by simulated annealing. *Science* **220**, 671 (1983), URL http://dx.doi.org/10.1126/science.220.4598.671.

[73] N. Metropolis, A. W. Rosenbluth, M. N. Rosenbluth, A. H. Teller, and E. Teller, Equation of state calculations by fast computing machines. *J. Chem. Phys.* **21**, 1087 (1953), URL http://dx.doi.org/10.1063/1.1699114.

[74] D. J. Wales and J. P. K. Doye, Global optimization by basin-hopping and the lowest energy structures of Lennard-Jones clusters containing up to 110 atoms. *J. Phys. Chem. A* **101**, 5111 (1997), URL http://dx.doi.org/10.1021/jp970984n.

[75] T. Bäck, *Evolutionary Algorithms in Theory and Practice* (OUP, Oxford, UK, 1996).

[76] C. W. Glass, A. R. Oganov, and N. Hansen, USPEX—evolutionary crystal structure prediction. *Comput. Phys. Commun.* **175**, 713 (2006), URL http://dx.doi.org/10.1016/j.cpc.2006.07.020.

[77] A. R. Oganov, J. Chen, C. Gatti, Y. Ma, Y. Ma, *et al.*, Ionic high-pressure form of elemental boron. *Nature* **457**, 863 (2009), URL http://dx.doi.org/10.1038/nature07736.

[78] L. Zhu, H. Liu, C. J. Pickard, G. Zou, and Y. Ma, Reactions of xenon with iron and nickel are predicted in the Earth's inner core. *Nature Chemistry* **6**, 644 (2014), URL http://dx.doi.org/10.1038/nchem.1925.

[79] C. J. Pickard and R. J. Needs, High pressure phases of silane. *Phys. Rev. Lett.* **97**, 045504 (2006), URL http://dx.doi.org/10.1103/PhysRevLett.97.045504.

[80] C. J. Pickard and R. J. Needs, Structure of phase III of solid hydrogen. *Nature Physics* **3**, 473 (2007), URL http://dx.doi.org/10.1038/nphys625.

[81] P. J. Hasnip, K. Refson, M. I. J. Probert, J. R. Yates, S. J. Clark, and C. J. Pickard, Density functional theory in the solid state. *Philos. Trans. R. Soc. A* **372**, 20130270 (2014), URL http://dx.doi.org/10.1098/rsta.2013.0270.

[82] B. Monserrat, N. D. Drummond, and R. J. Needs, Anharmonic vibrational properties in periodic systems: energy, electron-phonon coupling, and stress. *Phys. Rev. B* **87**, 144302 (2013), URL http://dx.doi.org/10.1103/PhysRevB.87.144302.

[83] M. T. Dove, *Structure and dynamics* (OUP, Oxford, UK, 2003).

[84] L. D. Landau and E. M. Lifshitz, *Course of Theoretical Physics, Volume 5: Statistical Physics, Part 1* (Butterworth-Heinemann, Oxford, UK, 1980), third edition.

[85] S. Baroni, S. de Gironcoli, A. D. Corso, and P. Giannozzi, Phonons and related crystal properties from density-functional perturbation theory. *Rev. Mod. Phys.* **73**, 515 (2001), URL http://dx.doi.org/10.1103/RevModPhys.73.515.

[86] K. Kunc and R. M. Martin, *Ab initio* force constants of GaAs: A new approach to calculation of phonons and dielectric properties. *Phys. Rev. Lett.* **48**, 406 (1982), URL http://dx.doi.org/10.1103/PhysRevLett.48.406.

[87] D. J. Hooton, A new treatment of anharmonicity in lattice thermodynamics: I. *Philos. Mag.* **46**, 422 (1955), URL http://dx.doi.org/10.1080/14786440408520575.

[88] B. Monserrat, E. A. Engel, and R. J. Needs, Giant electron-phonon interactions in molecular crystals and the importance of nonquadratic coupling. *Phys. Rev. B* **92**, 140302 (2015), URL http://dx.doi.org/10.1103/PhysRevB.92.140302.

[89] E. A. Engel, B. Monserrat, and R. J. Needs, Vibrational renormalisation of the electronic band gap in hexagonal and cubic ice. *J. Chem. Phys.* **142**, 244708 (2015), URL http://dx.doi.org/10.1063/1.4938029.

[90] E. A. Engel, B. Monserrat, and R. J. Needs, Anharmonic nuclear motion and the relative stability of hexagonal and cubic ice. *Phys. Rev. X* **5**, 021033 (2015), URL http://dx.doi.org/10.1103/PhysRevX.5.021033.

[91] L. S. Norris, M. A. Ratner, A. E. Roitberg, and R. B. Gerber, Møller–Plesset perturbation theory applied to vibrational problems. *J. Chem. Phys.* **105**, 11261 (1996), URL http://dx.doi.org/10.1063/1.472922.

[92] J. H. Lloyd-Williams and B. Monserrat, Lattice dynamics and electron-phonon coupling calculations using nondiagonal supercells. *Phys. Rev. B* **92**, 184301 (2015), URL http://dx.doi.org/10.1103/PhysRevB.92.184301.

[93] C. Kittel, *Introduction to solid state physics* (Wiley, New York, 1996).

[94] G. E. P. Box and M. E. Muller, A note on the generation of random normal deviates. *Ann. Math. Statist.* **29**, 610 (1958), URL http://dx.doi.org/10.1214/aoms/1177706645.

[95] W. K. Hastings, Monte Carlo sampling methods using Markov chains and their applications. *Biometrika* **57**, 97 (1970), URL http://dx.doi.org/10.1093/biomet/57.1.97.

[96] B. Monserrat, Vibrational averages along thermal lines. *Phys. Rev. B* **93**, 014302 (2016), URL http://dx.doi.org/10.1103/PhysRevB.93.014302.

[97] B. Monserrat, Correlation effects on electron-phonon coupling in semiconductors: Many-body theory along thermal lines. *Phys. Rev. B* **93**, 100301 (2016), URL http://dx.doi.org/10.1103/PhysRevB.93.100301.

[98] B. J. Alder and T. E. Wainwright, Studies in molecular dynamics. I. General method. *J. Chem. Phys.* **31**, 459 (1959), URL http://dx.doi.org/10.1063/1.1730376.

[99] R. Car and M. Parrinello, Unified approach for molecular dynamics and density-functional theory. *Phys. Rev. Lett.* **55**, 2471 (1985), URL http://dx.doi.org/10.1103/PhysRevLett.55.2471.

[100] J. Cao and G. A. Voth, The formulation of quantum statistical mechanics based on the Feynman path centroid density. I. Equilibrium properties. *J. Chem. Phys.* **100**, 5093 (1994), URL http://dx.doi.org/10.1063/1.467175.

[101] J. Cao and G. A. Voth, The formulation of quantum statistical mechanics based on the Feynman path centroid density. II. Dynamical properties. *J. Chem. Phys.* **100**, 5106 (1994), URL http://dx.doi.org/10.1063/1.467176.

[102] O. H. Nielsen and R. M. Martin, First-principles calculation of stress. *Phys. Rev. Lett.* **50**, 697 (1983), URL http://dx.doi.org/PhysRevLett.50.697.

[103] L. D. Landau, E. M. Lifshitz, A. M. Kosevich, and L. P. Pitaevskii, *Course of Theoretical Physics, Volume 7: Theory of Elasticity* (Butterworth-Heinemann, Oxford, UK, 1986), third edition.

[104] B. Monserrat, N. D. Drummond, C. J. Pickard, and R. J. Needs, Electron-phonon coupling and the metallization of solid helium at terapascal pressures. *Phys. Rev. Lett.* **112**, 055504 (2014), URL http://dx.doi.org/10.1103/PhysRevLett.112.055504.

[105] D. R. Cooper, B. D'Anjou, N. Ghattamaneni, B. Harack, M. Hilke, *et al.*, Experimental review of graphene. *Int. Sch. Res. Notices* **2012**, 501686 (2012), URL http://dx.doi.org/10.5402/2012/501686.

[106] A. H. Castro Neto, F. Guinea, N. M. R. Peres, K. S. Novoselov, and A. K. Geim, The electronic properties of graphene. *Rev. Mod. Phys.* **81**, 109 (2009), URL http://dx.doi.org/10.1103/RevModPhys.81.109.

[107] K. S. Novoselov, A. K. Geim, S. V. Morozov, D. Jiang, Y. Zhang, *et al.*, Electrical field effect in atomically thin carbon films. *Science* **306**, 666 (2004), URL http://dx.doi.org/10.1126/science.1102896.

[108] A. K. Geim and K. S. Novoselov, The rise of graphene. *Nature Materials* **6**, 183 (2007), URL http://dx.doi.org/10.1038/nmat1849.

[109] C. Lee, X. Wei, J. W. Kysar, and J. Hone, Measurement of the elastic properties and intrinsic strength of monolayer graphene. *Science* **321**, 385 (2008), URL http://dx.doi.org/10.1126/science.1157996.

[110] C. Faugeras, B. Faugeras, M. Orlita, M. Potemski, R. R. Nair, and A. K. Geim, Thermal conductivity of graphene in corbino membrane geometry. *ACS Nano* **4**, 1889 (2010), URL http://dx.doi.org/10.1021/nn9016229.

[111] A. A. Balandin, S. Ghosh, W. Bao, I. Calizo, D. Teweldebrhan, *et al.*, Superior thermal conductivity of single-layer graphene. *Nano Lett.* **8**, 902 (2008), URL http://dx.doi.org/10.1021/nl0731872.

[112] J. O. Sofo, A. S. Chaudhari, and G. D. Barber, Graphane: A two-dimensional hydrocarbon. *Phys. Rev. B* **75**, 153401 (2007), URL http://dx.doi.org/10.1103/PhysRevB.75.153401.

[113] S. Lebègue, M. Klintenberg, O. Eriksson, and M. I. Katsnelson, Accurate electronic band gap of pure and functionalized graphane from GW calculations. *Phys. Rev. B* **79**, 245117 (2009), URL http://dx.doi.org/10.1103/PhysRevB.79.245117.

[114] P. A. Denis and F. Iribarne, Comparative study of defect reactivity in graphene. *J. Phys. Chem. C* **117**, 19048 (2013), URL http://dx.doi.org/10.1021/jp4061945.

[115] O. V. Yazyev, I. Tavernelli, U. Rothlisberger, and L. Helm, Early stages of radiation damage in graphite and carbon nanostructures: A first-principles molecular dynamics study. *Phys. Rev. B* **75**, 115418 (2007), URL http://dx.doi.org/10.1103/PhysRevB.75.115418.

[116] F. Banhart, J. Kotakoski, and A. V. Krasheninnikov, Structural defects in graphene. *ACS Nano* **5**, 26 (2011), URL http://dx.doi.org/10.1021/nn102598m.

[117] O. Cretu, A. V. Krasheninnikov, J. A. Rodríguez-Manzo, L. Sun, R. M. Nieminen, and F. Banhart, Migration and localization of metal atoms on strained graphene. *Phys. Rev. Lett.* **105**, 196102 (2010), URL http://dx.doi.org/10.1103/PhysRevLett.105.196102.

[118] J. Kotakoski, A. V. Krasheninnikov, U. Kaiser, and J. C. Meyer, From point defects in graphene to two-dimensional amorphous carbon. *Phys. Rev. Lett.* **106**, 105505 (2011), URL http://dx.doi.org/10.1103/PhysRevLett.106.105505.

[119] J. C. Meyer, C. Kisielowski, R. Erni, M. D. Rossell, M. F. Crommie, and A. Zettl, Direct imaging of lattice atoms and topological defects in graphene membranes. *Nano Lett.* **8**, 3582 (2008), URL http://dx.doi.org/10.1021/nl801386m.

[120] T. Björkman, S. Kurasch, O. Lehtinen, J. Kotakoski, O. V. Yazyev, *et al.*, Defects in bilayer silica and graphene: common trends in diverse hexagonal two-dimensional systems. *Sci. Rep.* **3**, 3482 (2013), URL http://dx.doi.org/10.1038/srep03482.

[121] D. W. Boukhvalov and M. I. Katsnelson, Chemical functionalization of graphene with defects. *Nano Lett.* **8**, 4373 (2008), URL http://dx.doi.org/10.1021/nl802234n.

[122] A. J. Stone and D. J. Wales, Theoretical studies of icosahedral C_{60} and some related species. *Chem. Phys. Lett.* **128**, 501 (1986), URL http://dx.doi.org/10.1016/0009-2614(86)80661-3.

[123] J. Ma, D. Alfè, A. Michaelides, and E. Wang, Stone-Wales defects in graphene and other planar sp^2-bonded materials. *Phys. Rev. B* **80**, 033407 (2009), URL http://dx.doi.org/10.1103/PhysRevB.80.033407.

[124] L. Li, S. Reich, and J. Robertson, Defect energies of graphite: Density-functional calculations. *Phys. Rev. B* **72**, 184109 (2005), URL http://dx.doi.org/10.1103/PhysRevB.72.184109.

[125] A. A. El-Barbary, R. H. Telling, C. P. Ewels, M. I. Heggie, and P. R. Briddon, Structure and energetics of the vacancy in graphite. *Phys. Rev. B* **68**, 144107 (2003), URL http://dx.doi.org/10.1103/PhysRevB.68.144107.

[126] A. V. Krasheninnikov, P. O. Lehtinen, A. S. Foster, and R. M. Nieminen, Bending the rules: Contrasting vacancy energetics and migration in graphite and carbon nanotubes. *Chem. Phys. Lett.* **418**, 132 (2006), URL http://dx.doi.org/10.1016/j.cplett.2005.10.106.

[127] P. A. Thrower and R. M. Mayer, Point defects and self-diffusion in graphite. *Phys. Status Solidi A* **47**, 11 (1978), URL http://dx.doi.org/10.1002/pssa.2210470102.

[128] S. T. Skowron, I. V. Lebedeva, A. M. Popov, and E. Bichoutskaia, Energetics of atomic scale structure changes in graphene. *Chem. Soc. Rev.* **44**, 3143 (2015), URL http://dx.doi.org/10.1039/c4cs00499j.

[129] G.-D. Lee, C. Z. Wang, E. Yoon, N.-M. Hwang, D.-Y. Kim, and K. M. Ho, Diffusion, coalescence, and reconstruction of vacancy defects in graphene layers. *Phys. Rev. Lett.* **95**, 205501 (2005), URL http://dx.doi.org/10.1103/PhysRevLett.95.205501.

[130] L. Tsetseris and S. T. Pantelides, Adatom complexes and self-healing mechanisms on graphene and single-wall carbon nanotubes. *Carbon* **47**, 901 (2009), URL http://dx.doi.org/10.1016/j.carbon.2008.12.002.

[131] Y. Ma, Simulation of interstitial diffusion in graphite. *Phys. Rev. B* **76**, 075419 (2007), URL http://dx.doi.org/10.1103/PhysRevB.76.075419.

[132] P. O. Lehtinen, A. S. Foster, A. Ayuela, A. Krasheninnikov, K. Nordlund, and R. M. Nieminen, Magnetic properties and diffusion of adatoms on a graphene sheet. *Phys. Rev. Lett.* **91**, 017202 (2003), URL http://dx.doi.org/10.1103/PhysRevLett.91.017202.

[133] Y. H. Lee, S. G. Kim, and D. Tománek, Catalytic growth of single-wall carbon nanotubes: An *ab initio* study. *Phys. Rev. Lett.* **78**, 2393 (1997), URL http://dx.doi.org/10.1103/PhysRevLett.78.2393.

[134] M. T. Lusk and L. D. Carr, Nanoengineering defect structures on graphene. *Phys. Rev. Lett.* **100**, 175503 (2008), URL http://dx.doi.org/10.1103/PhysRevLett.100.175503.

[135] M. T. Lusk, D. T. Wu, and L. D. Carr, Graphene nanoengineering and the inverse Stone-Thrower-Wales defect. *Phys. Rev. B* **81**, 155444 (2010), URL http://dx.doi.org/10.1103/PhysRevB.81.155444.

[136] D. Orlikowski, M. B. Nardelli, J. Bernholc, and C. Roland, Ad-dimers on strained carbon nanotubes: A new route for quantum dot formation? *Phys. Rev. Lett.* **83**, 4132 (1999), URL http://dx.doi.org/10.1103/PhysRevLett.83.4132.

[137] O. Lehtinen, N. Vats, G. Algara-Siller, P. Knyrim, and U. Kaiser, Implantation and atomic-scale investigation of self-interstitials in graphene. *Nano Lett.* **15**, 235 (2015), URL http://dx.doi.org/10.1021/nl503453u.

[138] F. Banhart, Interactions between metals and carbon nanotubes: at the interface between old and new materials. *Nanoscale* **1**, 201 (2009), URL http://dx.doi.org/10.1039/B9NR00127A.

[139] K. Kong, Y. Choi, B.-H. Ryu, J.-O. Lee, and H. Chang, Investigation of metal/carbon-related materials for fuel cell applications by electronic structure calculations. *Materials Science and Engineering C* **26**, 1207 (2006), URL http://dx.doi.org/10.1016/j.msec.2005.09.039.

[140] J. A. Rodríguez-Manzo, O. Cretu, and F. Banhart, Trapping of metal atoms in vacancies of carbon nanotubes and graphene. *ACS Nano* **4**, 3422 (2010), URL http://dx.doi.org/10.1021/nn100356q.

[141] A. V. Krasheninnikov, P. O. Lehtinen, A. S. Foster, P. Pyykkö, and R. M. Nieminen, Embedding transition-metal atoms in graphene: Structure, bonding, and magnetism. *Phys. Rev. Lett.* **102**, 126807 (2009), URL http://dx.doi.org/10.1103/PhysRevLett.102.126807.

[142] L. Ci, L. Song, C. Jin, D. Jariwala, D. Wu, *et al.*, Atomic layers of hybridized boron nitride and graphene domains. *Nat. Mater.* **9**, 430 (2010), URL http://dx.doi.org/10.1038/nmat2711.

[143] A. H. Nevidomskyy, G. Csányi, and M. C. Payne, Chemically active substitutional nitrogen impurity in carbon nanotubes. *Phys. Rev. Lett.* **91**, 105502 (2003), URL http://dx.doi.org/10.1103/PhysRevLett.91.105502.

[144] N. Nemec, D. Tománek, and G. Cuniberti, Contact dependence of carrier injection in carbon nanotubes: An *ab initio* study. *Phys. Rev. Lett.* **96**, 076802 (2006), URL http://dx.doi.org/10.1103/PhysRevLett.96.076802.

[145] N. Bartlett, Xenon hexafluoroplatinate(v) $Xe^{+}[PtF_6]^{-}$. *Proc. Chem. Soc* p. 218 (1962), URL http://dx.doi.org/10.1039/PS9620000197.

[146] W. Grochala, Atypical compounds of gases, which have been called 'noble'. *Chem. Soc. Rev.* **36**, 1632 (2007), URL http://dx.doi.org/10.1039/B702109G.

[147] H. H. Claassen, H. Selig, and J. G. Malm, Xenon tetrafluoride. *J. Amer. Chem. Soc.* **84**, 3593 (1962), URL http://dx.doi.org/10.1021/ja00877a042.

[148] C. L. Chernick, H. H. Claassen, P. R. Fields, H. H. Hyman, J. G. Malm, *et al.*, Fluorine compounds of xenon and radon. *Science* **138**, 136 (1962), URL http://dx.doi.org/10.1126/science.138.3537.136.

[149] D. F. Smith, Xenon trioxide. *J. Am. Chem. Soc.* **85**, 816 (1963), URL http://dx.doi.org/10.1021/ja00889a036.

[150] H. Selig, H. H. Claassen, C. L. Chernick, J. G. Malm, and J. L. Huston, Xenon tetroxide: Preparation and some properties. *Science* **143**, 1322 (1964), URL http://dx.doi.org/10.1126/science.143.3612.1322.

[151] D. S. Brock and G. J. Schrobilgen, Synthesis of the missing oxide of xenon, XeO_2, and its implications for Earth's missing xenon. *J. Am. Chem. Soc.* **133**, 6265 (2011), URL http://dx.doi.org/10.1021/ja110618g.

[152] S. N. Britvin, S. A. Kashtanov, M. G. Krzhizhanovskaya, A. A. Gurinov, O. V. Glumov, *et al.*, Perovskites with the framework-forming xenon. *Angew. Chem. Int. Ed.* **54**, 14340 (2015), URL http://dx.doi.org/10.1002/anie.201506690.

[153] C. Sanloup, H.-K. Mao, and R. J. Hemley, High-pressure transformations in xenon hydrates. *Proc. Natl. Acad. Sci.* **99**, 25 (2002), URL http://dx.doi.org/10.1073/pnas.221602698.

[154] A. Dewaele, P. Loubeyre, P. Dumas, and M. Mezouar, Oxygen impurities reduce the metallization pressure of xenon. *Phys. Rev. B* **86**, 014103 (2012), URL http://dx.doi.org/10.1103/PhysRevB.86.014103.

[155] G. Weck, A. Dewaele, and P. Loubeyre, Oxygen/noble gas binary phase diagrams at 296 K and high pressures. *Phys. Rev. B* **82**, 014112 (2010), URL http://dx.doi.org/10.1103/PhysRevB.82.014112.

[156] A. P. Jephcoat, H.-K. Mao, L. W. Finger, D. E. Cox, R. J. Hemley, and C.-S. Zha, Pressure-induced structural phase transitions in solid xenon. *Phys. Rev. Lett.* **59**, 2670 (1987), URL http://dx.doi.org/10.1103/PhysRevLett.59.2670.

[157] H. Cynn, C. S. Yoo, B. Baer, V. Iota-Herbei, A. K. McMaham, *et al.*, Martensitic fcc-to-hcp transformation observed in xenon at high pressure. *Phys. Rev. Lett.* **86**, 4552 (2001), URL http://dx.doi.org/10.1103/PhysRevLett.86.4552.

[158] W. A. Caldwell, J. H. Nguyen, B. G. Pfrommer, F. Mauri, S. G. Louie, and R. Jeanloz, Structure, bonding, and geochemistry of xenon at high pressures. *Science* **277**, 930 (1997), URL http://dx.doi.org/10.1126/science.277.5328.930.

[159] K. A. Goettel, J. H. Eggert, I. F. Silvera, and W. C. Moss, Optical evidence for the metallization of xenon at 132(5) GPa. *Phys. Rev. Lett.* **62**, 665 (1989), URL http://dx.doi.org/10.1103/PhysRevLett.62.665.

[160] C. Sanloup, B. C. Schmidt, E. M. C. Perez, A. Jambon, E. Gregoryanz, and M. Mezouar, Retention of xenon in quartz and Earth's missing xenon. *Science* **310**, 1174 (2005), URL http://dx.doi.org/10.1126/science.1119070.

[161] C. Sanloup, S. A. Bonev, M. Hochlaf, and H. E. Maynard-Casely, Reactivity of xenon with ice at planetary conditions. *Phys. Rev. Lett.* **110**, 265501 (2013), URL http://dx.doi.org/10.1103/PhysRevLett.110.265501.

[162] D. Y. Jung, *Ab initio studies in high pressure geochemistry*, Ph.D. thesis, ETH Zürich (2008).

[163] Q. Zhu, D. Y. Jung, A. R. Oganov, C. W. Glass, C. Gatti, and A. O. Lyakhov, Stability of xenon oxides at high pressures. *Nature Chemistry* **5**, 61 (2013), URL http://dx.doi.org/10.1038/nchem.1497.

[164] A. Hermann and P. Schwerdtfeger, Xenon suboxides stable under pressure. *J. Phys. Chem. Lett.* **5**, 4336 (2014), URL http://dx.doi.org/10.1021/jz502230b.

[165] R. O. Pepin and D. Porcelli, Origin of noble gases in the terrestrial planets. *Rev. Mineral. Geochem.* **47**, 191 (2002), URL http://dx.doi.org/10.2138/rmg.2002.47.7.

[166] A. P. Jephcoat, Rare-gas solids in the Earth's deep interior. *Nature* **393**, 355 (1998), URL http://dx.doi.org/10.1038/30712.

[167] S. S. Shcheka and H. Keppler, The origin of the terrestrial noble-gas signature. *Nature* **490**, 531 (2012), URL http://dx.doi.org/10.1038/nature11506.

[168] K. Lejaeghere, G. Bihlmayer, T. Björkman, P. Blaha, S. Blügel, *et al.*, Reproducibility in density functional theory calculations of solids. *Science* **351**, 1415 (2016), URL http://dx.doi.org/10.1126/science.aad3000.

[169] R. B. Stewart, R. T. Jacobsen, and W. Wagner, Thermodynamic properties of oxygen from the triple point to 300K with pressures to 80 MPa. *J. Phys. Chem. Ref. Data* **20**, 917 (1991), URL http://dx.doi.org/10.1063/1.555897.

[170] O. Sifner and J. Klomfar, Thermodynamic properties of xenon from the triple point to 800K with pressures up to 350 MPa. *J. Phys. Chem. Ref. Data* **23**, 63 (1994), URL http://dx.doi.org/10.1063/1.555956.

[171] A. P. Hammersley, FIT2D: An introduction and overview, Technical Report ESRF97HA02, ESRF (1997).

[172] O. Mathon, A. Beteva, J. Borrel, D. Bugnazet, S. Gatla, *et al.*, The time-resolved and extreme conditions XAS (TEXAS) facility at the European Synchrotron Radiation Facility: the general-purpose EXAFS bending-magnet beamline BM23. *J. Synchrotron Rad.* **22**, 1548 (2015), URL http://dx.doi.org/10.1107/S1600577515017786.

[173] N. Ishimatsu, K. Matsumoto, H. Maruyama, N. Kawamura, M. Mizumaki, *et al.*, Glitch-free X-Ray absorption spectrum under high pressure obtained using nano-polycrystalline diamond anvils. *J. Synchrotron Rad.* **19**, 768 (2012), URL http://dx.doi.org/10.1107/S0909049512026088.

[174] B. Ravel and M. Newville, ATHENA, ARTEMIS, HEPHAESTUS: Data analysis for X-ray absorption spectroscopy using IFEFFIT. *J. Synchrotron Rad.* **12**, 537 (2005), URL http://dx.doi.org/10.1107/S0909049505012719.

[175] A. Dewaele, P. Loubeyre, and M. Mezouar, Equations of state of six metals above 94 GPa. *Phys. Rev. B* **70**, 094112 (2004), URL http://dx.doi.org/10.1103/PhysRevB.70.094112.

[176] S. Anzellini, A. Dewaele, F. Occelli, P. Loubeyre, and M. Mezouar, Equation of state of rhenium and application for ultra high pressure calibration. *J. Appl. Phys.* **115**, 043511 (2014), URL http://dx.doi.org/10.1063/1.4863300.

[177] Y. Akahama and H. Kawamura, Pressure calibration of diamond anvil Raman gauge to 410 GPa. *J. Phys.: Conf. Series* **215**, 012195 (2010), URL http://dx.doi.org/10.1088/1742-6596/215/1/012195.

[178] H. Shimizu, N. Wada, T. Kume, S. Sasaki, Y. Yao, and J. S. Tse, Pressure-induced structural transformation in solid xenon studied by Raman spectroscopy. *Phys. Rev. B* **77**, 052101 (2008), URL http://dx.doi.org/10.1103/PhysRevB.77.052101.

[179] H. Fujihisa, Y. Akahama, H. Kawamura, Y. Ohishi, O. Shimomura, *et al.*, O_8 cluster structure of the epsilon phase of solid oxygen. *Phys. Rev. Lett.* **97**, 085503 (2006), URL http://dx.doi.org/10.1103/PhysRevLett.97.085503.

[180] L. F. Lundegaard, G. Weck, M. I. McMahon, S. Desgreniers, and P. Loubeyre, Observation of an O_8 molecular lattice in the ϵ phase of solid oxygen. *Nature* **443**, 201 (2006), URL http://dx.doi.org/10.1038/nature05174.

[181] N. Bartlett, F. Einstein, D. F. Stewart, and J. Trotter, Crystal structure of $[XeF_5]+$ $[PtF_6]-$. *J. Chem. Soc. (A)* **7**, 1190 (1967), URL http://dx.doi.org/10.1039/J19670001190.

[182] R. F. W. Bader, *Atoms in Molecules – A quantum theory* (Oxford University Press, New York, USA, 1990).

[183] R. S. Mulliken, Electronic population analysis on LCAO–MO molecular wave functions. I. *J. Chem. Phys.* **23**, 1833 (1955), URL http://dx.doi.org/10.1063/1.1740588.

[184] A. J. Morris, R. J. Nicholls, C. J. Pickard, and J. R. Yates, OptaDOS: A tool for obtaining density of states, core-level and optical spectra from electronic structure codes. *Comp. Phys. Comm.* **185**, 1477 (2014), URL http://dx.doi.org/10.1016/j.cpc.2014.02.013.

[185] R. J. Nicholls, A. J. Morris, C. J. Pickard, and J. R. Yates, OptaDOS - a new tool for EELS calculations. *J. Phys.: Conf. Ser.* **371**, 012062 (2012), URL http://dx.doi.org/10.1088/1742-6596/371/1/012062.

[186] J. Yates, X. Wang, D. Vanderbilt, and I. Souza, Spectral and Fermi surface properties from Wannier interpolation. *Phys. Rev. B* **75**, 195121 (2007), URL http://dx.doi.org/10.1103/PhysRevB.75.195121.

[187] P. Vinet, J. Ferrante, J. Rose, and J. Smith, Compressibility of solids. *J. Geophys. Res.* **92**, 9319 (1987), URL http://dx.doi.org/10.1029/JB092iB09p09319.

[188] G. Weck, S. Desgreniers, P. Loubeyre, and M. Mezouar, Single crystal structural characterization of the metallic phase of oxygen. *Phys. Rev. Lett.* **102**, 255503 (2009), URL http://dx.doi.org/10.1103/PhysRevLett.102.255503.

[189] S. Desgreniers, Y. K. Vohra, and A. L. Ruoff, Optical response of very high density solid oxygen to 132 GPa. *J. Phys. Chem.* **94**, 1117 (1990), URL http://dx.doi.org/10.1021/j100366a020.

[190] Y. Akahama, H. Kawamura, D. Häusermann, M. Hanfland, and O. Shimomura, New high-pressure structural transition of oxygen at 96 GPa associated with metallization in a molecular solid. *Phys. Rev. Lett.* **74**, 4690 (1995), URL http://dx.doi.org/10.1103/PhysRevLett.74.4690.

[191] J. L. Huston and H. H. Claassen, Raman spectra and force constants for OsO_4 and XeO_4. *J. Chem. Phys.* **52**, 5646 (1970), URL http://dx.doi.org/10.1063/1.1672838.

[192] H. H. Claassen and G. Knapp, Raman spectrum of xenic acid. *J. Chem. Soc.* pp. 2341–2342 (1964), URL http://dx.doi.org/10.1021/ja01066a008.

[193] T. Seebeck, Magnetische Polarisation der Metalle und Erze durch Temperatur-Differenz. *Abhandlungen der Königlichen Preußischen Akademie der Wissenschaften zu Berlin* pp. 265–373 (1822).

[194] H. J. Goldsmid, *Introduction to thermoelectricity* (Springer, Heidelberg, 2010).

[195] A. Bulusu and D. G. Walker, Review of electronic transport models for thermoelectric materials. *Superlattices and Microstructures* **44**, 1 (2008), URL http://dx.doi.org/10.1016/j.spmi.2008.02.008.

[196] H. C. Ørsted, Nouvelles expériences de M. Seebeck sur les actions électromagnétiques. *Annales de Chimie et Physique* **22**, 375 (1823).

[197] J. C. A. Peltier, Nouvelles expériences sur la caloricité des courans électriques. *Annales de Chimie et de Physique* **2(LVI)**, 371 (1834).

[198] W. Thomson, On a mechanical theory of thermo-electric currents. *Proc. R. Soc. Edinb.* **III(42)**, 91 (1851).

[199] S. B. Riffat and X. Ma, Thermoelectrics: a review of present and potential applications. *Appl. Therm. Eng.* **23**, 913 (2003), URL http://dx.doi.org/10.1016/S1359-4311(03)00012-7.

[200] L. E. Bell, Cooling, heating, generating power, and recovering waste heat with thermoelectric systems. *Science* **321**, 1457 (2008), URL http://dx.doi.org/10.1126/science.1158899.

[201] X. Zhang and L.-D. Zhao, Thermoelectric materials: Energy conversion between heat and electricity. *J. Materiomics* **1**, 92 (2015), URL http://dx.doi.org/10.1016/j.jmat.2015.01.001.

[202] H. Zervos, Thermoelectric energy harvesting 2016–2026, Technical report, IDTechEx (2016), URL www.idtechex.com/thermo.

[203] M. S. Dresselhaus, G. Chen, M. Y. Tang, R. G. Yang, H. Lee, *et al.*, New directions for low-dimensional thermoelectric materials. *Advanced Materials* **19**, 1043 (2007), URL http://dx.doi.org/10.1002/adma.200600527.

[204] J.-F. Li, W.-S. Liu, L.-D. Zhao, and M. Zhou, High-performance nanostructured thermoelectric materials. *NPG Asia Materials* **2**, 152 (2010), URL http://dx.doi.org/10.1038/asiamat.2010.138.

[205] Y. Q. Cao, X. B. Zhao, T. J. Zhu, X. B. Zhang, and J. P. Tu, Syntheses and thermoelectric properties of Bi_2Te_3/Sb_2Te_3 bulk nanocomposites with laminated nanostructure. *Appl. Phys. Lett.* **92**, 143106 (2008), URL http://dx.doi.org/10.1063/1.2900960.

[206] B. Poudel, Q. Hao, Y. Ma, Y. Lan, A. Minnich, *et al.*, High-thermoelectric performance of nanostructured bismuth antimony telluride bulk alloys. *Science* **320**, 634 (2008), URL http://dx.doi.org/10.1126/science.1156446.

[207] L.-D. Zhao, B.-P. Zhang, W.-S. Liu, and J.-F. Li, Effect of mixed grain sizes on thermoelectric performance of Bi_2Te_3 compound. *J. Appl. Phys.* **105**, 023704 (2009), URL http://dx.doi.org/10.1063/1.3063694.

[208] J. R. Szczech, J. M. Higgins, and S. Jin, Enhancement of the thermoelectric properties in nanoscale and nanostructured materials. *J. Mater. Chem.* **21**, 4037 (2010), URL http://dx.doi.org/10.1039/C0JM02755C.

[209] O. Delaire, J. Ma, K. Marty, A. F. May, M. A. McGuire, *et al.*, Giant anharmonic phonon scattering in PbTe. *Nature Materials* **10**, 614 (2011), URL http://dx.doi.org/10.1038/nmat3035.

[210] Z. T. Tian, J. Garg, K. Esfarjani, T. Shiga, J. Shiomi, and G. Chen, Phonon conduction in PbSe, PbTe, and $PbTe_{1-x}Se_x$ from first-principles calculations. *Phys. Rev. B* **85**, 184303 (2012), URL http://dx.doi.org/10.1103/PhysRevB.85.184303.

[211] S. Kastbjerg, N. Bindzus, M. Sondergaard, S. Johnson, N. Lock, *et al.*, Direct evidence of cation disorder in thermoelectric lead chalcogenides PbTe and PbS. *Adv. Funct. Mat.* **23**, 5477 (2013), URL http://dx.doi.org/10.1002/adfm.201300722.

[212] T. Shiga, J. Shiomi, J. Ma, O. Delaire, T. Radzynski, *et al.*, Microscopic mechanism of low thermal conductivity in lead telluride. *Phys. Rev. B* **85**, 155203 (2012), URL http://dx.doi.org/10.1103/PhysRevB.85.155203.

[213] T. Shiga, T. Murakami, T. Hori, O. Delaire, and J. Shiomi, Origin of anomalous anharmonic lattice dynamics of lead telluride. *Applied Physics Express* **7**, 041801 (2014), URL http://dx.doi.org/10.7567/APEX.7.041801.

[214] J. P. Heremans, V. Jovovic, E. S. Toberer, A. Saramat, K. Kurosaki, *et al.*, Enhancement of thermoelectric efficiency in PbTe by distortion of the electronic density of states. *Science* **321**, 554 (2008), URL http://dx.doi.org/10.1126/science.1159725.

[215] Z. M. Gibbs, H. Kim, H. Wang, R. L. White, F. Drymiotis, *et al.*, Temperature dependent band gap in PbX (X = S, Se, Te). *Appl. Phys. Lett.* **103**, 262109 (2013), URL http://dx.doi.org/10.1063/1.4858195.

[216] Y. Pei, X. Shi, A. LaLonde, H. Wang, L. Chen, and G. J. Snyder, Convergence of electronic bands for high performance bulk thermoelectrics. *Nature* **473**, 66 (2011), URL http://dx.doi.org/10.1038/nature09996.

[217] L.-D. Zhao, V. P. Dravid, and M. G. Kanatzidis, The panoscopic approach to high performance thermoelectrics. *Energy Environ. Sci.* **7**, 251 (2014), URL http://dx.doi.org/10.1039/C3EE43099E.

[218] K. Biswas, J. Q. He, I. D. Blum, C. I. Wu, T. P. Hogan, *et al.*, High-performance bulk thermoelectrics with all-scale hierarchical architectures. *Nature* **489**, 414 (2012), URL http://dx.doi.org/10.1038/nature11439.

[219] X. W. Wang, H. Lee, Y. C. Lan, G. H. Zhu, G. Joshi, *et al.*, Enhanced thermoelectric figure of merit in nanostructured n-type silicon germanium bulk alloy. *Appl. Phys. Lett.* **93**, 193121 (2008), URL http://dx.doi.org/10.1063/1.3027060.

[220] R. Basu, S. Bhattacharya, R. Bhatt, M. Roy, S. Ahmad, *et al.*, Improved thermoelectric performance of hot pressed nanostructured n-type SiGe bulk alloys. *J. Mater. Chem. A* **2**, 6922 (2014), URL http://dx.doi.org/10.1039/C3TA14259K.

[221] A. I. Boukai, Y. Bunimovich, J. Tahir-Kheli, J.-K. Yu, W. A. Goddard III, and J. R. Heath, Silicon nanowires as efficient thermoelectric materials. *Nature* **451**, 168 (2008), URL http://dx.doi.org/10.1038/nature06458.

[222] M. Beekman, D. T. Morelli, and G. S. Nolas, Better thermoelectrics through glass-like crystals. *Nature Materials* **14**, 1182 (2015), URL http://dx.doi.org/10.1038/nmat4461.

[223] B. C. Sales, D. Mandrus, and R. K. Williams, Filled skutterudite antimonides: A new class of thermoelectric materials. *Science* **272**, 1325 (1996), URL http://dx.doi.org/10.1126/science.272.5266.1325.

[224] A. Saramat, G. Svensson, A. E. C. Palmqvist, C. Stiewe, E. Mueller, *et al.*, Large thermoelectric figure of merit at high temperature in Czochralski-grown clathrate $Ba_8Ga_{16}Ge_{30}$. *J. Appl. Phys.* **99**, 023708 (2006), URL http://dx.doi.org/10.1063/1.2163979.

[225] X. Shi, J. Yang, J. R. Salvador, M. Chi, J. Y. Cho, *et al.*, Multiple-filled skutterudites: High thermoelectric figure of merit through separately optimizing electrical and thermal transports. *J. Am. Chem. Soc.* **133**, 7837 (2011), URL http://dx.doi.org/10.1021/ja111199y.

[226] D. J. Voneshen, K. Refson, E. Borissenko, M. Krisch, A. Bosak, *et al.*, Suppression of thermal conductivity by rattling modes in thermoelectric sodium cobaltate. *Nature Materials* **12**, 1028 (2013), URL http://dx.doi.org/10.1038/nmat3739.

[227] S. Hebert, D. Berthebaud, R. Daou, Y. Breard, D. Pelloquin, *et al.*, Searching for new thermoelectric materials: some examples among oxides, sulfides and selenides. *J. Phys.: Condes. Matter* **28**, 013001 (2016), URL http://dx.doi.org/10.1088/0953-8984/28/1/013001.

[228] J. W. Fergus, Oxide materials for high temperature thermoelectric energy conversion. *J. Eur. Ceram. Soc.* **32**, 525 (2012), URL http://dx.doi.org/10.1016/j.jeurceramsoc.2011.10.007.

[229] J. He and Y. Liu, Oxide thermoelectrics: The challenges, progress, and outlook. *J. Mater. Res.* **26**, 1762 (2011), URL http://dx.doi.org/10.1557/jmr.2011.108.

[230] S. Chen and Z. Ren, Recent progress of half-Heusler for moderate temperature thermoelectric applications. *Materials Today* **16**, 387 (2013), URL http://dx.doi.org/10.1016/j.mattod.2013.09.015.

[231] C. Fu, S. Bai, Y. Liu, Y. Tang, L. Chen, *et al.*, Realizing high figure of merit in heavy-band p-type half-Heusler thermoelectric materials. *Nature Communications* **6**, 8144 (2015), URL http://dx.doi.org/10.1038/ncomms9144.

[232] Q. Zhang, Y. Sun, W. Xu, and D. Zhu, Organic thermoelectric materials: Emerging green energy materials converting heat to electricity directly and efficiently. *Adv. Mater.* **26**, 6829 (2014), URL http://dx.doi.org/10.1002/adma.201305371.

[233] L. D. Zhao, S. H. Lo, Y. Zhang, H. Sun, G. Tan, *et al.*, Ultralow thermal conductivity and high thermoelectric figure of merit in SnSe crystals. *Nature* **508**, 373 (2014), URL http://dx.doi.org/10.1038/nature13184.

[234] G. Shi and E. Kioupakis, Quasiparticle band structures and thermoelectric transport properties of p-type SnSe. *J. Appl. Phys.* **117**, 065103 (2015), URL http://dx.doi.org/10.1063/1.4907805.

[235] J. M. Skelton, L. A. Burton, S. C. Parker, A. Walsh, C.-E. Kim, *et al.*, Anharmonicity in the high-temperature *Cmcm* phase of SnSe: soft modes and three-phonon interactions. *Phys. Rev. Lett.* **117**, 075502 (2016), URL http://dx.doi.org/10.1103/PhysRevLett.117.075502.

[236] H. Zhang and D. V. Talapin, Thermoelectric tin selenide: The beauty of simplicity. *Angew. Chem. Int. Ed.* **53**, 9126 (2014), URL http://dx.doi.org/10.1002/anie.201405683.

[237] J. P. Heremans, Thermoelectric materials: The anharmonicity blacksmith. *Nature Physics* **11**, 990 (2015), URL http://dx.doi.org/10.1038/nphys3542.

[238] L.-D. Zhao, G. Tan, S. Hao, J. He, Y. Pei, *et al.*, Ultrahigh power factor and thermoelectric performance in hole-doped single-crystal SnSe. *Science* **351**, 141 (2016), URL http://dx.doi.org/10.1126/science.aad3749.

[239] C.-L. Chen, H. Wang, Y.-Y. Chen, T. Day, and G. J. Snyder, Thermoelectric properties of p-type polycrystalline SnSe doped with Ag. *J. Mater. Chem. A* **2**, 11171 (2014), URL http://dx.doi.org/10.1039/c4ta01643b.

[240] S. Sassi, C. Candolfi, J.-B. Vaney, V. Ohorodniichuk, P. Masschelein, *et al.*, Assessment of the thermoelectric performance of polycrystalline p-type SnSe. *Appl. Phys. Lett.* **104**, 212105 (2014), URL http://dx.doi.org/10.1063/1.4880817.

[241] F. Serrano-Sánchez, M. Gharsallah, N. M. Nemes, F. J. Mompean, J. L. Martinez, and J. A. Alonso, Record Seebeck coefficient and extremely low thermal conductivity in nanostructured SnSe. *Appl. Phys. Lett.* **106**, 083902 (2015), URL http://dx.doi.org/10.1063/1.4913260.

[242] J. Carrete, N. Mingo, and S. Curtarolo, Low thermal conductivity and triaxial phononic anisotropy of SnSe. *Appl. Phys. Lett.* **105**, 101907 (2014), URL http://dx.doi.org/10.1063/1.4895770.

[243] C. W. Li, J. Hong, A. F. May, D. Bansal, S. Chi, *et al.*, Orbitally driven giant phonon anharmonicity in SnSe. *Nature Physics* **11**, 1063 (2015), URL http://dx.doi.org/10.1038/nphys3492.

[244] J. Hong and O. Delaire, Electronic instability and anharmonicity in SnSe (2016), pre-print submitted to ArXiv:1604.07077v2 [cond-mat.mtrl-sci], URL https://arxiv.org/abs/1604.07077.

[245] S. Lee, K. Esfarjani, T. Luo, J. Zhou, Z. Tian, and G. Chen, Resonant bonding leads to low lattice thermal conductivity. *Nature Communications* **5**, 3525 (2014), URL http://dx.doi.org/10.1038/ncomms4525.

[246] A. J. Morris, C. J. Pickard, and R. J. Needs, Hydrogen/silicon complexes in silicon from computational searches. *Phys. Rev. B* **78**, 184102 (2008), URL http://dx.doi.org/10.1103/PhysRevB.78.184102.

[247] P. Zaleski-Ejgierd and P. M. Lata, Krypton oxides under pressure. *Sci. Rep.* **6**, 18938 (2016), URL http://dx.doi.org/10.1038/srep18938.

[248] A. P. Bartók, M. C. Payne, R. Kondor, and G. Csányi, Gaussian approximation potentials: The accuracy of quantum mechanics, without the electrons. *Phys. Rev. Lett.* **104**, 136403 (2010), URL http://dx.doi.org/10.1103/PhysRevLett.104.136403.

Appendix A

The Variational Method

The energy E of a system is the expectation value of the system's Hamiltonian $\hat{H}$ with respect to its wavefunction $|\Psi\rangle$:

$$E = \langle\Psi|\hat{H}|\Psi\rangle\,. \tag{A.1}$$

We can express $|\Psi\rangle$ in the basis of the eigenfunctions of the Hamiltonian, denoted by $|\psi_n\rangle$:

$$|\Psi\rangle \;=\; \sum_n a_n\,|\psi_n\rangle\,. \tag{A.2}$$

We normalise $|\Psi\rangle$ such that $\langle\Psi|\Psi\rangle = \sum_n |a_n|^2 = 1$. By inserting (A.2) into (A.1), we can obtain:

$$\begin{aligned} E \;&=\; \sum_n \sum_{n'} a_n^* a_{n'}\,\langle\psi_n|\,\hat{H}\,|\psi_{n'}\rangle \\ &=\; \sum_n \sum_{n'} a_n^* a_{n'} E_{n'} \delta_{n,n'} \\ &=\; \sum_n |a|^2 E_n \\ &=\; E_0 + \sum_n |a|^2\,(E_n - E_0)\,, \end{aligned} \tag{A.3}$$

where E_0 is the ground-state energy. In the last line we have made use of the normalisation condition on the coefficients $\{a\}$. Since $E_n \geqslant E_0$ (by the definition of the ground state energy), we conclude that

$$E_0 \leqslant \langle\Psi|\hat{H}|\Psi\rangle \tag{A.4}$$

for any wavefunction $|\Psi\rangle$. Thus the ground state energy is the variational minimum of the the expectation value of the Hamiltonian with respect to the wavefunction of the system.

Appendix B

Fitting Parameters for XAS Data

The fitting parameters for the Xe_2O_5 X-ray absorption spectroscopy (XAS) data are provided in Table B.1 below. Two models were used: a simple two-shell model, and a model assuming the Xe_2O_5 structure. The first part of the table lists the parameters for each model, and the second part of the table lists the values of the fitted parameters. ΔE is the energy offset parameter; N is the number of neighbours for a given shell, with R being the distance between the neighbours; $\Delta\sigma^2$ is the mean-squared relative displacement. Reduced χ^2 is the statistical mean square deviation between the data and the fit. The error bars correspond to a 67% level of confidence in the least square fit. Fitting of experimental data was performed by Agnès Dewaele and Sakura Pascarelli.

	Models					
	Two-shells fit			Xe_2O_5 fit		
Free fitting parameters	ΔE, δR_{O}, δR_{Xe}, $\Delta\sigma^2_{\mathrm{O}}$, $\Delta\sigma^2_{\mathrm{Xe}}$, N_{O}, N_{Xe}			ΔE, $\delta R_{\mathrm{O_S}}$, $\delta R_{\mathrm{O_L}}$, δR_{Xe}, $\Delta\sigma^2_{\mathrm{O}}$, $\Delta\sigma^2_{\mathrm{Xe}}$		
Number of free parameters	7			6		
Degrees of freedom	14			15		
	Fitted parameters values					
	Two-shells fit			Xe_2O_5 fit		
Reduced χ^2	55			38		
ΔE (eV)	10(1)			10.0(9)		
	N	R (Å)	$\Delta\sigma^2$ ($\times 10^{-3}$Å^2)	N	R (Å)	$\Delta\sigma^2$ ($\times 10^{-3}$Å^2)
Xe-O_S				0.5	1.814(8)	3.5(7)
Xe-O_S	3.0(5)	1.93(1)	3(1)	4	1.950(8)	3.5(7)
Xe-O_S				2	2.269(8)	3.5(7)
Xe-O_L				2	2.40(2)	3.5(7)
Xe-O_L				2	2.65(2)	3.5(7)
Xe-Xe	5.0(6)	3.165(5)	2.7(5)	4	3.162(4)	2.0(2)

Table B.1 Fitting parameters for Xe_2O_5 X-ray absorption spectroscopy data